12

Sönke Teichel

Optimized Design of Mixed Flow Compressors for an Active High-Lift System

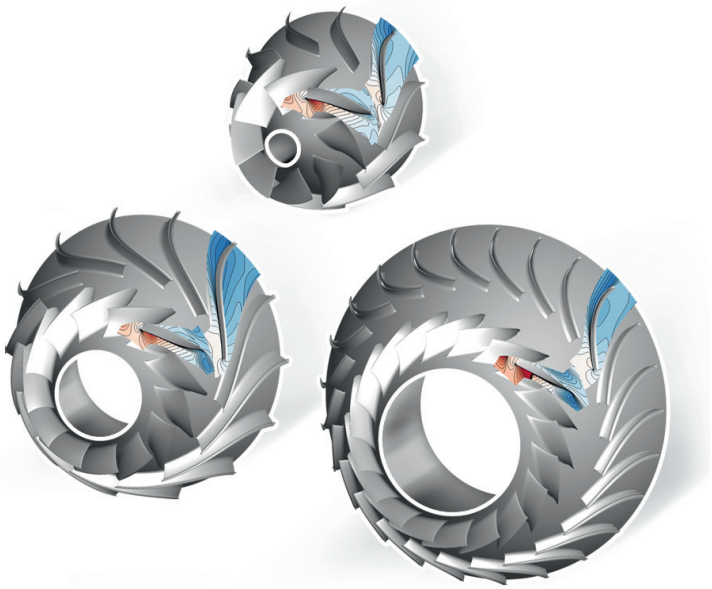

Berichte aus dem Institut für
Turbomaschinen und Fluid-Dynamik
Band 12/2018
Herausgeber: Jörg Seume

Institut für Turbomaschinen
und Fluid-Dynamik

Optimized Design of Mixed Flow Compressors for an Active High-Lift System

Von der Fakultät für Maschinenbau
der Gottfried Wilhelm Leibniz Universität Hannover
zur Erlangung des akademischen Grades
Doktor-Ingenieur
genehmigte Dissertation

von
Sönke Holger Teichel, M.Sc.

2018

Schlagwörter:
Auslegung, Diagonalverdichter, Optimierung

Keywords:
Design, Mixed-Flow Compressor, Optimization

1. Referent: Prof. Dr.-Ing. Jörg Seume
2. Referent: Prof. Dr. Tom Verstraete

Tag der Promotion: 14.12.2017

Zusammenfassung

Zur Unterstützung eines aktiven Hochauftriebssystems für künftige, zivile Verkehrsflugzeuge sind kompakte, elektrisch angetriebene Verdichter erforderlich, welche den aktuellen Stand der Technik bezüglich der Stufenbelastung und Kompaktheit überschreiten. Um die anspruchsvollen Verdichteranforderungen wie ein hohes Totaldruckverhältnis, geringe Größe, geringes Gewicht und hohen Wirkungsgrad (hohe Leistungsdichte) zu erfüllen, wird ein automatisierter Auslegungsprozess für einstufige, transsonische Verdichter entwickelt. Dieser Auslegungsprozess koppelt einen evolutionären Optimierungsalgorithmus mit automatisierten 3-D Strömungs- und Festigkeitssimulationen. Dadurch ist es möglich, einen weiten Auslegungsbereichs zu untersuchen und gleichzeitig die komplexen Randbedingungen in der aerodynamischen Verdichterauslegung zu berücksichtigen.

Die resultierenden Verdichter decken den benötigten Betriebsbereich vollständig ab. Sie erreichen Totaldruckverhältnisse über 2,3 bei korrigierten Massenströmen von 1,1 kg/s mit hohen Totalwirkungsgraden im Bereich von 85% bis 90%. Die Verdichter zeichnen sich durch eine signifikante radiale Strömungskomponente, hohe Seitenwandsteigung, niedrige Schaufel-Höhen-zu-Seiten-Verhältnisse und hohe Schaufelteilungs-zu-Sehnenlängen-Verhältnisse aus. Die Verdichter ähneln Diagonalverdichtern, haben allerdings typische Eigenschaften von Axialverdichtern wie rein axiale Ein- und Ausströmung. Aufgrund ihrer hohen Stufenbelastung und geringen spezifischen Drehzahl überschreiten die resultierenden Verdichter den konventionellen Auslegungsbereich von Diagonalverdichtern. Eine Auslegungsrichtlinie wird entwickelt, um die Erweiterung des Auslegungsbereichs für die zukünftige Auslegung ähnlicher Verdichter darzustellen.

Die Untersuchung des weiten Auslegungsbereichs hat deutliche Freiheitsgrade in der Auslegung der Verdichter für den gegeben Anwendungsfall gezeigt. Der geforderte Betriebsbereich kann mit Verdichtern unterschiedlicher Drehzahl und Größe bei vergleichbar hohen Wirkungsgraden abgedeckt werden. Dies erlaubt zukünftig die Berücksichtigung weiterer Auslegungsparameter des aktiven Hochauftriebssystems und die Optimierung des Gesamtsystems durch gezielte Auswahl eines geeigneten Verdichterentwurfs.

Für diese Maschinen wird ein charakteristischer, neuer Strömungseffekt beschrieben, der sich als flaches, ovales, Blasen-ähnliches Gebiet geringer Strömungsgeschwindigkeit am Austritt der Rotorpassage nahe dem Gehäuse bemerkbar macht. Es wird gezeigt, dass der Ursprung dieses Effekts nicht-viskos ist, viskose Effekte und der Einfluss der Schaufelspitzenströmung jedoch einen bedeutenden Einfluss auf die endgültige Form des resultierenden Gebiets geringer Strömungsgeschwindigkeit haben. Der Strömungseffekt ist eine direkte Folge aus der notwendigen, hohen Belastung der Verdichter, welche sich in der hohen Belastung der Rotorhinterkanten und großer Gehäusesteigung widerspiegelt. Der Strömungseffekt verursacht keine unverhältnismäßig hohen Verluste und wirkt sich daher nicht entscheidend negativ auf das Betriebsverhalten der Verdichter aus.

Abstract

To support an active high-lift system (AHLS) for future civil aircraft small, electrically powered compressors are required, which exceed the current state of the art concerning stage loading and compactness. To satisfy the requirements of these compressors concerning high pressure ratio, small size, low mass, and high efficiency (high power density) an automated design process for single stage, transonic compressors is developed. This designs process couples an evolutionary optimization algorithm with automated 3-D fluid and structural simulation processes. It allows to investigate a wide compressor design space to consider the significant requirements of the active high-lift system in the aerodynamic compressor design.

The resulting compressor designs cover the required operating range with total pressure ratios larger than 2.3 at a corrected mass flow of 1.1 kg/s and high total efficiencies above 85 to 90%. The compressor designs are characterized by a significant radial flow component, high endwall slope, low blade aspect ratio, and high solidity. The designs resemble mixed flow compressors but have typical characteristics of axial flow compressors like axial in- and outflow. Having very high stage loading at low specific speed, the designs significantly exceed the conventional design space of mixed flow compressors. A design guideline was developed to make use of this design space extension for future design processes of similar compressors.

By investigating a wide design space, it was found that there is a significant degree of freedom in the compressor design for this application. The required operating range is achieved by different compressors over a wide range of rotational speeds and sizes at high efficiency. This allows the future consideration of additional design parameters of the active high-lift system and the optimization of the overall system by purposefully selecting an appropriate compressor design.

For the developed compressor type a new, characteristic flow effect is described which is defined by a flat, oval, "bubble" shaped region of low flow momentum in the tip-trailing edge region of the rotor passage. It is shown that the origin of this effect is inviscid but that its final shape is largely determined by viscous effects and the interaction with the tip clearance flow. The flow effect is inherent to the design of highly loaded compressors with high rotor trailing edge loading and high shroud slope. It does not cause significant losses and therefore does not cause a considerable performance penalty.

Acknowledgments

The presented work was done as part of the project B4 "Compact Compressors" of the Collaborative Research Centre 880 "Efficient High-Lift for Future Civil Aircraft" which is funded by the German science foundation (DFG). I would like to thank the initiators of this project for the opportunity to work on this fascinating topic.

I am very grateful to my Ph.D. advisor Prof. Jörg Seume for the advice, support, and trust offered over the course of this Ph.D. project. The knowledge and experience acquired during this time is invaluable and will be an important enrichment of my future professional and personal life.

I am thankful to my second advisor Prof. Tom Verstraete for not only allowing the use of his optimization and turbomachinery design environment CADO and adjusting it to the needs of the project but also for the patience of introducing me to many new aspects of these fields.

Gratitude is also owed to the German Aerospace Center (DLR) for allowing the use their turbomachinery CFD suite TRACE.

Many thanks to my colleagues and especially to my officemate for the many helpful discussions, advice and friendship at any stage of this work.

Finally, thank you to my family for all the support.

The author

Table of Contents

List of Figures

List of Tables

Nomenclature

Abbreviations

Symbol	Description
a.s.l.	altitude **a**bove **s**ea **l**evel
blisk	**bl**aded d**isk**
CADO	**C**omputer **A**ided **D**esign and **O**ptimization Tool
CFD	**C**omputational **F**luid **D**ynamics
CSM	**C**omputational **S**olid **M**echanics
DFG	German science organization (German: **D**eutsche **F**orschungs**g**emeinschaft)
ISA	**I**nternational **S**tandard **A**tmopsphere
RANS	**R**eynolds **A**veraged **N**avier **S**tokes equations
TRACE	**T**urbomachinery **R**esearch **A**erodynamic **C**omputational **E**nvironment
AHLS	**A**ctive **H**igh-**L**ift **S**ystem
EPHLS	**E**lectrically **P**owered Active **H**igh-**L**ift **S**ystem
SFB	Collaborative Research Centre (German: **S**onder**f**orschungs**b**ereich)
STOL	**S**hort **T**ake- **O**ff and **L**anding

Dimensionless Numbers

Symbol	Description	Definition
ω_s	specific speed	Eqn. (4.1)
ϕ	compressor flow coefficient	Eqn. (2.21)
ψ	compressor work coefficient	Eqn. (3.11)
σ	solidity	Eqn. (3.8)
C_μ	jet momentum coefficient of the AHLS	Eqn. (2.1)
C_p	pressure recovery coefficient	Eqn. (2.3)
D_s	specific diameter	Eqn. (4.2)

r	compressor reaction	Eqn. (3.12)
DF	diffusion factor	Eqn. (3.7)
Ma	Mach number	Eqn. (2.19)

Greek Symbols

Symbol	**Description**	**Units**	**Definition**
α	absolute flow angles	$^\circ$	-
β	relative flow angles	$^\circ$	-
Δ	difference	-	Eqn. (2.10)
η	efficiency	-	Eqn. (2.9)
κ	specific heat ratio	-	Eqn. (2.1)
Π	pressure ratio	-	Eqn. (2.4)
ρ	density	$\frac{\mathrm{kg}}{\mathrm{m}^3}$	Eqn. (2.1)
Θ	flow turning	$^\circ$	Fig. 3.3

Roman Symbols

Symbol	**Description**	**Units**	**Definition**
a	speed of sound	$\frac{\mathrm{m}}{\mathrm{s}}$	Eqn. (2.19)
A	area	m^2	Eqn. (2.1)
c	absolute fluid velocity	$\frac{\mathrm{m}}{\mathrm{s}}$	Eqn. (2.1)
C	Essons number	$\frac{\mathrm{VAs}}{\mathrm{m}^3}$	Eqn. (3.23)
c_p	specific heat	$\frac{\mathrm{J}}{\mathrm{kg}\cdot\mathrm{K}}$	Eqn. (4.8)
d	diameter	m	Eqn. (3.23)
F	loss scaling factor	-	Eqn. (2.17)
h	enthalpy	$\frac{\mathrm{J}}{\mathrm{kg}}$	Eqn. (3.1)
J	mass momentum of inertia	$\mathrm{kg}\cdot\mathrm{m}^2$	Eqn. (5.7)
l	length	m	Eqn. (3.8)
M	torque	Nm	Eqn. (3.24)
$\dot{m}$	mass flow rate	$\frac{\mathrm{kg}}{\mathrm{s}}$	Eqn. (2.1)
n	rotational speed	s^{-1}	Eqn. (2.19)
P	power	W	Eqn. (3.23)

p	pressure	Pa	Eqn. (2.1)
r	radius	m	Eqn. (2.19)
R	gas constant for air	$\frac{\mathrm{J}}{\mathrm{kg \cdot K}}$	Eqn. (2.1)
s	blade spacing	m	Eqn. (3.8)
T	temperature	K	Eqn. (2.1)
u	circumferential velocity	$\frac{\mathrm{m}}{\mathrm{s}}$	Eqn. (3.3)
$\dot{V}$	volumetric flow rate	$\frac{\mathrm{m}^3}{\mathrm{s}}$	Eqn. (4.1)
w	velocity relative to rotating system	$\frac{\mathrm{m}}{\mathrm{s}}$	Eqn. (3.4)
$\dot{W}$	power	W	Eqn. (3.1)

Subscripts

Symbol	**Description**	**Definition**
∞	Undisturbed Free Stream	Eqn. (2.1)
u	circumferential velocity component	Eqn. (2.19)
1	reference plane rotor inlet	Eqn. (3.1)
2	reference plane rotor outlet	Eqn. (3.1)
3	reference plane stator outlet	Eqn. (3.1)
ax	axial velocity component	Eqn. (3.5)
comp	compressor	Eqn. (2.4)
corr	value corrected for ambient conditions	Eqn. (2.20)
isen	referencing isentropic change of fluid properties	Eqn. (4.1)
jet	blowing jet of the AHLS	Eqn. (2.1)
mot	electrical motor	Eqn. (2.15)
PE	power electronics	Eqn. (2.15)
poly	referencing polytropic change of fluid properties	Eqn. (2.9)
r	radial velocity component	Eqn. (3.5)
ref	reference	Eqn. (2.1)
s	static flow parameter	Eqn. (2.7)
t	total flow parameter	Eqn. (2.7)

1 Introduction

In the report "Flight Path 2050" by the European Commission (2011) a vision for future aviation in Europe is formulated. The pursuit of this vision aims at ensuring competitiveness of Europe as a global player in aviation technology as well as to foster integration and cohesion of the European Union through better mobility. Among increased safety, reliability, and improved social acceptance one of the central goals defined in this report is the efficient and seamless air travel. Exemplary, these goals are illustrated by the objective to achieve door-to-door travel times of less than 4 hours for 90% of European air travel, while reducing noise and emissions by more than 65% compared to the state of the art in 2000.

The Collaborative Research Centre 880 (in German: "Sonderforschungsbereich - SFB 880") was initiated to approach this objective. The underlying research idea is that aircraft with increased lift are able to service airports with shorter runways which can be located more closely to populated areas reducing the door-to-door travel time compared to conventional aircraft. The possible lower take-off and landing velocities due to higher lift decrease the level of noise immission. The steeper take-off and landing trajectories of these aircraft reduce the area which is subject to noise immission improving the integration of air travel in populated areas. The research hypothesis of the SFB 880 is that additional significant lift increase of civil aircraft can only be achieved with active high-lift systems (AHLS). These systems require additional power to increase the lift of an aircraft. When using AHLS the gain needs to be carefully balanced with the additional power demand, mass, and complexity introduced to the existing aircraft system. For these reasons the application of AHLS was in the past limited to military, and search and rescue aircraft for which short take-off and landing (STOL) capabilities were more critical than efficiency. For the application in future civil aircraft, the work of the SFB 880 focuses on the fundamental research of the technology of efficient AHLS (see (Radespiel 2015)).

The investigated AHLS uses a combination of Coanda jet blowing at the landing flap and boundary layer suction upstream of the flap. The Coanda jet allows high flow turning at the flap by energizing the boundary layer flow which would otherwise tend to separate. The boundary layer suction reduces the boundary layer thickness upstream of the jet and thus reduces the required power of the jet. Previous aircraft utilizing jet blowing for active lift generation, like the Lockheed F-104 Starfighter, usually used bleed air from the compressor of the aircraft engine to provide the required air mass flow rate. These systems are comparably simple and the increased mass due to the ducting in the wings does not influence the aircraft design drastically. One major disadvantage is that, due to the additional bleed air, a larger aircraft engine with larger intake needs to be incorporated leading to a significant efficiency penalty during cruise flight. In

the AHLS investigated by the SFB 880 the suction and blowing air mass flow rate is provided by distributed, electrically powered compressors at each flap of the wing. With the coupling of suction and blowing, lower blowing mass flow, higher system flexibility, and better integration into the concept of the "All Electric Aircraft" are expected to be advantages of this approach over a conventional bleed air system. The power required by the investigated AHLS is provided by the electric generators in the aircraft engines. Weiss and Heinze (2015) have shown that extracting additional shaft power from the jet engine instead of bleed air requires less enlargement of the aircraft engine intake leading to an efficiency advantage of the electrically powered AHLS during cruise flight. Despite the increased system mass and complexity of this electrically powered active high-lift system (EPHLS), presented in Teichel et al. (2015a), this efficiency advantage leads to lower direct operating costs of the aircraft (measured in costs per seat and kilometer) compared to the conventional bleed air system.

In close cooperation with the Institute of Drive Systems and Power Electronics of Leibniz Universität Hannover, Germany, which is in charge of the design of the electrical components of the system, the underlying project of this work focuses on the design of the compressors of the EPHLS. Since the compressor requirements of this application exceed the current state of the art concerning compactness and loading of the compressor, the conventional compressor design processes did not promise satisfying results. An automated design process, coupled to an optimization algorithm, is developed in order to investigate a wide range of the compressor designs to satisfy the requirements such as confined radial space, high pressure ratio, high power density, wide operating range and limited rotational speed of the electrical drive at high power. With this process, single stage, transonic compressors with corrected mass flow rates between 0.6 and 2 kg/s and total pressure ratios between 1.5 and 2.3 are designed. Preliminary design methods did not reliably represent the investigated design space. The automated design process therefore incorporates 3D CFD (Computational Fluid Dynamics) using RANS (Reynolds Averaged Navier Stokes equations) to model the fluid mechanics of the compressors and CSM (Computational Solid Mechanics) to model the structural loads of the compressor blading. The existing optimization tool CADO (Computer Aided Design and Optimization Tool) by Verstraete (2010a) is used for the optimization process and the parameterized generation of the compressor geometry. An automated design evaluation chain is developed using the CFD solver TRACE (Turbomachinery Research Aerodynamic Computational Environment) presented in Becker et al. (2010) and the CSM solver CalculiX by Dhondt (2004). A parameterization strategy is developed to efficiently cover a wide design space considering only feasible designs.

The consideration of a wide design space using advanced design methods is used to explore the potential for compact, highly loaded compressors for the given application. The underlying research hypothesis of this work is that advanced design methods allow the design of highly efficient, purpose adapted compressors outside the conventional compressor design space. The setup, adaptation, and use of such a design method for a given design task is presented in this work for the EPHLS of the SFB 880. The resulting, unconventional compressor designs are discussed and characterized. On this basis, design guidelines are deduced for the future design of similar compressor types.

2 Definition of the Design Task

In this chapter, the underlying design task of this thesis is described. The design task is defined by the combined requirements of the aircraft design which includes the particular requirements of the aircraft's subsystems. These requirements cover the fields of aerodynamics, structural design, aircraft dynamics and control, electrical component design, and aircraft engine design. As part of the SFB 880 these fields are treated by parallel projects which, through close collaboration, provide the required performance parameters of the EPHLS.

2.1 Fundamentals of the Electrically Powered Active High-Lift System

A reference aircraft design (Radespiel and Heinze 2014) is used to define the requirements and to evaluate the performance of the subsystems of the EPHLS. The reference aircraft considered in this work is shown in Fig. 2.1. The aircraft has a high-wing configuration, single aisle body design, and two turboprop engines in tractor configuration. It is designed to have an operating range of 2000 km, a transport capacity for 200 passengers, and to require a max. runway length of 800 m. Conventional aircraft of this size and operating task require roughly twice the runway length. The required lift to achieve the short take-off and landing capabilities is generated by a distributed active high-lift system which is powered by compressor systems at each of the six flaps of each wing. For further reference, the compressors are numbered starting with one at the aircraft fuselage to six at the aileron.

The cross section view of the wing profile in Fig. 2.2 illustrates the principle of the EPHLS. This system consists of an internally blown flap at the trailing edge of the wing, a flexible leading edge device, and an electrically powered compressor system. To motivate this layout for an active high-lift system some basic principles are introduced below:

In simplified terms, lift generation of a wing can be attributed to the degree of flow turning between the leading and the trailing edge of the wing. Any flow interacting with a wall (in this case the wing surface) develops a so called "boundary layer" flow region where the flow is decelerated from the undisturbed free flow velocity to the velocity of the wall surface (Schlichting and Gersten 2006). If the flow velocity in the boundary layer close to the wall is sufficiently high, the flow is attached and follows the surface camber. For this type of flow regime, wing camber can be used to control the flow turning. If the wing camber is too large or the flow velocity in the boundary layer is not sufficiently high, the flow separates from the surface and does not follow the wing

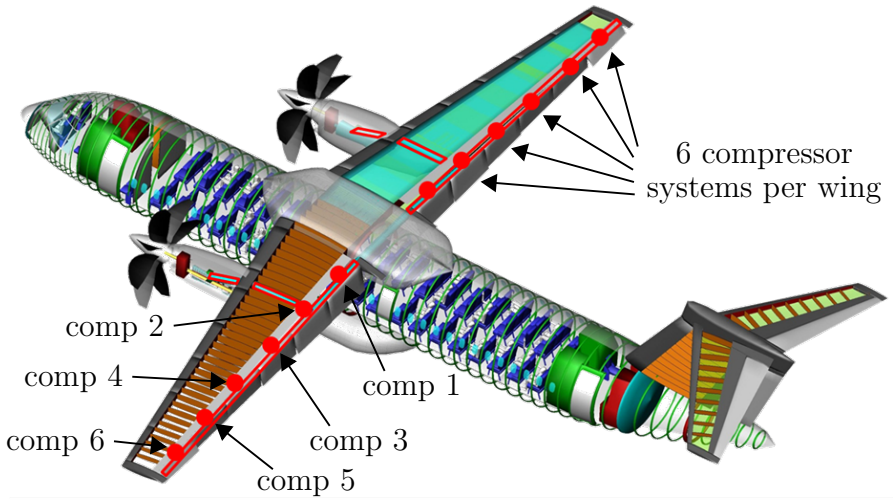

Figure 2.1: Reference aircraft with EPHLS, from Radespiel and Heinze (2014)

camber, decreasing the flow turning. It is therefore critical to prevent flow separation on the wing surfaces to generate lift efficiently. To increase the lift during take-off and landing flaps are used to increase the wing camber. These devices can be classified as passive high-lift systems since they do not require an energy input to generate lift. The active high-lift system illustrated in Fig. 2.2 uses an internally blown flap to avoid flow separation due to the very high camber at the flap. This is done by injecting air with high velocity into the boundary layer, accelerating the flow in this region. The energy required for this active high-lift system depends on the air mass flow rate and velocity of the jet (jet momentum) required to sufficiently accelerate the boundary layer flow.

Apart from increasing wing camber the aircraft's pitch angle is increased (the aircraft nose is directed upwards) to further increase the lift during take-off and landing. This leads to an increased angle of attack of the wing and causes a misalignment (incidence)

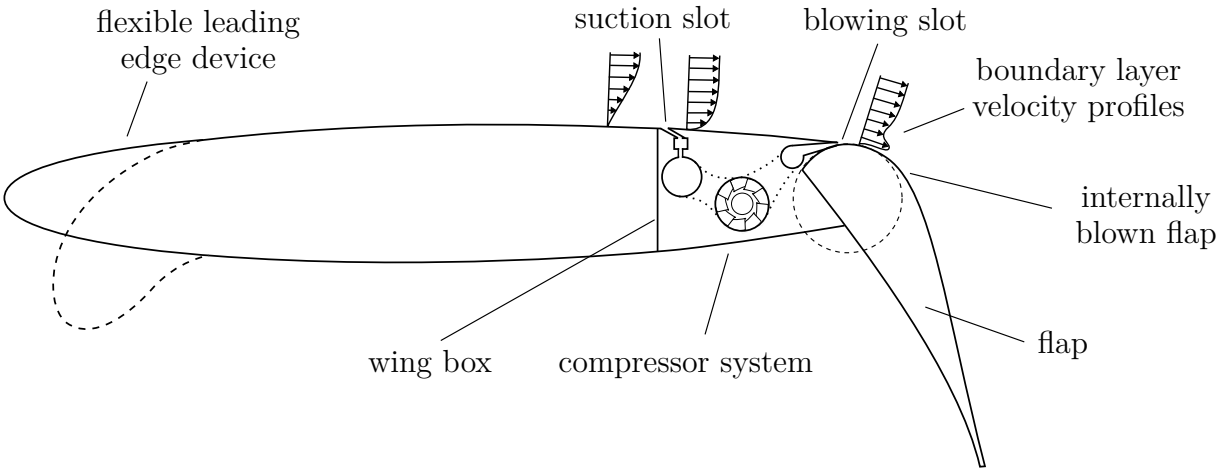

Figure 2.2: Profile of the wing with EPHLS.

of the flow. The flow is then directed towards the bottom (pressure) side of the wing. The pitch is limited by the maximum stall angle of attack of the wing. For higher flow angles of attack, flow separation (stall) on the upper (suction) side of the wing occurs due to the large flow turning required in the leading edge region. Burnazzi and Radespiel (2014) have shown for the EPHLS considered in this work that due to the internally blown flap the lift generation is increased but the maximum stall angle of attack of the wing is decreased. To avoid large flow turning in the leading edge region, leading edge devices are used to adjust the shape of the wing according to the flow direction. In the investigated high-lift system a gapless, flexible leading edge device is used to reduce flow losses and noise generation in comparison with conventional leading edge devices with a gap. With a properly designed leading edge shape, the stall angle of attack and the lift generation of the wing with internally blown flaps are increased which allows to reduce the required momentum of the jet to obtain the target lift generation.

In previous applications, like the Lockheed F-104 Starfighter or the Japanese search and rescue flying boat Shin Meiwa US-1A, the jet required by the internally blown flaps is provided either through bleed air from the aircraft engines or an additional centralized compressor. The use of distributed electrically powered compressors in each flap makes the inclusion of air intakes on the wing surface possible. This offers an additional measure to further increase efficiency of the lift system. Burnazzi and Radespiel (2013) have shown that by using the air intake upstream of the jet as a boundary layer suction slot, the low momentum region in the boundary layer can be significantly reduced. Consequently, the flow velocity in the boundary layer at the jet is higher requiring less blowing momentum to avoid flow separation at the flap than it would without upstream suction. The corresponding boundary layer velocity profiles in Fig. 2.2 illustrate the principle of the boundary layer suction and jet blowing.

In conclusion, the design task of the compressor presented in this work depends on the aerodynamic design of the wing, the resulting mass flow rates, and the pressure ratios required to supply the boundary layer suction and jet momentum. Due to the wing shape, the flaps contribute differently to the lift generation and therefore also the particular design requirements of EPHLS vary for each flap.

2.2 System Requirements

Figure 2.3 illustrates the packaging concept of the EPHLS. For each flap, the ducts, electrical components and the compressor are located in the wing box between the fuel tank inside of the wing and the flap. Each wing box has a spanwise length of 2067 mm; depending on the particular flap the chordwise length of the wing box varies between 300 mm and 630 mm and the height between 100 mm and 500 mm. In relation to their chord wise length and height the wing boxes are comparably long in spanwise direction with an aspect ratio between 0.1 and 0.25. The detailed dimensions of the wing box for each compressor are summarized in appendix A.1. To identify the different flaps with their corresponding compressor systems, the notation introduced in Fig. 2.1 is used.

The inlet duct was designed to provide a uniform suction profile along the full span

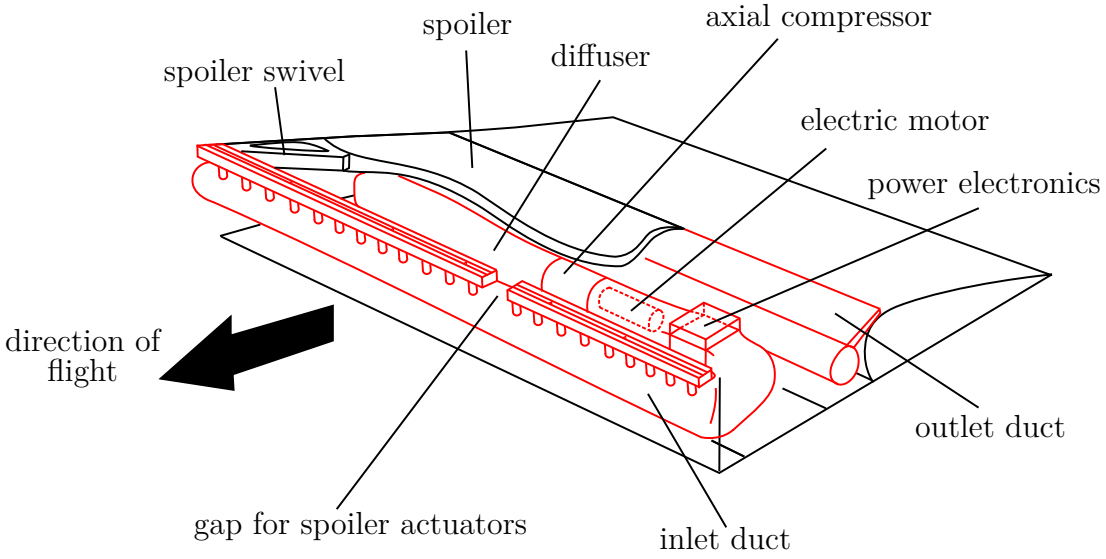

Figure 2.3: EPHLS for each flap.

of the wing box and to redirect the flow by 180° in spanwise direction to enter the compressor section. At the exit of the compressor section, the flow is turned again by 180° to enter the outlet duct. The compressor system generates the required pressure ratio to power the boundary suction and the blowing jet. Since pressure losses in the ducting add to this pressure ratio, the ducts are designed to have a low total pressure loss. This helps to minimize the required total pressure ratio of the compressor. Depending on the mass flow rate required at the particular operating point of the EPHLS, the total pressure loss in the inlet and outlet duct are each estimated to be in a range between 5 to 15% of the particular total inlet pressures (Herrmann 2013).

Since mass is a critical design parameter for any aircraft subsystem, the design of the investigated electrically powered compressor system is carried out with special regards to this aspect. Fundamental design considerations for aircraft design implementing this EPHLS including the generators in the aircraft engines and power lines are discussed in Teichel et al. (2015a). On the basis of a preliminary design process for each system of the EPHLS, the expected mass of each component is summarized in Fig. 2.4. In the current work, the detailed design is done only for the components in the wing boxes which are the compressors, motors, and power electronics. These components acount for more than 25% of the overall mass. The detailed design of these components provides the requirements needed for the upcoming detailed design of the other power supplying components.

To minimize the mass of the EPHLS, the wing box components are highly integrated with one another and tailored to the requirements of the aircraft application. The comparably short operating time of the EPHLS during take-off, approach, and landing allows the use of a transient cooling system. This means that the cooling system is not designed to transfer the complete waste heat generated by the electrical components to an external heat sink. Instead, during the maximum operating time of about 4 min in case of touch-and-go with subsequent landing, the waste heat is largely transferred

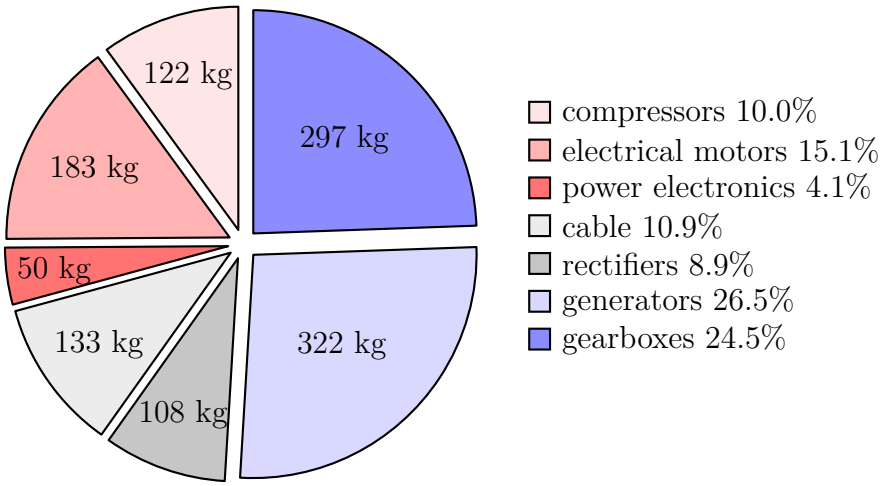

Figure 2.4: Distribution of the overall EPHLS mass from Teichel et al. (2015a)

to the casing and surrounding structures of the EPHLS. Considering this allows the use of a smaller cooling system than would be required for steady state-operation. The mass of the cooling system is reduced by integration of the electrical components namely the electric machine and the power electronics with the compressor. As illustrated in Fig. 2.5, the electric components are positioned in the inlet section of the compressor. This way the inlet air flow can be used to cool the power electronics and the motor. This integrated air cooling approach makes a more complex and heavier water cooling system unnecessary. The increased inlet temperature of the compressor, however, leads to increased power demand for the compression. The high temperature of the air at the compressor exit prohibits effective cooling of the electric components using the outlet air flow. The penalty of the compressor performance due to this particular cooling

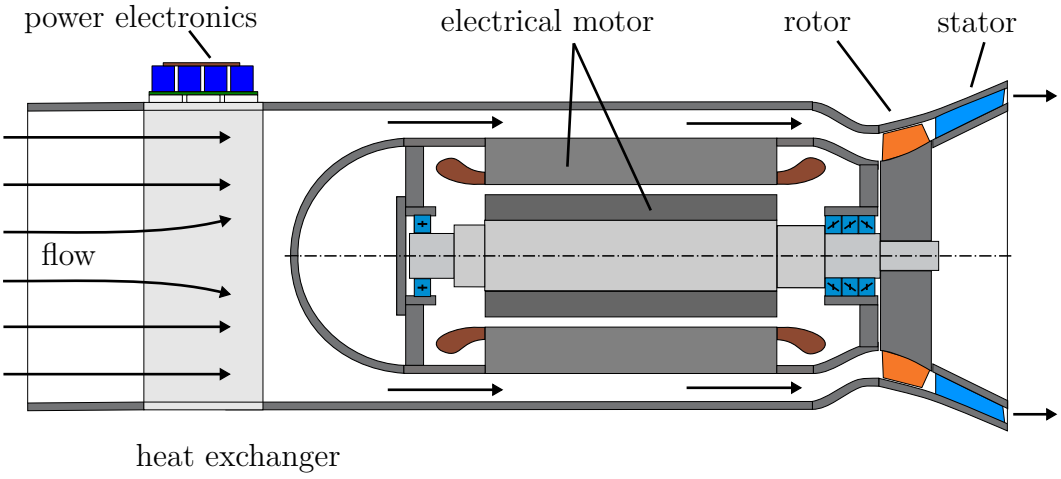

Figure 2.5: Cutaway of the electrically powered compressor system (EPHLS).

concept is accepted to allow a mass optimal system concept without water cooling. Additionally to the required careful thermal design due to the minimalistic, transient cooling system another design requirement of the electric components results from the direct drive of the compressor. Avoiding the additional mass of a gear box connecting motor and compressor this design feature requires higher rotational speeds of the motor which together with the comparably high power exceed the current state of the art for electric machinery.

2.3 Required Operating Points of the Compressors

To obtain the target lift generation of the EPHLS for a particular flight situation, the Coanda jet momentum needs to be adjusted accordingly. The corresponding jet parameters and ambient conditions of the EPHLS are deduced from the preliminary aircraft design process (Weiss and Heinze 2015). The jet momentum is evaluated by Burnazzi and Radespiel (2014) using the jet momentum coefficient C_μ in Eqn. (2.1). This coefficient relates the jet mass flow rate $\dot{m}_{\text{jet}}$ and jet velocity c_{jet} to the density and velocity of the ambient free stream (ρ_∞, c_∞), and a reference wing area A_{ref}.

$$C_\mu = \frac{c_{\text{jet}} \cdot \dot{m}_{\text{jet}}}{\frac{1}{2}\rho_\infty c_\infty^2 A_{\text{ref}}} \tag{2.1}$$

Table 2.1 summarizes the jet momentum coefficients C_μ and jet Mach numbers Ma_{jet} of each operating point of the EPHLS at the corresponding flap. The EPHLS is only in operation during take-off, approach and landing. To represent the varying ambient conditions experienced by the EPHLS application, the design process considers operation at altitudes between 0 m and 1500 m above sea level (a.s.l.). At sea level additionally to the international standard atmosphere (ISA) with $p_{\text{ref}} = 101325$ Pa and $T_{\text{ref}} = 288.15$ K ambient temperatures of -40°C and 50°C are considered. The corresponding ambient temperatures and pressures at 1500 m above sea level are determined using atmospheric models. These ambient conditions are selected according to data from existing airports in order to cover the majority of possible operating conditions of the EPHLS.

The primary task of the EPHLS in all flaps is to generate lift. In addition, the EPHLS in the aileron (flap 6) also needs to support aircraft roll maneuvers. This requires additional jet momentum to allow further increased flow turning of the flap. For a specific flap configuration the corresponding jet momentum coefficients and jet Mach numbers allow determining the required mass flow rate and pressure ratio of the compressors. The relations according to the underlying system of equations is illustrated in Fig. 2.6.

The parameters given in Tab. 2.1 are defined by Eqns. (2.1) to (2.3). With all ambient conditions, denoted by the index $_\infty$, and the pressure recovery coefficient C_p given, the missing parameter to determine the compressor requirements in Eqns. (2.4) and (2.5) is the static exit jet temperature $T_{\text{s,jet,out}}$. Modeling assumptions are summarized in Eqns. (2.11) to (2.18). Neglecting heat loss in the air ducts, the total temperature at the inlet of the EPHLS (i.e. the total inlet temperature of the power electronics $T_{\text{t,PE,in}}$) can be assumed to be equal to the total temperature of the ambient flow $T_{\text{t},\infty}$. With the

Table 2.1: Operating points of the EPHLS.

flight attitude	**altitude**	**EPHLS**	**flight modus**	**jet momentum coefficient**	**jet Mach number**
take-off and approach	0 m a.s.l.	flap 1 - 5	lift	0.024	0.7
		flap 6	lift	0.024	0.7
			maneuver support	0.043	0.96
	1500 m a.s.l.	flap 1 - 5	lift	0.024	0.77
		flap 6	lift	0.024	0.77
			maneuver support	0.043	1.06
landing	0 m a.s.l.	flap 1 - 5	lift	0.036	0.75
		flap 6	lift	0.024	0.75
			maneuver support	0.043	0.83
	1500 m a.s.l.	flap 1 - 5	lift	0.036	0.83
		flap 6	lift	0.024	0.83
			maneuver support	0.043	0.92

same assumption the total temperature of the jet exit flow $T_{\mathrm{t,jet,out}}$ can be taken to be equal to the total compressor outlet temperature $T_{\mathrm{t,comp,out}}$. These assumptions consider friction loss of the flow in the duct which causes total pressure loss through dissipation but does not influence the total temperature of the flow. To determine the compressor total inlet temperature the heat input of the motor and the power electronics to the flow is related to the compressor power (Eqn. (2.10)) in Eqns. (2.12) to (2.15) assuming a 95% efficiency of the power electronics (η_{PE}) and 90% efficiency of the electric machine (η_{mot}). In these equations c_p represents the heat capacity of the flow.

With the definition of the polytropic compressor efficiency in Eqn. (2.9) the total temperature ratio of the compressor can be related to the total pressure ratio of the compressor assuming an efficiency $\eta_{\mathrm{poly}} = 85\%$. To relate the total pressure at compressor outlet to the total pressure of the jet, a total pressure loss of 10% in the exit duct is assumed in Eqn. (2.18). The same pressure loss is assumed in the inlet duct (Eqn. (2.17)). These pressure losses are estimates of the achievable values for the final inlet duct design which is part of the final aircraft design in a later stage of the project. To close the system of equations, Eqns. (2.6) to (2.8) relate the jet mass flow rate $\dot{m}_{\mathrm{jet}}$ to the jet geometry and jet velocity. Also using the fundamental equations for compressible fluids the total and static state of the jet pressure and temperature can be related to the jet velocity. When solved iteratively the given system of equations provides the required compressor mass flow rate $\dot{m}_{\mathrm{comp}}$ and total pressure ratio $\Pi_{\mathrm{t,comp}}$ for all required oper-

Given Parameters:

$$C_\mu = \frac{c_{\text{jet}} \cdot \dot{m}_{\text{jet}}}{\frac{\rho_\infty}{2} {c_\infty}^2 A_{\text{ref}}} \tag{2.1}$$

$$Ma_{\text{jet}} = \frac{c_{\text{jet}}}{\sqrt{\kappa \cdot \text{R} \cdot T_{\text{s,jet,out}}}} \tag{2.2}$$

$$p_{\text{s,jet,out}} = C_p \cdot \frac{\rho_\infty}{2} {c_\infty}^2 + p_{\text{s},\infty} \tag{2.3}$$

Required Parameters:

$$\Pi_{\text{comp}} = \frac{p_{\text{t,comp,out}}}{p_{\text{t,comp,in}}} \tag{2.4}$$

$$\dot{m}_{\text{comp}} = \dot{m}_{\text{jet}} \tag{2.5}$$

Relations:

$$\dot{m}_{\text{jet}} = c_{\text{jet}} \cdot \frac{p_{\text{s,jet,out}}}{\text{R} \cdot T_{\text{s,jet,out}}} \cdot A_{\text{jet}} \tag{2.6}$$

$$\frac{T_{\text{t,jet,out}}}{T_{\text{s,jet,out}}} = \left(1 + \frac{\kappa - 1}{2} Ma_{\text{jet}}^2\right) \tag{2.7}$$

$$\frac{p_{\text{t,jet,out}}}{p_{\text{s,jet,out}}} = \left(1 + \frac{\kappa - 1}{2} Ma_{\text{jet}}^2\right)^{\frac{\kappa}{\kappa - 1}} \tag{2.8}$$

$$\frac{T_{\text{t,comp,out}}}{T_{\text{t,comp,in}}} = e^{\left(\frac{\kappa - 1}{\kappa} \cdot \frac{\ln(\Pi_{\text{comp}})}{\eta_{\text{poly}}}\right)} \tag{2.9}$$

$$P_{\text{comp}} = \dot{m} \cdot c_p \cdot \Delta T_{\text{t,comp}} \tag{2.10}$$

Assumptions:

$$T_{\text{t,PE,in}} = T_{\text{t},\infty} \tag{2.11}$$

$$T_{\text{t,comp,in}} = T_{\text{t},\infty} + \frac{P_{\text{loss,elec}}}{c_p \cdot \dot{m}} \tag{2.12}$$

$$P_{\text{loss,elec}} = P_{\text{loss,mot}} + P_{\text{loss,PE}} \tag{2.13}$$

$$P_{\text{loss,mot}} = P_{\text{comp}} \left(1 - \eta_{\text{mot}}\right) \tag{2.14}$$

$$P_{\text{loss,PE}} = \frac{P_{\text{comp}}}{\eta_{\text{mot}}} \left(1 - \eta_{\text{PE}}\right) \tag{2.15}$$

$$T_{\text{t,jet}} = T_{\text{t,comp,out}} \tag{2.16}$$

$$p_{\text{t,comp,in}} = p_{\text{t},\infty} \cdot F_{\text{loss,duct}} \tag{2.17}$$

$$p_{\text{t,comp,out}} = p_{\text{t,jet}} \cdot F_{\text{loss,duct}} \tag{2.18}$$

Figure 2.6: System of equations to determine compressor requirements.

ating points of the EPHLS. A detailed summary of all resulting compressor operating points is given in App. A.2.

Comparing the compressor's mass flow rate of each operating point in Figs. A.2 through A.5 is misleading since the intake pressure and temperature differ. For the same mass flow rate at different ambient conditions this leads to different volumetric flow rates and therefore different axial flow velocities in the compressor. Operating points which seem to be similar in these figures concerning pressure ratio and mass flow rate can therefore result in very different operating conditions of the compressor concerning the internal flow. To allow better comparison of the operating points at different inlet conditions the particular ambient conditions are usually corrected to a reference condition using a criterion of similarity. In this case similarity in terms of circumferential Mach number and flow coefficient is targeted. For a constant circumferential Mach number the definition in Eqn. (2.19) can be used to relate the rotational speed n at a specific temperature T to a reference rotational speed n_{ref} at a reference temperature T_{ref} (Eqn. (2.20)).

$$Ma_u = \frac{u}{a} = \frac{2\pi r \cdot n}{\sqrt{\kappa R T}} = \frac{2\pi r \cdot n_{\text{ref}}}{\sqrt{\kappa R T_{\text{ref}}}} \Rightarrow \frac{n}{\sqrt{T}} = \frac{n_{\text{ref}}}{\sqrt{T_{\text{ref}}}} \tag{2.19}$$

$$n_{\text{corr}} = n_{\text{ref}} = n\sqrt{\frac{T_{\text{ref}}}{T}} \tag{2.20}$$

The flow coefficient relates the axial flow velocity to the circumferential velocity of the stage of a turbomachine at the mean radius (Eqn. (2.21)). It therefore relates the through flow of a stage to its rotational speed indicating whether the machine has high or low through flow in relation to its rotational speed. Similarity of the flow coefficient in relation to the ambient conditions allows to define a reference mass flow rate. Together with Eqn. (2.20) the corrected mass flow rate $\dot{m}_{\text{corr}}$ in Eqn. (2.22) considers similarity in both circumferential Mach number and flow coefficient.

$$\phi = \frac{c_{ax}}{u} = \frac{\frac{\dot{m}}{\rho A}}{2\pi r \cdot n} = \frac{\frac{\dot{m}_{\text{ref}}}{\rho_{\text{ref}} A}}{2\pi r \cdot n_{\text{ref}}} \Rightarrow \frac{\dot{m}}{\rho \cdot n} = \frac{\dot{m}_{\text{ref}}}{\rho_{\text{ref}} \cdot n_{\text{ref}}} \tag{2.21}$$

$$\dot{m}_{\text{ref}} = \dot{m} \cdot \frac{\rho_{\text{ref}}}{\rho} \cdot \frac{n_{\text{ref}}}{n} = \dot{m} \cdot \frac{p_{\text{ref}}}{p} \cdot \frac{T}{T_{\text{ref}}} \cdot \sqrt{\frac{T_{\text{ref}}}{T}} \tag{2.22}$$

$$\dot{m}_{corr} = \dot{m}_{\text{ref}} = \dot{m} \cdot \frac{p_{\text{ref}}}{p} \cdot \sqrt{\frac{T}{T_{\text{ref}}}} \tag{2.23}$$

Using this definition to plot the required compressor operating points in Fig. 2.7 the data show well defined duty lines for each compressor. The ambient temperature of each operating point is color coded with blue symbols denoting -40°C, gray symbols 15°C, and red symbols 50°C. The shape of the symbol illustrates the flight attitude circular symbols represent take-off, triangles approach, and diamonds landing. Filled symbols represent operating points at sea level and non-filled symbols operating points 1500 m above sea level.

It becomes apparent that compressor 1 to 5 have very similar requirements concerning the pressure ratio and mass flow operating range, while only the magnitude of the mass flow rate changes. This results from the same required jet momentum coefficients and jet Mach numbers specified in Tab. 2.1. Compressor 1, located in the largest flap closest to the aircraft fuselage, needs to provide the largest mass flow rates; the mass flow rate decreases with the decreasing flap size towards the aileron. The requirements of compressor 6 are different due to the significantly higher pressure ratios and the wider operating range concerning both pressure ratio and mass flow rate. This is due to the additional operating points required for maneuver support but also from the lower jet momentum coefficients required during landing. This also extends the operating range further to low mass flow rates and pressure ratios. Low temperatures and high altitudes lead to the most challenging operating points of the compressors with highest through flow and highest pressure ratios. While for the compressors 1-5 this occurs during landing, the maneuver support during approach and take-off is the critical operating point for the aileron compressor 6.

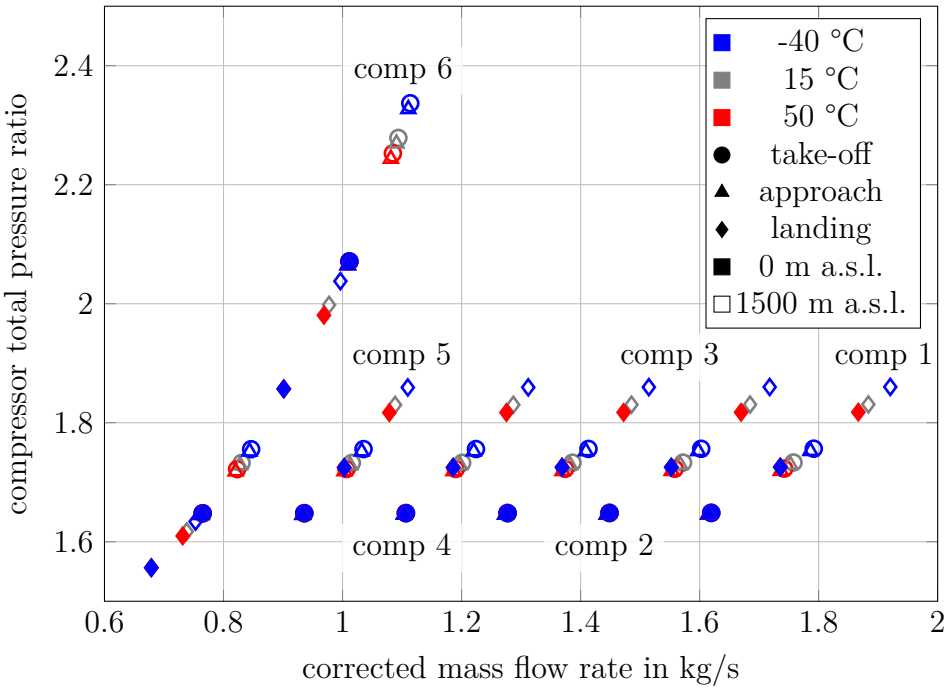

Figure 2.7: Required compressor operating points, mass flow rate normalized to standard atmosphere

The compressor design in this work focuses on compressor 6 to satisfy these challenging requirements. The resulting methodology can then be used to design compressors 1 to 5. For compressor 6 two design points are particularly critical. For aerodynamic design considerations, the operating point during landing at 1500 m a.s.l. and -40°C is most relevant since it requires the highest total pressure ratio of 2.33 and highest through-flow with a corrected mass flow rate of 1.11 kg/s. For system design considerations, the operating point during landing at 1500 m a.s.l. and 50°C is used since it requires the highest isentropic power of more than 65 kW.

3 Fundamentals of the Design Methodology

The following chapter introduces the fundamentals of the methodology used to design compressors for the EPHLS. These include fundamental considerations of compressor design and the methods used to evaluate the corresponding compressor aerodynamics and the structural integrity. Since the design of the compressor depends on the electric machine design, the underlying design principles will be presented briefly. As part of the automated compressor design process, an optimization algorithm is used. The principles introduced here are meant as a reference for the later introduction to the developed design process and results analysis. If not otherwise stated the fundamentals of turbomachinery presented in this section are based on Dixon and Hall (2010) and Traupel (2001).

3.1 Fundamentals of Compressor Design

The distinct feature of turbo compressors is the transfer of energy to a continuous flow of fluid through the use of rotating blades. The purpose of this energy transfer is to maintain a specified flow rate against a pressure gradient. In general, compressor stages are comprised of a rotor blade row to accelerate the flow and a downstream row of stagnant blades, the stator, to decelerate the flow and thereby converting the flow's kinetic energy to thermal energy, i.e. raising the static pressure. This conversion of kinetic energy to thermal energy in turbomachinery is illustrated in Eqn. (3.1). This formulation of the first law of thermodynamics considers only steady state conditions, omits heat transfer and change in potential energy (Traupel 2001). These assumptions are valid over wide range of turbomachinery application since both, heat transfer and change in potential energy generally do not have significant influence on turbomachinery performance.

$$\frac{\dot{W}}{\dot{m}} = (h_2 - h_1) + \frac{1}{2}\left(c_2^2 - c_1^2\right) \tag{3.1}$$

$$h_{tot} = h + c^2 \tag{3.2}$$

Following this formulation the total enthalpy h_{tot} in Eqn. (3.2) is defined as a measure of the total specific energy carried by a fluid. The total enthalpy corresponds to the total temperature T_{tot} and total pressure p_{tot} which themselves relate the kinetic energy of the fluid to the temperature and pressure. The definitions of these parameters for compressible flow were introduced earlier in Eqns. (2.7) and (2.8). Total state variables

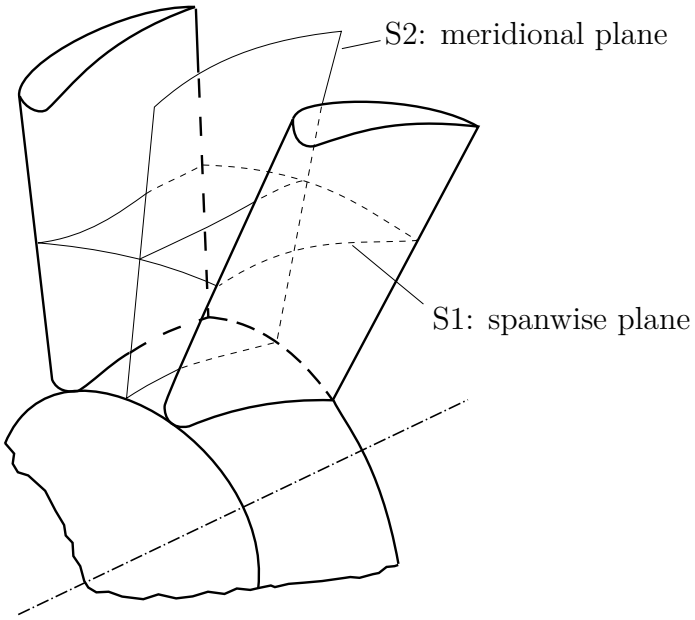

Figure 3.1: Reference planes of an axial compressor, adapted from Grote et al. (2014)

can be interpreted as the state variables present if the flow would be brought to a standstill without losses. In such a process, the kinetic energy would completely converted into rise of pressure and temperature resulting in the total pressure and total temperature. An important question for any turbomachinery design task is to what extend the kinetic energy of the exit flow can be utilized for the specified application. Depending on this design decision, the parameters to evaluate the machine performance are either determined using total or static state variables.

To be able to describe the complex three dimensional flow in turbomachinery with simplified analysis methods, representative planes are used. Figure 3.1 shows a typical blade passage of an axial compressor and the position of these reference planes. The S_2-plane is an axial-radial representation of the flow field in the compressor in which usually circumferentially averaged parameters are regarded. The focus of analysis in this reference plane is the spanwise distribution of flow parameters. The S_1-plane represents the flow between the blades usually at constant spanwise position. The analysis of the representation of the flow in a plane at midspan allows a comprehensive understanding of the fundamental design features of turbomachinery. The fundamental equation used in this reference plane is the Euler work equation (Eqn. (3.3)) which can be deduced from the law of conservation of angular momentum for a steady-state flow as:

$$\frac{\dot{W}}{\dot{m}} = h_{\mathrm{tot},2} - h_{\mathrm{tot},1} = \Delta h_{\mathrm{tot}} = u_2 \cdot c_{u2} - u_1 \cdot c_{u1} \tag{3.3}$$

This equation relates the specific work of a turbomachine to the change of flow swirl (c_u) and blade speeds (u) between rotor inlet ($_1$) and exit ($_2$). To illustrate the flow velocity vectors in a compressor stage, so called velocity triangles are used. Figure 3.2 shows a schematic of a compressor stage blading with the corresponding flow vectors in

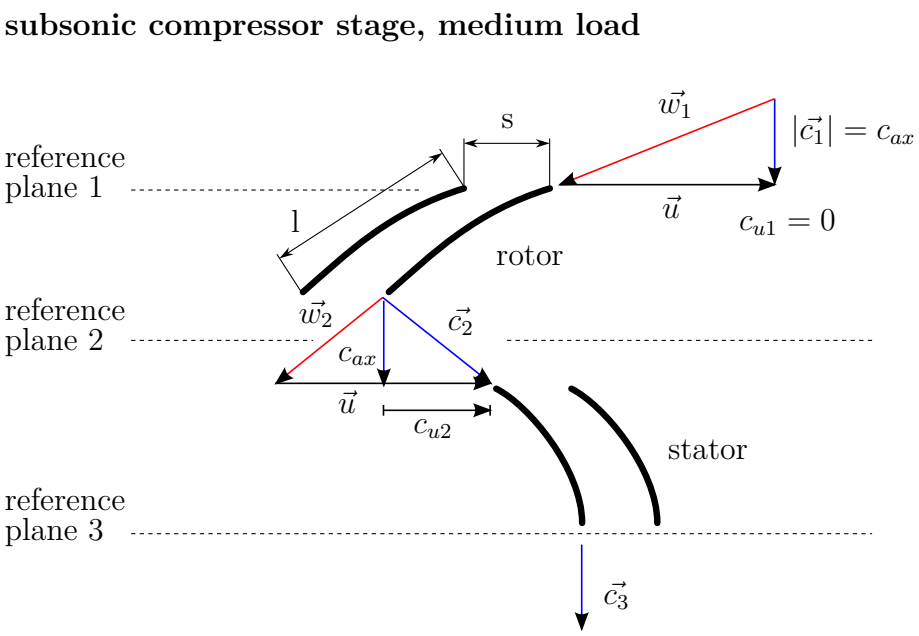

Figure 3.2: Velocity triangles and blading of a typical axial compressor stage in S1 plane.

the S_1-plane. Due to the interaction of the rotating and the stagnant blade row the flow vectors in the relative system $\vec{w}$ and the flow vectors in the absolute system $\vec{c}$ need to be distinguished. These flow vectors are related by the circumferential blade speed $\vec{u}$ according to Eqn. (3.4). The vector components are defined according to the reference system in turbomachinery using the machine axis $(_{ax})$, circumferential direction $(_u)$, and spanwise direction $(_r)$. Each flow vector $\vec{w}$ and $\vec{c}$ is comprised of these components as shown in Eqn. (3.5). For analysis at midspan the radial velocity components are often omitted since they do not contribute to the specific work of the machine and are often negligibly small in the midspan region.

$$\vec{c} = \vec{w} + \vec{u} \tag{3.4}$$

$$|\vec{i}| = \sqrt{{i_{ax}}^2 + {i_u}^2 + {i_r}^2} \quad \text{with:} \quad i = \{w, c\} \tag{3.5}$$

In Fig. 3.2 the flow vectors at rotor inlet (reference plane 1), rotor exit (reference plane 2), and stator exit (reference plane 3) are given. With these relations the Euler work equation can also be formulated in terms of the absolute and relative flow velocities c and w according to Eqn. 3.6.

$$\Delta h_{\text{tot}} = \frac{1}{2}\left[\left({u_2}^2 - {u_1}^2\right) + \left({w_1}^2 - {w_2}^2\right) + \left({c_2}^2 - {c_1}^2\right)\right] \tag{3.6}$$

Without an inlet guide vane there, is no inlet swirl and at the rotor inlet the absolute flow velocity is equal to the axial flow velocity. Since the blades of the rotor rotate, they

do not experience the axial inlet flow $\vec{c_1}$ but the flow vector $\vec{w}_1$ observed in the relative frame of reference. The stagnant stator blading in contrast is subject to the flow vectors in the absolute system of reference. It is characteristic for compressors that the blade passages act as diffusers in their frame of reference. In Fig. 3.2 it is evident that the flow velocity decreases in each blade row: $\vec{w_1} > \vec{w_2}$ and $\vec{c_2} > \vec{c_3}$. Regarding the flow vectors of the rotor in the absolute frame of reference it can be seen that the work input of the rotor blade results in the acceleration of the fluid ($\vec{c_2} > \vec{c_1}$). These relations of the flow vectors illustrate the functional principle of the two blade rows in a compressor stage: The rotor provides the work input and accelerates the flow in the absolute frame of reference increasing the total pressure, while the stator decelerates the flow resulting in increased static pressure.

The diffusion in the blade rows is limited by boundary layer separation on the blade surface. The de Haller criterion $\frac{|\vec{w_2}|}{|\vec{w_1}|}$ and the diffusion factor DF are widely used parameters to assess the degree of diffusion of a blade and to provide established diffusion limits as a guidance in compressor design processes. A deceleration ratio of $\frac{|\vec{w_2}|}{|\vec{w_1}|} \gtrapprox 0.7$ was determined by de Haller (1953) as a limit before boundary layer flow separation causes significant loss in a compressor blade row. Lieblein et al. (1953) defined the diffusion factor DF in Eqn. (3.7), here formulated for the rotor. Additionally to the de Haller number it includes the flow turning ($c_{u2} - c_{u1}$) and the geometric flow guidance of the blade channel (σ). Low values of the diffusion factor imply low diffusion; DF < 0.6 is generally used as limiting range to avoid excessive loss (Cumpsty 2004). The flow guidance is represented using the solidity σ illustrated in Fig 3.2. It is defined in Eqn. (3.8) as the chord (l) to pitch (s) ratio of the blade representing the ratio of blade channel length in relation to blade channel width. High values indicate comparably narrow and long blade channels which provide good flow guidance but also high blockage and increased friction loss. The solidity is often used to determine the number of blades required for a given machine diameter and a given chord length. In that sense high values of solidity indicate a large number of comparably long blades for a given machine.

$$\mathrm{DF} = \left(1 - \frac{|\vec{w_2}|}{|\vec{w_1}|}\right) + \left(\frac{c_{u2} - c_{u1}}{2|\vec{w_1}|}\right) \frac{1}{\sigma} \tag{3.7}$$

$$\sigma = \frac{l}{s} \tag{3.8}$$

Wennerstrom (2000) combines the introduced criteria with Euler's work equation (Eqn. (3.3)) to demonstrate the limiting parameters when increasing the specific work of a compressor stage. Neglecting radius change in the stage this leads to:

$$\Delta h_{\mathrm{tot}} = u \cdot (c_{u2} - c_{u1}) = 2\sigma \cdot u \cdot |\vec{w_1}| \cdot \left(\mathrm{DF} - 1 + \frac{\vec{w_2}}{\vec{w_1}}\right) \tag{3.9}$$

Equation (3.9) shows that with limited blade diffusion, highly loaded compressor stages (i.e. stages with high work input Δh_{tot}) will tend to have high solidity, high rotational speed and increased inlet flow velocities.

The flow vectors of the stage can be characterized using non-dimensional parameters: The flow coefficient ϕ, introduced earlier in Eqn. (2.21), is a measure of the flow capacity

of the machine in relation to its rotational speed. The work coefficient ψ relates the specific work of the machine to the rotational speed according to Eqn. (3.10). Assuming the same rotational speed at rotor in- and outlet this definition simplifies to Eqn. (3.11). Another widely used parameter to characterize turbomachine stages is the reaction r, a measure which indicates the load balance between rotor and stator. Values less than 0.5 indicate a higher loading of the stator while values greater than 0.5 indicate a higher loading of the rotor. There are different definitions used in the literature for the reaction. In this work the most commonly used definition (e.g. (Dixon and Hall 2010), (Traupel 2001)) relating the static enthalpy rise in the rotor to the static enthalpy rise of the stage is used (Eqn. (3.12)). Assuming no inlet swirl, the reaction is a result of the specified flow and load coefficient.

$$\psi = \frac{\Delta h_{\mathrm{tot}}}{u^2} \tag{3.10}$$

$$\psi = \frac{c_{u2} - c_{u1}}{u} \quad \text{for:} \quad u_1 = u_2 = u \tag{3.11}$$

$$\mathrm{r} = \frac{h_2 - h_1}{h_3 - h_1} \tag{3.12}$$

With the flow coefficient, work coefficient,, the state of the fluid at the rotor inlet , and a specified rotational speed, the flow vectors are completely defined. In Fig. 3.3 the flow vectors of different compressor stage designs are illustrated. For the purpose of this analysis, the solidity of all blade rows was set to 1.5. On the top left, with ψ=0.4, a moderately loaded stage with subsonic inflow is represented. Considering a repeating stage ($\vec{c_1} = \vec{c_3}$) and no losses in the stator the resulting reaction is 0.8, the flow deflection Θ in the rotor is about 13°. To make optimum use of the work input of the rotor in a single stage compressor it is desirable to obtain complete flow turning in the stator with no swirl at the stator exit. This way the rotor exit swirl (c_{u2}) is either diffused or turned into the axial flow direction which can be converted into static pressure in a downstream diffuser. To obtain no stator exit swirl, would require a stator flow turning of about -39° for this configuration. The negative sign of the flow turning indicates turning against the direction of rotation. The diffusion in the blade rows is below the limits given by Lieblein et al. (1953).

Dixon and Hall (2010) illustrate the significant parameters to achieve high total pressure ratios in compressors by combining the definition of the polytropic compressor efficiency (η_{poly}) in Eqn. (3.13) with the definition of the stage loading in Eqn. (3.10). According to Eqn. (3.14) high total pressure ratios are obtained for compressors with high stage loading, high rotational speed, and high efficiency.

$$\eta_{\mathrm{poly}} = \frac{\kappa - 1}{\kappa} \frac{\ln\left(\frac{p_2}{p_1}\right)}{\ln\left(\frac{T_2}{T_1}\right)} \tag{3.13}$$

$$\Pi_{\mathrm{tot}} = \left(\frac{\psi \; u^2}{c_p \; T_{\mathrm{tot,in}}} + 1 \right)^{\frac{\kappa \;\; \eta_{\mathrm{poly}}}{\kappa - 1}} \tag{3.14}$$

Increasing the load of the stage to ψ=0.6 without increasing the rotational speed on the bottom left of Fig. 3.3 requires excessive blade turning in both blade rows leading to

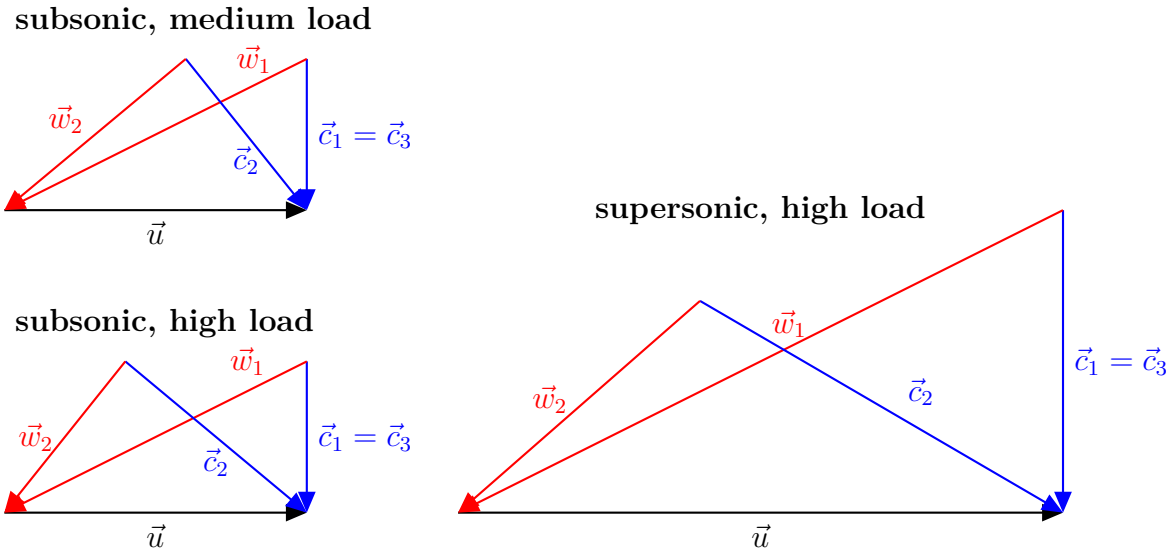

					rotor			stator		
compressor	ϕ	ψ	r	$\lvert\vec{w}_1\rvert$	Θ	$\frac{\lvert\vec{w}_2\rvert}{\lvert\vec{w}_1\rvert}$	DF	Θ	$\frac{\lvert\vec{c}_3\rvert}{\lvert\vec{c}_2\rvert}$	DF
subsonic, medium load	0.5	0.4	0.8	0.6 Ma	13°	0.7	0.42	−39°	0.78	0.43
subsonic, high load	0.5	0.6	0.7	0.6 Ma	25°	0.57	0.61	−50°	0.64	0.62
supersonic, high load	0.5	0.6	0.7	1.2 Ma	15°	0.48	0.7	−60°	0.72	0.57

Figure 3.3: Velocity triangles of repeating axial compressor stages with different specific stage work.

high diffusion factors. To maintain axial inlet flow, the reaction of the stage is lower which increases the load of the stator.

To further increase the specific work of the compressor, the rotational speed is increased for the compressor stage illustrated on the bottom right of Fig. 3.3. This leads to supersonic inlet rotor velocities of Ma=1.2, while the flow velocity in the absolute frame of reference remains subsonic. Decelerating the supersonic flow in the rotor results in a shock wave characterized by a sudden deceleration of the flow, and strong increase in static pressure and density. The consequent decrease of axial velocity reduces the rotor flow turning required in the relative system by about 10° to obtain a specified flow turning in the absolute system compared to the highly loaded subsonic compressor stage. The increased loading of the rotor and the increased stator inlet flow velocity lead to acceptable required diffusion in the stator despite the increased flow turning. The diffusion required in the rotor however violates the traditional limits. Dickens and Day (2011) have shown that highly loaded compressor stages can work efficiently down to de Haller numbers of 0.64 before large stator hub corner separations develop. They have

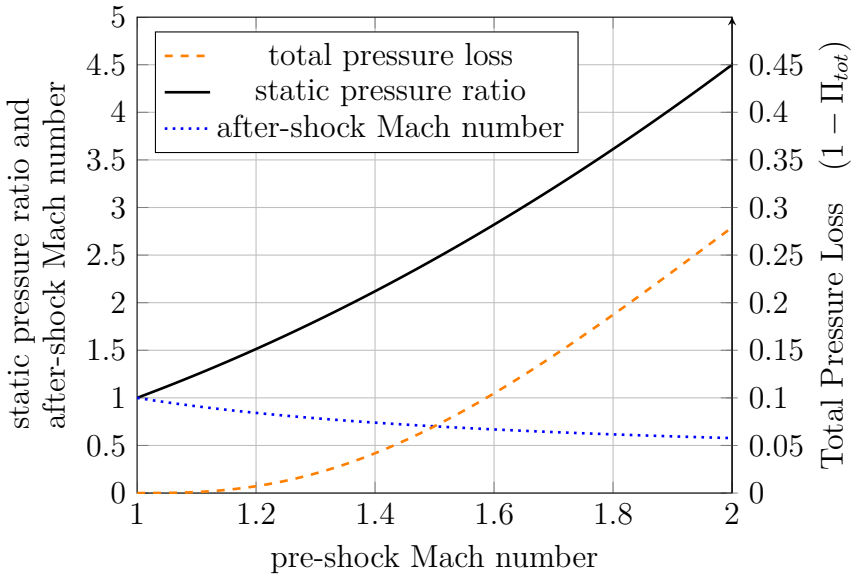

Figure 3.4: Pressure rise and loss in a normal shock adapted from Bölcs and Suter (1986) and Anderson (2003)

also shown that rotor blades are more tolerant against low de Haller numbers which suggests the strategy to increase the loading of the rotor when increasing specific stage work.

The compression shock developing due to the supersonic blade inlet flow velocities allows very high static pressure ratios but can also introduce significant flow losses due to the corresponding supersonic flow phenomena. This is illustrated in Fig. 3.4 using compressible flow relations for a normal shock as given by Bölcs and Suter (1986) and Anderson (2003). For inlet Mach numbers of 1.4 a normal shock decelerates the flow to an after-shock Mach number of about 0.74 resulting in a static pressure ratio of about 2.1. For low pre-shock Mach numbers the losses attributed to the compression are very low. In this case about 4% of the pre-shock total pressure are dissipated. For higher pre-shock Mach numbers higher static pressure ratios are obtainable but the total pressure loss also rises significantly, making inlet Mach numbers higher than 1.6 unattractive for compressor design. Apart from the losses attributed to the shock itself, the sudden deceleration of the flow destabilizes the boundary layer which is very likely to cause flow separation in the highly loaded blade passage. Excessive boundary layer flow separation due to shock interaction was in fact the major reason for poor performance of early supersonic compressors. Lieblein and Johnsen (1961) and Calvert and Ginder (1999) describe early and more recent design consideration of compressors with supersonic flow regime. To reduce flow separation very, thin blades, with thickness-to-chord ratios in the range of a few percent, sharp leading edges, and low camber are used. To reduce losses, these compressors usually are not designed to develop a compression shock across the full blade span, but only in the tip region. The flow in the hub region remains subsonic. These type of machines are called transonic compressors. With an appropriate design, transonic compressors can attain efficiencies above 90% with stage pressure ratios

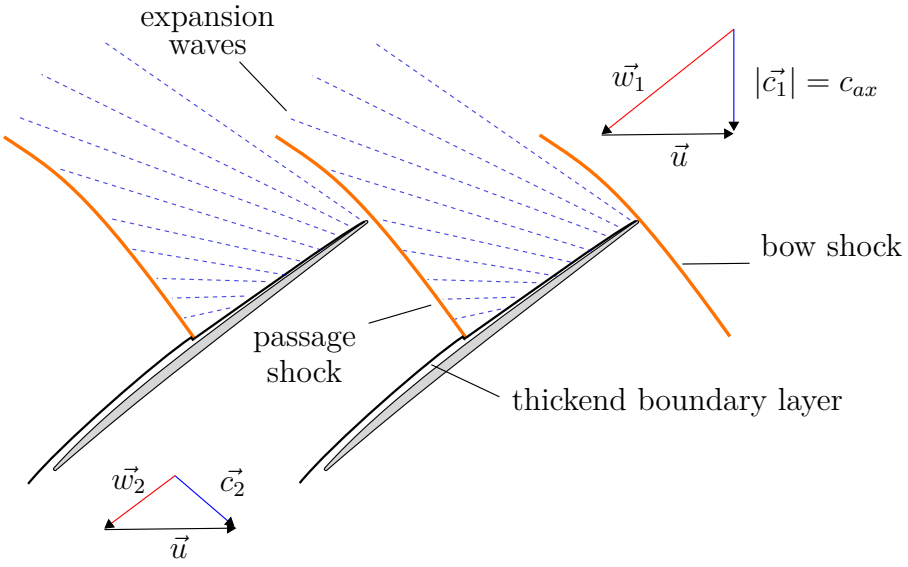

Figure 3.5: Ideal flow pattern of a supersonic compressor blade passage, adapted from Dixon and Hall (2010).

between 1.6 and 1.8. (Dixon and Hall 2010). Although the typical compressor blade loading limits - diffusion factor and de Haller criterion - were deduced from studies in low speed NACA profiles, Kerrebrock (1981) shows that these criteria are still applicable to transonic compressors. The established limiting values of these criteria however cannot be directly transfered from subsonic to transonic compressors.

A characteristic flow pattern in the supersonic flow region of a compressor is shown in Fig. 3.5. At the leading edge of the compressor a bow shock occurs which impinges on the suction surface of the neighboring blade. Downstream of the shock the flow is re-accelerated on the suction surface leading to expansion waves. To avoid excessive expansion, the blade camber is usually very low in this region. A thin leading edge helps to keep the bow shock attached to avoid additional losses. Towards the throat of the blade passage, the flow is accelerated and eventually develops a passage shock. The position of the passage shock at the leading edge of the blade in Fig. 3.5 represents an ideal flow pattern at design conditions. Towards the choke limit of the compressor, the passage shock travels downstream. For operating points closer to the stall limit, the passage shock travels upstream out of the passage, transitions into the the bow shock, and typically detaches from the leading edge.

The introduced fundamentals of compressors have so far been focused on a specific type: the axial compressor. It is characterized by axial in- and axial outflow of the rotor and only limited change of meanline radius in one stage. Euler's work equation of turbomachinery (Eqn. (3.3)) suggests an additional approach to increase specific compressor work other than increasing rotational speed, flow turning, and inlet velocity: to increase the difference of rotational speed $(u_2 - u_1)$ between stage in- and outlet. Compressors focused on utilizing this principle are known as centrifugal compressors. Characteristic of this compressor design type is a significant flow turning in the stage from mostly axial flow at the inlet to mostly radial flow at the outlet. The diffuser of centrifugal

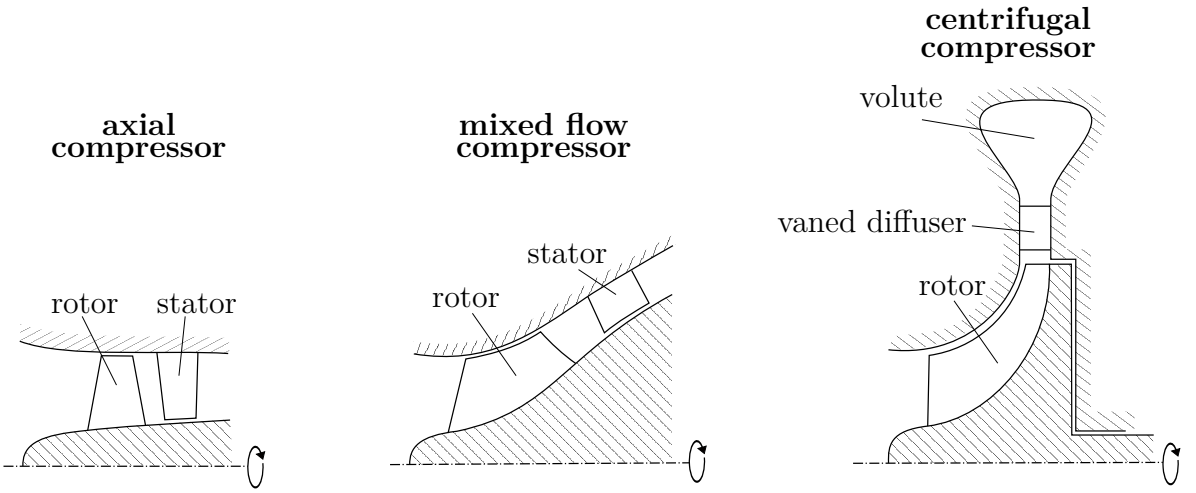

Figure 3.6: Compressor stage design types: axial compressor, mixed flow compressor, centrifugal compressor

compressors is a radial extension of the flow path and may be unbladed or bladed as it is the case in axial compressors. While axial compressor stages are characterized by comparably high flow capacity, high efficiency, and low total pressure ratios of up to 2 per stage, centrifugal compressors can obtain total pressure ratios above 6 in one stage (Osborne et al. 1974) at comparably low flow capacity and lower efficiency. For a given pressure ratio, axial compressors tend to have higher stage numbers and are larger in axial direction while centrifugal compressors build larger in radial direction. The radial outlet flow of the diffuser is collected in the spiral shaped volute and redirected to an outlet duct which exits normal to the rotor axis. The volute adds significantly to the radial space required by a centrifugal compressor.

A compromise between axial- and centrifugal compressor designs is the so called mixed flow compressor characterized by axial rotor inflow and significant axial- as well as radial-flow component at the rotor outlet. In most applications mixed-flow compressors resemble centrifugal compressors with significant axial outflow component. This design allows higher flow rates compared to centrifugal compressors but still higher stage total pressure ratios as in typical axial compressor stages. Fig. 3.6 illustrates the different design types.

According to Casey (2008), the reaction defined in Eqn. 3.12 can be reformulated to represent the fractions of work done by the turbomachine due to blade diffusion and due to centrifugal work. For this purpose the numerator in Eqn. 3.12 is represented in terms of velocity components in Eqns. 3.15 to 3.17:

$$h_2 - h_1 = \left(h_{2,tot} - \frac{{c_2}^2}{2}\right) - \left(h_{1,tot} - \frac{{c_1}^2}{2}\right) = \Delta h_{tot,21} - \frac{{c_2}^2}{2} + \frac{{c_1}^2}{2} \tag{3.15}$$

$$\Delta h_{tot,21} = \frac{1}{2}\left[\left({u_2}^2 - {u_1}^2\right) + \left({w_1}^2 - {w_2}^2\right) + \left({c_2}^2 - {c_1}^2\right)\right] \tag{3.16}$$

$$h_2 - h_1 = \frac{1}{2}\left[\left({u_2}^2 - {u_1}^2\right) + \left({w_1}^2 - {w_2}^2\right)\right] \tag{3.17}$$

Including Eqn. 3.17 in the definition of the reaction in Eqn. 3.12 leads to Eqn. 3.18. This formulation of the reaction now allows the separation of the rotor work in blade diffusion (${w_1}^2 - {w_2}^2$) and centrifugal work (${u_2}^2 - {u_1}^2$).

$$\mathrm{r} = \frac{\frac{1}{2}\left[({u_2}^2 - {u_1}^2) + ({w_1}^2 - {w_2}^2)\right]}{h_3 - h_1} \tag{3.18}$$

$$\mathrm{r_{blade}} = \frac{\frac{1}{2}\left({w_1}^2 - {w_2}^2\right)}{h_3 - h_1} \tag{3.19}$$

$$\mathrm{r_{centrifugal}} = \frac{\frac{1}{2}\left({u_2}^2 - {u_1}^2\right)}{h_3 - h_1} \tag{3.20}$$

$$\mathrm{r} = \mathrm{r_{blade}} + \mathrm{r_{centrifugal}} \tag{3.21}$$

In ideal axial compressors, the mean radius of the rotor does not change between inlet and outlet, for these machines $u_2 = u_1$ and therefore $\mathrm{r_{centrifugal}} = 0$ and $\mathrm{r_{blade}} = r$. For the case of compressors with no inlet swirl, Casey (2008) simplifies Eqn. 3.20 to Eqn. 3.22:

$$\mathrm{r_{centrifugal}} = \frac{1 - \frac{{D_1}^2}{{D_2}^2}}{2\frac{c_{u2}}{u_2}} \quad \text{for } \mathrm{c_{u1}} = 0 \tag{3.22}$$

For typical centrifugal compressors in turbocharger application, which have similar pressure ratios and mass flow rates as required in this work and no inlet swirl, Casey (2008) gives reference values of $\mathrm{r_{centrifugal}} \approx 0.41$. This value is based on typical shroud diameter ratios (the so called trim) of $\frac{D_1}{D_2} \approx 0.65$ and exit swirl to blade speed ratios of $\frac{c_{u2}}{u_2} \approx 0.7$ of these centrifugal compressors.

3.2 Fundamentals of Electrical Component Design

In a collaborative publication with the Institute of Drive Systems and Power Electronics of Leibniz Universität Hannover (Teichel et al. 2015a), the fundamentals of the electrical machine design for the investigated compressor are presented. The basic underlying principles are briefly introduced below. The power of an electrical machine can be described according to Eqn. (3.23). The power depends on the Essons number C, the volume of the rotating electromagnetic part of the machine $\pi/4d^2l$, and the rotational speed n. The Essons number rates the loading of the electromagnetic components of the machine. Since the electromagnetic loading is limited by the size of the machine and its resistance to thermal stress, the Essons number varies according to machine design, machine size, and the capacity of the cooling system (Müller et al. 2011).

$$P = C \cdot \frac{\pi}{4} d^2 \cdot l \cdot n \tag{3.23}$$

$$M = \frac{P}{2\pi n} = \frac{C \cdot d^2 \cdot l}{8} \tag{3.24}$$

To achieve the required compressor power the machine can either provide high torque at low rotational speed or low torque at high rotational speed (Eqn. (3.24)). For a fixed electromagnetic loading, high-speed motors require lower volume, and therefore add less mass to the EPHLS for which low mass is a critical design feature.

The circumferential speed of rotors with surface mounted permanent magnets (SPM) is limited by the centrifugal stress in the bandages on the rotor surface which secure the magnets. This mechanical constraint limits the rotational speed and diameter of the rotor. The circumferential speed limit of SPM machines with current technology is given by Gerada et al. (2014) as about 300 m/s. To avoid excessive stress in the bandages, rotors with the same volume but lower diameter and increased length can be used. This strategy is however limited by the rotor-dynamics of the rotor. Long, low diameter rotors tend to have lower bending frequencies which interfere with the operating range at high rotational speed. Also relevant to the EPHLS application is that long rotors allow more effective air cooling systems. Additionally, high power, high speed electrical machines require a suitable power supply. At high rotational speeds the excitation frequency provided by the power supply needs to be carefully controlled. The design of suitable, compact power electronics for this application is presented in Teichel et al. (2015a).

Figure 3.7 illustrates the limits of combining high power and high rotational speed of SPM machines. The gray band illustrates the limit of the currently available electrical machines on the basis of existing machines (black circles) by Fischer-Engineering (2014). Gerada et al. (2014) defined a current technological limit for this type of machine by determining the property limits of the critical components on the basis of an extensive literature survey. They quantify this limit using the product of the rotational speed in min^{-1} and the square root of the power in kW which was first introduced by van Millingen and van Millingen (1991). This limit of $8 \cdot 10^5$ $\mathrm{min}^{-1}\sqrt{\mathrm{kW}}$ is used to determine the red line in Fig. 3.7. As a reference, the required power and rotational speed of compressor 6 as approximated in Sec. 4.1 (assuming an isentropic efficiency of 80 %) is indicated by the triangle shaped symbol in this figure. While the compressor requirements are well below the technological limit of SPM machines they clearly exceed the current available technology. This illustrates the demanding requirements imposed by the compressor design on the design of the electrical system.

Consequently, the design considerations of the electrical components interact with the design space of the compressor. The feasible balance of power and rotational speed of the electrical machine limits the freedom in compressor design and imposes requirements on the compressor efficiency. The direct coupling of electrical machine and compressor in this application illustrates the demand for highly loaded compressors with high efficiency and relatively low rotational speed.

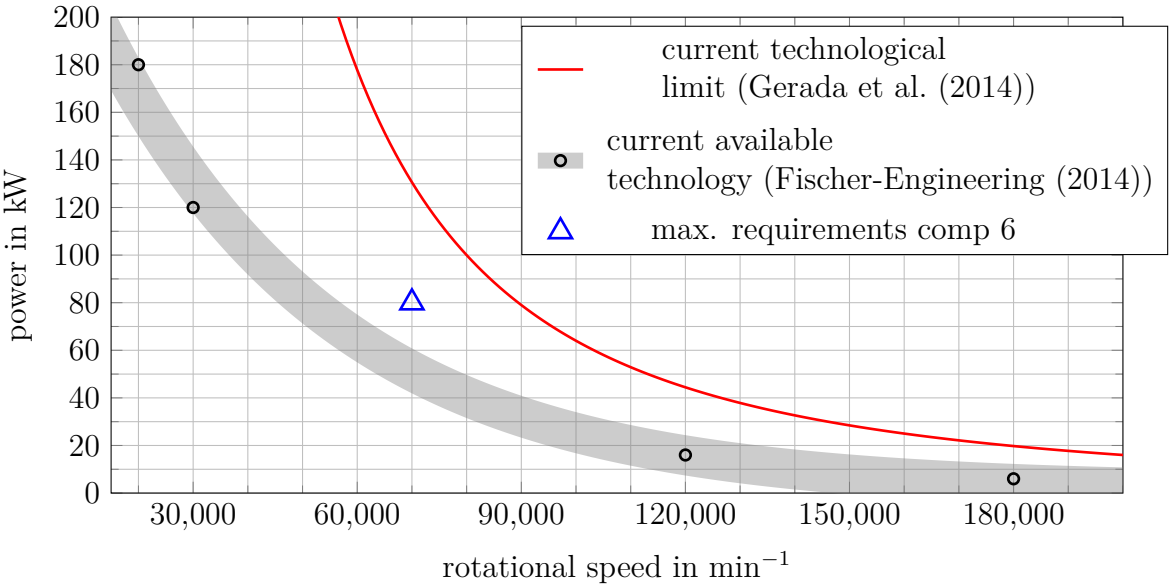

Figure 3.7: Current power limitation of high speed SPM machines.

3.3 Fundamentals of Automated Design Optimization

In any engineering process which aims at designing a new or improving an existing, complex technical system, automated optimization offers a time effective way to achieve the design objectives by taking into account the various interactions of the system parameters. For this purpose, the evaluation process of the system performance is automated. In an automated optimization process, the system parameters are varied within the user-defined limits (the design space), and the system's performance is predicted according to the user-defined objectives. This way the relation between the parameter variation and the objectives is determined indirectly. This indirect relation is recognized by a suitable optimization algorithm which selects system variants of which an improvement of the objectives is expected. A good overview of different optimization strategies for engineering design processes is given by Verstraete (2010b) and Cavazzuti (2013).

Optimization algorithms are search algorithms usually set up to minimize the objective function which defines the optimization problem. These algorithms can be classified according to one of the two fundamental principles: Deterministic Algorithms or Stochastic Algorithms.

3.3.1 Deterministic Algorithms

Characteristic to deterministic algorithms is an underlying reversible mathematically search strategy which only relies on the prediction of the system model and does not incorporate any random influences. With the same initialization deterministic algorithms produce the same output when run repeatedly. To determine search direction and step size for each system parameter, deterministic algorithms generally need to evaluate the gradient or curvature (Hessian matrix) of the objective function. So called gradient-free

deterministic search algorithms which do not require any gradient information are not considered here. These algorithms generally require large numbers of system model runs and are unsuitable for the optimization of fluid-dynamic systems where every system model run is very time consuming. Well known gradient-based algorithms are "steepest decent" and "Newton's method" (Cavazzuti 2013). The simplest approach to obtain the gradient is the finite difference method which requires the same magnitude of evaluations $(n + 1)$ as design parameters (n) to approximate the gradient information. In turbomachinery design where the objective function usually requires numerical simulations of the flow (CFD) to solve the underlying physical partial differential equation and the consideration of a large number of design parameters, this approach is computationally expensive. In the last years the development of the adjoint method for turbomachinery application ((Gauger 2008), (Giannakoglou et al. 2010)) offered a computationally less expensive way to obtain the gradient information for a specific aerodynamic objective. Using the adjoint method, additionally to the physical partial differential equation an adjoint equation needs to be solved for each objective independent on the number of design parameters (Verstraete 2010b). Solving the adjoint equation for each objective requires comparable computational effort as solving the physical partial differential equation. The implementation of the adjoint equation in the solver is however very time consuming and needs to be done for each objective separately.

The major advantage of gradient-based deterministic optimization methods is their efficiency which means that for many applications they can find an optimum requiring comparably few evaluations of the system. Also the distance to the optimum (the rate of convergence) can be evaluated using the gradient information. Using the adjoint method large numbers of design parameters can be considered without additional computational effort. For the inclusion of every objective and constraint however an additional adjoint evaluation is required. Typical disadvantages are the sensitivity to noise and discontinuities of the objective function. Multiple objectives and constraints can only be evaluated by the combination to a single pseudo-objective optimization. The major disadvantage of deterministic algorithms is however that in presence of local minima of the objective function they are not able to reliably determine the global optimum. The result of the optimization process here depends on the starting position of the search process. Truly gradient-based deterministic algorithms will converge to the minimum closest to the starting point which is not necessarily the global minimum in the search space.

3.3.2 Stochastic Algorithms

In many regards, stochastic algorithms apply a contrary approach to deterministic algorithms in that they rely on randomness in their search pattern. The simplest method is known as random search (Verstraete 2010b). It randomly selects system variations for evaluation and keeps the best individual. More sophisticated stochastic algorithms such as simulated annealing, particle swarm, or evolutionary algorithms use a similar random search method but with a more efficient selection of the search space based on previous search results. Due to the randomness, stochastic algorithms require a large number of evaluations of system variations in order to find the optimum. The resulting database

of the system performance evaluations allows the consideration of multiple independent objectives and constraints as part of the optimization. The randomness of the search prevents the algorithm getting trapped in local minima and allows the detection of the global minimum. Deterministic and stochastic search methods can be combined to "hybrid methods" to apply directed search but also explore the design space "outside" of the local minimum.

A particularly successful stochastic optimization algorithm type is the evolutionary algorithm which mimics Darwinian evolution. Rechenberg (1973) was one of the first to introduce this method into optimization of engineering applications. Evolutionary algorithms use populations of individuals (system variations) which are selected according to their fitness (the objectives). Successful individuals are more likely to pass their properties to the next generation. The transfer of properties from parents to child is done by cross-over (or recombination) of the properties between successful parents and mutation (random variation) of singular properties of the child. The selection process of successful individuals to generate new individuals ensures progression and optimization in each generation. The creation of new individuals itself however has a randomized component and therefore allows improvement but also radical changes to avoid local minima. Many individuals, approximately in the order of system parameters n, need to be evaluated in each population to cover the search space. Since these evaluations are not depending on each other, evolutionary algorithms can be highly parallelized. The number of population evaluations required to achieve convergence depends on the complexity of the system behavior.

3.3.3 Selection of Optimization Algorithms

The selection of a suitable optimization algorithm for a given optimization problem greatly improves the efficiency and the result of the optimization process. This matching process is necessary since there is no single optimization process that generally outperforms another. This "no free lunch" (NFL) theorem for optimization problems was formulated by Wolpert and Macready (1997) who proved that considering every possible optimization problem, the average performance of every optimization algorithm is identical. Any optimization algorithm which outperforms another for a certain application is therefore inferior for other applications. This theorem can be nicely illustrated if one of the optimization algorithms is "random search". Any optimization algorithm resulting in a more efficient optimization process than "random search" for a certain set of optimization problems will do worse than "random search" in all other sets of optimization problems. This thought experiment is useful and humbling in that it puts the performance of different optimization algorithms into perspective. For a defined set of optimization problems it is nevertheless possible to determine superior optimization strategies which outperform others with regards to efficiency and quality of the optimum.

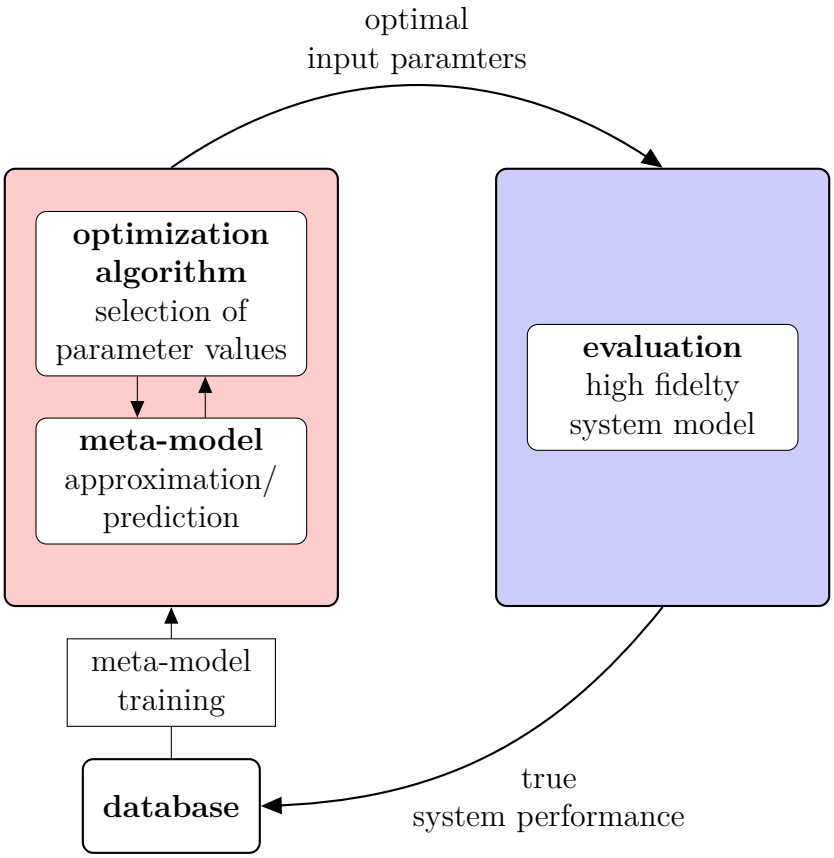

Figure 3.8: Process flow chart of the used optimization tool (Verstraete 2010a).

3.3.4 Meta-Models and Design of Experiments

In turbomachinery design applications detailed numerical simulations are required to evaluate the performance of an individual. The large number of individual evaluations required as part of an evolutionary optimization process is therefore computationally very expensive. To reduce the computational effort, thereby accelerating the optimization process, meta-models are widely used. The basic idea of this method is to approximate the system model on the basis of a representative database of already evaluated system variations. Response surface modeling (Cavazzuti 2013) can then be used to estimate the performance of new system variations at computationally low effort. This allows the evaluation of a large number of individuals as part of the evolutionary optimization process before testing the most promising ones using the high fidelity system model. New high fidelity evaluations can be added to the database of the meta-model to improve the prediction over the course of the optimization process. In such a setup, the meta-model is self-learning. The described process is illustrated in Fig. 3.8.

To generate the initial database at the beginning of the optimization process, Design of Experiments (DOE) methods are applied to minimize the number of evaluations required to accurately represent the system behavior by the meta-model. Using a full factorial design (Montgomery 2013) 2^n evaluations are required to represent linear inter-

action between all parameters. This way, the influence of each optimization parameter n is tested using a lower and an upper bound of the allowed variation. With numbers of optimization parameters of $n > 10$, full factorial design leads to required numbers of high fidelity evaluations of > 1024 to create the initial database. In this situation the use of a meta-model seems unfeasible since for such high numbers of evaluations direct evolutionary optimization without meta-model can already lead to reasonable optimization results. In turbomachinery application, where numbers of optimization parameters of more than 30 may be required, fractional factorial design 2^{n-p} is used instead to reduce the number of individuals required in the initial database. This approach omits the interaction of p less significant parameters, which requires the intervention of the designer. Since the self-learning meta-model focuses on the significant part of the design space over the course of the design process, it is generally able to handle a coarse initial database with significantly less than a full factorial design. However, the self learning meta-model still requires a representative initial database to progress in the correct direction in the beginning of the optimization process. An ill-trained meta-model on the basis of a non-representative database can compromise the convergence of the optimization when it falsely confines the high-fidelity evaluation to a non-optimal part of the design space, preventing improvement through self-learning.

Some of the most widely used meta-models are polynomial response surface models (PRSM), Kriging methods, and Artificial Neural Networks (ANN) (Verstraete 2010c). The accuracy of the methods strongly depends on the shape of the approximation, the number of optimization parameters, and the sample size used to train the model. PRSM use polynomial regression and therefore represent polynomial shaped approximation best. The training time and prediction time of the model is fast (Jin et al. 2001) but the required sample size is comparably large and depends on the number of optimization parameters. PRSM are therefore not well suited for high dimensional optimization problems which require computationally expensive evaluations.

ANN are able to accurately represent complex systems without requiring an assumption about the shape of the approximation. They mimic the functionality of brain cells with parallel, interconnected layers of neurons which process and transfer signals. An accurate prediction based on this strategy requires a thorough training which is often not achievable with a small database (Cavazzuti 2013).

In contrast to PRSM and ANN, Kriging methods are able to exactly reproduce the training samples. The Kriging method is based on similar principle as PRSM and was developed for application in the field of geostatistics to predict gold occurrences on the basis of scarce data. It requires comparably long training and prediction times for large sample numbers (Jin et al. 2001) but generally performs well in engineering optimization processes (Cavazzuti 2013).

In any case, the acceleration of the optimization process through the use of meta-models reduces the accuracy of the optimization process. This was illustrated by Chahine et al. (2012) who have shown that direct optimization of a centrifugal compressor using differential evolution leads to higher efficiencies than using ANN meta-model assisted optimization with the same degrees of freedom. As discussed above possible causes of error using meta-models can be insufficient, non-representative training or

systematic prediction errors of the meta-models due to the underlying approximation methodology. Due to the limited feasible size of the initial database in turbomachinery applications, high numbers of optimization parameters can only be successfully handled by a meta-model assisted optimization if the parameters are sufficiently interdependent. This interdependency effectively reduces the degree of freedom according to the principle of fractional factorial design and allows a successful approximation of the system model with only limited numbers of evaluations. For any optimization process, the advantages of the use of meta-models therefore need to be balanced with the possible disadvantages.

3.3.5 CADO - Multi-Objective Optimization of Turbomachinery

In this work the optimization environment CADO (Computer Aided Design and Optimization Tool), developed by Verstraete (2010a), is used. It combines a meta-model assisted, differential evolutionary algorithm which allows constrained, multi-objective optimization with parameterized turbomachinery geometry generation tools. The CADO environment allows the user to fully control the evaluation process, the parameterization strategy, and the objective function. The included geometry generation tools provide a fully parameterized generation of axial and radial turbomachinery on the basis of Bézier control points. The aerodynamic geometry can be exported to the appropriate file formats for mesh generation in Numeca AutoGrid NUMECA-International (2016) or G3DHexa. A direct process for CSM (Computational Solid Mechanics) evaluation using CalculiX Dhondt (2004) is available. This process includes the meshing of the solid body as well as the preprocessing to evaluate centrifugal stresses, the job management, and the postprocessing. A CAD (Computer Aided Design) export is available to transfer the geometry to the further mechanical design process.

The optimization environment uses the differential evolution (DE) algorithm, which was developed by Storn and Price (1997) with the goal to provide a fast, robust and easy to use evolutionary algorithm. They demonstrated that DE is easy to integrate in a computer program, converges quickly, and is insensitive over a wide range of the few control variables required. The underlying principle, as it is used in CADO, is illustrated in Fig. 3.9. Starting from a randomized generation t each individual x_t is used to generate a child z_t. For a multi-objective optimization, as illustrated in Fig. 3.9, three additional, Pareto optimal parents (a_t, b_t, c_t) are included in the generation of the child. In contrast to natural evolution, in DE each child has four parents. The concept of Pareto optimality, named after the Italian engineer and economist Vilfredo Pareto (1848–1923), is used to evaluate the trade-off between different individuals when more than one, independent objective is considered.

Pareto optimal individuals represent a unique trade-off between the objectives which means that none of the objectives can be improved without worsening another. The so called Pareto front includes all Pareto optimal individuals. The selection of the Pareto optimal parents is redone for each child and considers a uniform distribution of the parents on the Pareto front for better representation of the current optimum. For each design parameter (denoted by the subscript $_i$) the Pareto optimal parents are used to generate a mutated design parameter y_i (see Fig. 3.9, top center). The

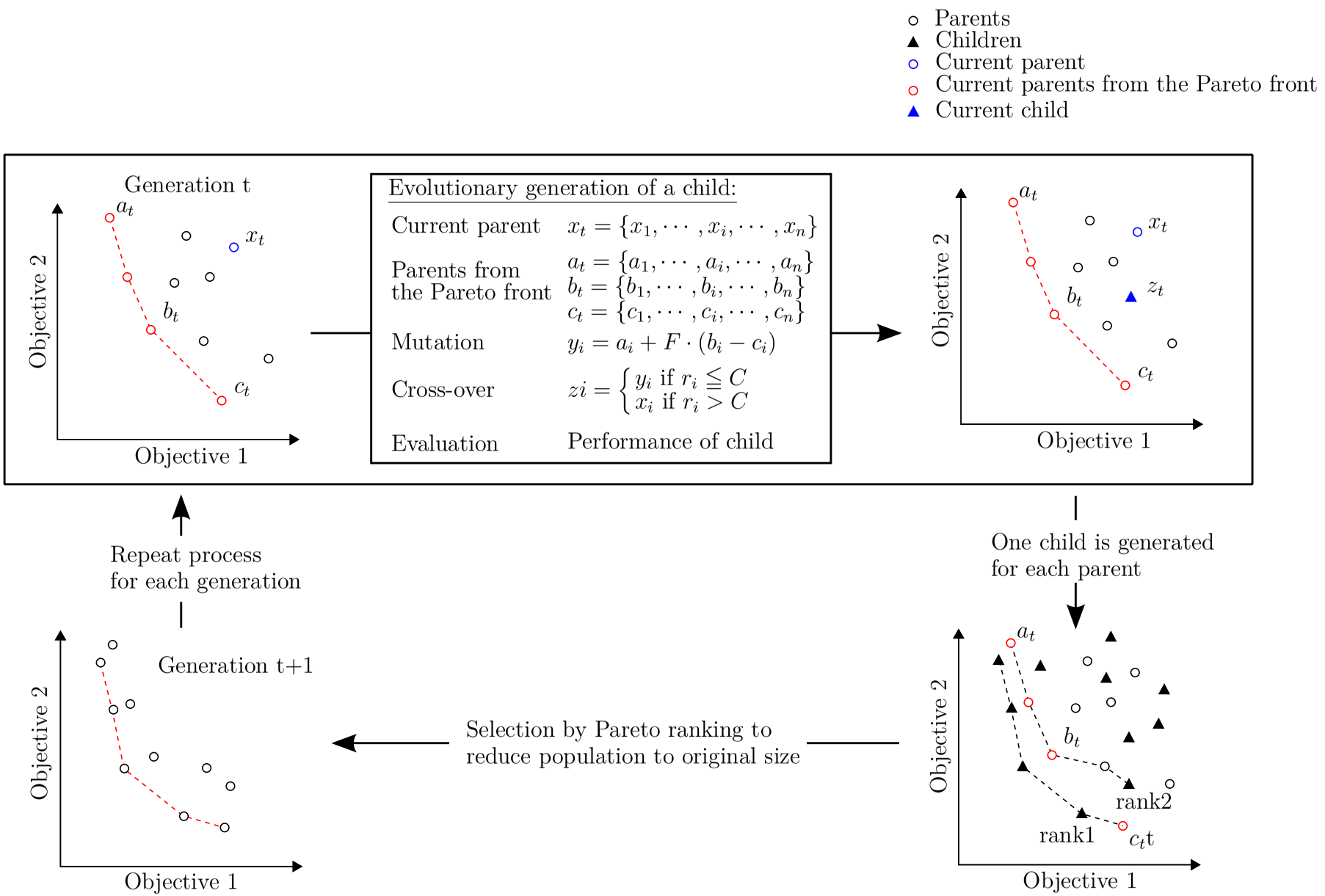

Figure 3.9: Multiobjective Differential Evolutionary Algorithm, adapted from Verstraete (2010c)

mutation factor F is user-defined and can have values between 0 and 2. Using cross-over the final design parameter of the child z_i is determined. In this process the random number $r_i \in [0, 1]$ is compared to the user-defined cross-over constant $C \in [0, 1]$ to decide whether the parent parameter x_i or the mutated parameter y_i shall be adopted as the child parameter z_i. Once all design parameters of the child z_t are fixed, the performance of the child is evaluated and included in the parent generation t. This process is done for every individual of generation t acting as parent x_t; the generation t has now doubled in size (Fig. 3.9, bottom right). The child generation process is well suited for parallelization which allows to consider large generations without slowing down the process if sufficient computation resources are available. Parents and children are ranked according to their fitness using Pareto optimality. To obtain the new generation $t + 1$ the fittest individuals of the previous generation are selected until the original generation size is reached (Fig. 3.9, bottom left). In this way, a decline of fitness is avoided since superior parents can be adopted in the new generation.

As part of the Pareto ranking, multi-objective constraints can be considered directly in this optimization method used in CADO. Constraints are used to confine the objective space to a relevant range for the given design goal considering any number of system performance parameters. An established way is the indirect handling of constraints by introduction of penalty functions to the objective if the constraint is active. This so called 'exterior penalty method' is illustrated in Fig. 3.10 for a minimization problem of Obj(x) within the constrained range of performance parameter x. Outside the relevant region, the objective value Obj(x) is increased by the penalty functions $g_1(x)$ and $g_2(x)$ to shift the optimum into the relevant region. The major disadvantage of this method is that the selection of the penalty function has an effect on the resulting optimum. An unsuitable penalty function can lead to local optima outside the relevant region. This method is necessary for optimization processes which require a continuous objective function.

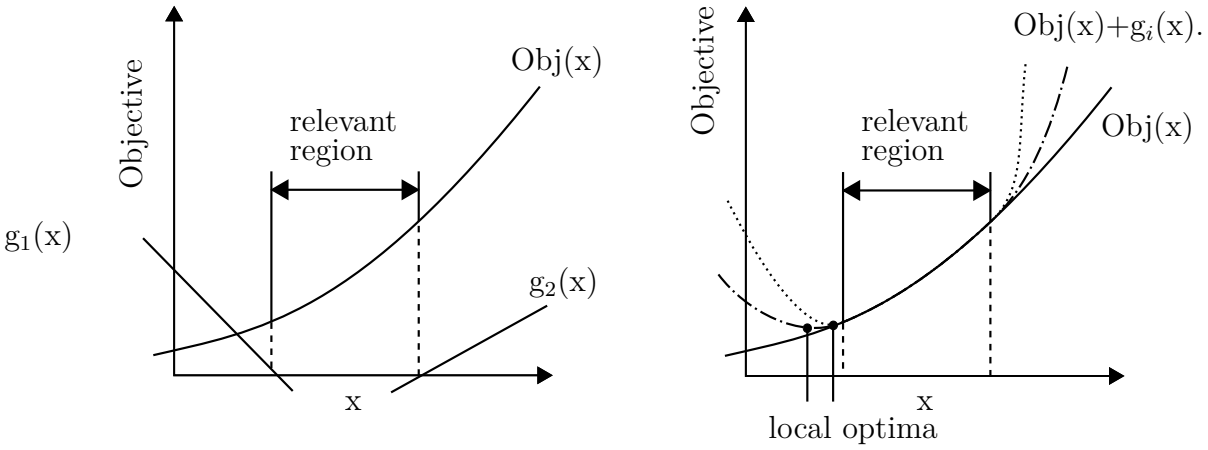

Figure 3.10: Indirect handling of constraints for a single objective, adapted from Verstraete (2010b).

Direct handling of constraints, as illustrated in Fig. 3.11, in contrast, does not require penalty functions. Here individuals outside the relevant objective space are not considered in the Pareto ranking and thus excluded from the further optimization process. This allows to find the optimum inside the relevant region without knowledge of the objective function. To improve convergence in the early phase of the optimization process, individuals outside the relevant region can be considered as parents for the next generation if not enough relevant parents exist. For these reasons, direct handling of constraints leads to a more accurate and more robust optimization process compared to a 'exterior penalty method' and is therefore also better suited for complex turbomachinery design applications.

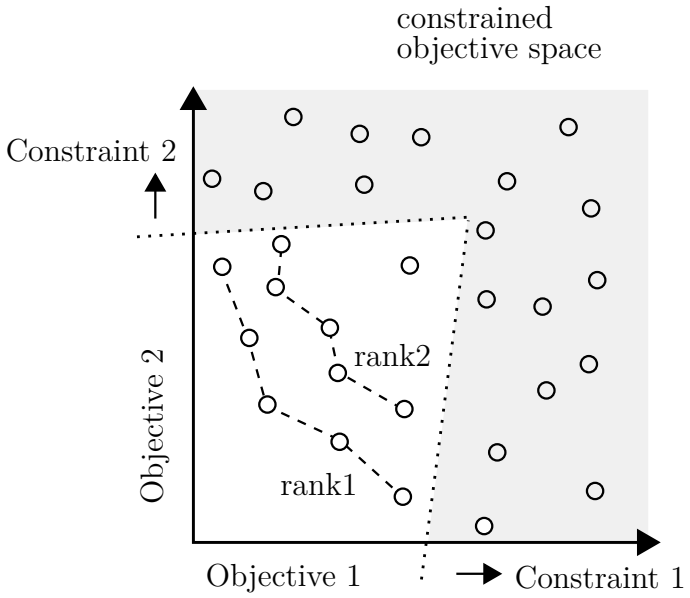

Figure 3.11: Direct handling of constraints for 2 objectives

4 Preliminary Compressor Design

In the beginning of a compressor design process, fundamental decisions about the machine type and the basic machine parameters such as diameter, rotational speed, and number of stages need to be made. Dimensional analysis is a widely used approach to fix these parameters. Further design features such as the shape of the meridional flow path, blade numbers, blade angles, and blade profiles can later be determined on the basis of preliminary design tools. The preliminary design phase is the most decisive phase since it fixes the major design parameters. It is therefore critical to make these design decisions on the basis of a valid performance prediction methodology. According to Cumpsty (2010), faulty decisions in this design phase cannot be compensated in the later detailed design phase where usually only detailed, less decisive parameters like the final three-dimensional blade shape are determined.

4.1 Dimensional Analysis

To decide which type of compressor is most appropriate for a specific design task dimensional analysis methods are used. The established method originally proposed by Cordier (1953) uses the non-dimensional parameters specific speed and specific diameter to characterize the different types of turbomachinery. On the basis of successful existing designs the so-called Cordier-Diagram (e.g. Grote et al. (2014)) was developed. It indicates the relation between machine speed and machine size to achieve peak efficiency for a specific type of turbomachinery. Epple et al. (2010) have confirmed these relations with an analytical approach. On the basis of Cordier (1953) and extensions from others, Casey et al. (2010) presented a Cordier-type non-dimensional design approach specifically including mixed flow compressors. For the purpose of this work, this method has the advantage that it uses meaningful performance parameters for mixed and centrifugal machines, which adequately represent the centrifugal pressure rise component of these compressor types. Another advantage is that, in contrast to Cordier (1953), the method by Casey et al. (2010) provides the optimal "Cordier range" in a quantitative way.

With reference to the established Cordier coefficients, Casey et al. (2010) introduce the non-dimensional design coefficients specific speed ω_s and specific diameter D_s (Eqns. (4.1) and (4.2)).

$$\omega_\mathrm{s} = \omega \frac{(\dot{V}_1)^{\frac{1}{2}}}{(\Delta h_\mathrm{tot,isen})^{\frac{3}{4}}} \tag{4.1}$$

$$D_\mathrm{s} = D_2 \frac{(\Delta h_\mathrm{tot,isen})^{\frac{1}{4}}}{(\dot{V}_1)^{\frac{1}{2}}} \tag{4.2}$$

These coefficients normalize the angular velocity ω and the maximum rotor diameter D_2 of a compressor using the inlet volumetric flow rate $\dot{V}_1$ and the isentropic specific work of the machine $h_{\mathrm{tot,isen}}$, all in SI-units. These non-dimensional design coefficient ω_s and D_s are related to the non-dimensional performance parameters global flow coefficient ϕ_g and isentropic work coefficient $\psi_{\mathrm{g,isen}}$ according to Eqns. (4.3) to (4.4).

$$\omega_\mathrm{s} = 2\frac{(\phi_\mathrm{g})^{\frac{1}{2}}}{(\psi_{\mathrm{g,isen}})^{\frac{3}{4}}} \tag{4.3}$$

$$D_\mathrm{s} = \frac{(\psi_{\mathrm{g,isen}})^{\frac{1}{4}}}{(\phi_\mathrm{g})^{\frac{1}{2}}} \tag{4.4}$$

These new parameters are introduced because the established flow coefficient ϕ and load coefficient ψ for axial compressors (Eqns. 4.12 and 3.10) provide unreasonable results for mixed flow compressors since they use the inlet geometry as a reference. When applied to compressors with significant radius increase, these performance parameters use the unrepresentatively low inlet circumferential velocity as a reference for a high stage work which can usually only be achieved due to the centrifugal pressure rise component. This leads to excessively high work coefficients and also overestimates the flow coefficients. Instead, the definitions used by Casey et al. (2010) and Hazby et al. (2014) use the maximum circumferential speed, usually at the rotor exit, as reference, which makes them also appropriate to use for mixed and centrifugal compressors. The global flow coefficient ϕ_g is defined in Eqn. (4.5) as the ratio of inlet volumetric flow rate and the product of the rotor tip speed and the square of the maximum rotor diameter. The use of the inlet volumetric flow rate and exit circumferential speed instead of the inlet axial velocity and inlet mean circumferential speed in the conventional flow coefficient definition (Eqn. 4.12) allows an easier use of the global flow coefficient in design processes. When volumetric flow rates are given in a design task, knowledge about the inlet area and the mean diameter as well as assumptions about the axial velocity distribution are required to determine the conventional flow coefficient. This is not necessary when using the global flow coefficient. The global isentropic work coefficient $\psi_{\mathrm{g,isen}}$ relates the isentropic, total enthalpy rise to the rotor tip speed (Eqn. (4.6)). The established range of values for these parameters is illustrated Fig. 4.1b.

$$\phi_\mathrm{g} = \frac{\dot{V}_1}{{D_2}^2 u_2} \tag{4.5}$$

$$\psi_{\mathrm{g,isen}} = \frac{\Delta h_{\mathrm{tot,isen}}}{{u_2}^2} = \frac{c_p \cdot T_{\mathrm{tot},1}\left(\Pi_{\mathrm{tot}}^{\frac{\gamma-1}{\gamma}} - 1\right)}{{u_2}^2} \tag{4.6}$$

Casey et al. (2010) present a correlation for the Cordier line on the basis of existing correlations which specifically accounts for centrifugal pressure rise effects in machines with a significant radial flow component (Eqn. (4.7)). As stated above, the Cordier range indicates the relation between machine speed and machine size which results in

Table 4.1: Cordier correlation coefficient values according to Casey et al. (2010).

	Cordier line	lower bound	upper bound
ψ_{low}	0.45	0.35	0.55
ψ_{medium}	0.55	0.4	0.7
ψ_{high}	0.02	0.01	0.025

peak efficiency for a specific type of turbomachinery.

$$\psi_{\text{g,isen}} = \psi_{\text{medium}}(1-A) + \psi_{\text{high}}A + (\psi_{\text{medium}} - \psi_{\text{low}})B \tag{4.7}$$
$$A = \frac{1}{1+\mathrm{e}^{-t_1}}; \qquad B = \mathrm{e}^{-t_2}$$
$$t_1 = k_1 \cdot (k_2 + \log_{10}\omega_s); \qquad t_2 = k_3 \cdot (k_4 + \log_{10}\omega_s)$$

The appropriate values of ψ_{low}, ψ_{medium}, and ψ_{high} to represent the Cordier line and its upper and lower bound according to Casey et al. (2010) are given in Tab. 4.1. For all of these cases the following values are used: $k_1 = 4$, $k_2 = -0.3$, $k_3 = 5$, and $k_4 = 1$.

The resulting Cordier Diagram is shown in Fig. 4.1a with the conventional range for radial, centrifugal, mixed, and axial compressors given by Casey et al. (2010). The diagram differentiates centrifugal compressors with axial inlet- and radial outlet flow from radial compressors with radial in- and outlet flow. The gray area represents the range of Cordier optimal designs. On the basis of the design space illustrated in Fig. 4.1a first design decisions for compressors of the EPHLS are made below using dimensional analysis.

In the presented design task, the mass flow rate $\dot{m}$, the total pressure ratio Π_{tt} as well as the inlet total pressure $p_{\text{t,in}}$ and the inlet total temperature $T_{\text{t,in}}$ are given by the requirements of the AHLS (Sec. 2.3); rotational speed n and maximum rotor diameter D_2 are design parameters. The requirements of each compressor are summarized in App. A.2. To reduce the complexity of the EPHLS, the same compressor type is to be used for the different compressor systems in each flap of the wing. The dimensional analysis therefore focuses on the aileron compressor (comp 6) with the most challenging operating conditions (see Fig. 2.7). From the results of the dimensional analysis of this compressor, the parameters of all other compressors are then deduced by scaling. To determine the Cordier coefficients, the isentropic stage work and the inlet volumetric flow rate need to be deduced from the design task. The isentropic stage work can be determined according to Eqn. (4.8) from the temperature difference resulting from the required isentropic compression. To determine the inlet volumetric flow rate from the mass flow rate, it is necessary to determine the density which is a function of static temperature and static pressure (Eqn. (4.9)). Using the relations for compressible fluids in Eqns. (4.10) and (4.11), this requires the determination of the inlet flow velocity c_{in}. To define the inlet axial velocity, the flow coefficient ϕ is used as an additional design parameter. According to Eqn. (4.12) this parameter relates the axial velocity to the midspan circumferential velocity at rotor inlet. With a given rotational speed and maximum diameter, the inlet area needs to be determined in order to fix the midspan

diameter (Eqns. (4.13) and (4.14)). In this simplified design process, a constant shroud diameter is assumed,the shroud diameter d_{shr} is equal to the maximum diameter D_2. Also, axial inflow with uniform spanwise distribution is assumed to be $c_{\mathrm{in}} = c_{\mathrm{ax}}$.

$$\Delta h_{\mathrm{tot,isen}} = c_{\mathrm{p}} \cdot T_{\mathrm{t,in}} \left(\Pi_{\mathrm{tt}}^{\frac{\kappa-1}{\kappa}} - 1 \right) \tag{4.8}$$

$$\dot{V}_{\mathrm{in}} = \frac{\dot{m}}{\rho_{\mathrm{in}}} = \frac{\dot{m}}{\frac{p_{\mathrm{in}}}{R \cdot T_{\mathrm{in}}}} \tag{4.9}$$

$$\frac{T_{\mathrm{t,in}}}{T_{\mathrm{in}}} = \left(1 + \frac{\kappa - 1}{2} \frac{{c_{\mathrm{in}}}^2}{a} \right) \tag{4.10}$$

$$\frac{p_{\mathrm{t,in}}}{p_{\mathrm{in}}} = \left(1 + \frac{\kappa - 1}{2} \frac{{c_{\mathrm{in}}}^2}{a} \right)^{\frac{\kappa}{\kappa-1}} \tag{4.11}$$

$$\phi = \frac{c_{\mathrm{ax}}}{u_{\mathrm{m}}} \tag{4.12}$$

$$u_{\mathrm{m}} = \pi \cdot n \cdot d_{\mathrm{m}} = \pi \cdot n \cdot \frac{d_{\mathrm{shr}} + d_{\mathrm{hub}}}{2} \tag{4.13}$$

$$\dot{m} = \rho_{\mathrm{in}} \cdot c_{\mathrm{ax}} \cdot A_{\mathrm{in}} = \rho_{\mathrm{in}} \cdot c_{\mathrm{ax}} \cdot \pi \left(d_{\mathrm{shr}}^2 - d_{\mathrm{hub}}^2 \right) \tag{4.14}$$

This system of equations is solved iteratively for each compressor system at the operating point with peak pressure ratio and through flow. The diameter of the aileron compressor 6 and its rotational speeds at peak lift generation and peak maneuver support are selected to achieve good performance according to the dimensional analysis method by Casey et al. (2010). The diameters and rotational speeds of the other compressors are then deduced by scaling the peak lift operating condition of comp 6 using turbomachinery scaling laws. Due to the varying inlet conditions, corrected mass flow rates are used as a reference.

In order to achieve similar compressor performance (i.e. pressure ratio and efficiency) at different mass flow rates, geometric scaling aims at changing the size (and thereby the cross-sectional area) of the machine without changing the flow vectors. According to Euler's work equation (Eqn. (3.3)) this is achieved by keeping the circumferential velocity u and the specific stage work Δh_{tot} constant in the scaling process. Considering the continuity equation (Eqn. (4.15)), assuming all fluid parameters to remain unchanged, the mass flow rate is proportional to the square of the outer diameter of the machine. Equation (4.16) illustrates the relation between rotational speed and machine diameter and mass flow rate, respectively.

$$\dot{m} = \rho c_{\mathrm{ax}} A \Rightarrow \dot{m} \propto A \propto d^2 \tag{4.15}$$

$$u = \pi d n = \text{const.} \Rightarrow n \propto \frac{1}{d} \propto \frac{1}{\sqrt{\dot{m}}} \tag{4.16}$$

Considering these proportionalities, the scaling laws in Eqns. (4.17) and (4.18) between

two designs A and B can be formulated:

$$\frac{D_\mathrm{A}}{D_\mathrm{B}} = \frac{\sqrt{\dot{m}_\mathrm{A}}}{\sqrt{\dot{m}_\mathrm{B}}} \tag{4.17}$$

$$\frac{n_\mathrm{A}}{n_\mathrm{B}} = \frac{\sqrt{\dot{m}_\mathrm{B}}}{\sqrt{\dot{m}_\mathrm{A}}} \tag{4.18}$$

The maximum diameter of the aileron compressor 6 was chosen as 120 mm which is a reasonable limit to still be able to fit the compressor system into the wingbox (see App. A.1). Smaller designs are avoided since these result in higher rotational speeds and would exceed the currently available electric machine technology concerning the combination of high power and high speed (see Fig. 3.7). With this diameter, the rotational speed at peak pressure ratio and through-flow during lift support is selected as 60.000 min^{-1} and as about 70.000 min^{-1} at peak pressure ratio during maneuver support. With these design parameters, the compressor designs are located close to the Cordier line indicating near peak efficiency. The flow coefficient for all compressors at peak lift generation was set to 0.45 in accordance with the design guideline by Smith (1958). On the basis of simplified physical modeling and experimental testing, he deduced that flow coefficients of slightly less than 0.5 lead to compressor stages with increased stall pressure ratio and increased stability. Considering the combined requirements of a maximum mass flow rate around 1 kg/s and a pressure ratio of around 2.3 the design pushes the traditional bounds of typical axial and centrifugal compressor stages. While the flow rate is low and the pressure ratio high for a typical centrifugal compressor stage the opposite is true for a typical axial compressor stage. The flow coefficient of 0.45 allows to cover both compressor types as illustrated in Fig. 4.2.

The resulting non-dimensional parameters from these basic design considerations for each compressor system are illustrated in the Cordier Diagram in Fig. 4.1a for the respective operating point at maximum pressure ratio and through-flow. Since the pressure ratio and inlet conditions are identical, the non-dimensional parameters are not changed as part of the scaling process and the scaled compressor systems 1 to 5 coincide such as they appear as a single symbol. The underlying operating point of the aileron compressor at peak lift generation which was used for the scaling process differs slightly and therefore it's non-dimensional parameters also differ. From the Cordier-Diagram, it is apparent, that in principle mixed flow compressors with both predominantly centrifugal- or predominantly axial flow compressor characteristics are appropriate machine types for this design task. While the specific speeds and global flow coefficients are too high for typical centrifugal compressors, the isentropic work coefficient is too high for typical axial compressor stages.

To further evaluate the compressor type for a given design task, Grote et al. (2014) provide a comparison of the operating range and obtainable efficiency of centrifugal and axial compressors in Fig. 4.2. Here the typical non-dimensional operating range of the two machine types is illustrated using the flow coefficient and a modified load coefficient, the so-called enthalpy parameter. It is defined in Eqn. (4.19) and relates the

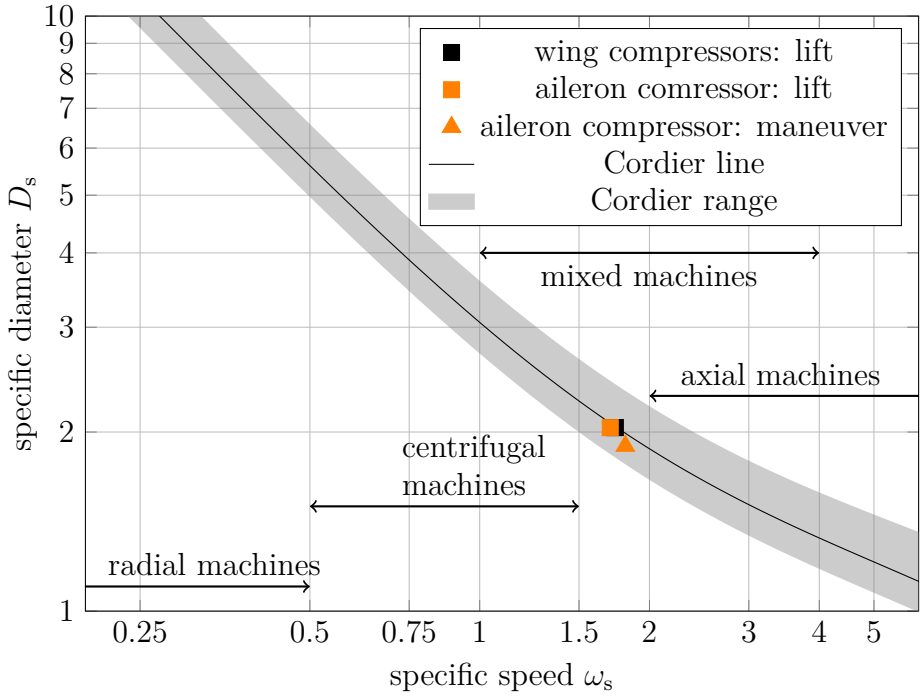

(a) Design space illustrated in a Cordier-type diagram.

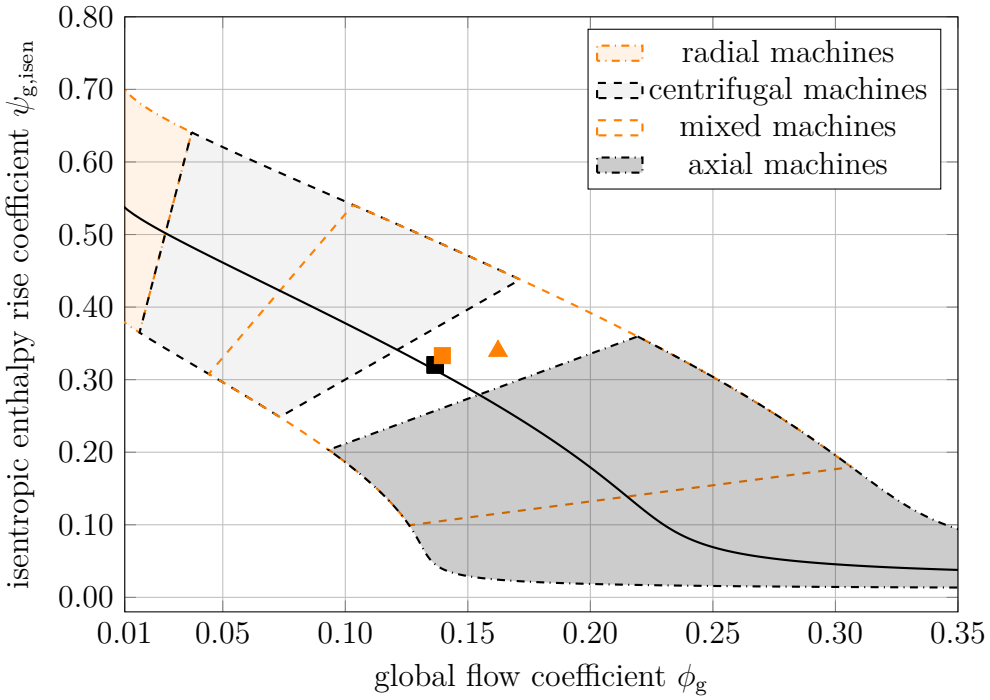

(b) Performance space illustrated in a non-dimensional operating range diagram.

Figure 4.1: Rotor designs in the conventional compressor design space according to Casey et al. (2010)

static, specific stage work to the midspan circumferential velocity at the rotor exit.

$$\psi_{h,\mathrm{comp}} = \frac{2 \cdot \Delta h_{\mathrm{stat,comp}}}{u_{\mathrm{exit}}^2} \tag{4.19}$$

To determine these parameters, further design parameters of the compressor need to be fixed. For this simplified analysis the compressor is assumed to be a repeating stage, i.e. the outflow vector equals the inflow vector, analogously to the compressor analysis illustrated in Fig. 3.3 earlier. With axial inflow, the repeating stage assumption requires complete flow turning in the stator and therefore represents a desirable ideal case for turbomachinery design where no exit swirl is unused.

With this assumption, the static specific stage work equals the total specific stage work. Constant axial flow velocity and a reaction of 0.6 are assumed for all compressors to be able to determine the axial flow velocity and density at rotor exit. In compressor design, significant axial diffusion or axial acceleration is usually avoided to prevent increased flow instability near the end walls on one side and to avoid static pressure ratio decrease on the other. The shape of the meridional flow path is usually controlled according to the density change of the flow to approximate constant axial velocity. Constant midspan axial flow velocity is consequently a commonly used assumption in most simplified compressor design processes. The increased reaction of 0.6 takes the high stage loading into account and shifts loading to the more robust rotor (Dickens and Day 2011). With these assumptions, the same fundamental system of equations used to determine the midspan radius at the inlet is now used to determine the enthalpy parameter of Eqn. (4.19).

Considering the resulting operating points in Fig. 4.2, it is apparent that, from an aerodynamic point of view, axial compressors are more suitable for this design task than centrifugal compressors. Although the through-flow is comparably low and the loading is high for axial compressors, the operating points still better fits into with the axial compressor range than into the typical centrifugal compressor range.

As stated in Teichel et al. (2015b), large turbocharger compressors meet the required flow rates but these machines are meant to operate at higher total pressure ratios (Garrett 2016) and reach maximum efficiencies around 80%. The capability of mixed-flow compressors of covering the required operating range is demonstrated by Hazby et al. (2015). In their work, a mixed-flow compressor for corrected mass-flow rates of 0.4 kg/s to 1.5 kg/s and pressure ratios of up to 3 were achieved with max. total-to-total efficiencies of about 80%. The mixed-flow compressor presented by Hazby et al. (2015) has predominantly centrifugal compressor characteristics including significant radial rotor outflow, splitter blades, vaneless diffuser, and an outlet volute. According to the authors, a recirculating bleed technique was required for this machine to achieve an acceptable operating range.

Due to the higher obtainable efficiency of about 90% of axial compressors, less power is required by the electrical system which drives the compressors. Although low power consumption is not the critical design objective with regards to the aircraft application, high efficiency leads to increased power density. This helps to reduce the mass not only of the compressors but of all components required for the power supply. In addition to the

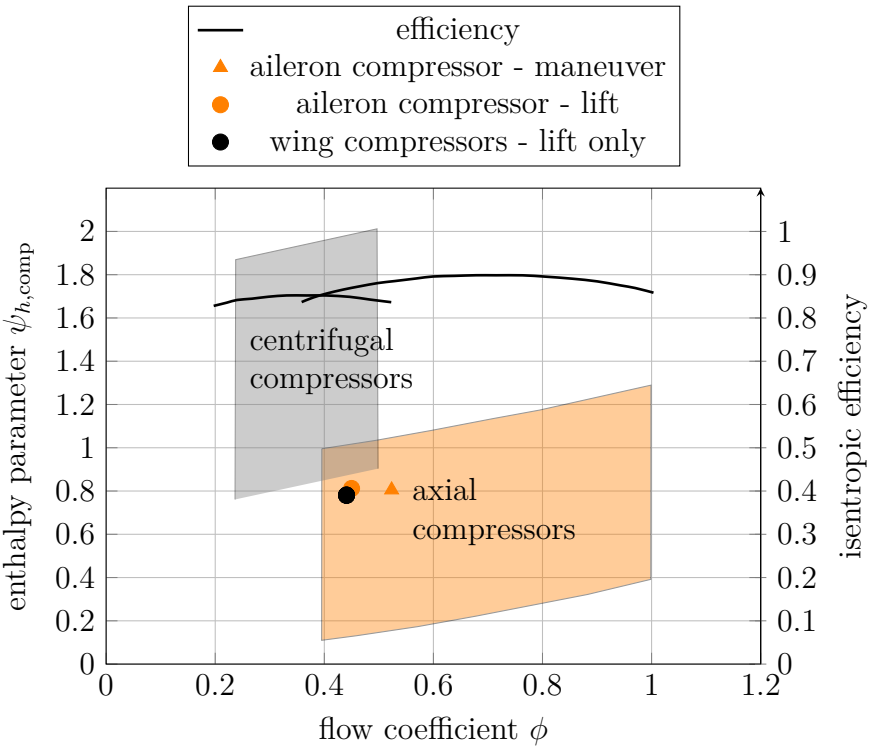

Figure 4.2: Comparison of compressor operating range and efficiency adapted from Grote et al. (2014)

power density advantage, axial compressors are also expected to have an advantage over centrifugal compressors regarding the radial size. As shown in App. A.1 the wingboxes provide sufficient space in spanwise direction but are confined in height as well as in chordwise direction. This restricts the radial size of the compressors if the EPHLS wingbox layout is carried out as presented in Figs. 2.3 and 2.5. Other configurations would require an angle gear introducing additional mass and losses and would not allow the integrated cooling of motor and power electronics.

The given pressure ratios and mass flow rates lead to comparable maximum rotor diameters for centrifugal and axial compressors. The radial diffuser and volute required to diffuse and collect the radial outlet flow of the centrifugal compressor, however, increase the overall radial size significantly. As a result of these considerations, mixed flow compressors with predominantly axial compressor characteristics are selected for this design task using axial compressor design methods. To be able to obtain the high total pressure ratios of up to 2.3 in a single stage, a significant radial flow path component is incorporated in the design process to mimic a mixed flow type compressor as demonstrated by Hazby et al. (2015) or Mårtensson et al. (2007). The single stage design results in minimal compressor mass and size compared to a suitable two-stage compressor. According to Kerrebrock (1981), the reduction to a single compressor stage also helps to reduce the noise generation compared to a multi-stage compressor. This improves the integration of the compressors in the EPHLS. By avoiding stage mismatching at off-design points,

Table 4.2: Compressor parameters from the dimensional analysis.

compressors	comp 6	comp 5	comp 4	comp 3	comp 2	comp 1
max. total pressure ratio	2.34	1.86				
max. corrected mass flow rate	1.11 kg/s	1.11 kg/s	1.31 kg/s	1.52 kg/s	1.72 kg/s	1.92 kg/s
max. isentropic power	65 kW	46 kW	54 kW	62 kW	71 kW	79 kW
$d_{\max}$	120 mm	133 mm	145 mm	156 mm	166 mm	175 mm
max. rotational speed	70,000 $\min^{-1}$	54,100 $\min^{-1}$	49,700 $\min^{-1}$	46,300 $\min^{-1}$	43,500 $\min^{-1}$	41,100 $\min^{-1}$
flow coefficient ϕ	0.52	0.45				
work coefficient $\psi_{h,\text{comp}}$	0.81	0.78				
reaction r	0.6					

single stage designs also allow a wider operating range. No inlet guide vanes are used to avoid additional mass, system complexity, and additional total pressure loss. To achieve the required high total pressure ratio in a single-stage axial compressor, a transonic flow regime is required as discussed in Ch. 3. The compressor parameters resulting from the dimensional analysis are summarized in Tab. 4.2.

4.2 Optimized Preliminary Design

After fixing the most fundamental design parameters of the compressor using dimensional analysis, further design parameters concerning the basic blade shape and flow path shape are usually fixed using preliminary design tools. These tools typically represent the flow in the meridional plane along predefined streamlines applying simplified physical principles combined with empirically based loss correlations. While the physical principles are generally valid for any kind of compressor design task, the quality of the prediction depends on the loss correlations. Since these correlations are mostly deduced from existing experimental performance data, the range of validity is limited to a conservative compressor design space. Most established loss models ((Lieblein 1960), (Koch and Smith 1976)) are based on traditional blade profile families like C4, C7, NACA-65, DCA (Double Circular Arc) or MCA (Multiple Circular Arc) and do not necessarily represent modern blade profiles accurately. In industrial turbomachinery design processes, calibrated correlations for a given machine type on the basis of comparable previous designs can lead to exceptionally reliable performance prediction. In these cases, preliminary design tools are preferred over more detailed design tools due to their low computational effort, allowing a faster design process.

This capability suggests the coupling of preliminary design methods with an auto-

mated optimization process. Requiring only little computational resources, this method can be used to explore a wide range of design parameters to find an optimum design. The result can then be used as a baseline for subsequent detailed optimization using high fidelity simulation methods to consider complex three dimensional flow phenomena.

Following this approach, two optimized preliminary design processes were setup for the AHLS application and compared in Teichel et al. (2013). In these processes the same optimization process but different preliminary design tool were used. For an operating range comparable to compressor 1 (comp1) the resulting designs were characterized by high solidity, low aspect ratio blade rows with large mean radius. Although a wide design space was considered, both tools only converged to designs comparable to a scaled version of NASA's transonic fan Stage 37 (Reid and Moore 1978). More modern designs of highly loaded compressors stage such as presented by Mårtensson et al. (2007) and Mårtensson et al. (2013) with higher aspect ratios (>1), lower mean radius, and significant hub slope were not found by the optimized preliminary design processes. While the dimensional analysis suggested mixed-flow type compressors to be well suited for this application, the optimized preliminary design process also failed to represent this type of compressor design (Hazby et al. 2015). Since these design types promise high compressor total pressure ratios at high efficiency and a more compact design, the applied optimized preliminary design processes seem to not represent the design space for this application accurately. Considering the small size and low flow capacity of the target compressor design, it is not surprising that conventional preliminary design models which are calibrated for axial flow compressors with flow rates five to ten times the size of the target flow rate are not reliable.

Disregarding the validity of the models in terms of compressor scale, the design task also requires exceeding the conventional axial compressor design space limits in terms of loading. This is illustrated in Fig. 4.3 on the basis of design considerations summarized by Aungier (2003).

Considering a repeating stage with constant mean diameter, constant axial velocity, and no losses in the stator the flow vectors of the stage can be determined using the flow coefficient, load coefficient, and stage reaction (see Sec. 3.1). Imposing the de Haller diffusion limit, rotor flow angles $\beta < 70°$ relative to the machine axis, and a work coefficient $\psi < 1$ to ensure stability near surge (see Smith (1958)), the resulting conventional compressor design space for a reaction of 0.6 is given in Fig. 4.3. It can be seen that the required operating points for this application, resulting from dimensional analysis, exceed the conventional design space. It is therefore questionable if conventional loss correlations are applicable for this design task of highly loaded compressors. Since preliminary design tools do not reliably represent the design space for this application, and therefore exclude promising design types, optimized preliminary design does not seem to be a feasible way to fix critical design parameters for the later detailed design phase.

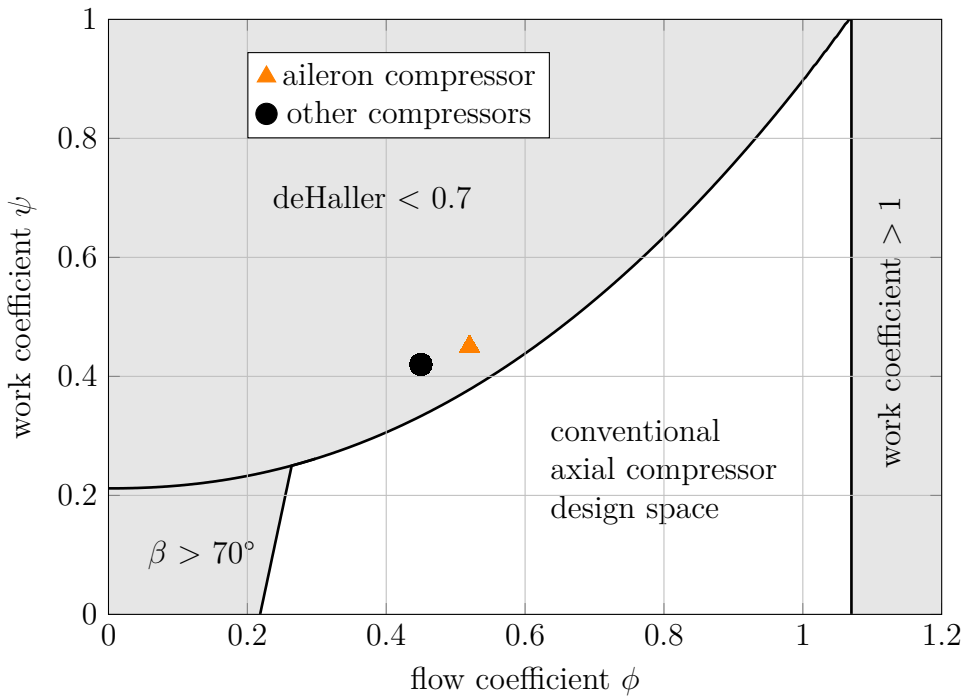

Figure 4.3: Conventional axial compressor design space limits for a reaction of 0.6, adapted from Aungier (2003).

5 Optimized High Fidelity Compressor Design

In this chapter, the development of the compressor design process is described in detail. A strategy is presented to design suitable compressors for the given application considering a wide design space to fulfill the complex requirements such as compact size, high power, and low mass.

Optimized high fidelity compressor design generally focuses on detailed design features such as blade profile shape and blade stacking considering three dimensional flow features by the use of high fidelity models. The basic compressor design parameters of the blade rows and the flow path shape such as size, blade numbers, and rotational speeds are fixed beforehand on the basis of simplified design tools. This helps to reduce computational effort by reducing the degree of freedom and design space in the detailed design phase, thereby reducing the number of high fidelity design evaluations required.

Due to a lack of accurate simplified design tools, a reliable performance prediction for this application (see Sec. 4.2), however, requires the use of high fidelity models to also fix the basic design parameters. It is therefore necessary to develop an efficient, detailed design method to be able to cover the wide range of compressor designs considering axial as well as mixed flow types. This method requires an efficient high fidelity model allowing comparably fast evaluation and a parameterization strategy which covers a wide range of compressor designs while requiring as few degrees of freedom as possible. These are the critical components of the compressor design process described below.

5.1 Numerical Compressor Model

The accurate representation of all significant flow features is a critical requirement of the high fidelity compressor model used in this design process. Aerodynamic optimization naturally results in minimized blade thickness to reduce flow displacement and drag in order to achieve improved compressor performance. Since structural integrity needs to be ensured, the minimum blade thickness is limited by the structural loads the blade can withstand. To determine an optimal compromise between aerodynamic performance and structural integrity of the complex three-dimensional blade shape, both need to be modeled accordingly.

5.1.1 Computational Fluid-Dynamics (CFD)

The three-dimensional flow field of the compressor is represented by using Computational Fluid Dynamics Methods (CFD). The steady-state Reynolds-Averaged-Navier-Stokes

(RANS) simplification of the fundamental fluid relations of the conservation of mass, momentum, and energy together with the fluid properties (Navier-Stokes-Equations) is the established way to numerically model the flow in turbomachinery for design purposes. To solve these equations numerically, a computational grid needs to be generated which discretizes the flow domain according to the required spatial resolution of the flow phenomena. Boundary layer effects are accounted for by using turbulence models which model the unsteady, fluctuating component of the fluid parameters. The underlying fundamentals of this CFD method and its detailed implementation are well documented in open literature e.g. Ferziger and Perić (2008), Cebeci (2005). More detailed CFD modeling techniques such as unsteady RANS or methods which do not rely as much on turbulence models such as Large Eddy Simulation (LES) require excessive computational resources. For design purposes, which require a large number of iterative simulations, these methods are therefore not suitable.

In this work, the CFD software suite TRACE (Turbomachinery Research Aerodynamic Computational Environment) developed by DLR (German Aerospace Center; in German: Deutsches Zentrum für Luft- und Raumfahrt) is used since it is well suited for automation and parallelization. The software is well validated for turbomachinery applications (e.g. Becker et al. (2010)) and also used in commercial design applications. The structured grid of the compressor domain is generated using the software NUMECA AutoGrid5 (NUMECA-International 2016). To minimize the grid size and required computational power, the rotational symmetry for the blade rows is utilized. Applying the established assumption of symmetric flow, only a single, periodic blade section is meshed and modeled in all presented CFD results in this work. An illustration of the computational domain and the grid topology is given in Fig. 5.1 exemplarily for the compressor design presented in Teichel et al. (2015b).

To consider tip leakage/passage flow interaction, which can have a critical influence on the compression shock position in the tip region, the rotor tip gap is included in the grid. Fillet radii are included for both rotor and stator since they can have significant influence on the endwall flow. The rotor fillet radius is a critical design parameter for the structural analysis determining the stresses in the blade root region. Including the fillet in the flow field analysis allows considering the trade-off between structural integrity and aerodynamic performance in the blade hub region. In earlier applications of this design process (Teichel et al. 2015b) the native grid generation software G3DHexa of the TRACE suite was used. G3DHexa allows easy integration in the TRACE CFD-process chain as well as easy automation and parallelization. Compared the to NUMECA AutoGrid5 however it did not reliably provide good grid quality over the wide variation of compressor designs investigated.

It can be argued that, for design purposes, omitting tip gap and fillet radii are valid simplifications of the CFD model to reduce computational effort. Ellbrant et al. (2014) have shown that for their application these simplifications lead to good agreement with experimental data and with more detailed CFD models including tip gap. However, they point out that omitting these features in the design process might favor designs which are sensitive to the omitted flow phenomena (i.e. tip leakage flow, end wall flow) and may lead to under-performance of the designs. Since in the present application a wide

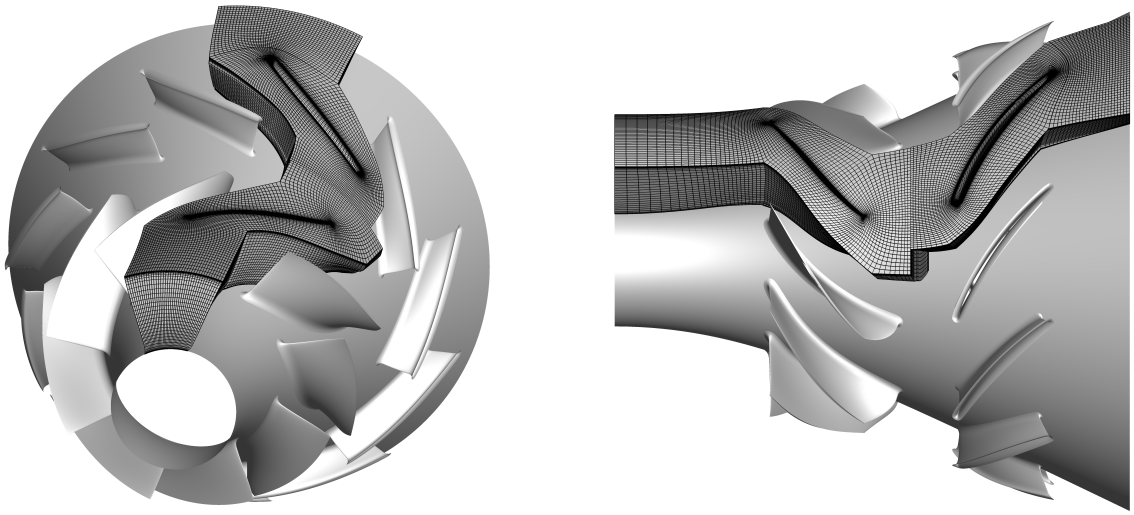

(a) front view (b) side view

Figure 5.1: Exemplary illustration of the computational domain and grid topology for the compressor design presented in Teichel et al. (2015b).

variation of compressor designs is considered, insensitivity of the designs to tip leakage flow and fillet endwall flow cannot be assumed. Including these features is therefore necessary to achieve a representative CFD model.

Applying steady state simulation technique for Turbomachinery applications requires a modeling assumption about the interaction of the rotating rotor passage and the stationary stator passage. In contrast to an unsteady simulation, the changing pitch-wise position of the rotor relative to the stator due to rotation cannot be modeled directly in a steady state simulation. Two different models are widely used to transfer the flow information from the rotating rotor domain to stationary stator domain: The zonal interface model (also known as frozen rotor interface model) transfers the exiting flow field of the rotor directly to the stator domain. The non-uniformity of rotor exit flow field is conserved, but the pitch wise position of the rotor remains unchanged and therefore the wake of the rotor always impinges the stator at the same location. The zonal interface model is well suited for applications where the focus of the steady-state analysis lies on the investigation of rotor-stator interaction. It is less suitable for the determination of the global performance data of a turbomachine such as efficiency since the constant rotor wake position generally leads to a misrepresentation of the mean stator inflow over a full passing cycle of the rotor blade. For these applications the mixing plane model (also known as stage interface) is preferred and therefore also exclusively used in this work. The mixing plane model transfers an averaged flow field from the rotor to the stator domain and generally better represents the mean stator inlet flow flied. Flow non-uniformities are however mixed out using this approach.

Another critical aspect of any CFD setup is the definition of the aerodynamic operating point of the system. For turbomachinery application, this includes the definition of the rotational speed of the machine as well as the flow conditions at inlet and outlet.

The standard set of inlet and outlet flow conditions to fully define the fluid-dynamic system is to impose a turbulent intensity, total temperature, total pressure and velocity distribution at the inlet and a static pressure distribution at the outlet. These base boundary conditions can be controlled in order to match other predefined values at the boundaries. The TRACE CFD software for example allows to impose mass flow rate at the outlet, which is achieved by appropriately controlling the outlet static pressure. Which parameter is best suited as boundary condition depends on the behavior of the fluid-dynamic system and the objective of the simulation. The stability of a compressor simulations significantly depends on the boundary condition and the compressor characteristic in the investigated operating range. To illustrate this, the compressor map presented in Ch. 6, Fig. 6.2 is considered. The characteristic of a compressor simulation as a function of mass flow rate and pressure ratio is represented by a line of constant rotational speed in the upper half of the figure. Towards high mass flow rates the slope of the speed line is very high, resulting in large changes of compressor pressure ratio and therefore of the flow field with little changes of mass flow rate. Directly imposing the outlet pressure as a boundary in this region therefore leads to a more stable simulation since the flow field does not change as much during the iterative solving process. Towards lower mass flow rates, the speed line flattens out, leading to little changes of pressure ratio as a function of mass flow rate. Here, directly imposing mass flow rate as an outlet boundary condition results in a more stable simulation. Since the design point of the compressor in this work is at high rotational speed and high pressure ratio the compressor characteristic in this region is expected to be have a high slope, resulting in better suitability of the outlet pressure boundary condition when considering simulation only stability.

From a design standpoint, the pressure boundary condition has the disadvantage that the mass flow rate of the compressor is not fixed. The design objective in this work is to match the required operating point at predefined mass flow rate and total pressure ratio. The outlet static pressure is therefore not an available fixed parameter which could be used for all investigated designs. The automated design process developed in this work is used to cover a wide design space and results in large variation of compressor designs with different sizes. Imposing exit static pressure ratio in this application has two disadvantages: Firstly, the resulting mass flow variation of the designs would require scaling of each design to match the required operating point. This would not allow a direct comparison of the efficiency since scaling does have a non-negligible effect on the compressor efficiency. The change of the machine size increases the relative influence of boundary layer and other viscous effects which would lead to a seeming advantage of larger designs over small designs. Secondly and most importantly, the obtainable static pressure rise for a given target total pressure rise of the compressor is an essential result of the optimization process. Predefining an outlet static pressure would constrain the design space significantly by excluding compressor designs which are able to achieve the required total pressure at lower or higher outlet static pressure. For these reasons, mass flow rate is imposed as an outlet boundary condition in this work.

For turbulence modeling the k-ω approach by Wilcox (1988) is used according to the established CFD compressor design standards in TRACE. To model the velocity profiles

Table 5.1: Summary of CFD model settings.

physical modeling	
physical model	RANS
turbulence model	k-ω
transition model	γ-Re_Θ
wall velocity model	Low Reynolds
frame change model	Mixing Plane, Fourier, flux averaged
geometric features	
	fillet radius included
	tip clearance included
boundary conditions	
inlet	total temperature, total pressure, axial inflow, 5% turbulent intensity
outlet	mass flow rate (radial equilibrium distribution)

in the boundary layer, the "Low Reynolds" approach model is preferred over the "Wall Functions" approach since it models the flow in the viscous sublayer more accurately. This is critical to correctly represent the tip leakage flow which is strongly dependent on the boundary layer flow in the tip gap. Since the Reynolds numbers range from about $4 \cdot 10^5$ to $1 \cdot 10^6$ depending on the operating point and design, fully turbulent flow in the compressor cannot necessarily be assumed. To account for laminar-turbulent transitional effects, the γ-Re_Θ transition model based on Menter et al. (2006) is applied. A summary of the settings in the used CFD model is given in Tab. 5.1. Using the "Low Reynolds" approach requires increased grid resolution in the boundary layer region. As part of the optimization process a large number (up to 3000) of CFD simulations need to be run. To obtain manageable optimization duration, using reasonable computational resources, it is critical to reduce the number of grid elements as much as possible while still representing the compressor performance accurately.

To determine the appropriate grid resolution and the associated sensitivity of the compressor performance, a grid convergence study was done. A formal grid convergence study according to the procedure documented in ASME (2009) requires the evaluation of at least three grids with identical grid topology and grid cell shape. This is usually obtained through coarsening of a fine grid by omitting every second grid coordinate in all three spatial directions. Every coarsening process therefore divides the number of grid cells by the factor 8. This results in very high grid sizes for the finest grid to still obtain

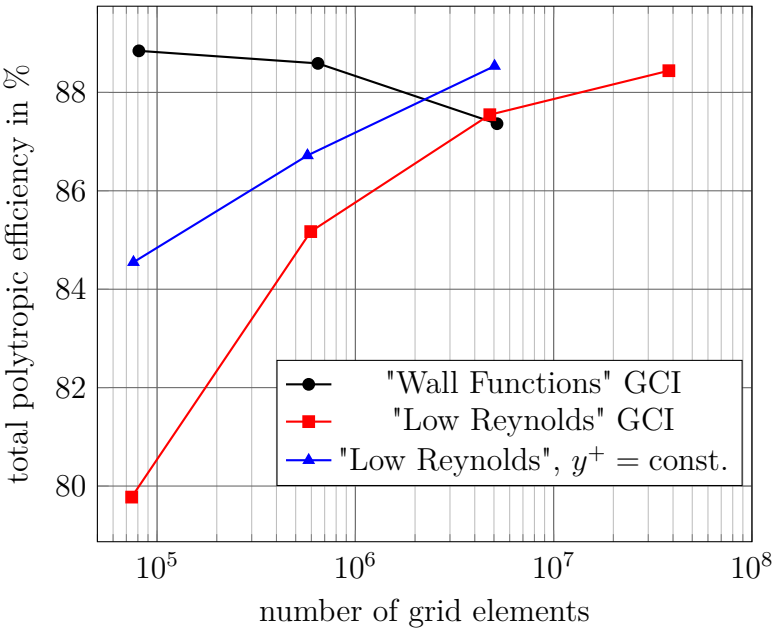

Figure 5.2: Grid sensitivity of reference compressor from Teichel et al. (2015b).

feasible grid resolution for the coarsest grid. This coarsening process is also done in the boundary layer which leads to a significant change of the boundary layer resolution for each grid level. The boundary layer resolution is evaluated using the non-dimensional wall distance of the nearest grid node y^+ which is defined in Eqn. 5.1 as a function of the friction velocity u_*, the wall distance y and the kinematic viscosity ν.

$$y^+ = \frac{u_* \, y}{\nu} \tag{5.1}$$

The wall velocity models "Low Reynolds" and "Wall Functions" require specific ranges of y^+ to work correctly. While the "Low Reynolds" model requires a comparably fine boundary layer resolution with $y^+ < 5$, the "Wall Functions" needs a coarser boundary layer resolution with $y^+ \approx 30$. Since the y^+ value doubles with each coarsening process it is difficult to retain an optimal boundary layer resolution for each grid level.

Following the formal grid convergence study according to ASME (2009), a so called Grid Convergence Index (GCI) is determined which evaluates the relative error of a given performance parameter compared to an idealized solution grid independent solution. A GCI study was done using the compressor design presented in Teichel et al. (2015b) (see Fig. 5.1) considering "Wall Functions" and "Low Reynolds" approach. The results are illustrated in Fig. 5.2, detailed data and figures of the used grids are summarized in appendix A.3. Grid levels are selected with approx. $7.5 \cdot 10^3$, $0.6 \cdot 10^6$, and $5 \cdot 10^6$ grid elements. A finer grid could not reasonably be achieved for the "Wall Functions" study due to the comparably large required wall distance. In the grid convergence study, the performance parameters, in this case efficiency, should ideally converge asymptotically with increasing number of grid elements. This indicates the approach to a "grid element number independent" solution. Since this is not the case, a fourth grid was generated for

the "Low Reynolds" GCI study with about $40 \cdot 10^6$ elements which is close to the feasible limits for this application and the available computational resources. The representation of the grid in Fig. A.14 in the appendix illustrates the excessive gird resolution for this case. Even at this excessive grid resolution, the solution is still sensitive to grid resolution. The difference in efficiency is greater than 0.5% between the two finest "Low Reynolds" GCI study grids with a tendency for further efficiency increase with increasing grid element number. Since the very fine grid resolution is already unfeasibly high for design purposes further grid element increase is not considered.

From Fig. 5.2 it can be seen that the simplified boundary layer flow model with the "Wall Functions" approach differs from the physically more accurate "Low Reynolds" approach significantly. It also does not seem to converge with the "Low Reynolds" results with increasing grid resolution. This suggests that the "Wall Functions" approach is not suitable for this application. The results of the "Low Reynolds" GCI study suggest that considering design processes unfeasibly high grid resolution above $5 \cdot 10^6$ is required to obtain a grid element number independent flow solution. This study, however, necessarily relies on non-ideal, comparably coarse boundary layer resolution for the lower grid sizes due to the coarsening process. To avoid the coarsening of the boundary layer grid and to focus on the effect of the flow field resolution outside of the boundary layer a third, non GCI conformal grid sensitivity study is done. Here, three independent grids are generated with grid element numbers similar to the "Wall Functions" GCI study but with a constant, "Low Reynolds"-ideal y^+ values of approx. 1. The results of this so called "$y^+ = \text{const.}$" study are illustrated in Fig. 5.2 by the blue symbols. In comparison with the "Low Reynolds" GCI study, similar results are obtained by the $y^+ = \text{const.}$" study requiring significantly less grid elements. This is also true for the total pressure ratio as shown in Fig. A.19. It is concluded that the grid resolution of passage flow is less critical than the grid resolution of the boundary layer to achieve good performance prediction. Using the same physical models, a comparable quality of performance prediction can be achieved with a coarser grid resolution of the passage as long as the boundary layer resolution is appropriate. As a compromise between accurate physical representation and low computational effort through reduced grid size, the grid configuration of the $y^+ = \text{const.}$ study with grid element numbers around $0.6 \cdot 10^6$ for the complete compressor stage are selected. If not otherwise stated, this grid template is used for all CFD analysis below.

5.1.2 Computational Solid Mechanics (CSM)

To evaluate the structural integrity of the design, the available process chain in CADO is used. Structural integrity is considered to avoid unreasonable compressor designs in the process of the aerodynamic optimization. In this way, adapted limits for fillet radius, blade thickness, blade chord length, and blade span are determined for each design. The critical loads of the compressor in this regard are the centrifugal loads on the rotor blades. The latter therefore are the focus of the structural analysis. In comparison, other components like the aerodynamic forces on rotor and stator blades and vibrational loads are negligibly small. Due to its small size, the blades and rotor

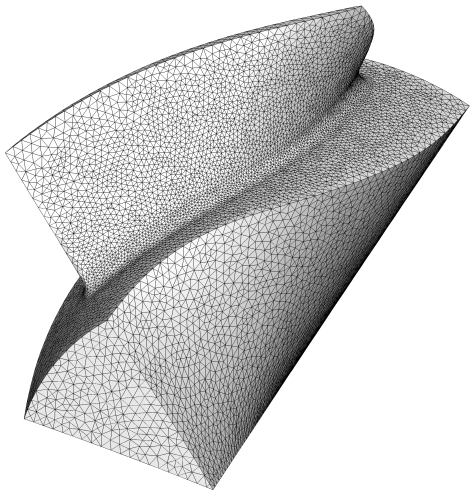

Figure 5.3: Exemplary unstructured mesh used in the automated centrifugal stress analysis from Teichel et al. (2015b)

hub are to be manufactured from one piece as a so-called blisk (**bl**aded d**isk**). The representative geometry for the structural analysis is a periodic section of the blisk with one rotor blade. For this element, an unstructured grid is generated for each design as part of the automated evaluation process. With about 130,000 tetrahedral elements and increased element density in the blade and the hub fillet region, the mesh sufficiently resolves the geometry. An exemplary grid is shown in Fig. 5.3. Using the open source software CalculiX (Dhondt 2004), a static analysis is performed imposing centrifugal loads by rotation about the machine axis and fixing a grid point on the front face of the blisk. Considering not only the blade but also the associated disk section allows realistic modeling of the stress propagation in the blade root region. The blisk material is assumed to be aluminum 7075, the material properties are given in DIN EN 586-2 for the corresponding semi-finished product.

The stress distribution is evaluated using the equivalent tensile stress (von Mises stress). A safety factor of 1.5 to the yield strength of the material is required as part of the optimization to ensure structural integrity of the rotor blades.

5.2 Parameterization Strategy

The CADO optimization environment provides a parameterized geometry generation tool for turbomachinery on the basis of Bézier surfaces (Verstraete 2010a). These surfaces are defined on the basis of established blade row design parameter distributions. The parameter distributions are represented by Bézier curves as illustrated in Fig. 5.4. This approach has the advantage that complex shapes can be controlled with very few parameters. An intrinsic disadvantage of Bézier curves is however that there is no intuitive way to exactly impose specific values for the controlled shape. Consequently, the range specified for the Bézier control point does not directly translate into the range of values of the corresponding design parameter.

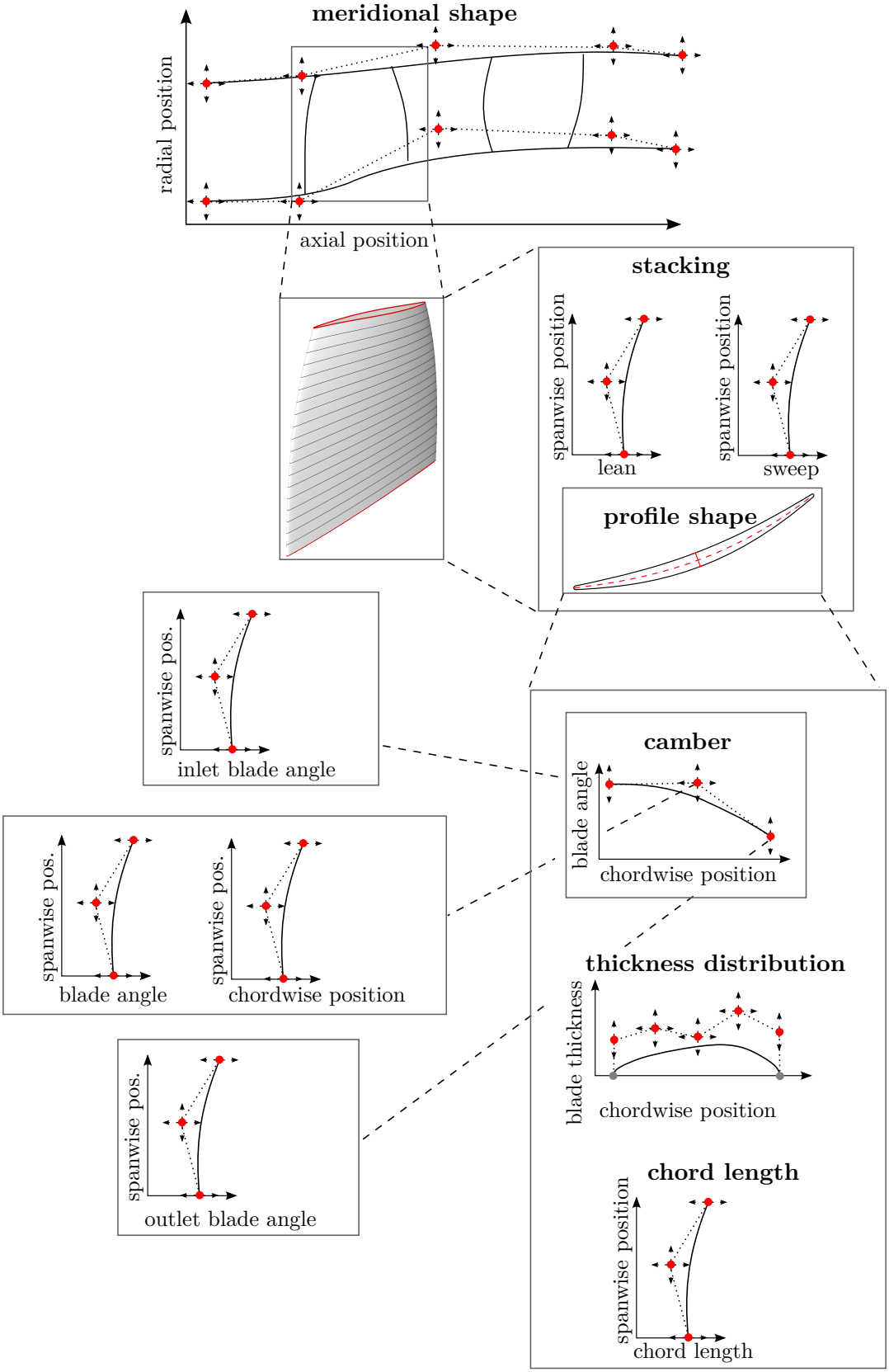

Figure 5.4: Bézier curve based parameterization in CADO adapted from Joly et al. (2014)

CADO allows the designer to adjust the number of control points of each Bézier curve to achieve the desired level of detail of the geometry control. Starting with the meridional shape, Bézier control points define the size of the machine and the slope progression of hub and shroud. The blade position is set using the axial position of the center of gravity of the blade. The blade shape is defined by stacking of spanwise distributed, user-defined blade profiles. The underlying stacking curve combines the spanwise distributions of the profile displacement in chordwise direction (sweep) and of the profile displacement perpendicular to the chordwise direction (lean). Profiles can be individually defined at different spanwise positions by specifying a chordwise thickness distribution, the blade camber, and the spanwise distribution of chord length. The profile camber is defined by three control points: the inlet and outlet blade angle, and an intermediate blade angle. These angles are again defined by a spanwise distribution specified using a user-defined number of Bézier control points. The intermediate blade angle can assume values in the range between the inlet and outlet angle. Its chordwise location is also specified as a spanwise distribution. In contrast to traditional compressor design, no predefined blade profile family is imposed, instead the blade shape can be adapted to the present flow field without shape restrictions.

5.2.1 Parameterization of the Compressor

Since mixed flow designs are to be considered in this study, complex meridional shapes need to be represented by the parameterization. This requires shape and size control not only at the in- and outlet of the machine but also at the in- and outlet of each blade row. Therefore hub and shroud contour are each defined by five control points (see Fig. 5.4).

The dimensional analysis (see Sec. 4.1) suggests comparably small blade heights in the range of 2 - 3.5 cm. Specifying profile shapes at two spanwise positions (hub and shroud) is therefore regarded to provide sufficient degree of freedom for the blade design. Considering the rotor design, this allows on one hand to specifically control the required thin profiles in the tip region to account for the local, high speed flow regime and on the other hand the structurally highly loaded, thicker blade profiles in the hub region. From these two blade profiles, the blade shape at other spanwise positions is deduced according to the resulting parameter distribution. For longer blades, such as typical jet engine fan blades, the definition of profiles at additional spanwise position might be appropriate to allow adjustment of the blade according to midspan flow phenomena. This is however not regarded necessary for this application.

For each of the two profiles, a thickness distribution is specified using five independent control points. While the first and last control point determine the leading and trailing edge thickness the remaining three specify the blade thickness at 25%, 50%, and 75% chord length.

To allow a nonlinear, spanwise blade camber distribution, the inlet, outlet, and intermediate blade angles are each specified with three control points (see Fig. 5.4), requiring twelve parameters in total. For the chord length, lean, and sweep distribution also three control points are defined each to control the spanwise distribution. All spanwise distributions are specified at 0%, 50%, and 100% span width. Additional optimiza-

tion parameters for each blade row are blade count and fillet radius. For the rotor, an appropriate rotational speed needs to specified to achieve the design point.

With the presented parameterization strategy 76 parameters are required in total to completely define a stage design. This includes 10 parameters to define the meridional shape, 34 parameters for the rotor, and 32 for the stator. This number is obviously unfeasible to be considered in a single evolutionary optimization since it requires an excessive number of evaluations to investigate the interaction of all parameters.

5.2.2 Efficient Rotor and Stator Parameterization

A first step to reduce the computational effort of the optimization is to split the process and design the blade rows separately, see Fig. 5.5. This way, basic machine characteristics such as inlet size and rotor tip speed can be investigated in detail as part of the rotor optimization. The subsequent stage optimization focuses mainly on the stator design but also needs to include significant parameters of the upstream rotor to enable adequate blade row matching. Although this two-step design process significantly reduces the number of parameters which need to be considered in one optimization, further reduction is required to obtain an efficient parameterization. Particularly for the rotor, it makes no sense to arbitrarily vary all parameters without considering their interaction. For a given mass flow rate, the inlet area, tip diameter and rotational speed of a compressor can, for example, not be varied independently of each other in a wide range without resulting in excessive blade tip speeds or unreasonable axial flow velocities. Fundamental compressor design considerations can be used to impose limits on the parameter ranges to avoid unreasonable designs and also to reduce the number of independent parameters by taking into account their interactions.

Figure 5.6 illustrates the strategy used in this work to efficiently parameterize the rotor design. To cover a wide design space, not only blade shape but also preliminary design parameters such as diameter, size, rotational speed, and blade number are design parameters. The compressor design operating point is specified by a given mass flow rate ($\dot{m}$) and given inlet conditions (pressure p, temperature T, density ρ). To limit the range of

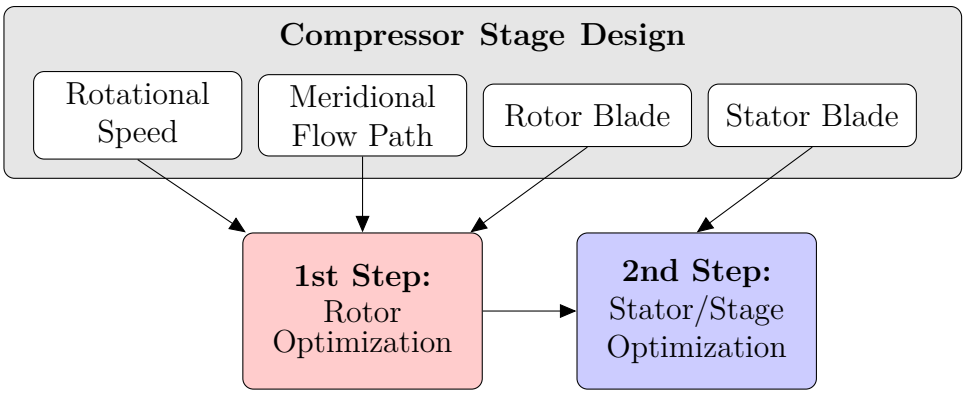

Figure 5.5: Two step compressor stage optimization strategy

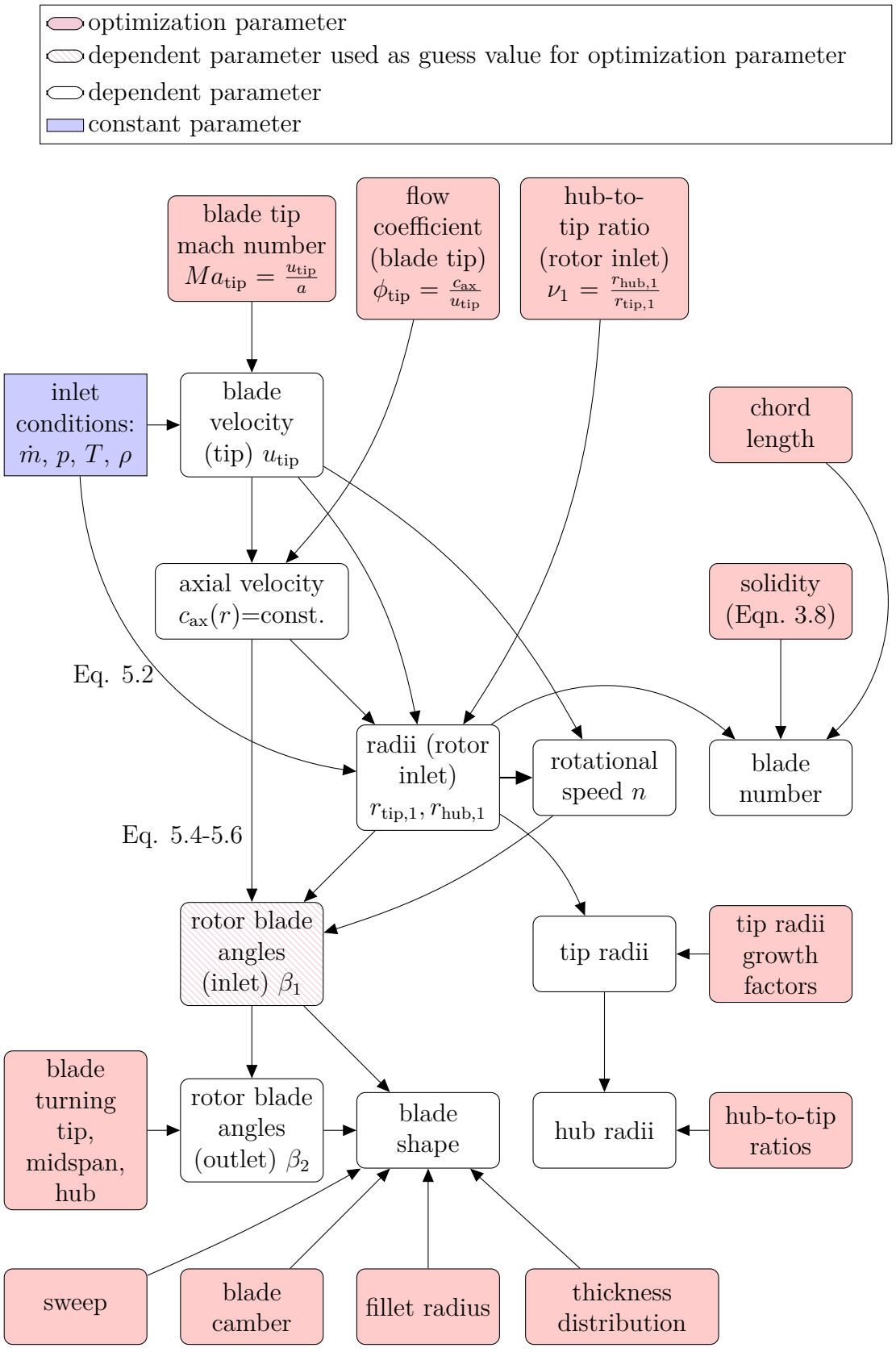

Figure 5.6: Parameterization strategy of the rotor and flow passage

the geometrical parameter defining the compressor design, established non-dimensional compressor design parameters are used. The design parameters are illustrated in Fig. 5.6 by red boxes. In the optimization process a range of variation for each of the design parameters is specified to ultimately define the range of the geometrical parameters presented in Fig. 5.4. While it is difficult to select sensible limits of the interacting geometrical parameters directly, it is more intuitive for the designer to specify ranges of non-dimensional compressor design parameters. Selecting these limits carefully allows to exclude unreasonable compressor designs from the design space, increasing the efficiency of the optimization process.
The first, most decisive geometrical parameters inlet tip radius, blade height, and rotational speed are defined using the blade tip Mach number Ma_{tip}, the blade tip flow coefficient ϕ_{tip}, and the hub-to-tip ratio at rotor inlet ν_1. The formulation of the continuity equation in Eqn. (5.2) represents the relation between these parameters and the tip radius at rotor inlet; a_1 denotes the speed of sound. With the blade tip radius $r_{\text{tip},1}$, the rotational speed n can be determined from the blade tip Mach number Ma_{tip} according to Eqn. (5.3).

$$\dot{m} = \rho_1 \cdot (\phi_{\text{tip}} \cdot Ma_{\text{tip}} \cdot a_1) \cdot \left(\pi \cdot r_{\text{tip},1}^2 \left(1 - \nu_1^2\right)\right) \tag{5.2}$$

$$n = \frac{Ma_{\text{tip}} \cdot a_1}{2\pi r_{\text{tip},1}} \tag{5.3}$$

After the hub and tip radius are defined the mean radius can be determined. The chord length distribution is set to approximate spanwise constant axial chord length with regards to the twisted blades. By scaling this predefined chord length distribution only one parameter is necessary to define the rotor chord length. Specifying a solidity then allows to determine the appropriate number of rotor blades. Assuming a constant spanwise axial velocity distribution at the rotor inlet, the spanwise inlet blade angle distribution can be determined according to Eqns. (5.4) to (5.6). The resulting distribution is used as a guess value for the optimization. The final blade angles are allowed vary around theses values to determine the optimum incidence.

$$\tan\left(\beta_{\text{in,tip}}\right) = \phi_{\text{tip}} = \frac{c_{\text{ax}}}{u_{\text{tip}}} \tag{5.4}$$

$$\tan\left(\beta_{\text{in,midspan}}\right) = \frac{c_{\text{ax}}}{u_{\text{midspan}}} = \frac{c_{\text{ax}}}{2\pi r_{\text{midspan}} \cdot n} \tag{5.5}$$

$$\tan\left(\beta_{\text{in,hub}}\right) = \frac{c_{\text{ax}}}{u_{\text{hub}}} = \frac{c_{\text{ax}}}{2\pi r_{\text{hub}} \cdot n} \tag{5.6}$$

The outlet blade angles are defined from the inlet blade angles by applying a spanwise range for the blade turning distribution. To allow a sufficient degree of freedom for the spanwise rotor work distribution, the three parameters $\beta_{\text{out,hub}}$, $\beta_{\text{out,mean}}$ and $\beta_{\text{out,tip}}$ are required.

The detailed blade shape is defined by the blade camber and blade thickness distribution. As described earlier the rotor blade profiles at hub and tip need to be adapted to different flow regimes. While at the hub a conventional profile can be used for the

subsonic flow regime the tip profile experiences transonic flow with compression shock phenomena and needs to be shaped accordingly. Typical transonic compressor blade profiles mimic wedge type profiles ((Reid and Moore 1978), (Biollo and Benini 2012)). These profiles are characterized by a comparably thin, low cambered (wedge-like) front part of the blade to reduce losses at the blade tip and enable an efficient compression shock on the suction side. The low camber and local optimization of the blade shape to control the boundary layer at the shock location minimizes shock induced flow separation allowing highly loaded blades with low losses (Kerrebrock 1981). The location of maximum camber and maximum thickness of these blades is located downstream of the shock towards the trailing edge. This allows efficient flow turning of the subsonic after-shock flow. Typical subsonic compressor blade profiles have thicker leading edges to improve tolerance to incidence. The location of maximum thickness and camber is located closer to the leading edge to avoid excessive blade loading in the rear part of the blade which may cause flow separation due to the increased boundary layer thickness.

In this application, as a result of early sensitivity studies, detailed control of the camber distribution showed to be more critical than the detailed control of the profile thickness. The thickness variation is therefore limited to the region of maximum thickness of the blade while the overall thickness distribution remains mostly unchanged. For the camber control through the intermediate blade angle, all six parameters are varied according to Fig. 5.4.

Concerning the thickness distribution at the tip profile, only the central control point and its neighboring control point towards the trailing edge are varied. The other points are set constant to approximate a wedge type profile with reasonably thin blade edges. In earlier optimizations, it was found that the blade tip thickness at leading and trailing edge approached the minimal allowed value eventually since this minimizes aerodynamic loss. Weakening of the blade is not critical in this region of the blade due to the low structural loads. As a reference for ambitious but feasible blade thicknesses the profile data of NASA's established transonic Rotor 37 (Reid and Moore 1978) is used. There the spanwise leading edge thicknesses distribution from hub to tip varies between 0.5 and 0.26 mm. For the trailing edge, these values range from 0.6 to 0.18 mm. Considering that these values represent the limiting range for manufacturing accuracy even today, the thickness control points of the present design process are set to always exceed these values. Due to the parameterization method in CADO of using Bézier control points to specify the blade thickness neither the true blade thickness nor the shape of leading and trailing edge can be controlled directly in a straight forward way.

For the hub profile, the three central blade thickness control points are varied to control the structural integrity of the blade root. The control points determining the leading and trailing edge thickness are set to be equal to the neighboring points towards the center. This results in comparably large leading and trailing edge thicknesses at the hub but helps to insure structural integrity at the blade root and helps to compensate for the very small leading and trailing edge thicknesses at blade tip.

For the rotor stacking curve only sweep is considered. While lean was often reported as a successfully measure to reduce endwall loading in the stator, avoiding corner stall (Fischer et al. 2003), sweep is a widely used way to influence endwall flow in transonic

rotors ((Wadia et al. 1998), (Govardhan et al. 2007)). Generally, forward sweep near the tip was shown to reduce leading edge tip loading and can therefore be used to reduce shock losses in this region. At the same time, it increases leading edge hub loading which might promote hub separation in the rotor. Biollo and Benini (2012) illustrated that these counteracting mechanisms can be balanced by using s-shaped sweep (forward sweep near the tip and backward sweep near the hub). To include this blade shape variation in the design space of the compressor model, two control points (at 50% and 100% span) are allowed to vary. The control point at the hub is set constant to avoid axial shift of the blade.

The shape definition of the meridional flow path is done in relation to the inlet radii at hub and shroud. To allow increased shroud radii which are characteristic to mixed-flow type compressors, tip growth factors are defined at rotor inlet, rotor outlet, stator outlet and compressor outlet. Due to the nature of the parameterized model, these factors control the position of the Bézier control points and only indirectly determine the shroud radius. To avoid significant shroud slope at rotor inlet, the corresponding control point is set equal to the inlet radius. For the three downstream control points, only shroud expansion is allowed with a maximum exit shroud radius of two times the inlet radius. The associated hub radii are then determined from the corresponding hub-to-tip ratios. The inlet hub-to-tip ratio variation is set to allow a large design space with rotor blade heights between 30% and 94% of the shroud diameter. Like for the shroud, significant hub slope upstream of the rotor inlet is avoided by setting the Bézier control point at the rotor inlet equal to the inlet of the stage. The exit hub-to-tip ratio is determined on the basis of a reasonable guess for the exit cross sectional area. With the given mass flow rate and an assumed rotor exit density for the given operating point, the exit cross sectional area can be determined on the basis of the exit axial flow velocity. Allowing an exit axial flow velocity range between 25% deceleration and 50% acceleration compared to the inlet axial velocity fixes the exit hub-to-tip ratio within physically reasonable limits. The two hub-to-tip ratios at intermediate positions are allowed to vary so that hub radii vary towards the exit hub radius with a reasonable slope. It is noteworthy that the length of the meridional flow path remains unchanged with varying blade length. This may lead to a modeling error since the distance of the inlet and outlet interfaces to the blade changes possibly, resulting in different flow conditions and varying interface-flow interactions. To avoid this effect, the meshing process is adjusted to shift the inlet and outlet section within the range of the meridional flow path to achieve a distance of approximately 1/3 axial chordlength from blade leading and trailing edge respectively. This results in varying axial inlet and outlet position for each design depending on its axial chordlength. Finally, the fillet radius of the rotor is varied between 1 and 2.5 mm to investigate the optimal trade-off between structural integrity and increased blockage of the hub end-wall flow.

Following the presented design considerations, 31 parameters are required to define the rotor design including the rotational speed, shape of the meridional flow path, blade number, and detailed blade shape. Applying physically based simplifications the number of parameters is reduced by 3 without notably constraining the design space. Using established design parameters such as tip Mach number, flow coefficient, and solidity, a

Table 5.2: Optimization parameters of the rotor and the stator/stage optimization.

	rotor optimization		stator/stage optimization	
meridional shape	flow coefficient	1		
	hub to tip ratios	4	area factor	2
	tip growth factors	3	mean radius factors	2
blade shape	chord length	1	chord length	1
	thickness	5	thickness	6
			rotor outlet angle	3
	inlet angle	3	stator inlet angle	3
	outlet angle	3	stator outlet angle	3
	camber	6	camber	6
	sweep	2	lean	1
	fillet	1		
blade row	tip Mach number (rotational speed)	1		
	solidity	1	solidity	1
sum		31		28

sensible range of variation could be defined for all significant machine parameters. This allows the investigation of a wide design space, excluding unreasonable designs.

The same approach was also applied to specify the design space for the stator downstream of the rotor. The degree of freedom of the stator blade design is analogous to the presented rotor design method. The thickness distribution at 0 % and 100% span is each defined with three control points at 1/6, 1/3, and 1/2 chord length respectively. Early sensitivity studies showed that the control of the leading region of these subsonic compressor blade profiles had a greater impact on the performance than the control of the trailing edge region. These trailing edge control points are fixed to provide a smooth transition from the thicker leading edge region to the thinner trailing edge region of the blade. The three spanwise stator blade inlet angle control points are set to vary about the absolute rotor exit flow angles to achieve optimal incidence. Like for the rotor, the stator flow turning is also adjusted by three spanwise control points. To allow wide variability of the blade camber, all six parameters are allowed to vary. The stator chord length is scaled globally with a single factor. The stator blade number is specified using the solidity. Following the argument made in the section above for the stacking curve of the stator blade only lean at 50 % span is varied. This is done to allow stator bow in order to reduce blade loading and avoid flow separation in the end-wall regions (Fischer et al. 2003). The stator fillet is fixed to 2 mm which was determined to be a reasonable trade-off between manufacturability constraints and aerodynamic constraints. Since the

structural loads on the stator blades due to the flow field are insignificantly small it is not necessary to consider the interaction of the fillet size and the aerodynamic stator design as part of the automated design process as it was done for the rotor.

To achieve optimal stage matching between rotor and stator, the rotor blade and meridional flow path shape are also adjusted as part of the stator design process. The rotor blade exit angles are allowed to vary about the initial values resulting from the rotor design process. For the meridional flow path, the hub, and shroud radii at exit region of stator and stage are varied. This is done by variation of scaling factors for the cross sectional area and the mean radius at these sections requiring four additional parameters. The variation allows expansion as well as contraction of the flow path as well as radial shift inwards and outwards. All in all 28 parameters are required for the stator/stage design reducing the number by 4 compared to the initial approach in Sec. 5.2.1. A summary of all used optimization parameters for the rotor and the stator/stage optimization is given in Tab. 5.2.

5.3 Objectives and Constraints

The optimization method and the underlying algorithm used in this process are described above in Sec. 3.3.5. After the selection of the degrees of freedom of the optimization problem in the section above (Sec. 5.2.2),the selection of the optimization objective and constraints is discussed below. The optimization objectives steer the automated design process to search designs in a particular region of the design space. The selection of the objectives therefore needs to be considered carefully to precisely define the desired results. For complex optimization problems, this often requires the consideration of more than one performance parameter. This is often done by combining multiple performance parameters into one objective. These so called pseudo-multiobjective optimization methods result in a particular point of the Pareto Front according to the formulation of the objective. Since the design process in this work aims at considering a wide range of trade-offs between the different objectives, true multiobjective optimization methods are required.

For each rotor and stator/stage optimization three objectives are used. These objectives are used to steer the design process in order to fulfill the desired design goals. In this case these design goals are to achieve the required compressor performance (pressure rise), to reduce losses (efficiency), and to cover a wide design space concerning rotor speed and size. The last design goal later allows to select a compressor design which considers the requirements, and interactions with the surrounding system. In case of the EPHLS these interactions include the matching of the compressors rotational speed and power with the design limitations of the electric motor as well as to match size and mass of the compressor with the packaging concept of the system. Design consideration in this regard are the feasibility of the compressor-motor configuration, the feasibility of the bearing system and of the drive shaft rotordynamics, and on the other side the consideration of the available space in the wing box (see Figs. 2.3 and 2.5).

The performance design goal of the rotor is covered by aiming at maximum total-total

pressure ratio with the first objective. Using a constraint, the search space is constricted to total pressure ratios higher than 1.7 to exclude designs with insignificant pressure rise. This still allows a wide range of resulting total pressure ratios considering the specific target pressure ratio of approx. 2.35 but provides reliable convergence of the process. Redefining this objective to match the target pressure ratio and constraining the search space around this target would provide a greater number of designs in the relevant pressure ratio range. However, it makes it also more difficult for the design process to find valid results which can lead to slower convergence of the optimization.

The other two objectives of the rotor optimization are used to control the design process to investigate a wide range of rotational speeds. The rotational speed was selected as the guiding parameter since it has a major influence on the design of the EPHLS. It scales the size, mass, power density, and loading of the compressor as well as of all electric components. The rotational speed also determines the structural integrity of the rotor due to the associated centrifugal load. Structural integrity is ensure by a constraint excluding design with mechanical safety factors less than 1.5. This requires a CSM evaluation of each design at the individual rotational speed. Two conflicting objectives control the investigated design space. On one hand, the minimization of the rotational speed is used as a second objective. As a result, rotor designs with increased diameter are favored by the automated design process. This way the high circumferential speeds, necessary to achieve the required high aerodynamic loading (see Sec. 3.1 and Eqn. (3.9)) are obtainable at low rotational speed. To counteract the tendency of the design process towards large diameter rotors on the other hand, the minimization of the rotor mass moment of inertia J is introduced as a third objective. This not only leads to small diameter rotors but also reduces rotor mass and relieves the later rotordynamic design of EPHLS. Since the evaluation tools used do not provide the exact value of the mass momentum of inertia of the rotor, it is approximated by using the definition of the mass momentum of inertia of a cylinder in Eqn. (5.7). This way all significant parameters determining the actual mass momentum of inertia, namely mass m, radius r and length l, are considered.

$$J_{\text{pseudo,rotor}} = \frac{1}{2} \cdot m_{\text{rotor}} \cdot r^2_{\text{rotor,max}} + \frac{1}{12} \cdot m_{\text{rotor}} \cdot l^2_{\text{rotor}} \tag{5.7}$$

Although these objectives do not directly include the minimization of loss, this optimization problem leads to designs with high efficiency since for a given work input and fixed compressor mass flow rate low loss leads to high total pressure ratios. To limit the results to designs with low loss, a constraint which requires all designs to have efficiencies greater than 85% is included. All constraints used to limit the objective space in the rotor and stator/stage optimization are summarized in Tab. 5.3.

For the stator/stage optimization, the stator performance is evaluated by the static-to-static pressure ratio which is an intuitive measure of the stator's ability to increase the static pressure. To ensure sufficient total pressure rise, the axial total-to-total stage pressure ratio $\Pi_{\text{tt,ax}}$ is to be maximized. It is defined in Eqn. (5.8) using the total pressure definition for compressible fluids only considering the kinetic energy in axial direction. This way, exit swirl due to incomplete stator flow turning is not considered as

Table 5.3: Constraints of the rotor and the stator/stage optimization.

Constraints Rotor optimization	**Constraints Stator optimization**
converged, valid evaluation	converged, valid evaluation
mechanical safety factor > 1.5	static pressure ratio > 1.1
total pressure ratio > 1.7	$1.8 <$ total pressure ratio < 2.5
total polytropic efficiency $> 85\%$	

Table 5.4: Objectives of the rotor and the stator/stage optimization.

Rotor optimization		**Stator optimization**	
objectives	design goals	objectives	design goals
maximize: total-total rotor pressure ratio	obtain required performance	maximize: axial total-total stage pressure ratio	obtain required performance
minimize: rotational speed	cover wide design space in terms of rotational speed	maximize: static-static stator pressure ratio	improve stator performance
minimize: mass momentum of inertia		maximize: total-total polytropic stage efficiency	minimize losses

a usable form of energy for EPHLS and stator designs with low swirl are favored (Teichel et al. 2015b).

$$\Pi_{\mathrm{tt,ax}} = \frac{p_{\mathrm{tot,ax,out}}}{p_{\mathrm{tot,in}}} = \frac{p_{\mathrm{stat,out}} \cdot \left(1 + \frac{\gamma-1}{2} \cdot \left(\frac{c_{\mathrm{ax,out}}}{a_{\mathrm{out}}}\right)^2\right)^{\frac{\gamma}{\gamma-1}}}{p_{\mathrm{tot,in}}} \tag{5.8}$$

To specifically target low stage losses in this final optimization process, the maximization of the total-to-total polytropic stage efficiency was included as a third objective. The objectives and the underlying design goal for both optimization processes are summarized in Tab. 5.4.

5.4 Optimization Method: Meta-model Assisted vs. Direct Optimization

The following study is meant to illustrate the sensitivity of the optimization result to the optimization method (meta-model assisted or direct optimization) and the number of evaluations per iteration. Instead of a computationally expensive CFD model, analytical test functions are used to evaluate the optimization result in comparison to the known

minimum of the test functions. Since the optimization method is non-deterministic, a statistical analysis of the results over multiple runs of the optimization process would be required to allow statistically significant statements about the behavior of the process. For the purposes in this work, the behavior of a single optimization run for each case is however sufficient to illustrate the basic behavior of the used optimization process. To mimic the given turbomachinery optimization problem the Zitzler-Dep-Thiele test functions one (ZDT 1) and three (ZDT 3) are used. Among others these functions were proposed by Zitzler et al. (2000) as test functions for multi-objective optimization algorithms. The general approach of all their test functions is given in Eqn. (5.9).

$$\begin{aligned} \text{minimize objectives: } & \mathrm{Obj}_1(x_1), \mathrm{Obj}_2(x_1, ..., x_m) \\ \text{with: } & \mathrm{Obj}_2 = g(x_2, ..., x_m) \cdot h(\mathrm{Obj}_1, g) \\ \text{optimization parameters: } & x_1, ..., x_m \text{ ; with } x_i \in [0, 1] \text{ ; } m = 30 \\ \text{Pareto Front for: } & g = 1 \end{aligned} \tag{5.9}$$

The ZDT test functions are characterized by having two objectives and a comparably large number of optimization parameters usually selected to be $m = 30$. The shape of the Pareto Front differs, depending on the particular test function. ZDT1 given in Eqns. (5.10) to (5.12) has a continuous, convex Pareto Front which represents the result of a typical turbomachinery optimization problem (see Figs. 5.7,5.9 and 5.11).

$$\mathrm{Obj}_1 = x_1 \tag{5.10}$$

$$g = 1 + 9 \cdot \sum_{i=2}^{m} \frac{x_i}{m-1} \tag{5.11}$$

$$h = 1 - \sqrt{\frac{\mathrm{Obj}_1}{g}} \tag{5.12}$$

ZDT3 (Eqns. (5.13) to (5.15)) represents a more complex case with a discontinuous Pareto Front with four local minima (see Figs. 5.8,5.10 and 5.12).

$$\mathrm{Obj}_1 = x_1 \tag{5.13}$$

$$g = 1 + 9 \cdot \sum_{i=2}^{m} \frac{x_i}{m-1} \tag{5.14}$$

$$h = 1 - \sqrt{\frac{\mathrm{Obj}_1}{g}} - \frac{\mathrm{Obj}_1}{g} \cdot \sin\left(10\pi \mathrm{Obj}_1\right) \tag{5.15}$$

For these two optimization problems the performance of direct optimization (DIR) vs. meta-model assisted optimization (using Artificial Neural Networks, ANN) is compared in terms of quality of the result, the required number of evaluations, and the suitability for turbomachinery application. Additionally, the sensitivity of the result to the number of evaluations per iteration is illustrated for the direct optimization. In Tab. 5.5, the required number of evaluations and iterations at two significant states of the optimization are summarized for each test case. The first state represents the approximate identification of shape of the Pareto Front considering the results of all available evaluations at

Table 5.5: Sensitivity of the optimization result to the optimization settings.

Test Case	meta-model	Test Function	Evaluations per Iteration	Pareto Front Identification	Pareto Front Representation
DIR-ZDT1-IND10	direct	ZDT 1	10	570 Eval. Iteration 55	1370 Eval. Iteration 135
DIR-ZDT3-IND10	direct	ZDT 3	10	2520 Eval. Iteration 250	5020 Eval. Iteration 500
ANN-ZDT1-IND10	ANN	ZDT 1	10	337 Eval. Iteration 8	657 Eval. Iteration 40
ANN-ZDT3-IND10	ANN	ZDT 3	10	707 Eval. Iteration 45	4257 Eval. Iteration 400
DIR-ZDT1-IND30	direct	ZDT 1	30	1410 Eval. Iteration 45	2310 Eval. Iteration 75
DIR-ZDT3-IND30	direct	ZDT 3	30	1860 Eval. Iteration 60	4860 Eval. Iteration 160

this point. At the second state enough evaluations are in close proximity of the Pareto Front for correct, quantitative representation of its shape.

As expected, meta-model assisted optimization requires less evaluations to adequately represent the Pareto Front. For the simpler Pareto Front of ZDT1, the direct optimization method requires up to almost 4 times as many evaluations to achieve Pareto Front identification and Pareto Front representation. For the more complex Pareto Front of ZDT3 this difference less significant.

The resolution of the objective space of each test case is shown in Figs. 5.7 to 5.12. Considering Figs. 5.7 to 5.10 it is apparent that resolution of the Pareto Front using the meta-model assisted optimization strategy is sparse compared to direct optimization with otherwise same settings. On one hand, this due to the lower number of evaluations required with meta-model assisted optimization. On the other hand, it becomes clear that the search space of this method is comparably confined. For both test cases, ANN assisted optimization does not obtain a good resolution of the Pareto Front since a large number of evaluations is clustered near the upper and lower bounds of the objective space. Although there are sufficient individuals to adequately represent the Pareto Front, the number of individuals in the area near the Pareto Front is very limited. This makes it harder to obtain meaningful information about the influence of the design parameters in this region.

In the test cases illustrated in Figs. 5.11 and 5.12 the number of evaluations per iteration was increased to match the number of optimization parameters. A higher number of evaluations per iteration allows a better resolution of the Pareto Front in each optimization iteration. Particularly for complex Pareto Front shapes (ZDT3) this allows the

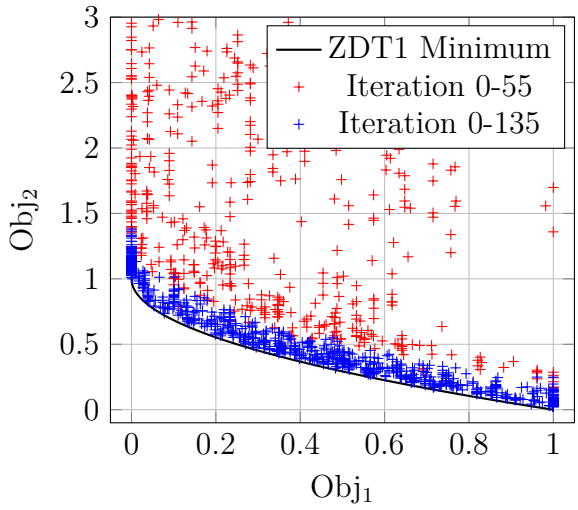

Figure 5.7: DIR-ZDT1-IND10

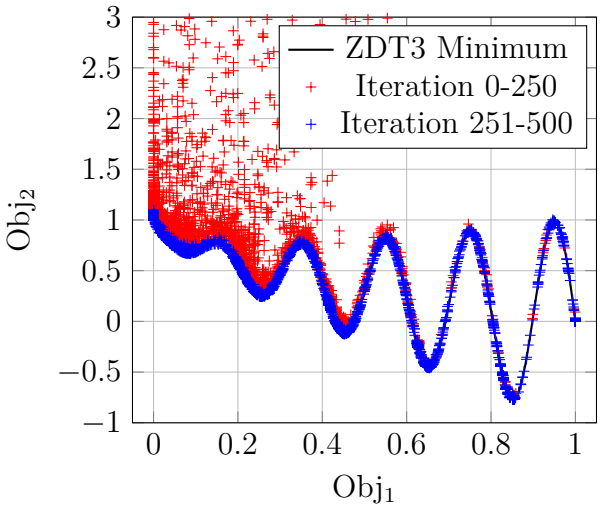

Figure 5.8: DIR-ZDT3-IND10

optimization algorithm to converge more directly since no permanent rearrangement of the Pareto-optimal individuals on the front is necessary. For a given number of overall evaluations however less iterations can be completed when the number of evaluations per iteration is increased. This results in less opportunity for improvement in the optimization process and might result in slower convergence. Evidently there seems to be a trade-off in the selection of the number of evaluations per iteration to achieve best convergence of the optimization process. Additionally, matching the number of evaluations per iteration to the number of optimization parameters allows a more complete representation of the optimization problem in each iteration. This way each parameter can be varied in each iteration allowing to better account for parameter interaction. For these reasons, the direct optimization test case with 30 evaluations per iteration is able to converge to an optimum with less iterations, for the complex Pareto Front Shape of ZDT 3 even with less evaluations than the direct optimization strategy with 10 evaluations per iteration. Comparing Figs. 5.11 and 5.12 to Figs. 5.7 and 5.8, the higher number of evaluations per iteration leads to a better resolution of the objective space which allows a more complete representation of the optimization problem.

With the given task for the optimized investigation of a wide design space of a highly loaded compressor stage, additional considerations need to be taken into account. Optimizing a high fidelity numerical model instead of an idealized test function requires a high degree of robustness of the optimization process with respect to failed evaluations. Although the parameterization (see Sec. 5.2.2) was chosen in a way to avoid unreasonable results, only part of the resulting designs are able to achieve the required high pressure ratios. Over the course of the rotor optimization, typically about half of the CFD evaluations did not obtain sufficient convergence. In the early phase of the optimization process, this fraction was even greater, often preventing an adequate training of the meta model and consequently unreliable convergence of the optimization process.To

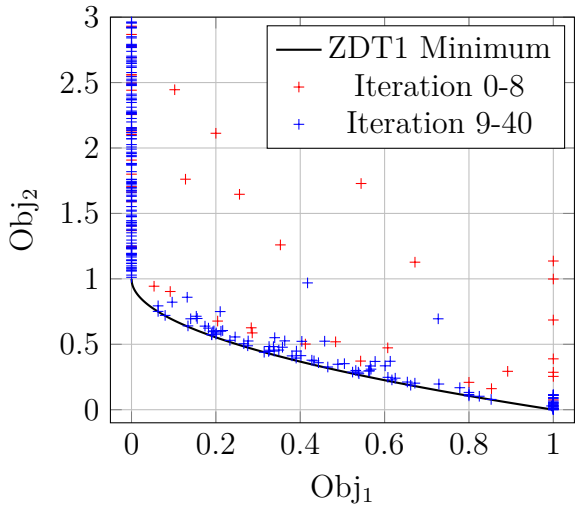

Figure 5.9: ANN-ZDT1-IND10

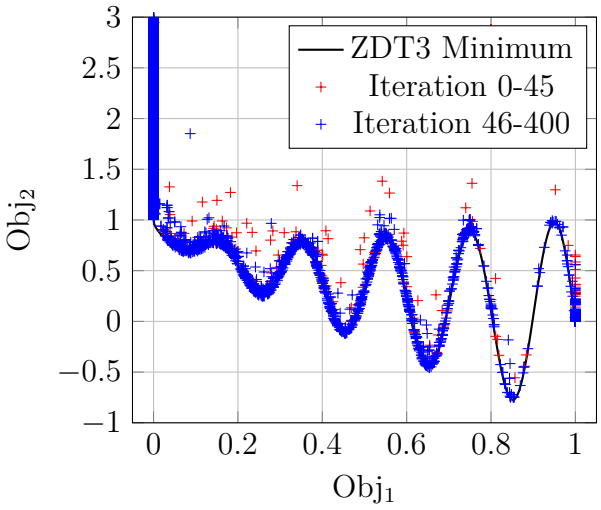

Figure 5.10: ANN-ZDT3-IND10

minimize the number of evaluations required to obtain an optimum solution, meta-model assisted optimization seems to be the better approach. But since for research purposes a reliable, detailed representation of the optimum region of the objective space is more critical in this application, the direct optimization method is preferred.

Since for this work the inclusion of a third objective was necessary to control the objective space in greater detail, a comparably high number of evaluations per iteration is required to provide sufficient resolution of the objective space. Due to the comparably large number of design parameters in this application (see Sec. 5.2.2) the number of evaluations is matched accordingly, which leads to 31 evaluations per iteration.

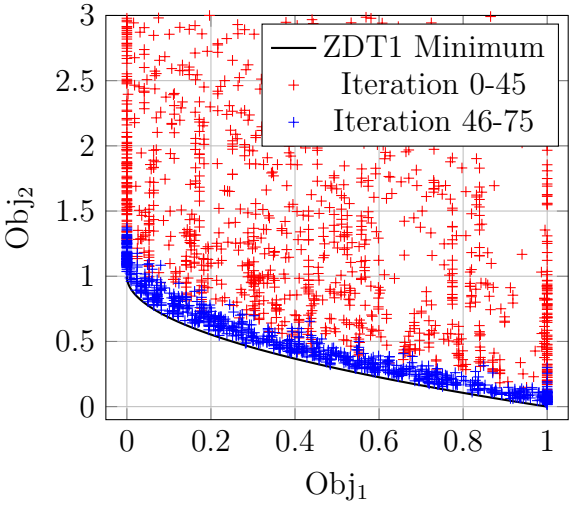

Figure 5.11: DIR-ZDT1-IND30

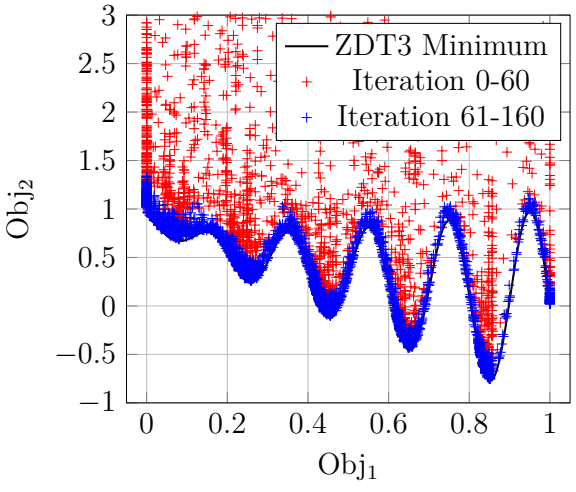

Figure 5.12: DIR-ZDT3-IND30

5.5 Design-Point vs. Multi-Point Optimization

Additionally to the consideration of multiple physical models to evaluate the performance of a system, also the selected operating point for which the performance is evaluated determines the result of an optimized design process. Generally, the most demanding operating point or the most relevant operating point for later operation is selected as the design point. In this application, the design point is the operating point with highest total pressure ratio and highest corrected mass flow rate.

The use of one design point in the optimized design process can lead to confined optimization of the system in one particular area of the operating range and might not lead to satisfying performance in other areas of the operating range. To ensure optimal performance over a wide operating range, the so called multi-point optimization considers multiple operating points. The inclusion of each additional operating point multiplies the number of evaluations, considerably increasing the required computational power for the design process. For a successful multi-point optimization also a proper definition of all boundary conditions defining the operating points is required. This definition can be difficult when designing new systems with unknown operating range. In the presented design process this is the case since the size and rotational speed of the compressors at the design point is subject to change as part of the optimized design process. To specify the boundary conditions at a specific part-load operating point requires an assumption about the compressor operating range characteristic to select the appropriate rotational speed. This assumption then becomes part of the objective function penalizing designs with different characteristics. This can lead to ill-convergence of the automated design process when designs are not considered due to their apparently inferior performance at the specified operating point only because it is specified at an inappropriate rotational speed for the particular design.

Considering the compressor maps of the designs presented in the following Figs. A.24 to A.25 in the appendix illustrate this difficulty. Just from the given rotational speed at the design point at high pressure ratio and corrected mass flow rate, there is no reliable way to guess an appropriate rotational speed to represent a high efficiency part load operating point for all available designs. Moreover, it can be seen that for this application multi-point optimization is not required since high efficiency at the design point is associated with high efficiency over the full operating range. For this reason, the given design process only considers one operating point and utilizes the reduced computational power to cover a wider design space.

5.6 Optimization Results - Rotor Designs

The results of the described automated rotor design process are illustrated in Fig. 5.13. 115 populations with overall more than 3600 individuals were evaluated. All converged individuals which satisfy the constraints and have efficiencies greater than 90 % are shown. Figures 5.13a through 5.13c illustrate the objective space defined by the three objectives total pressure ratio, rotational speed, and mass momentum of inertia.

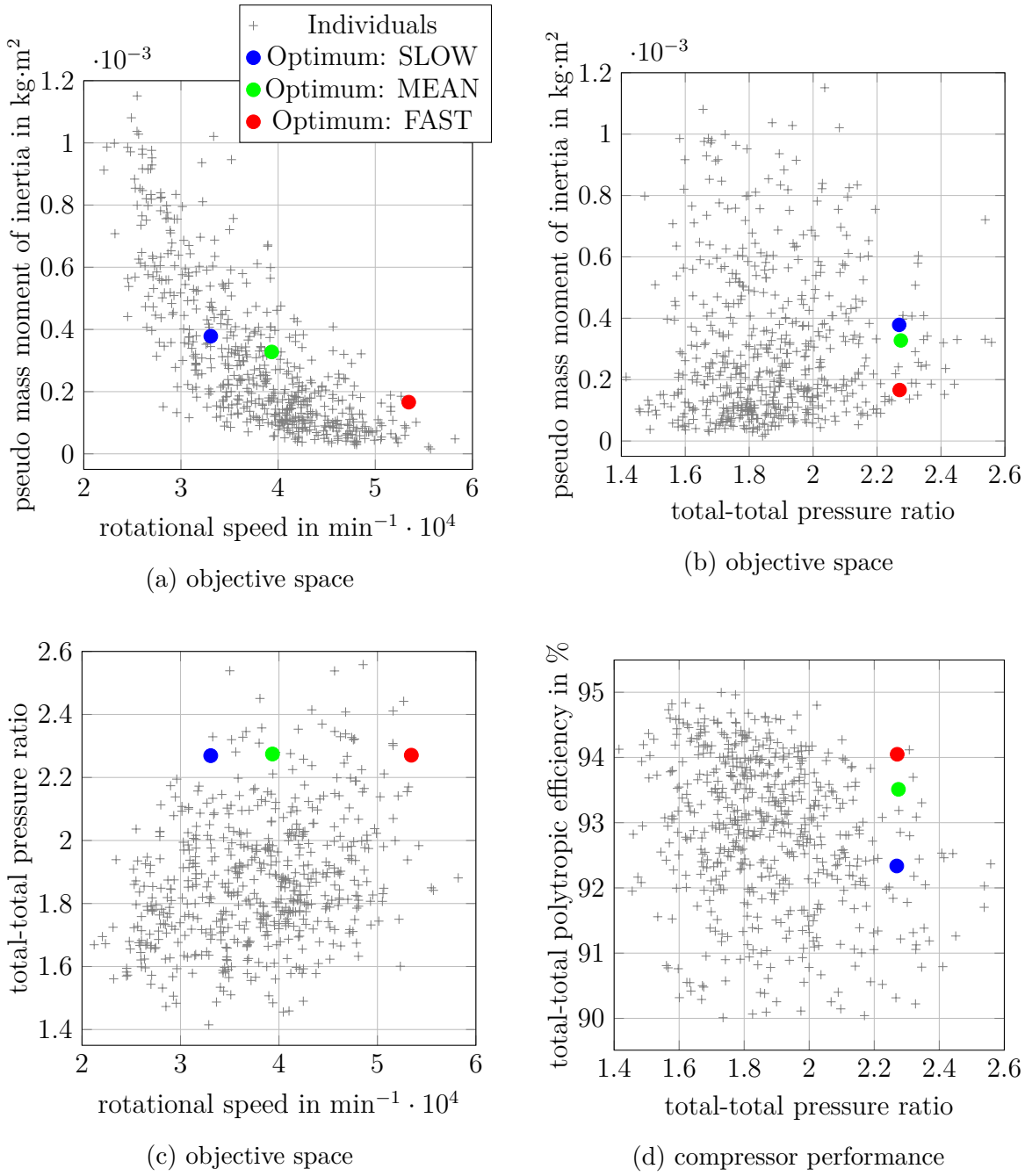

(a) objective space

(b) objective space

(c) objective space

(d) compressor performance

Figure 5.13: Results of the rotor optimization: Objective space and compressor performance of all relevant individuals.

Since the Pareto Front is three-dimensional, these two-dimensional representations do not show a distinct, sharp Pareto Front like it is common for two dimensional optimizations. In fact the third objective leads to a significantly increased objective space so that a majority of the shown evaluations are part of the Pareto Front.

The distribution of the designs in Fig. 5.13a illustrates the counteraction of rotational speed and mass momentum of inertia: high rotational speeds result in low momentum of inertia and vice versa. The total pressure does not show any distinct trend in relation to the other two objectives (Fig. 5.13b and Fig. 5.13c). Interestingly, high pressure ratios can consequently be achieved over a wide range of rotational speeds.

Figure 5.13d illustrates the compressor performance of all designs in terms of total pressure and total polytropic efficiency. The bulk of designs provides pressure ratios lower than 2.2 but there are also designs which exceed the required total pressure ratio of approx. 2.35. Generally the total-total, polytropic efficiency decreases towards higher pressure ratios but remains on a high level above 90 %. To investigate the resulting range of relevant compressor designs, three individuals were selected which achieve the required total pressure rise at comparable efficiency but differ in rotational speed. The FAST design, illustrated by the red dot, has a corrected rotational speed of 59431 min^{-1}; the MEAN design, illustrated by the green dot, has a corrected rotational speed of 43750 min^{-1}; the SLOW design, illustrated by the blue dot, has a corrected rotational speed of 36777 min^{-1}.

A comparison of the geometrical shape of these three designs is shown in Fig. 5.14. Detailed performance and geometrical design parameters of the rotors are summarized in Tab. 5.6. As expected, the diameter of the rotor increases with decreasing rotational speed to achieve similar circumferential speeds. The maximum machine Mach number $\text{Ma}_{\text{u,tip}}$ of all rotors is just below the outlet speed of sound. With increasing rotor radius, the hub-to-tip ratios and the blade numbers increase, the chord length and solidity decreases. The aspect ratio of the blades of all rotors is with 0.3 comparably low.

The results of the structural analysis of the rotors are illustrated in Fig. 5.15 for the reference designs. More, detailed illustration can be found in App. A.4 in Figs. A.21, and A.20. The figures show the von Mises stress distribution in the blade due to centrifugal load. In the figures, it can be seen that the maximum centrifugal stress occurs at the back of the blisk at the center of rotation. This is the intuitive region for high centrifugal stresses which here result from the large radial size of the blisk. The large blisk radius results in a comparably large mass at high circumferential speeds causing high centrifugal loads. Especially for the FAST rotor design high stresses can also be observed at the blade root which is here caused by a comparably thin hub blade profile and low fillet radii. For all cases the maximum stresses are well below the yield stress of about 390 MPa of the selected material aluminum 7075. The maximum stresses and the resulting structural safety factors are summarized in Tab. 5.6. With safety factors in the range from 1.67 to 4.15 the designs are considered feasible considering structural loads.

All rotors have a significant, almost linear endwall slope towards the radial direction. The hub slope of all rotors is similar with 23° to 25°; the shroud slope increases with decreasing rotational speed from approx. 12° to approx. 19°. The slope of the flow path leads to a significant radial component of the flow, resembling mixed flow type

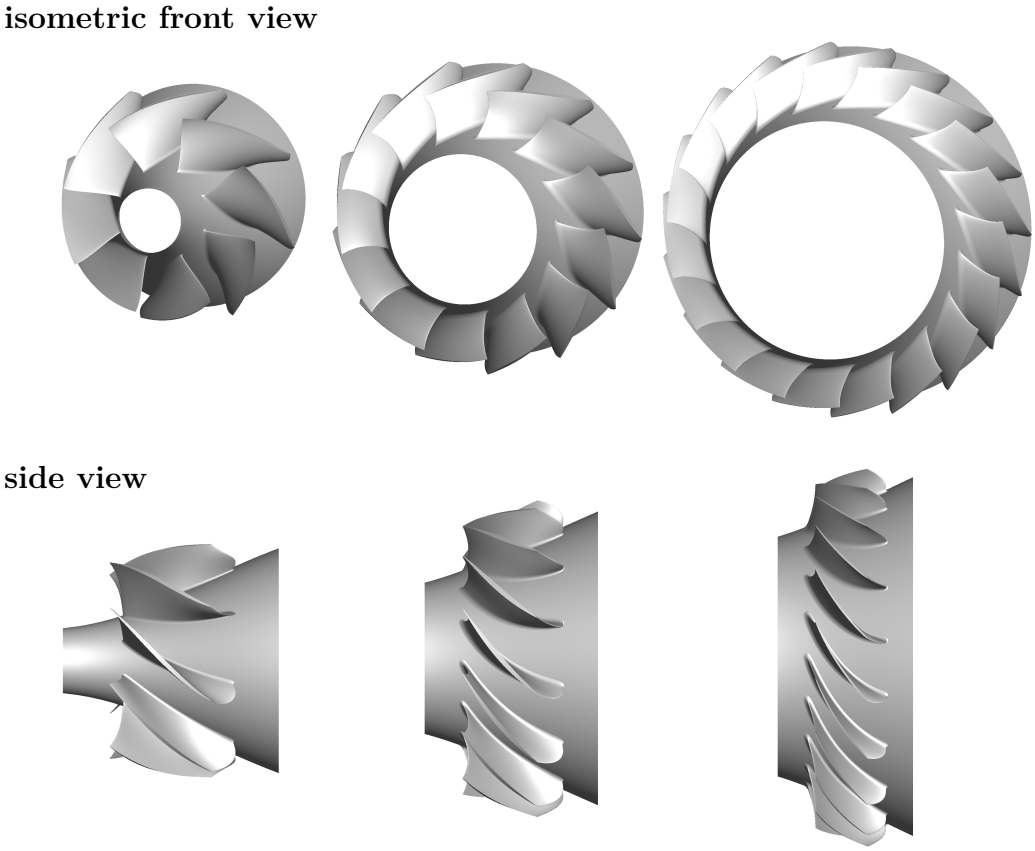

compressor: FAST
n_{corr}=59431 min^{-1}

compressor: MEAN
n_{corr}=43750 min^{-1}

compressor: SLOW
n_{corr}=36777 min^{-1}

Figure 5.14: Geometries of the three investigated rotor designs shown all at the same scale.

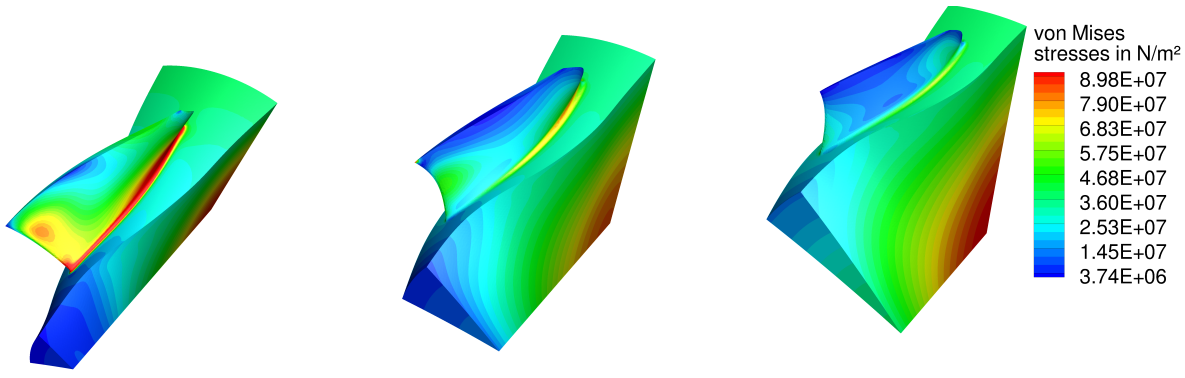

(a) FAST (b) MEAN (c) SLOW

Figure 5.15: von Mises stress of the rotor designs.

compressors. It does not, however, exceed the slope of existing highly loaded axial compressor stages which according to Wennerstrom (2000) is usually limited to 30°. With mean radius ratios $\frac{r_{\mathrm{m},2}}{r_{\mathrm{m},1}}$ between 1.35 for the FAST rotor and 1.19 for the SLOW rotor the contribution of the centrifugal effect to the overall total pressure rise is significant. Despite the increase in radius, the flow path contracts significantly with area ratios $\frac{A_2}{A_1}$ ranging from 0.81 for the FAST rotor and 0.65 for the SLOW rotor. This results in axial flow acceleration, illustrated by the axial velocity density ratios, of greater than unity. This acceleration is expected to stabilize the flow by counteracting the diffusion in the blade rows.

Due to the significant radius increase, the established definitions of flow and load coefficients for axial compressors provide unreasonable results for this type of design. Instead, the definitions used by Casey et al. (2010) and Hazby et al. (2014) which are also appropriate for mixed and centrifugal compressors are used below (see Eqns. (4.5) and (4.6)). Considering aerodynamic performance parameters, all rotors are highly loaded with global isentropic work coefficients ranging from 0.57 for the FAST rotor to 0.63 for the SLOW rotor. The through-flow is comparably low but also varies significantly for each rotor. While the FAST rotor has a global flow coefficient of 0.21, this value is only 0.085 for the SLOW rotor. Despite the high loading, the FAST rotor manages to comply with established design limits having a diffusion factor of 0.39 (< 0.6, see Sec. 3.1) and a de Haller number of 0.77 (> 0.7, see Sec. 3.1). The MEAN and SLOW rotors exceed these limits with diffusion factors in the range of 0.6 to 0.65 and de Haller number in the range of 0.58 to 0.54. It will be shown in the section below (Fig. 5.18), that the resulting compressor designs have a considerable centrifugal compression work component. The applicability of conventional axial compressor design limits to these designs is therefore limited.

Table 5.6: Performance and geometrical design parameters of the selected rotor designs.

rotor design	FAST	MEAN	SLOW
rotor performance parameters			
corrected rotational speed	59431 min^{-1}	43750 min^{-1}	36777 min^{-1}
corrected mass flow rate	1.106 $\frac{\text{kg}}{\text{s}}$	1.107 $\frac{\text{kg}}{\text{s}}$	1.107 $\frac{\text{kg}}{\text{s}}$
total-total pressure ratio	2.271	2.274	2.269
total-total polytropic efficiency	94.05%	93.51%	92.34%
global flow coefficient ϕ_{g}	0.21	0.12	0.085
isentropic work coefficient $\psi_{\text{g,isen,rotor}}$	0.57	0.63	0.63
diffusion factor	0.39	0.6	0.65
de Haller number	0.77	0.58	0.54
machine Mach number $\text{Ma}_{u,\text{tip}}$	0.99	0.94	0.94
axial velocity density ratio, AVDR=$\frac{\rho_2 \cdot c_{ax,2}}{\rho_1 \cdot c_{ax,1}}$	1.21	1.04	1.16
structural safety factor	1.67	3.77	4.15
maximum von Mises Stresses in MPa	234	103	94
rotor geometrical design parameters			
max. rotor diameter	117 mm	151 mm	180 mm
rotor hub-to-tip ratio, inlet	0.45	0.64	0.75
rotor hub-to-tip ratio, outlet	0.75	0.81	0.87
rotor chord length at mean radius	67 mm	60 mm	57 mm
rotor mean aspect ratio $\frac{\text{mean blade height}}{\text{mean chord length}}$	0.30	0.31	0.30
rotor blade number	8	13	19
rotor solidity at mean radius	2.4	2.3	2.2
rotor mean radius ratio $\frac{r_{\text{m},2}}{r_{\text{m},1}}$	1.35	1.32	1.19
rotor area ratio $\frac{A_2}{A_1}$	0.81	0.77	0.65
rotor ramp angle, hub	23.6°	23.4°	24.7°
rotor ramp angle, shroud	12.4°	17.3°	18.5°

5.7 Optimization Results - Stage Designs

The resulting stage designs obtained on the basis of the FAST, MEAN and SLOW rotors are presented below. Since the same design process and selection process was applied to all three stages, the results are only discussed in detail for the MEAN stage in Fig. 5.16 in this section. The analogous presentations of the results for the FAST and SLOW stage are given in App. A.5 (Figs. A.22 and A.23).

As described in Sec. 5.3, the objectives used in the stator/stage optimization aim at maximizing the static-static pressure rise of the stator, the axial total pressure ratio of the stage, and the total-total polytropic efficiency of the stage. These three objectives define the objective space which is represented in Figs. 5.16a, 5.16b, and 5.16c. The resulting stage designs are represented by cross symbols, relevant designs considered for this application are marked with larger black symbols. The selected optimum design is marked by a colored circle symbol. For each of the three stage design processes about 2000 to 3000 evaluations were required to achieve sufficient convergence of the optimization process.

It can be seen that increased total pressure of the rotor generally also leads to increased stator static pressure rise. The increased kinetic energy at stator inlet allows increased static pressure recovery. Increased axial total pressure rise of the stage and increased static pressure rise in the stator however lead to increased losses illustrated by decreased efficiency in Figs. 5.16b and 5.16c.

For the selection of the optimum stage from the available designs additionally to the three objectives also the exit flow angle is considered. Significant stage exit swirl tends to destabilize the flow in a downstream diffuser and consequently can make the efficient use of the available total pressure impossible. The introduction of the axial total pressure ratio, defined in Eqn. (5.8), as an objective for the stage design process was intended to penalize designs with excessive exit swirl but as shown in Fig. 5.16d, still a large number of designs with high exit flow angles exist. Interestingly, Fig. 5.16d does not support the intuitive expectation that increased flow turning (i.e. low exit flow angle) is directly associated with high static pressure ratio. Although there can be seen a such trend, even the higher static pressure ratios around 1.3 can be obtained by designs with exit flow angles ranging from about -5° to -30°. The negative sign here indicates incomplete flow turning (i.e. a remaining circumferential flow component directed in the opposite direction of the rotor rotation). These designs of high static pressure ratios are, however, not associated with a particularly efficient stator design. Instead the high static pressure ratio is only possible due to the high rotor total pressure ratio of these designs which leads to lower stage efficiency.

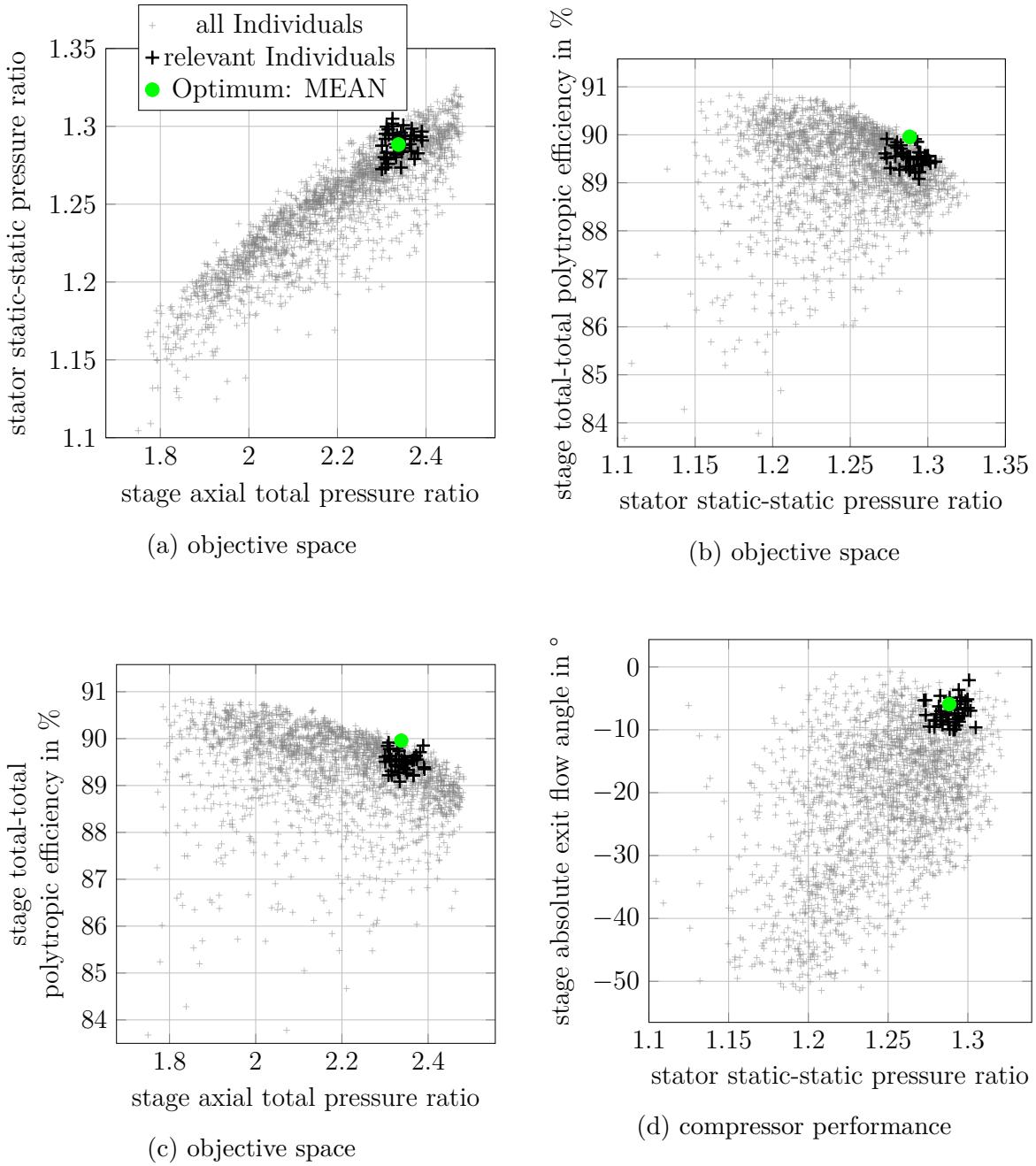

(a) objective space

(b) objective space

(c) objective space

(d) compressor performance

Figure 5.16: Results of the stage optimization with MEAN rotor: Objective space and compressor performance of all relevant individuals.

For this application, only stage designs with axial total pressure ratios between 2.3 and 2.4, high efficiency (in this case above 89 %) and exit flow angle less than 10° are considered. These designs are marked by larger, black crosses in the Fig. 5.16. Since these designs all provide the required total pressure ratio, the selection of the optimum design focuses on accommodating additional design considerations of the EPHLS. To decrease flow losses in the downstream ducting, which connects the compressor to the blowing slot, the optimum design is selected to achieve highest static outlet pressure at lowest exit flow angle. To minimize the power required for the EPHLS, which scales the mass of the electrical components of the system, maximum efficiency of the compressor is targeted. Considering these targets for the relevant designs shown in Fig. 5.16 the optimum design is marked by the green circle symbol. Analogously, this selection process is done for the stator/stage design processes on the basis of the FAST and SLOW rotor in Figs. A.22 and A.23.

The introduction of additional criteria and constraints in the final selection process, which were not included in the design process, significantly reduces the number of relevant designs. While the design process of the MEAN stage results in about 40 relevant designs, less than 10 relevant designs are available from the FAST and SLOW stage design processes. Specifying the used selection criteria directly as optimization objective in the design process to increase the number of relevant designs however, would result in a very constrained design space and consequently poor convergence of the optimization process. It would also make it impossible to sufficiently resolve the system behavior in order to learn about interdependency of the design and performance parameters.

Detailed information about blade row designs of the selected optimum stage designs are summarized in Tab. 5.7. The performance parameters of the selected optimum stage designs are summarized in Tab. 5.8. To illustrate the change of the rotor due to rotor-stator matching as part of the stage design process, Tab. 5.7 first summarizes major rotor performance parameters in the stage configuration. As part of the stage optimization, the total pressure ratios of the rotors are increased to compensate for the total pressure loss in the stator and still achieve the required stage pressure ratio. Consequently, the aerodynamic loading of the rotors is increased to diffusion factors in the range of 0.6 to 0.65 and de Haller numbers in the range of 0.55 to 0.6, exceeding conventional limits of axial compressors. Despite the different sizes and rotational speeds, the performance parameters of all rotors are in a similar range.

Table 5.7: Performance and geometrical design parameters of the selected stage designs based on the rotor designs in Tab. 5.6.

stage design	FAST	MEAN	SLOW
blade row performance parameters			
rotor total-total pressure ratio	2.44	2.45	2.55
rotor total-total polytropic efficiency	95%	94.5%	90.7%
rotor isentropic work coefficient $\psi_{\mathrm{g,isen,rotor}}$	0.59	0.65	0.63
rotor diffusion factor	0.62	0.65	0.59
rotor de Haller number	0.55	0.55	0.59
rotor axial velocity density ratio, AVDR=$\frac{\rho_2 \cdot c_{ax,2}}{\rho_1 \cdot c_{ax,1}}$	0.95	1.1	1.08
stator flow turning	60°	62°	64°
stator exit angle	-6°	-6°	-4°
stator static-static pressure ratio	1.26	1.30	1.24
stator pressure rise coefficient c_p	0.61	0.72	0.60
stator total pressure loss coefficient ζ_{loss}	0.15	0.14	0.22
stator dynamic pressure coefficient ζ_{dyn}	0.24	0.14	0.18
stator diffusion factor	0.72	0.79	0.74
stator de Haller number	0.46	0.36	0.41
stator axial velocity density ratio, AVDR=$\frac{\rho_3 \cdot c_{ax,3}}{\rho_2 \cdot c_{ax,2}}$	1.37	1.22	1.42
stator geometrical design parameters			
max. stator diameter	163 mm	236 mm	286 mm
stator hub-to-tip ratio, inlet	0.81	0.87	0.92
stator hub-to-tip ratio, outlet	0.87	0.91	0.95
stator chord length at mean radius	82 mm	114 mm	85 mm
stator mean aspect ratio $\frac{\text{mean blade height}}{\text{mean chord length}}$	0.14	0.09	0.09
stator blade number	11	14	25
blade number ratio $\frac{\text{stator blade number}}{\text{rotor blade number}}$	1.38	1.08	1.3
stator solidity at mean radius	2.4	3	3.0
stator mean radius ratio $\frac{r_{\mathrm{m},3}}{r_{\mathrm{m},2}}$	1.25	1.34	1.25
stator area ratio $\frac{A_3}{A_2}$	1.08	1.23	1.0
stator ramp angle, hub	15°	20°	22°
stator ramp angle, shroud	10°	17°	21°

Similarly to the rotor designs, the performance of the stator designs also does not alter significantly despite their different sizes. The achieved flow turning with 60° to 64° is comparably high leading to stator exit flow angles below 6°. The non-dimensional parameters c_p, ζ_{loss}, and ζ_{dyn} can be used to evaluate the stator performance. The pressure rise coefficient c_p, defined in Eqn. (5.16), relates the static pressure rise in the stator to the available kinetic energy at the stator inlet which could be converted to static pressure by diffusion. The total pressure loss coefficient ζ_{loss}, defined in Eqn. (5.17), relates the stator total pressure loss to the kinetic energy at stator inlet. The remaining kinetic energy of the fluid at stator exit that is neither converted to static pressure nor lost by dissipation is evaluated by the dynamic pressure coefficient ζ_{dyn} in Eqn. (5.18). High pressure rise coefficients and low total pressure loss coefficients with low dynamic pressure coefficients lead to high stator static-static pressure ratios.

$$c_p = \frac{p_{\text{s,out}} - p_{\text{s,in}}}{p_{\text{t,in}} - p_{\text{s,in}}} \tag{5.16}$$

$$\zeta_{\text{loss}} = \frac{p_{\text{t,in}} - p_{\text{t,out}}}{p_{\text{t,in}} - p_{\text{s,in}}} \tag{5.17}$$

$$\zeta_{\text{dyn}} = \frac{p_{\text{t,out}} - p_{\text{s,out}}}{p_{\text{t,in}} - p_{\text{s,in}}} \tag{5.18}$$

$$1 = c_p + \zeta_{\text{loss}} + \zeta_{\text{dyn}} \tag{5.19}$$

Considering these parameters it can be deduced that the stator designs convert about 60 to 70% of the available kinetic energy to static pressure. About 15 to 20% of the available kinetic energy is dissipated and about 15 to 25% passes the stator without contributing to the static pressure rise. The comparably high losses in the stator of the SLOW stage require an increased total pressure ratio of the rotor to obtain the required stage pressure ratio. This in turn leads to decreased rotor efficiency and ultimately to decreased stage efficiency (see Tab. 5.8).

Figure 5.17 gives an overview of the geometric shapes of the three selected stage designs. The stators are characterized by having very low aspect ratios and very high solidity leading to highly stacked, long blades with low blade height. The chord length of the stators is significantly greater than of the rotors. This design provides good flow guidance and allows the high flow turning required to achieve low exit flow angles. A significant radial flow component of the stators supports the flow diffusion acting as a radial flow type diffuser. With increasing rotor diameter, the stator ramp angles at hub and shroud increase leading to a significant radius increase of the stator. As for the rotors, the hub slope is greater than the shroud slope, the flow channel does however not contract but expand with area ratios between 1.0 and 1.23.

Considering the stage performance parameters in Tab. 5.8, the designs achieve the required total pressure ratio. Comparing the total-to-total pressure ratio to the total-to-static pressure ratio, a large fraction of the exit total pressure is not associated with kinetic energy but with static pressure illustrating the good performance of the stator.

Table 5.8: Performance and geometrical design parameters of the selected stage designs based on the rotor designs in Tab. 5.6.

stage design	FAST	MEAN	SLOW
performance parameters			
stage total-total polytropic efficiency	89.78 %	90.00 %	84.64 %
stage total-total pressure ratio	2.32	2.35	2.4
stage total-total, axial pressure ratio	2.3	2.34	2.38
stage total-static pressure ratio	2.15	2.24	2.27
stage global flow coefficient ϕ_{g}	0.19	0.11	0.07
stage isentropic work coefficient $\psi_{\mathrm{g,isen,stage}}$	0.56	0.62	0.58
stage reaction r	0.71	0.67	0.72

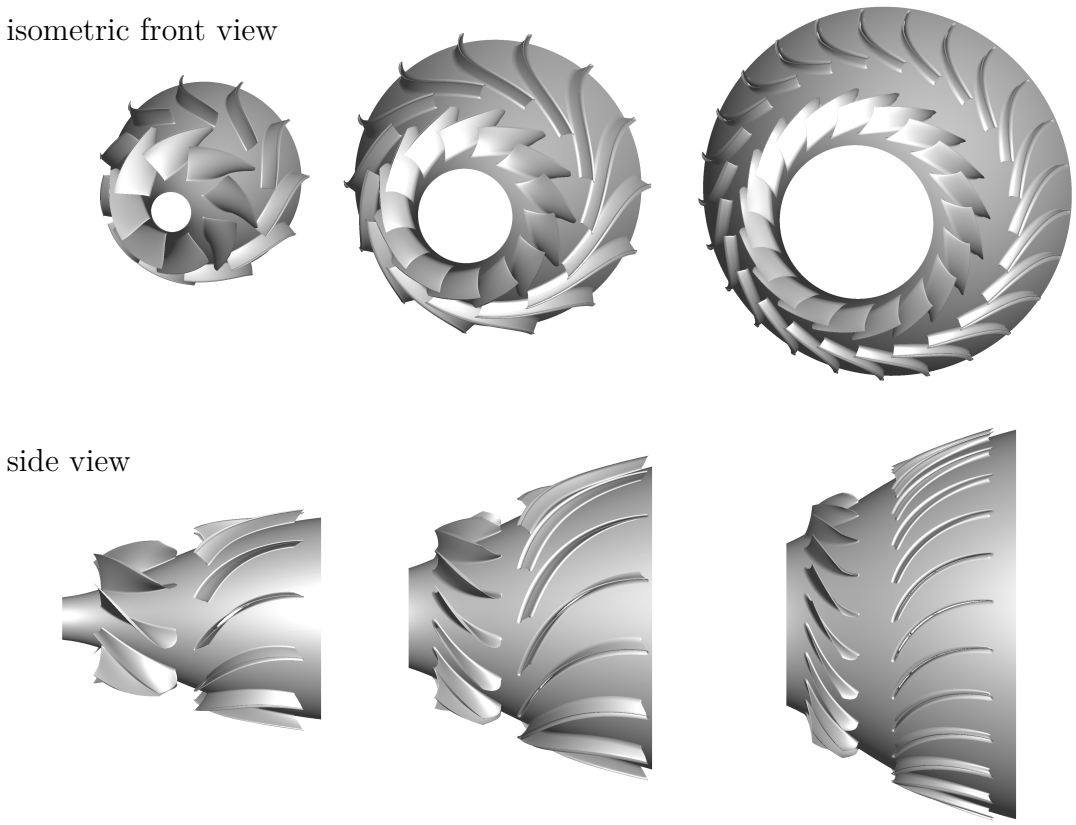

Figure 5.17: Geometries of the three investigated stage designs shown all at the same scale.

Considering the axial total pressure ratio, it can be stated that only a small fraction of the kinetic energy is not associated with axial velocity which should allow efficient use of the kinetic energy in a downstream diffuser. As it was the case for the rotor designs, the stage designs have extremely low global flow coefficients (i.e. low through-flow with regard to the given circumferential speed) considering their axial/mixed flow type nature. Typically, these types of compressors are characterized by higher flow coefficients as the resulting designs. The isentropic work coefficients of 0.56 to 0.62 are comparably high. The resulting reaction from the stage design process of 0.67 to 0.72 is high, indicating an increased loading of the rotor. As described earlier, this is a typical design feature for highly loaded axial compressors, since it allows to reduce the load of the aerodynamically less stable stator.

The mixed flow character of the compressor designs is quantified in Fig. 5.18 using the method from Casey (2008) presented in Sec. 3.1. This method is based on the reformulation of the compressor reaction to represent the fractions of the diffusion and of the centrifugal compressor work as the reactions $\mathrm{r_{centrifugal}}$ and $\mathrm{r_{diffusion}}$. The sum of both is the compressor reaction, that is the fraction of compression work done by the rotor compared to the over all compression work of the stage. The fraction of centrifugal compression work in a typical centrifugal compressor with similar performance as required in this work is approx. 0.41, according to Casey (2008). For ideal axial compressors with constant mean radius, the fraction of centrifugal compression work is zero. As illustrated in Fig. 5.18, the fraction of centrifugal compression work of the compressor designs are in a range between about 0.1 and 0.35. This means that these designs are utilizing centrifugal compressor work to a significant extent but not as much as typical centrifugal compressors. The fraction of centrifugal compression work directly correlates with the degree of change in mean radius ($\frac{r_{\mathrm{m},2}}{r_{\mathrm{m},1}}$ in Tab. 5.6). This is why the FAST designs generally have higher centrifugal compression work fractions than the MEAN and SLOW designs. Considering the sum of diffusion and centrifugal compression work fractions, it becomes apparent that for the FAST design, centrifugal compression is the dominant mechanism, while for the SLOW design, diffusion is the dominant mechanism of compression. As a result of this analysis it becomes clear that the compressor designs significantly utilize centrifugal compression work and can therefore not be considered as typical axial compressors but as a type of mixed-flow compressor. Due to their rotor-stator stage setup and the significant diffusion compression work fraction these compressors have greater similarity with axial compressors than typical mixed flow compressors like Hazby et al. (2014). For future reference, these designs are regarded as mixed flow compressors with predominantly axial compressor features in contrast to the more common mixed flow compressors based on typical centrifugal compressor designs.

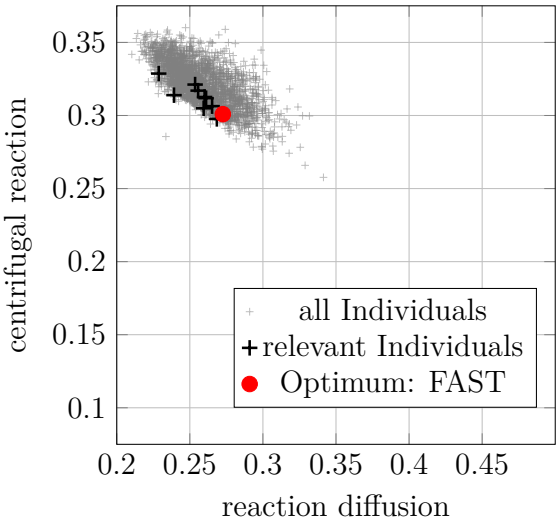

(a) stage: FAST

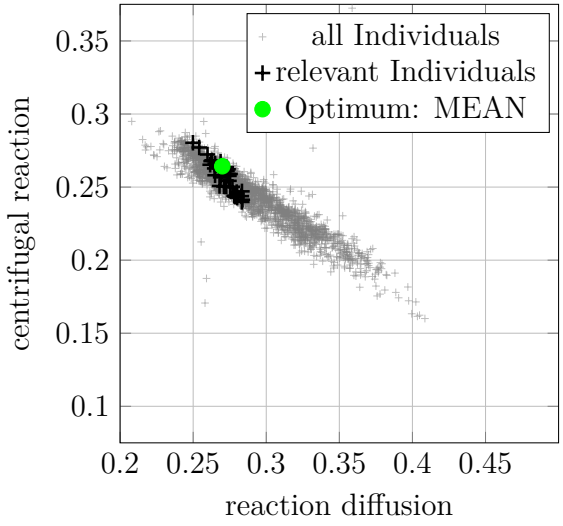

(b) stage: MEAN

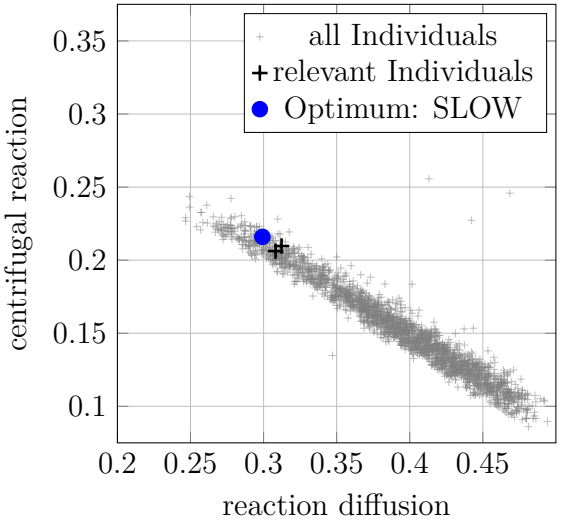

(c) stage: SLOW

Figure 5.18: Representation of fractions of compression work done by diffusion and centrifugal work from Casey (2008) presented in Sec. 3.1.

5.8 Numerical Sensitivity

In this section the "Low Reynolds" $y^+ = \text{const}$ study presented in Sec. 5.1.1 is repeated for the three reference stage designs FAST, MEAN and SLOW. This is done to evaluate the validity of the selected grid resolution over the wide compressor design space. An important issue of the design optimization using numerical simulations is that not the actual design, but a discretized representation of the design is evaluated. In the automated design process this discretization cannot be specifically fitted for each design. The underlying grid generation relies on templates which result in varying grid qualities depending on the design type. These processes therefore have the inherent risk of systematically penalizing a specific design type because of a misprediction due to low grid quality. Figure 5.19 shows the dependence of the total polytropic efficiency of each design to the grid resolution. It can be observed that the relation is similar for each design and accords with the behavior seen in the grid convergence study in Sec. 5.1.1. This confirms the validity of the grid configuration used in the optimized design process. For the investigated designs there is no significant grid quality effect conceivable which might introduce non-physically influences to the predicted performance.

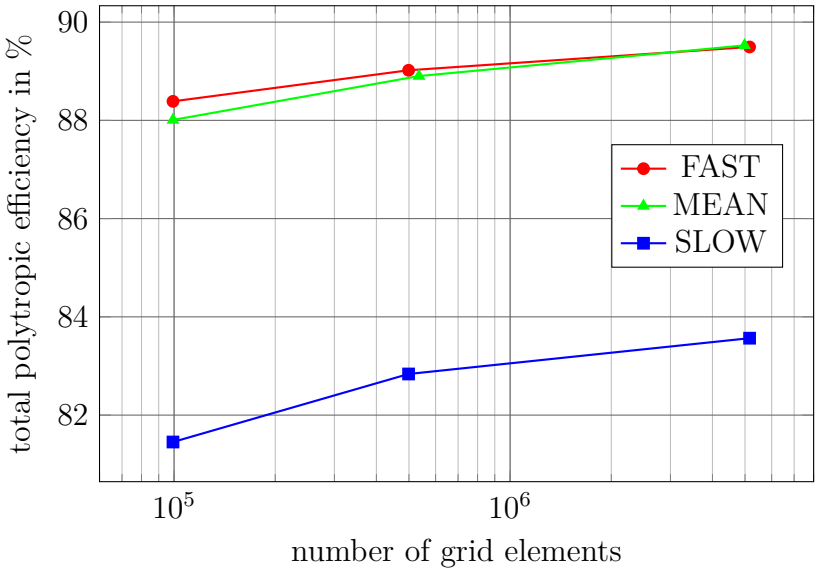

Figure 5.19: Grid sensitivity of optimum stage designs

6 Analysis of the Designs

In this chapter the results of the optimized design processes are analyzed in detail. This includes the performance analysis of the resulting stages over the relevant operating range, the comparison of the covered design and performance space with existing, conventional designs, and the investigation of the governing physical effects of the flow field.

6.1 Operating Range / Compressor Map

The operating range of the selected compressor stages is evaluated below to determine the compressor performance at the required operating points of the EPHLS. In the automated process used to simulate predefined speed lines of each of the selected compressor designs, the same CFD setup as used for the optimization process is applied. For each speed line, the first operating point is simulated at a total to static pressure ratio of 1.05. After successful convergence, the pressure ratio is increased by 0.05 for the following operating point using the previous, converged result as an initial solution. This procedure is repeated until simulations of operating points with further pressure increase do not successfully converge anymore. This usually occurs in the region of the speed line where the slope approaches zero (see Fig. 6.1). In this region, the outlet pressure is not a stable boundary condition for the operating point anymore since small changes in pressure ratio result in large changes in compressor mass flow rate. To simulate this region of the speed line, the mass flow rate is used as a boundary condition starting from the last converged operating point. After successful simulation, the mass flow rate is step-wise reduced by 0.02 kg/s. The stability limit of the compressor is reached when no convergence with the mass flow rate boundary condition can be obtained anymore. This limit does not necessarily represent the actual surge limit of the compressor, but provides a reasonable approximation of the operating range limit using steady state simulations. To detect the surge limit more accurately, unsteady flow effects need to be considered which requires an unreasonably large computational effort for design purposes.

Figure 6.1 illustrates an overlay of the relevant speed lines of the selected three designs and the required operating points of the EPHLS. It can be seen that the operating range of all compressors agrees very well despite the different sizes and rotational speed levels. The detailed map of the MEAN compressor is shown in Fig. 6.2, the compressor maps of the other stages are given App. A.6. As described in Sec. 2.3, the design point of the compressors is at the highest pressure ratio and the highest corrected mass flow rate of the required EPHLS operating points. The optimization of the design therefore naturally leads to high efficiency and stable operation with sufficient stall margin in

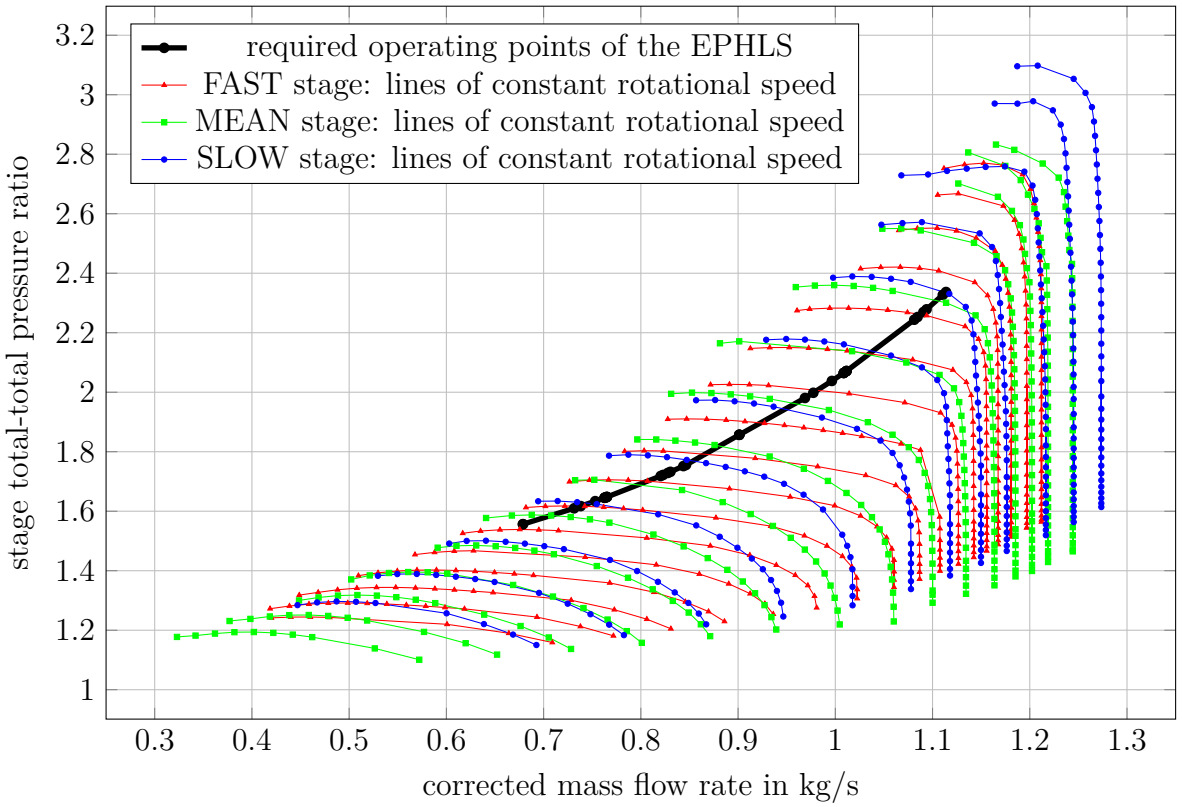

Figure 6.1: Overlay of operating ranges of the 97.5% scaled FAST, MEAN and SLOW compressor.

this region. For this reason, the operating points of the EPHLS are located well within the operating range of all stages at high pressure ratios and mass flow rates. However, for the lower operating points of the EPHLS it was necessary to geometrically scale all designs to 97.5% size ($\approx$ 95% mass flow rate) to achieve sufficient "stall margin". All given compressor maps represent these scaled designs; the further presented analyses of the flow field however were, if not otherwise stated, done for the original, unscaled geometries. In the region of lower pressure ratios, the slope of the EPHLS duty line is lower than the slope of the nearby compressor characteristic. The duty line therefore tends to approach the stability limit of the compressor if the design point at high pressure ratio is located at peak pressure ratio of its corresponding speed line. With about 0.1 kg/s, the margin to the duty line to the compressor stability limit is regarded as sufficiently large to allow save operation.

In the detailed compressor maps of the FAST (Fig. A.24), MEAN (Fig. 6.2), and SLOW (Fig. A.25) stage design, the compressor efficiency and speed levels of the compressor operating range are given. The efficiencies obtained for the EPHLS operating points are interpolated from the simulated operating points. The figures show that the EPHLS duty line is covered within a 15,000 to 20,000 min^{-1} speed band by the compressor designs but at different levels. The required peak rotational speeds for the FAST, MEAN and SLOW design are approx. 61,500 min^{-1}, 46,000 min^{-1} and 37,500 min^{-1},

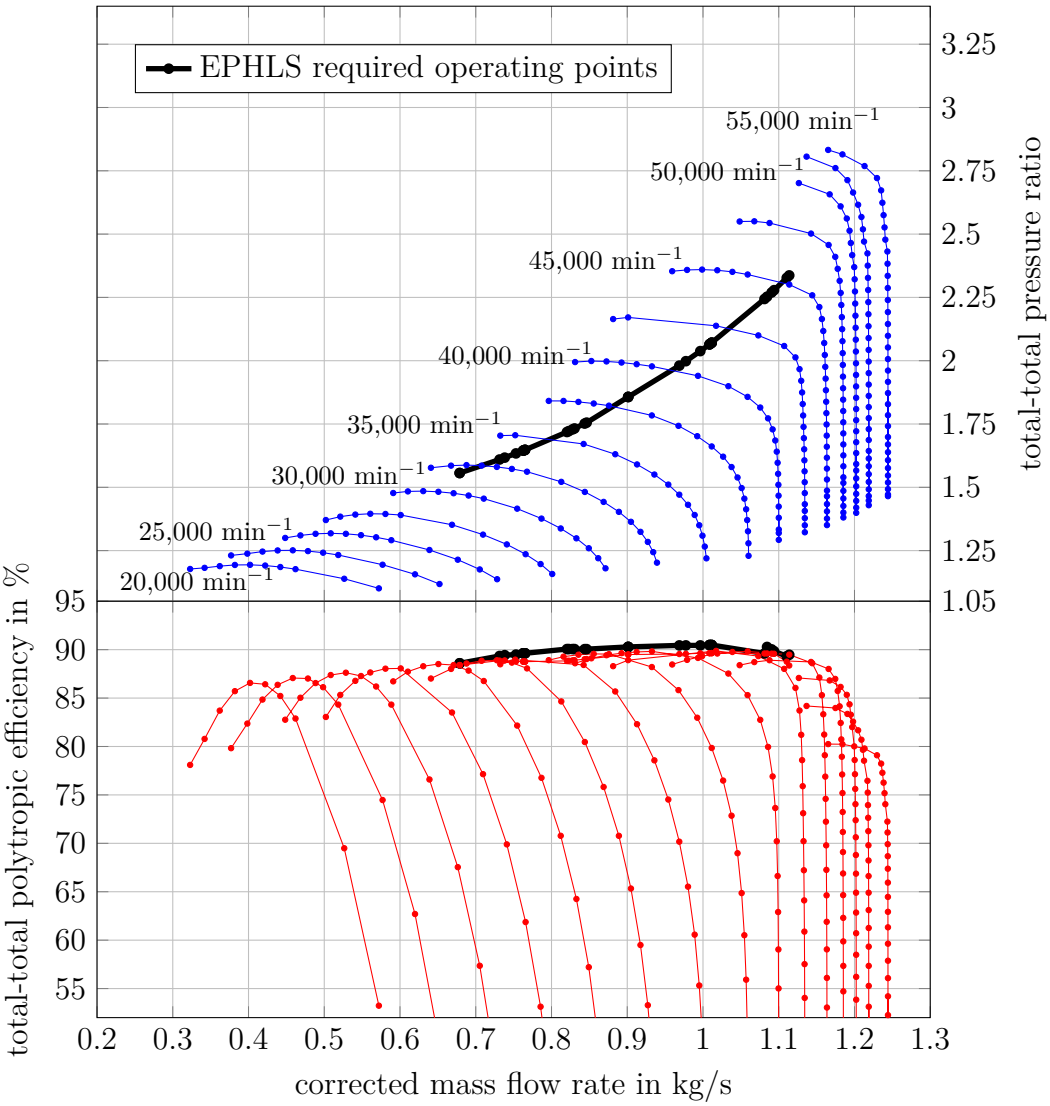

Figure 6.2: Compressor map of scaled MEAN compressor.

respectively. The corresponding required compressor power is 100 kW, 102 kW and 108 kW. At over-speed, all designs are able to obtain considerably higher total pressure ratios than required (2.75 to 3) providing the possibility of further power enhancement of the EPHLS. The duty line is covered by all compressors at almost constant efficiency with slightly decreasing efficiency towards very high and very low load duty points. While the FAST and MEAN compressor achieve total-to-total polytropic efficiencies of 88 to 90% over the EPHLS duty line, the SLOW compressor achieves efficiencies in the range of 84 to 85%.

6.2 Non-Dimensional Design Space

The Cordier Diagram presented in Sec. 4.1 can be used to illustrate the design and performance space which is covered by the results of the optimized design process. Analogously to Fig. 4.1, Fig. 6.3 shows the Cordier Diagram by Casey et al. (2010) including the rotor designs presented in Sec. 5.6 marked in gray cross symbols. These rotor designs have total polytropic efficiencies greater than 90 %, total pressure ratios greater 1.4, mechanical safety factors greater 1.5, and are numerically converged. The three selected, representative optimal rotor designs and the associated stage designs (see Sec. 5.7) are marked with the appropriately colored symbols.

In Fig. 6.3a it can be seen that the rotor designs are aligned in a range parallel to the Cordier line. Since only rotor designs with total polytropic efficiencies greater than 90 % are considered, this confirms the general trend of the Cordier line which is meant to represent the relation of specific diameter and specific speed of highly efficient designs. The selected rotor designs FAST, MEAN and SLOW are located in the according area of high, mean and low specific speed respectively and therefore represent the design space well. According to this Cordier diagram, the FAST and MEAN rotor are located in an area of the design space where typically mixed and centrifugal compressors are appropriate. The SLOW rotor is located in the conventional centrifugal operating range only. Considering the actual rotor designs they are clearly more similar to axial- or mixed flow compressor designs than to centrifugal compressors. This indicates that, with the design methods used in this work, the conventional design space of mixed flow compressor types with axial compressor characteristics can be significantly extended.

Analogously to Fig. 6.3a, the performance space is represented in Fig. 6.3b in terms of flow and load coefficient using the same Cordier line and the same conventional machine limits. It is obvious that the rotor designs resulting from the developed design process exceed the loading of conventional, highly efficient compressor designs. The flow coefficients of the newly developed rotor designs are significantly lower than for conventional axial/mixed flow type compressors.

6.2.1 Extended Non-Dimensional Design Guideline

The rotor designs resulting from the presented design process show that it is possible to obtain highly efficient compressors well beyond the conventional design space. The presented designs have smaller specific diameters at lower specific speeds than conventional compressor designs. This results in higher loading for a given flow coefficient. The results also show that not only the conventional performance parameters can be exceeded but also the conventional limits of a given machine type. All designs have mostly axial directed flow at in- and outlet as well as the intended setup in a rotor-stator configuration. They clearly have distinct features characteristic for axial and mixed flow type compressors. The significant radius change associated with significant endwall slope of the designs results in a considerable centrifugal pressure rise component but not to a degree that they could be attributed to centrifugal type compressors. Nevertheless, the specific speed range and flow coefficient range of the slower designs only match the

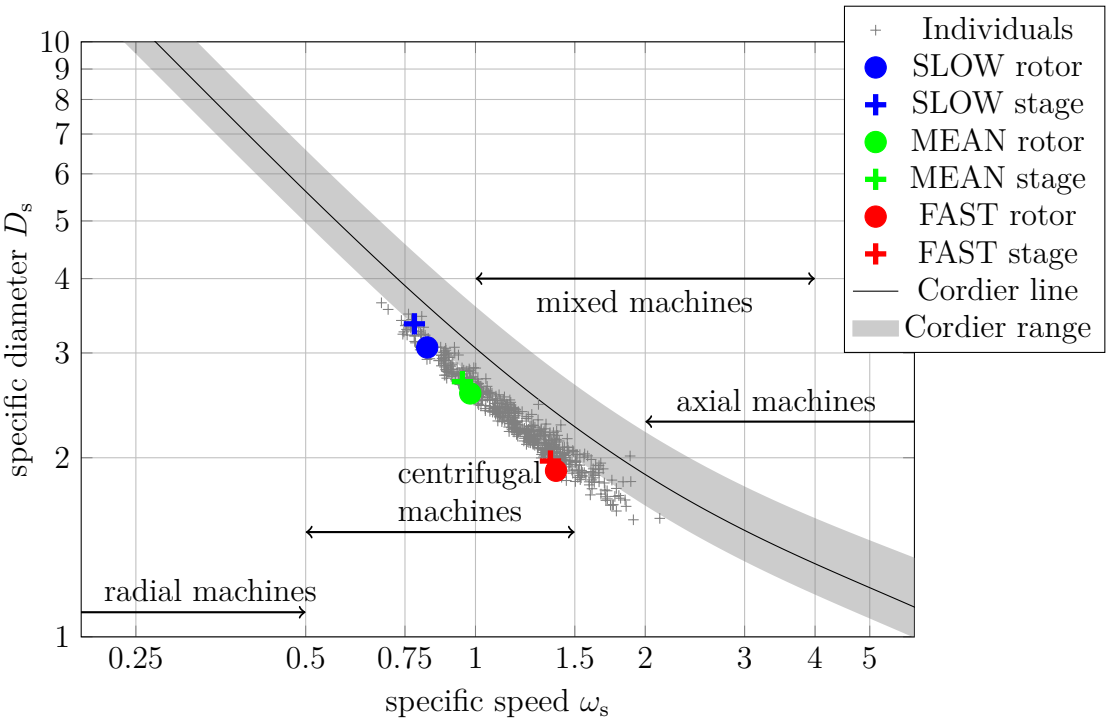

(a) Design space illustrated in a Cordier-type diagram.

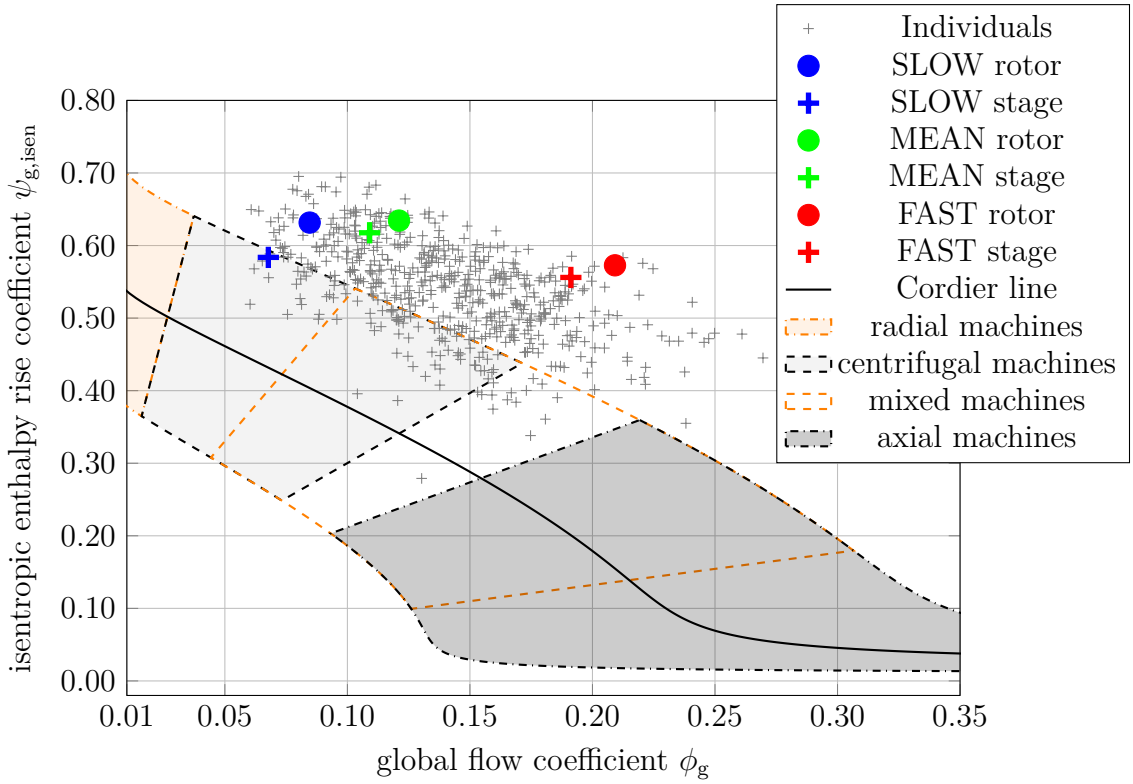

(b) Performance space illustrated in a non-dimensional operating range diagram.

Figure 6.3: Rotor designs in the conventional compressor design space according to Casey et al. (2010)

Table 6.1: Extended Cordier correlation coefficient values.

	correlation coefficients (Casey et al. 2010)			extended upper bound: highly loaded mixed flow compressors
	Cordier line	lower bound	upper bound	
ψ_{low}	0.45	0.35	0.55	0.55
ψ_{medium}	0.55	0.4	0.7	0.9
ψ_{high}	0.02	0.01	0.025	0.025

conventional design space of centrifugal compressors. This is true for the isolated rotor designs but also for the available stage configurations.

To account for the shown extension of the design space of highly loaded mixed flow type compressors, Figs. 6.4a and 6.4b suggest modified Cordier limits on the basis of the conventional limits provided by Casey et al. (2010). In Fig. 6.4a, the specific speed range for mixed flow compressors was extended from ω_{s}=1 to ω_{s}=0.65 to include all available, highly efficient mixed flow designs. Applying Eqn. (4.7), the upper bound of the Cordier range was adjusted as shown in Tab. 6.1 to include all designs with high loading. All other parameters are used according to Casey et al. (2010) in Sec. 4.1. The s-shaped characteristic of the upper bound, as defined by Casey et al. (2010), was preserved. Nevertheless the extension can only be regarded as valid in the range of $0.05 < \phi_{\text{g}} < 0.25$ and $0.2 < \psi_{\text{g,isen}} < 0.7$ where mixed flow rotor designs are available from this design process. It is expected that the presented design methodology would result in a comparable design space extension when applied to the other machine types and the other regions of the design space. These areas were however not covered by the presented design process since they are not relevant for the given design task.

In the range of validity, the extended Cordier limit can be a useful guideline for the preliminary design of highly loaded mixed flow compressors with similar design characteristics as the designs given in Sec. 5.6. These include: endwall ramp angles between 10° to 20°, mean radius ratios $\frac{r_{\text{m,3}}}{r_{\text{m,2}}}$ of about 1.2 to 1.3, hub-to-tip ratios of about 0.8 to 0.9, blade aspect ratios of about 1.5, and solidities in the range of 2.5 to 3. The extended Cordier limits do not suggest that mixed flow compressors are superior to centrifugal or axial compressors in their particular design range. It simply illustrates that mixed flow compressors can be successfully applied over a wider design space than conventionally established.

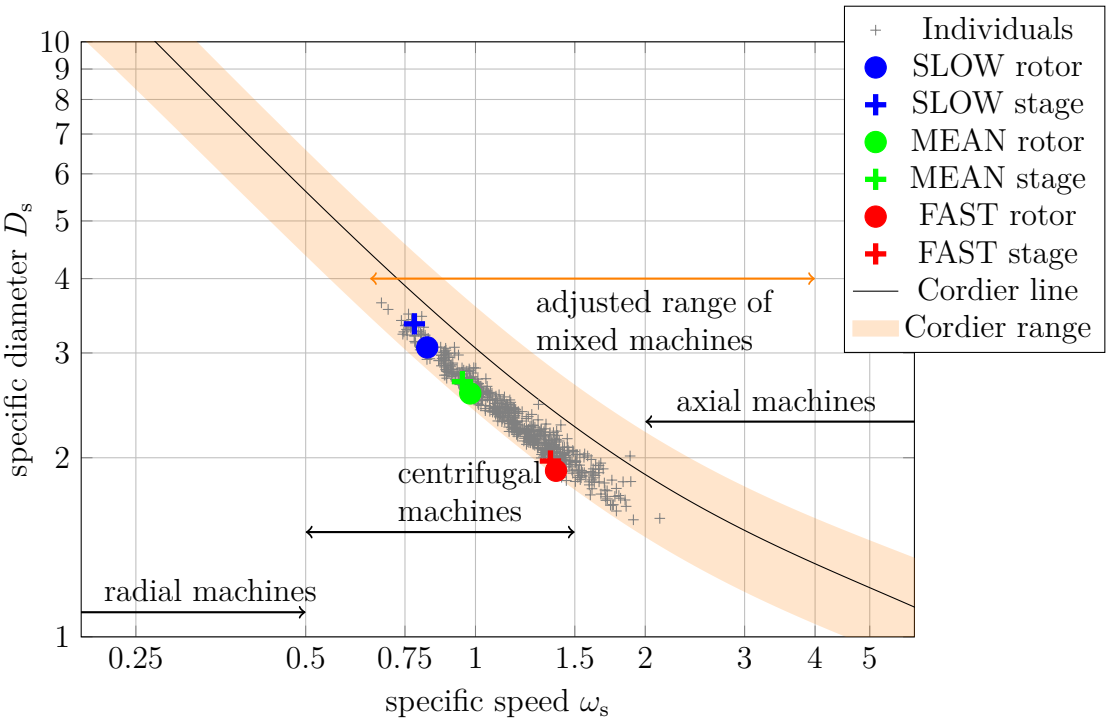

(a) Extended design space illustrated in a Cordier-type diagram.

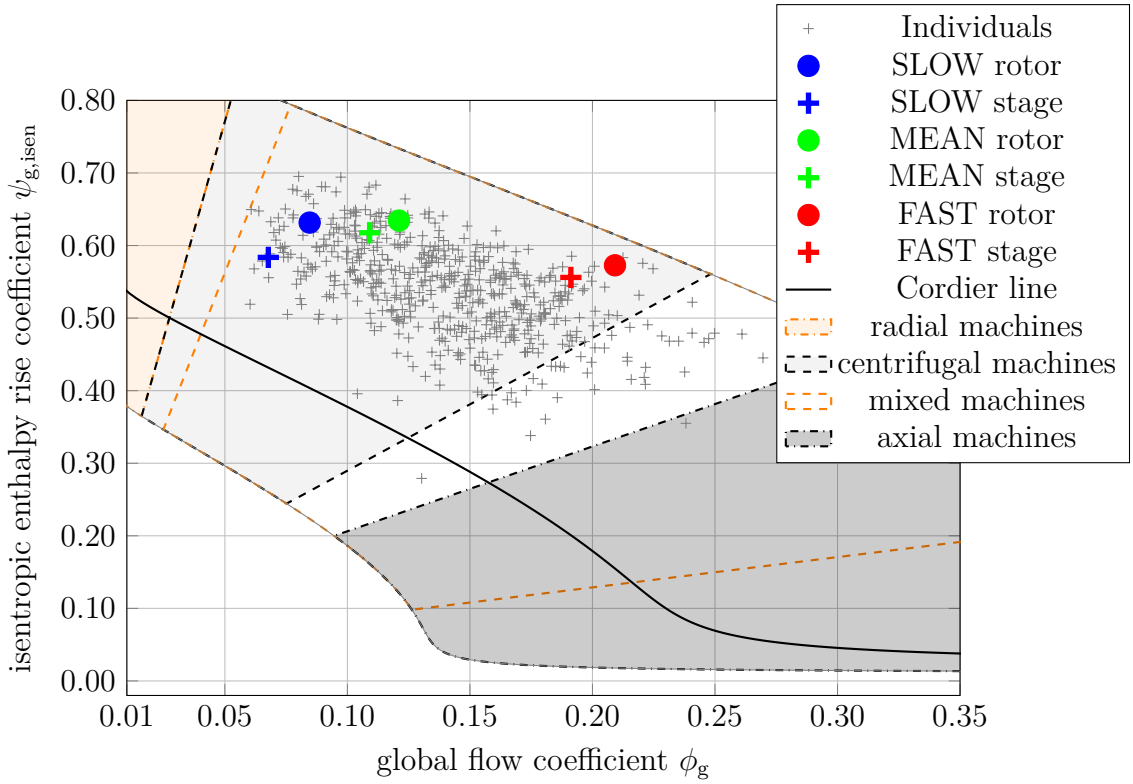

(b) Extended performance space illustrated in a non-dimensional operating range diagram.

Figure 6.4: Rotor designs in extended compressor design space on the basis of Casey et al. (2010).

6.3 Aerodynamic Characterization / Physical Effects

In this section, the flow fields of the compressors are analyzed in detail to identify the characteristics of the designs. As it is done in the design process, the analysis is done separately for the rotor and the stage to be able to identify the effects resulting from the optimized design process.

6.3.1 Aerodynamic Characterization of the Operating Range

Figure 6.5 gives an overview of the flow field of the MEAN stage at different operating conditions of the MEAN compressor. In the figure, contours of relative Mach number at constant span ($\approx 95\%$) near the blade tip are shown for different compressor speeds. The speed lines are selected to represent the minimum, maximum and mean compressor speed required to cover the duty line of the EPHLS, illustrated as a bold black line in Fig. 6.5. The selected operating points, marked with red triangle symbols, represent operating conditions near compressor stall (towards high pressure ratios and low flow rates), near the EPHLS duty line and near compressor choke (towards low pressure ratios and high flow rates). Analogous illustrations for the FAST and SLOW stage are given in the appendix in Figs. A.26 and A.27.

At low speed, here for the MEAN stage 32,500 min^{-1}, the design point is very close to the numerical stability limit and therefore only one operating point is illustrated for design and near stall conditions. Comparing the near stall operating conditions at the different speeds (here for the MEAN stage 40,000 and 45,000 min^{-1}) generally low flow velocity in rotor and stator can be observed. With increasing rotational speeds, a small transonic flow region with a small shock region develops in the leading edge region of the rotor. Towards the EPHLS duty line at lower pressure ratios and higher flow rates the transonic flow region in the rotor increases in size and intensity and moves downstream in the passage. It is however still located upstream of the passage throat. Near the choke limit, at very high flow rates and low pressure ratio, the high volumetric flow rate in the stator due to the low compression leads to transonic flow in the stator. For the low compressor speed, this region starts to develop on the suction side of the stator blade downstream of the passage throat such that the rotor flow remains subsonic. The higher flow rates at higher speeds lead to a large, strong shock structure in the stator passage. This structure causes increased losses and limits the flow rate in the passage, indicating the compressor choke limit. At higher rotational speeds, the compression shock in the rotor passage also increases significantly in strength and moves downstream of the passage throat. At maximum speed, two shock structures can be observed: The first, weaker one developing on the suction side of the blade upstream of the throat and a second stronger one developing near on the pressure side downstream of the throat.

The illustrated flow pattern at the different operating conditions agrees with the known behavior of transonic compressor at part load and over load. There are no critical flow misalignments or flow separations observable, indicating appropriate rotor stator matching. The rotor and stator blades have appropriate flow incidence at design and near stall with small, comparably weak transonic flow regions resulting in highly efficient

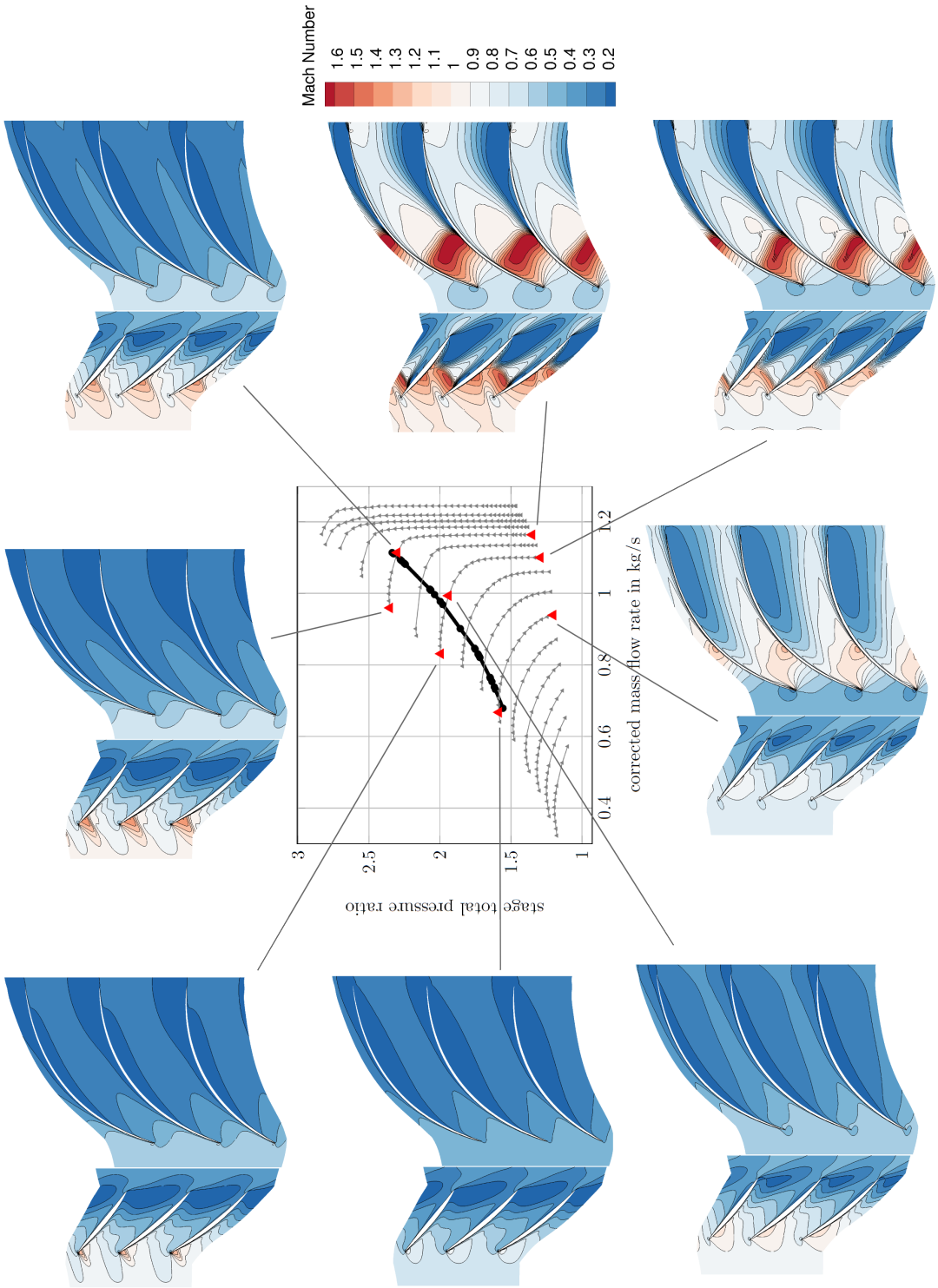

Figure 6.5: Mach contours at different operating conditions of the MEAN stage.

compression (see Fig. 6.2). As expected, the high flow rate leads to a suction side incidence in the stators which becomes apparent by the low velocity flow region on the suction surface near the trailing edge due to the shift of the stagnation point. The losses associated with the strong shock structures in rotor and stator at high speed near compressor choke lead to the efficiency drop in this region observed in the compressor maps in Fig. 6.2.

6.3.2 Rotor

As part of the analysis of the rotor optimization results, it was found that there is a considerable degree of freedom in terms of machine diameter and machine speed to obtain the required performance at the given design point. This degree of freedom is represented by the three selected rotor designs FAST, MEAN and SLOW. To identify general flow features with significance over the complete design space, the rotor analysis is done for all three reference rotors. Figure 6.6 illustrates the relative Mach number distribution in the rotors near the blade tip at $\approx 95\%$ span at the design point given in Tab. 5.6. As in all other figures shown in this work, the flow is generally directed from left to right. In Fig. 6.6 it can be seen that the flow pattern is similar for all rotors. The relative inlet velocity is subsonic; therefore no bow shock at the leading edge occurs. Starting at the leading edge, the flow is then accelerated on the suction surface (the lower side of the blade in the picture) until it reaches supersonic relative flow velocities of around Mach 1.3. A compression shock occurs at about 20% to 30% chord length upstream of the passage throat, which is located at the beginning of the blade channel. All rotors have a visible region of low flow velocity developing in the downstream half of the pressure side (the upper side of the blade in the picture). Most prominent however is the larger oval shaped area of low flow momentum starting from the suction side trailing edge and spanning almost over the complete passage exit. Downstream of the blades, this region does not propagate tangentially to the blade trailing edge but exhibits a significant deviation towards the suction side (opposite the sense of rotor rotation). Streamlines illustrate the flow field in the rotor exit region exemplary for the MEAN rotor in Fig. 6.6d.

Description of the "bubble" flow phenomenon

The development of this characteristic region of low flow momentum is not limited to isolated rotors or operating points with high load and high rotational speed. Varying in size and momentum deficit, the low flow momentum region can be observed at any operating point in single rotor and stage configurations of the investigated designs. Figures A.28a to A.28c in the appendix illustrate this exemplarily for low speed stage operating points with subsonic relative flow and low pressure ratio. The Figures A.28 correspond to operating points of the selected compressor designs near a mass flow rate of 0.75 kg/s and a total pressure ratio of about 1.45.

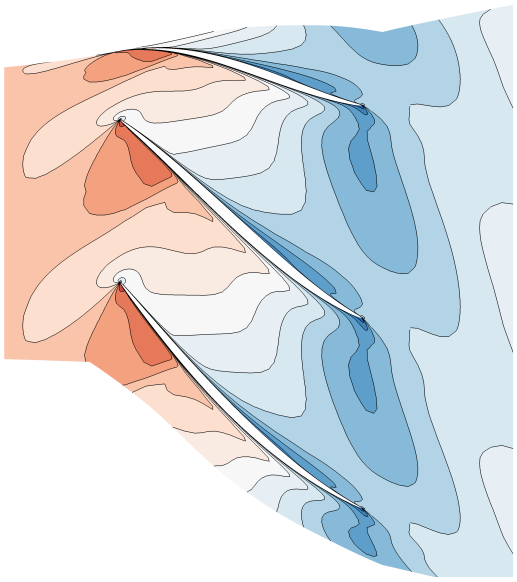

(a) Mach slice of rotor: FAST

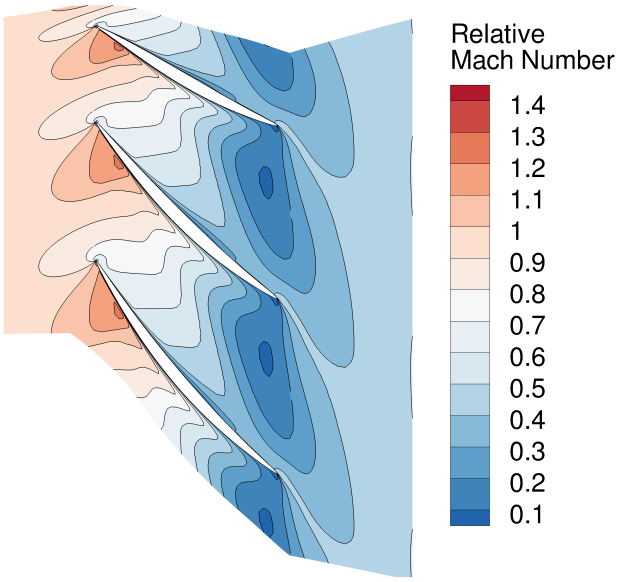

(b) Mach slice of rotor: MEAN

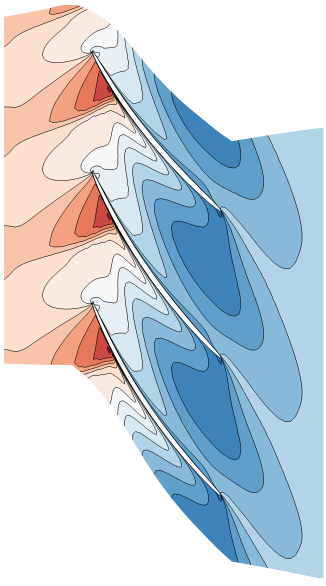

(c) Mach slice of rotor: SLOW

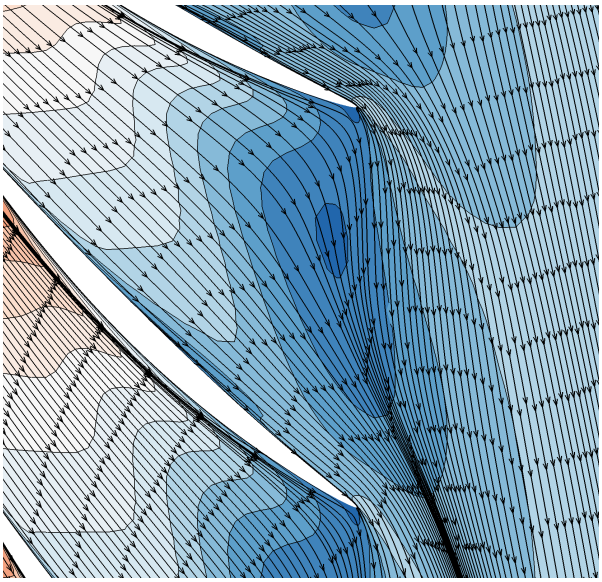

(d) Streamlines in the trailing edge region of the MEAN rotor.

Figure 6.6: Mach slice in the tip region of the rotors (≈ 95% span).

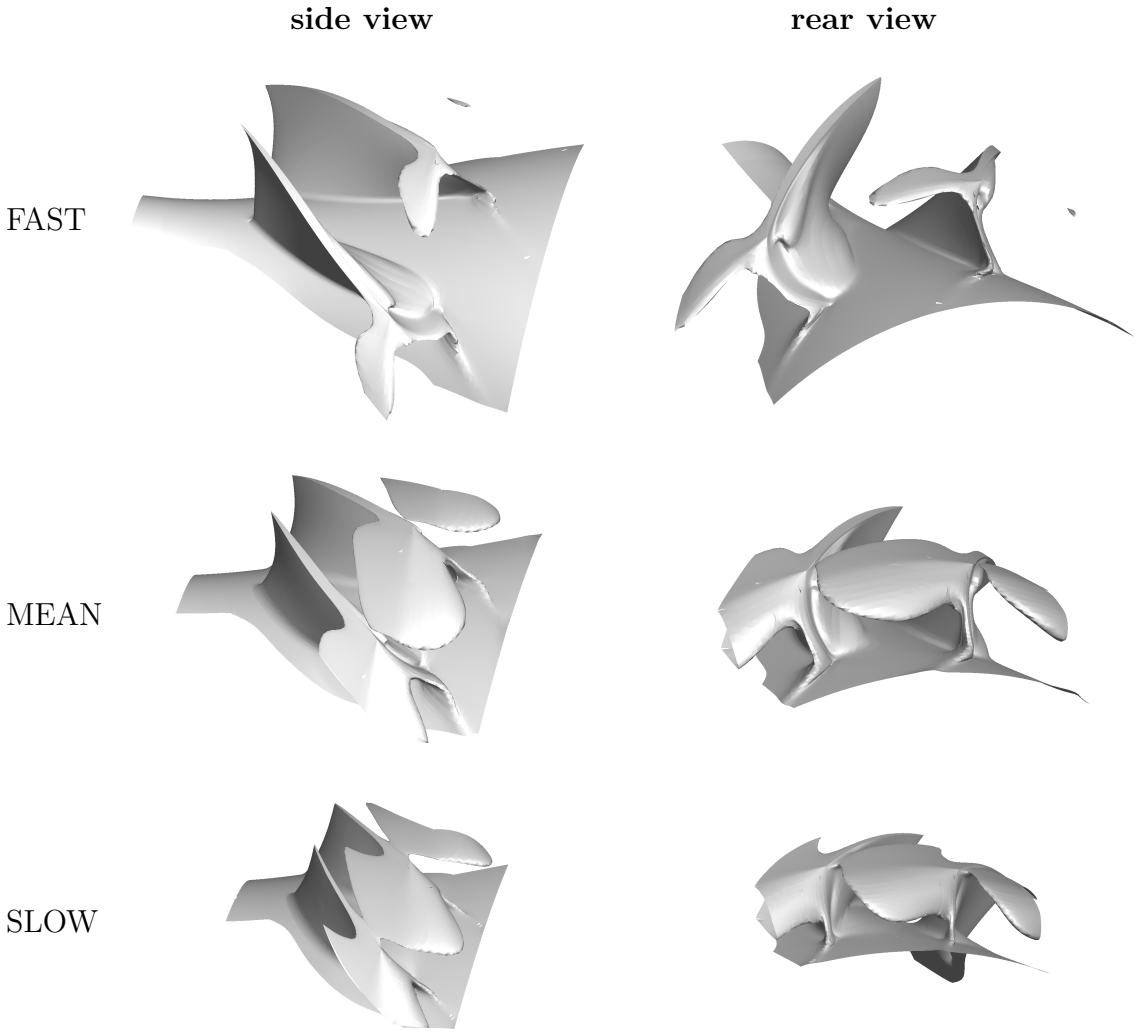

Figure 6.7: Relative Mach Number = 0.3 iso-volumes in the three rotors to illustrate the bubble-like region of low momentum in the blade passage (figures are to scale).

To resolve the low momentum flow regions three-dimensionally, Fig. 6.7 shows a side and rear view of each rotor with iso-volumes of the relative Mach number. All cells enclosed by the gray surfaces have relative Mach numbers below 0.3. The rotors are represented to scale which is why the blade of the slow rotor is smaller than the other rotor blades. For all rotors, the main region of low momentum is confined to the tip region of the passage. It generally has a flat, oval shape which is further denoted as a "bubble"-like shape. This region blocks about the upper 10% span and about half of the passage in the FAST rotor. For the MEAN and SLOW rotor this region is significantly greater, blocking almost the complete passage starting from the trailing edge spanning more than 50% blade height.

The region of low momentum on the pressure side is also visible in Fig. 6.7, most prominently in the rear view of the FAST rotor. It is an isolated region near the tip

which does not seem to interact with the bubble region in a critical way. Since the tip leakage flow generally induces vortex structures on the suction side only, this region is most likely caused by the scraping vortex. This vortex structure develops due to the interaction of the shroud boundary layer with the flow displacement of the moving blade pressure side. In the iso-volume representation in Fig. 6.7 also a region of low momentum flow developing in the pressure side hub region near the trailing edge is visible for all rotors.

The chordwise and spanwise rotor blade loading characteristics can be deduced from the isentropic Mach number distributions in Fig. 6.8. From the peaks in isentropic Mach number on the suction side it can be seen that all rotors have a transonic flow regime, with supersonic flow in the tip region and subsonic flow in the hub region. The SLOW rotor experiences the highest flow velocities with near sonic velocities even in the hub region. On the suction side, downstream of the shock, a steady deceleration of the flow occurs in the tip region of the blades. Towards the hub the flow deceleration becomes less uniformly distributed. Here it is focused in the region downstream of the Mach number peak and at the trailing edge. On the pressure side, the flow is decelerated in the upstream part of the blade, levels out and is re-accelerated in the rear part with a sudden acceleration towards the trailing edge. The sudden change of velocity at the trailing edge indicates a comparably high pressure difference between suction and pressure side in this region. Generally, for a conventional axial compressor a steady approach and eventual equalization of the flow velocities and pressures of suction and pressure side is expected. The area enclosed by the profile velocity distribution illustrates the work done in this blade section. The significant velocity difference near the trailing edge therefore implies increased loading of the blades. High blade loading in this region is typically seen in centrifugal compressors where the associated velocity difference is one of the causes for the later described slip flow (Cumpsty 2004).

The through-flow distribution in the flow path can be illustrated by using the product of axial velocity and density. This parameter can be interpreted as an area normalized mass flow rate. Figure 6.9 shows the circumferential averaged axial velocity-density (AVD) distributions of the rotors in the so called S2 plane. The thick black line represents the end-walls of the channel and the leading and trailing edge of the rotors. The rotor inlet and outlet plane varies for each design since the length of the inlet and outlet section of each design is controlled to be approximately 1/3 axial chordlength from blade leading and trailing edge (see Sec. 5.2.2). This was done to achieve comparable inlet and outlet flow pattern, interface interaction, and losses for each design independent of rotor size. In Fig. 6.9, regions of comparably low AVD indicate low through-flow, i.e. blockage. It can be seen that the low momentum bubble leads to increased blockage at the trailing edge tip region of all rotors. While this region of high blockage is comparably small for the FAST rotor it increases significantly for the MEAN and SLOW rotor. The blockage results in a displacement of the high momentum flow from the tip region to the hub region while moving through the blade channel. A representation of the relative Mach number distribution in this reference plane is given in the appendix, Fig. A.29 to confirm the description of the flow field given above.

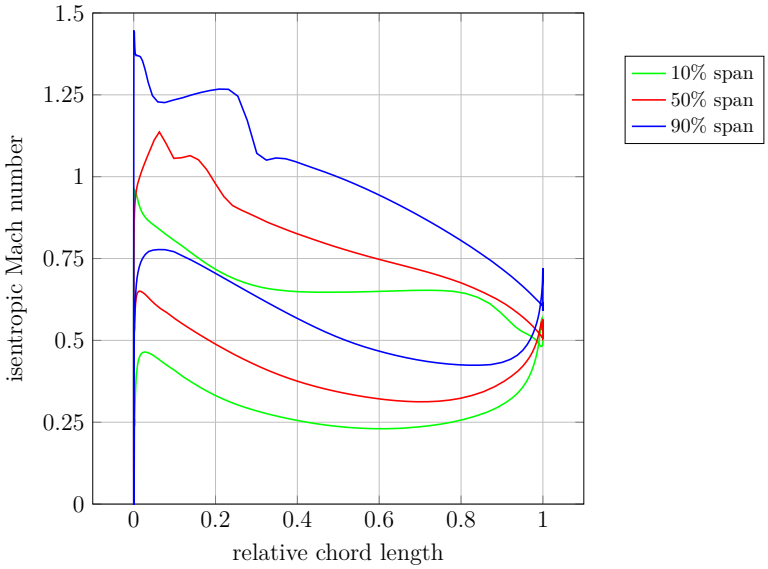

(a) S1 blade plot of rotor: FAST

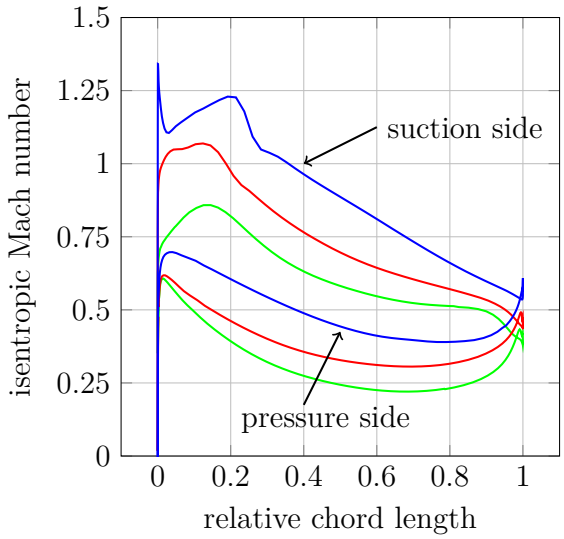

(b) S1 blade plot of rotor: MEAN

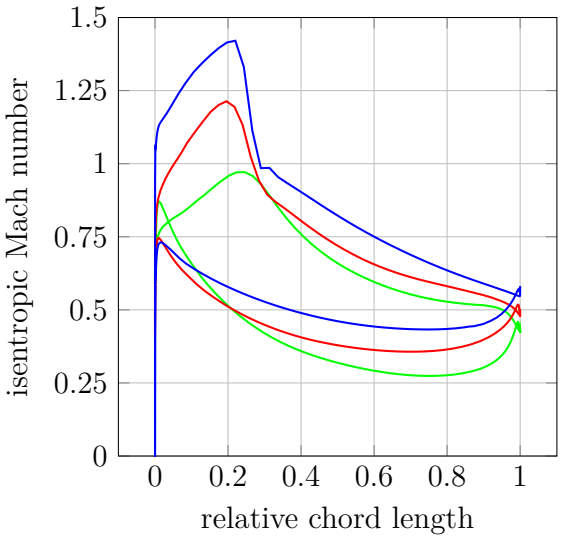

(c) S1 blade plot of rotor: SLOW

Figure 6.8: S1 (constant span) blade plots of the isentropic Mach number of the rotors.

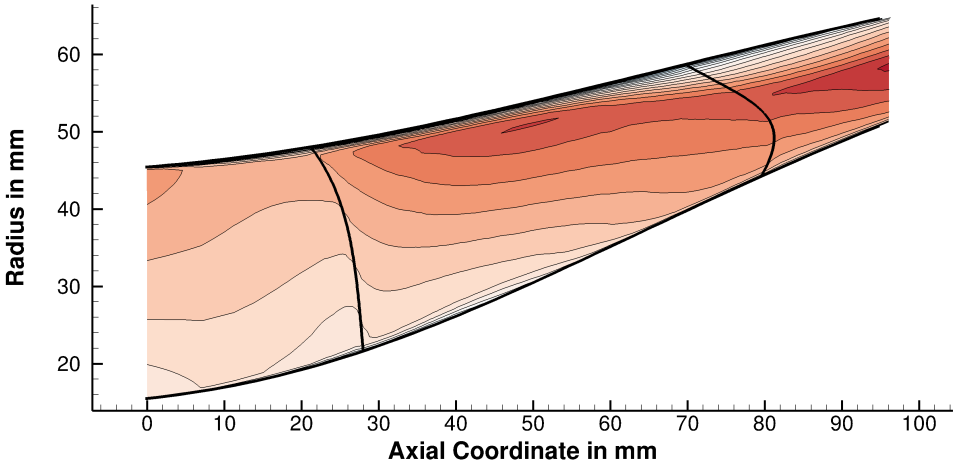

(a) S2 axial velocity-density contour of rotor: FAST

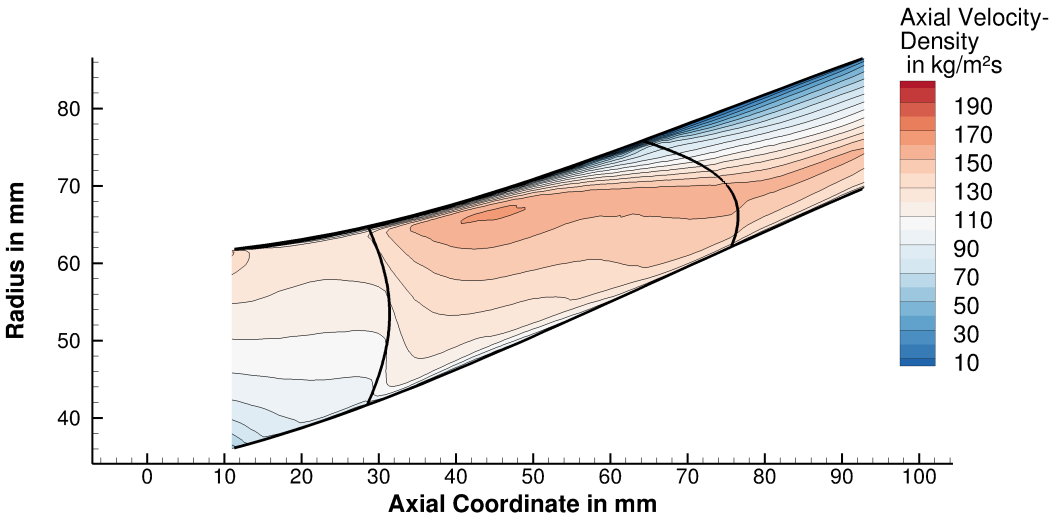

(b) S2 axial velocity-density contour of rotor: MEAN

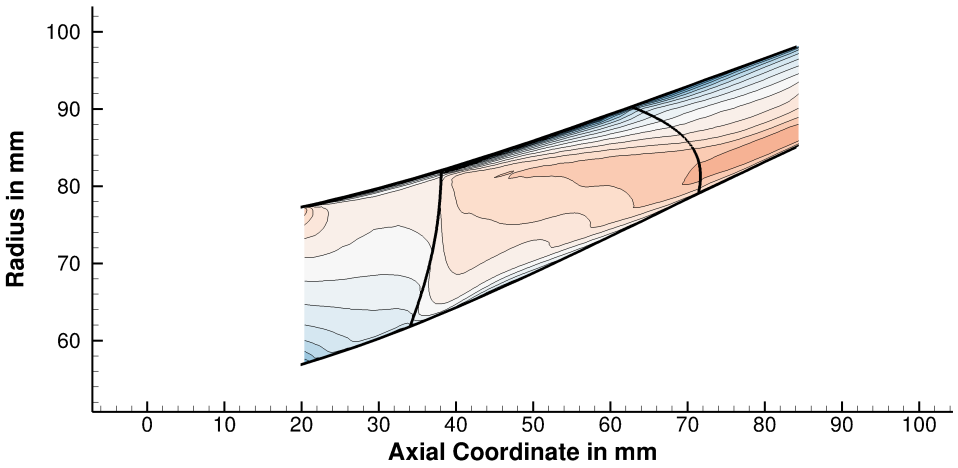

(c) S2 axial velocity density contour of rotor: SLOW

Figure 6.9: S2 (meridional) circumferentially averaged axial velocity-density contours of the rotors.

The losses caused by the bubble region in the rotors are illustrated in Fig. 6.10. As a meaningful, non-dimensional measure for the losses, a local interpretation of the total-to-total polytropic efficiency is used. The spanwise constant inlet boundary conditions of the CFD simulation are used as reference values for the inlet total pressure and temperature in Eqn. (3.13). The local efficiency is obtained by relating the local total temperature and pressure to these inlet conditions according to the definition of the polytropic compressor efficiency. In the region upstream of the rotor, the local efficiency is zero since there is no work input to the fluid. Averaging errors lead to high efficiency artifacts at the inlet shroud region and the leading edge region of the FAST and SLOW rotor. Starting from the rotor leading edge with local efficiencies near 80%, the efficiency increases to above 97% towards the rotor outlet in the hub region. The high efficiency in the hub region of the compressor indicates low losses in this region. This can be affirmed from the flow field in Fig. 6.6, where no significant, loss associated flow features can be observed in the hub region. In the tip trailing edge region, an area of low efficiency, corresponding to the low momentum bubble, is present. Despite the significant flow deceleration and flow turning in this region, the efficiency drops only to about 80% inside the bubble region. Since the through-flow (AVD) is low in this area, the associated losses of this flow area are comparably small and do not deteriorate the compressor's performance. The overall rotor performance is indicated by averaging the efficiencies at rotor outlet with highest efficiency for the FAST rotor and lowest efficiency for the SLOW rotor.

One reason why the low momentum bubble is not associated with high losses is that it does not cause flow separation on the blades. In the appendix, Figs. A.30 to A.33 show the wall shear stress distribution on the shroud, hub and blade surfaces of the rotors. Negative wall shear stresses indicated reversed boundary layer flow and consequently flow separation. For the rotor designs, flow separation can be observed on the shroud wall in the region of the blade tip. This is caused by the tip leakage flow which is directed against the direction of the passage flow due to the high stagger angle of the blades. In the trailing edge region, the flow separation propagates more into the blade passage following the shape of the low momentum bubble. On the hub, no major flow separation is present. The blades also do not exhibit a region of flow separation associated with the low momentum bubble. At the trailing edge on the suction side, a small spanwise flow separation can be observed which is caused by the significant flow deviation.

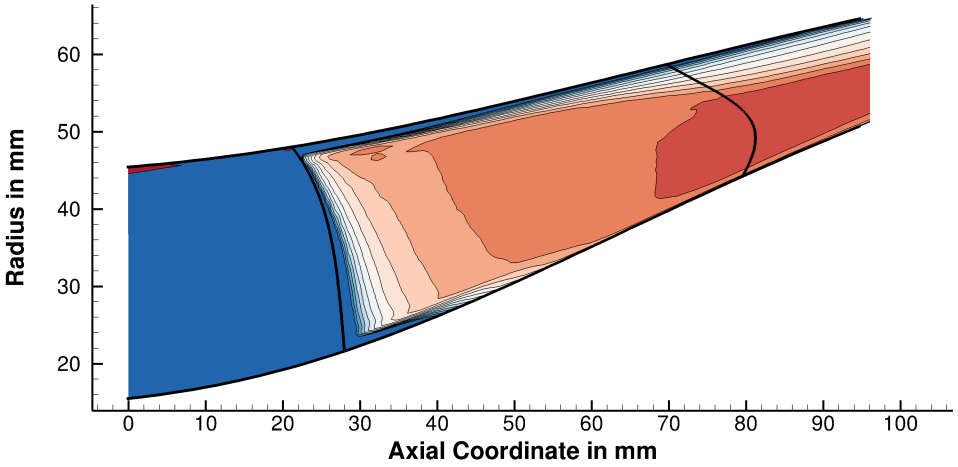

(a) S2 total-total polytropic efficiency contour of rotor: FAST

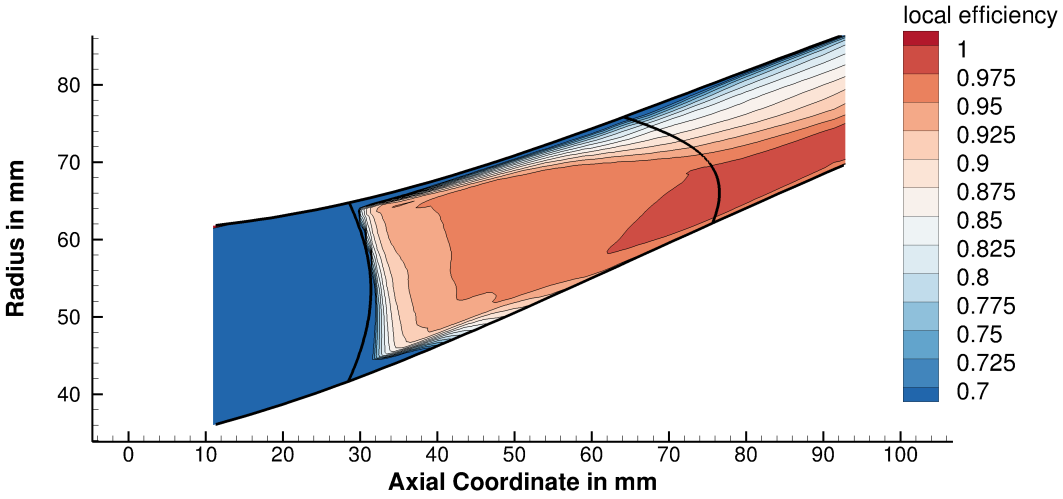

(b) S2 local total-total polytropic efficiency contour of rotor: MEAN

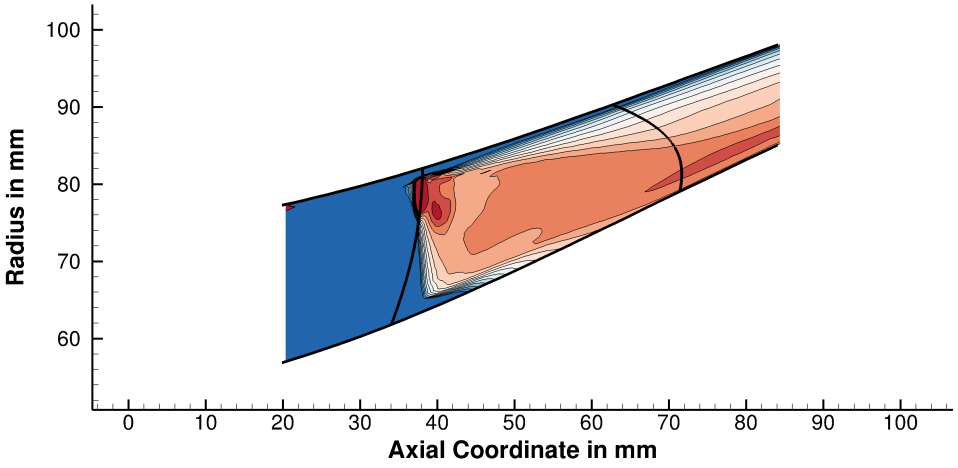

(c) S2 local total-total polytropic efficiency contour of rotor: SLOW

Figure 6.10: S2 circumferentially averaged local total-total polytropic efficiency contours of the rotors.

Table 6.2: Overview of CFD studies to identify the governing physical mechanism of the low momentum flow region.

CFD study name	**targeted physical mechanism**	**CFD model modification**
"no gap"	tip clearance flow	model without tip clearance
"Euler"	boundary layer separation	no wall friction
	secondary flow phenomena	inviscid flow (Euler flow)
	tip clearance flow	model without tip clearance
"straight"	centrifugal effects (design)	straight channel, no radius change
	boundary layer separation	no wall friction
	tip clearance flow	model without tip clearance

Analysis of the underlying physical effects of the "bubble" flow phenomenon

Below, the cause for the low momentum bubble in the tip region and for the significant flow deviation in the rotor exit region of all rotors is investigated in more detail. These flow features typically do not occur in axial type compressors. A bubble like region of low momentum in the tip region of the blade exit was not previously described in the open literature to the author's best knowledge. Possible causes for the development of the low momentum region are tip clearance flow interactions, boundary layer separation, secondary flow phenomena, or flow effects inherent to the design. To identify the governing effect, the underlying physical mechanisms need to be separated. This is done by excluding the physical mechanisms through suitable modifications of the CFD-model. The analyzed set of CFD-model studies is summarized in Tab. 6.2. These studies are performed for all three reference rotors, the results are discussed exemplarily for the mean rotor. The analogous figures for rotors FAST and SLOW can be found in App. A.7. The operating point changes due to the CFD model modification study complicate a direct comparison of the flow field. Since it is used as a boundary condition, the mass flow rate remains unchanged for all simulation studies fixing the design through-flow. The efficiency and pressure ratio rise when loss generating mechanisms such as the tip clearance, wall friction, and viscous effects are omitted. Without the centrifugal component of the work input due to the straight channel, the pressure ratio is however much lower as summarized in Tab. A.10 in the appendix. The same grid topology as used in the design process is used in these studies. However for the studies which do not model boundary layer- or viscous flow effects, a fine boundary layer grid resolution leads to unstable numerical convergence. For these cases the boundary layer grid resolution was significantly coarsened, the remaining grid was left unchanged.

Figure 6.11 shows an overview of low momentum region for the comprehensive CFD model as a reference for comparison with the modified CFD models shown below. As done above the flow field is represented by a spanwise relative Mach number slice near the shroud ($\approx 95\%$ span) on the left and an iso-volume representation of the low momentum

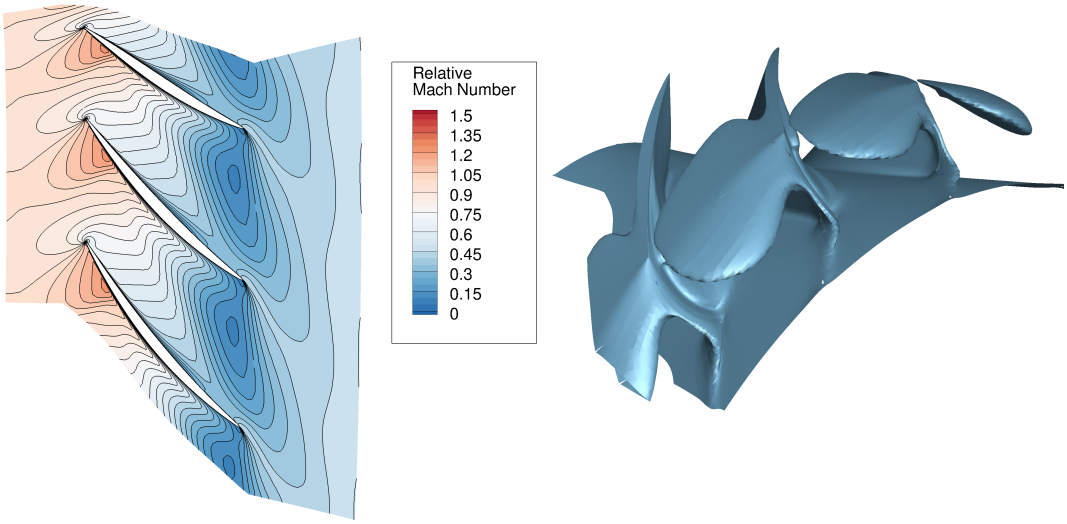

Figure 6.11: Overview of low momentum region of the comprehensive CFD model.

bubble at relative Mach numbers of 0.3 on the right. To better illustrate the position of the bubble in the blade passage, the rotor surface is shown gray. It can not be seen for the comprehensive model since the iso-volume encloses the complete blade due to boundary layer. In the first step, the influence of the tip clearance flow is investigated in Fig. 6.12 by not modeling the tip gap. Without tip clearance flow, the bubble seems to have weakened. It does not progress as far upstream the blade channel and is more attached to the blade. The tip clearance flow seems to feed the low momentum flow region and to displace it away from the suction side towards the center of the channel. The general features such as low momentum and significant deviation however remain unchanged. Without tip clearance flow, the low momentum flow region on the pressure side is increased. The iso-volumes representation of the flow field in Fig. 6.12 shows two separate structures of low momentum flow originating each from the tip and hub region of the pressure side. Without tip clearance flow the pressure side flow seems to have destabilized. These regions are however not associated with boundary layer separation. This becomes evident when considering the wall shear stresses of the rotor blades (Fig. A.32) and hub (Fig. A.31) in the appendix. Increased boundary layer displacement thickness, however, indicates a highly loaded, thick boundary layer in this region due to high flow diffusion.

To further exclude boundary layer effects and viscous flow effects, Fig. 6.13 illustrates the inviscid flow field of the rotor with frictionless walls. Using this physical representation of the flow, the low momentum structure on the pressure side tip region, which was attributed to the scraping vortex above, is not present. This supports the assumption that this flow feature originates from viscous/boundary layer effects. Near the hub, the region of low momentum on the pressure side significantly increases, resulting in increased blockage of the blade passage. This blockage seems to be a result of the flow path design and diffusion distribution inherent in the rotor designs since viscous/boundary layer effects are not included in this flow field model. Compared to the viscous flow

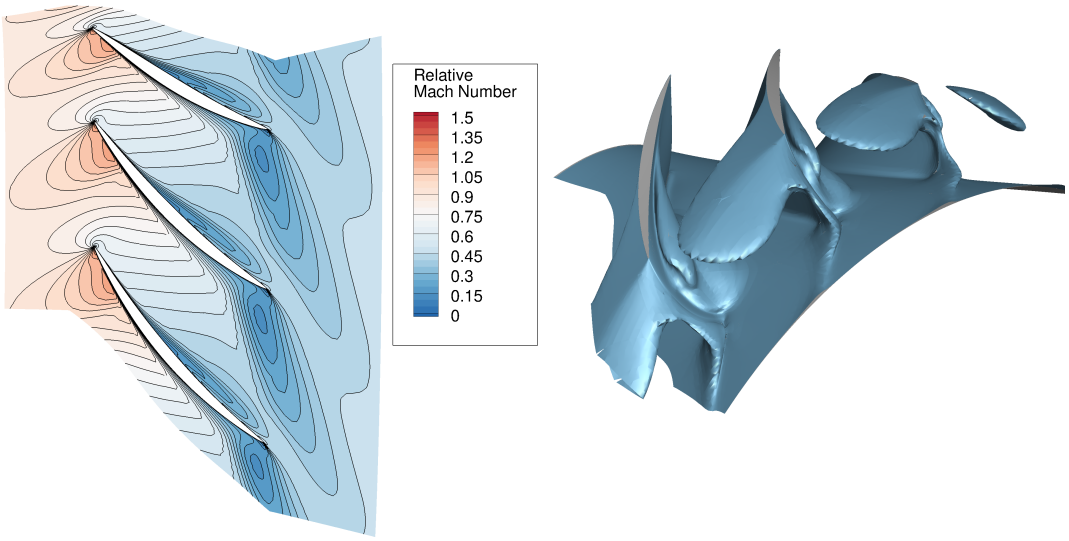

Figure 6.12: Overview of low momentum region of the CFD "no gap" model without tip clearance.

models with wall friction in Figs. 6.11 and 6.12, the size of the bubble again significantly decreases but does not change its characteristic features in Fig. 6.13. Viscous effects obviously have a significant effect on the size and propagation of the bubble but they are not the underlying cause. In Fig. 6.13, the low momentum bubble resembles a deviated blade-wake like region which cannot be caused by a momentum deficit due to boundary layer flow. Instead the underlying cause for the development of the bubble and the significant flow deviation at the trailing edge of the rotor must be inviscid effects.

Cumpsty (2004) describes viscid and inviscid mechanisms causing flow deviation at the blade trailing edge. The predominant viscid cause for deviation is flow separation on the suction side near the trailing edge is due to excessive flow diffusion, leading to incomplete flow turning. While this mechanism may contribute to the flow deviation and the development of the bubble in the presented compressor designs, the "Euler" study shows that the flow deviation also occurs in flow fields without flow separation (i.e. frictionless walls).

The underlying inviscid mechanism, which can generally occur in both axial and centrifugal compressors, according to Cumpsty (2004), is caused by high blade loading near the trailing edge. While inside the blade passage, the work input of the blades (blade forces) sustains the pressure difference between pressure side and suction side of the blade, the two flow regimes mix as soon as they exit the blade passage. As part of the equalization of this pressure difference, downstream of the trailing edge, the so called "slip flow" develops from pressure to suction side. This flow component of the exiting flow, directed opposite to the blade rotation, causes flow deviation and reduces the work of compressors. This effect intensifies with increased blade loading since the pressure difference between suction side and pressure side corresponds to the work input of the blade. In compressors with significant radial flow component (i.e. centrifugal and mixed flow compressors), the Coriolis acceleration of the flow interacts with this effect as

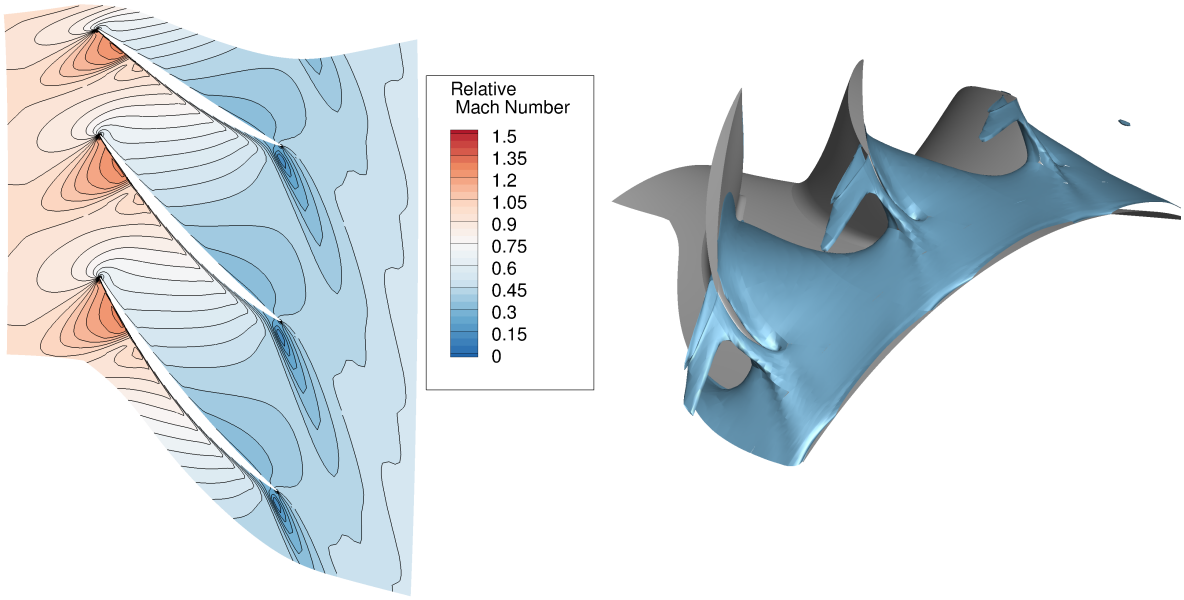

Figure 6.13: Overview of low momentum region of the CFD "Euler" model without tip clearance, wall friction, and viscous flow effects.

a second inviscid mechanism for slip flow. For radial flow directed from hub to shroud, the Coriolis acceleration results in a displacement opposite to the blade rotation. It therefore induces slip flow in itself but also increases the blade loading, enhancing the two aforementioned effects.

Slip flow is generally not observed in typical axial compressors since here, the blade loading is gradually reduced towards the trailing edge to avoid excessive losses. According to Cumpsty (2004), the blade loading of axial compressors is mainly generated by flow turning through the blade camber. This mechanism is disturbed by slip flow which significantly reduces the flow turning. In axial compressors this results in stall and the associated losses. The blade loading of centrifugal compressors in turn is predominantly caused by the Coriolis acceleration of the flow, according to Cumpsty (2004). Together with the centrifugal compression mechanism in these machines, the compression is less sensitive to deviation which is why significant slip flow can be tolerated.

To exclude centrifugal compression effects and Coriolis acceleration, the "straight" study considers the rotor designs without endwall slope and radius change. The parameterized geometry tool used in the design process is now used to generate straight rotor geometries with constant hub and shroud radius. The radii are chosen to achieve a comparable compressor mass flow rate. The blade parameters remain unchanged to achieve similarity of the blade shape. Again, tip clearance flow and wall friction are neglected in the physical model, viscous flow however is considered. The resulting flow field is shown in Fig. 6.14.

It can be seen that, instead of the a low momentum bubble in the trailing edge region of the blade passage, a wake flow without significant deviation occurs. In the iso-volume representation of the flow field, it can be seen that there is no accumulation

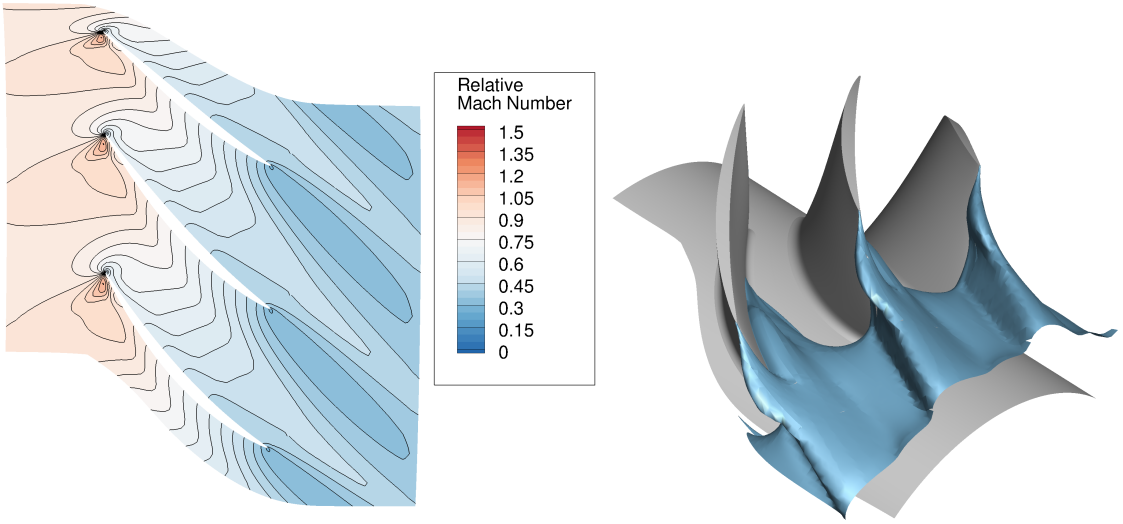

Figure 6.14: Overview of low momentum region of the CFD "straight" model without tip clearance and wall friction, and with a straight meridional channel.

of low momentum flow in the tip region. Instead, a low momentum wake develops over the complete span of the blade downstream of the trailing edge. Starting from the pressure side, the blockage in the hub region increases and propagates downstream of the trailing edge. Consequently, the underlying cause for the low momentum bubble and the flow deviation has to originate from the significant radial component of the mixed flow compressor design.

The effect of this radial component can be illustrated in S2 averaged contour plots of the static pressure normalized by the absolute total inlet pressure in Fig. 6.15. Considering the static pressure contours it can be seen that the isobaric contour lines are almost vertical and highly stacked near the leading edge of the blade indicating comparably high, spanwise uniform pressure rise. Approaching the trailing edge, the isobaric lines curve towards the hub which illustrates decreased pressure rise in this region. Eventually the isobaric lines progress horizontally indicating no further pressure rise due to axial diffusion. This pressure distribution is, according to the Euler work equation (Eqn. (3.3)), mainly caused by the increased circumferential speed in the tip region of the blade since the compressors have uniform swirl free inlet flow and approximately uniform spanwise flow turning of the blades.

Comparing the mixed flow designs in Figs. 6.15a to 6.15c with the axial design in Fig. 6.15d it can be observed that this effect increases with increasing exit radius, leading to higher pressure at the rotor tip at the trailing edge. Additionally, due to the radius increase, the meridional flow path acts as a diffuser leading to additional static pressure rise. This becomes evident in the meridional flow path section downstream of the rotor. Due to diffusion, the exit static pressure is significantly higher than the pressure at the rotor trailing edge. Two diffusion mechanisms are relevant in this type of flow path

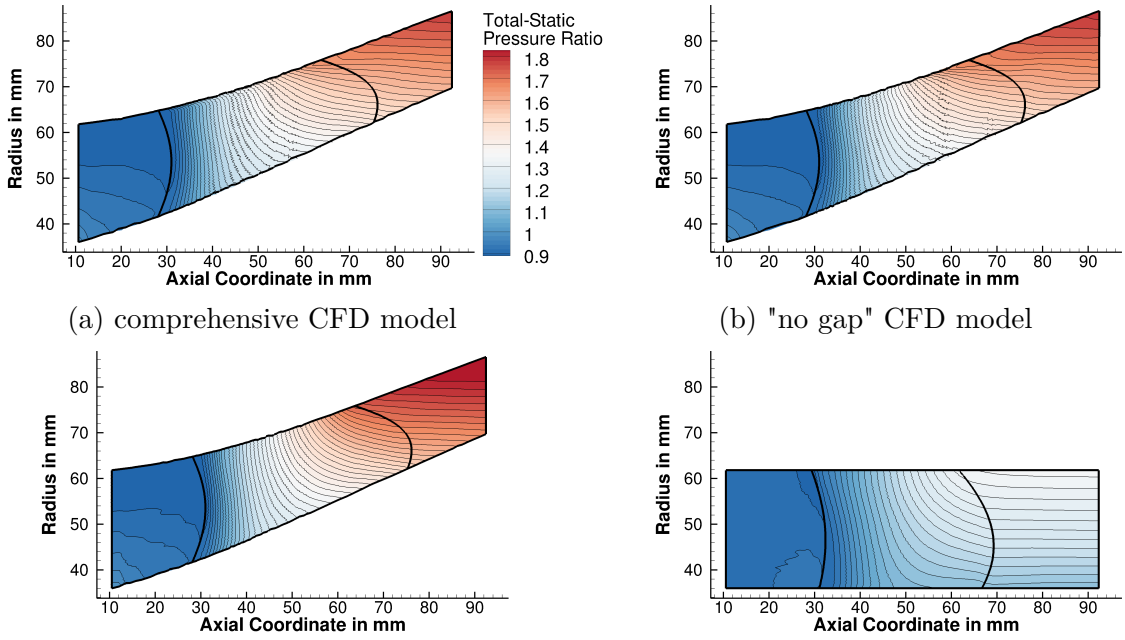

(a) comprehensive CFD model

(b) "no gap" CFD model

(c) "Euler" CFD model

(d) "straight" CFD model

Figure 6.15: S2 static pressure contours of MEAN rotor normalized by the absolute total inlet pressure.

shape. While the slope of the endwalls leads to a local acceleration of the flow at the hub, stabilizing the flow, it acts as local axial diffuser in the tip region. By increasing the axial cross sectional area in this region the local axial flow velocity is reduced leading to localized static pressure increase and destabilized flow. The radial diffusion caused by the radius increase leads to a more spanwise uniform static pressure rise. Here the underlying mechanism is radial flow deceleration due to the increase of the cross sectional area and reduction of the flow swirl due to radius increase. To conserve the angular momentum, a swirling flow naturally reduces the swirl velocity when the swirl radius is increased leading to increased pressure.

The superposition of the increased Euler work due to high circumferential speed with the high diffusion due to radius increase of the meridional flow path and due to the slope of the casing leads to particularly high pressure rise and consequently destabilized flow in the tip region of the blade. This explains why the trailing edge tip region is susceptible to flow collapse which ultimately leads to low flow velocity and high blockage - the features of the "bubble" region.

As described earlier, the high blade load due to the radius increase, which leads to centrifugal compression and Coriolis acceleration of the flow, the high rotational speed, and high flow turning leads to large pressure difference between pressure and suction side of the blade. This is illustrated in Fig. 6.16 by comparing the normalized profile pressure of the "comprehensive" and "straight" CFD model of the MEAN rotor. It can be seen that the "comprehensive", mixed flow design achieves significantly higher pressures in the exit region of the blade than the "straight", axial design. The higher work input of

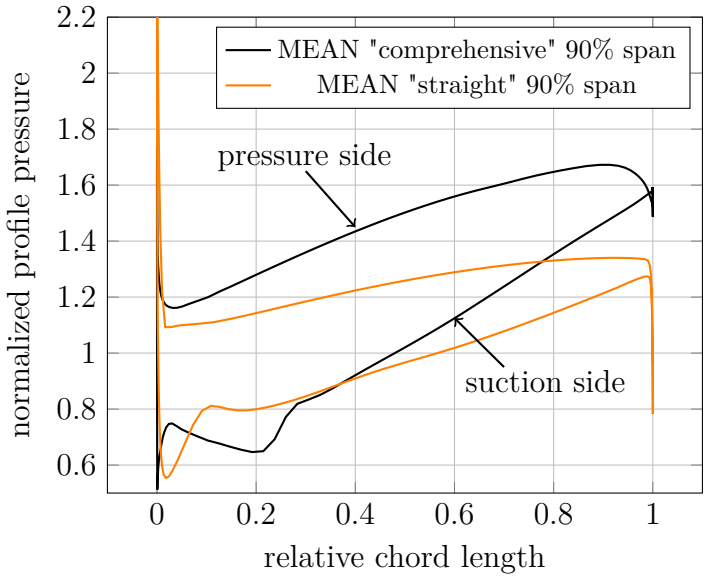

Figure 6.16: Comparison of the profile pressure distribution, normalized with the absolute total inlet pressure.

the mixed design, which is represented by the area enclosed by pressure side and suction side pressure, leads to increased pressures in the order of 1.5 times the pressure of the axial design in the last 20% of the blade. This pressure difference is present over the complete span of the blade and is, together with the Coriolis acceleration, responsible for the slip flow which causes the flow deviation.

In the trailing edge tip region of the rotor, the slip flow coincides with the highly loaded, destabilized flow. The additional turning due to the slip flow finally overloads the tip region flow and results in significant deceleration. This deceleration is the underlying physical mechanism for the observed "bubble" phenomenon. Boundary layer effects on the shroud and blade surfaces, viscous flow effects, and tip clearance flow effects further destabilize the flow and lead to a greater, bubble-shaped low momentum flow region.

To illustrate the effect of flow deceleration in the bubble region, the spanwise flow vectors of the MEAN rotor are shown in Fig. 6.17. With increasing span, the circumferential speeds at inlet $\vec{u}_1$ and exit $\vec{u}_2$ increase. $\vec{u}_2$ is always greater than $\vec{u}_1$ due to the radius increase of the compressor. The approximately constant spanwise flow coefficient, which was specified in the design process, leads to increased, swirl free absolute inlet velocity $\vec{c}_1$ and increased relative inlet velocity $\vec{w}_1$. Going from hub to shroud, in the hub region below 50% span, the exit velocity $\vec{w}_2$ turns further counter the direction of blade rotation. The axial exit velocity does not change significantly in this region in spanwise direction. In the tip region at 90% span, the deceleration due to the compression shock, the slip flow and the associated "bubble" effect lead to significantly reduced relative $\vec{w}_2$ and axial exit velocity. A detailed evaluation shows that the reduction of $\vec{w}_2$ overcompensates the reduction of the axial exit velocity leading to increased absolute exit swirl c_{u2} and consequently increased specific work in this region.

A measure for the negative impact of slip flow is the so-called slip factor σ_{slip}. It is

defined in Eqn. (6.1) as the ratio of the actual exit swirl to the ideal exit swirl if there was no deviation. It can be interpreted as a measure for the rotor work reduction due to deviation. The slip factor is determined from the circumferential velocity u, the axial velocity c_x and the blade angle β_{out} in Eqn. (6.1).

$$\sigma_{\text{slip}} = \frac{c_u}{c_{u,\text{ideal}}} = \frac{c_u}{u - c_x \cdot \tan(\beta_{\text{out}})} \tag{6.1}$$

The spanwise slip factor distribution for the FAST, MEAN and SLOW rotor using the "comprehensive" CFD model are shown in Fig. 6.18. The slip factor progressively decreases with increasing span starting from high values at the hub. At the beginning of the bubble, which is at about 50% span for the SLOW rotor and about 70% span for the FAST rotor, the slip factor increases. This is due to the increase of the axial velocity and the slightly increased absolute swirl in the bubble which lead to convergence of the actual and ideal swirl components. The increased losses near the shroud wall again lead to reduced work input and decreased slip factors. For typical axial compressors, the slip factors are comparably high. Veres (2009) states global slip factors in the range of 0.9-0.95 for typical axial compressor stages such as the NASA Stage 37. The observed slip factors agree with the typical range for centrifugal compressors with global slip factors from 0.7 to 0.9 (Traupel 2001). The increased flow swirl and the higher slip factors lead to increased specific Euler work according to Eqn. 3.3 in the bubble region. This increased specific work input does however not compensate the increased blockage in this region (see Fig. 6.9). The mass flow displacement from tip to hub leads to the overall lower work input in the bubble region.

Concluding the aerodynamic characterization of the rotor, it can be stated that the

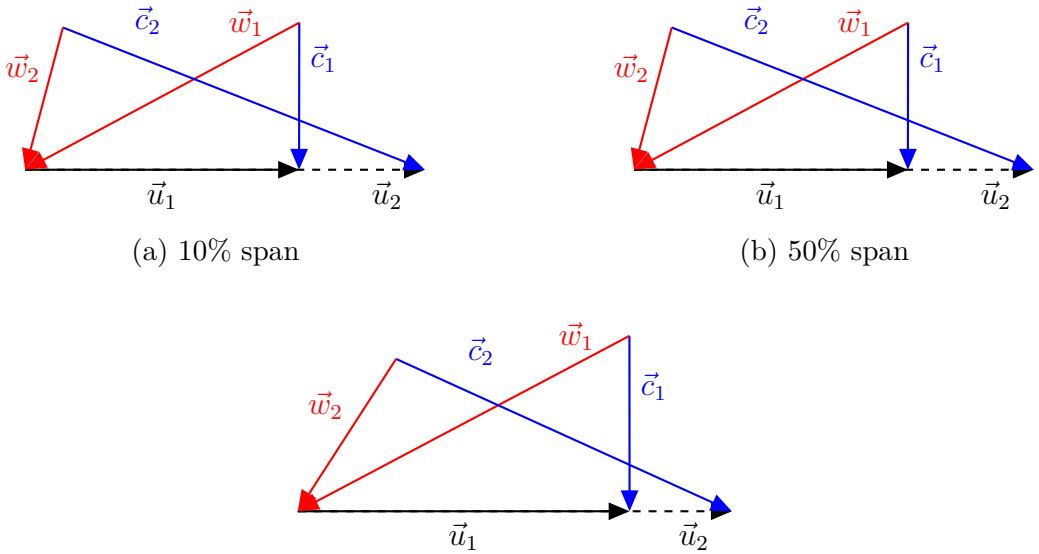

(a) 10% span

(b) 50% span

(c) 90% span

Figure 6.17: Comparison of the velocity triangles of the MEAN rotor, "comprehensive" CFD model at different spanwise positions.

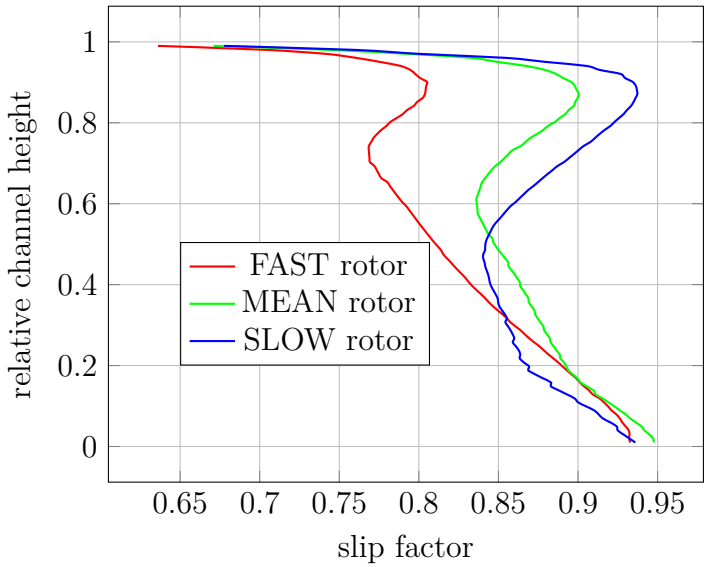

Figure 6.18: Rotor slip factors of the FAST, MEAN and SLOW rotor using the "comprehensive" CFD model.

designs achieve high work output due to the high rotational speeds, transonic flow velocities, and significant radius increase. The low momentum bubble region is a consequence of these design features. It can be found for any high pressure, high efficiency rotor design resulting from the presented optimized design process. The reason why this feature is accepted by the optimized design process is that the associated losses and negative effects are not excessively reducing the overall compressor performance. There can be no designs found in the design space which do not exhibit the bubble phenomenon and are able to achieve the required performance.

6.3.3 Stator/Stage

The flow characteristics of the compressor stages will now be analyzed. On the left side of Fig. 6.19 the Mach number contour of a slice near the shroud of each compressor at about 90% span is shown. On the right side in the figure, the corresponding isentropic Mach number distributions of each stator is shown for three spanwise positions.

As described earlier, the low momentum bubble in the exit region of the rotor passage is not limited to isolated rotor designs but is also present in the final rotor designs in stage configuration. Compared to the rotor blades, the stator blades have high chord length and low blade thickness. This provides good flow guidance and allows high flow turning. Although the structural loads on the stator are significantly lower than on the rotor it might still be necessary to increase the stator blade thickness before these designs can be evaluated on a test rig. The current, low blade thickness requires to push the technical feasibility limit in the manufacturing process to obtain an accurate model of the design. Increasing the blade thickness would be a way to reduce cost and effort in the manufacturing process. In this shrouded design the stator blades are attached to

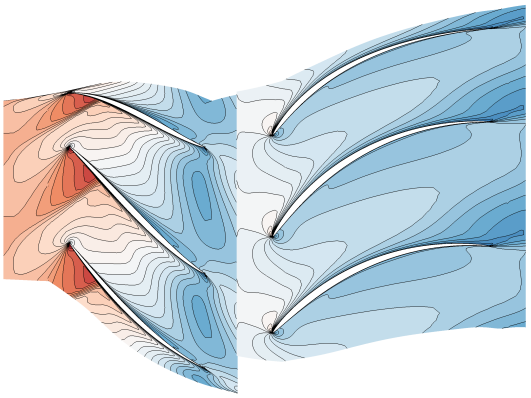

(a) Mach slice of stage: FAST

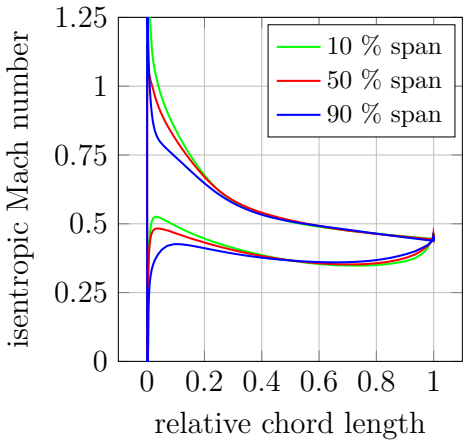

(b) S1 blade plot of stator: FAST

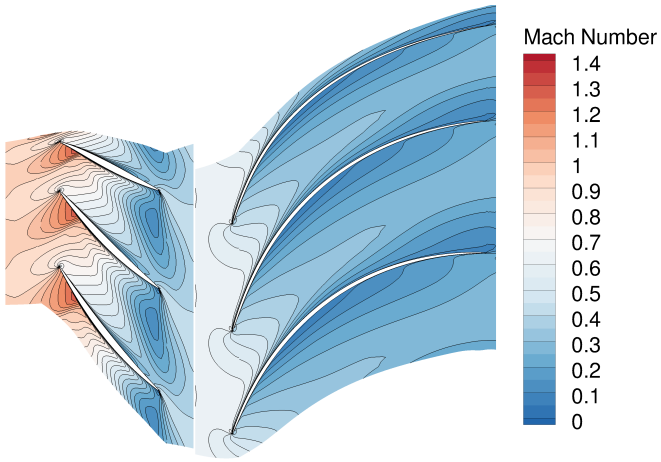

(c) Mach slice of stage: MEAN

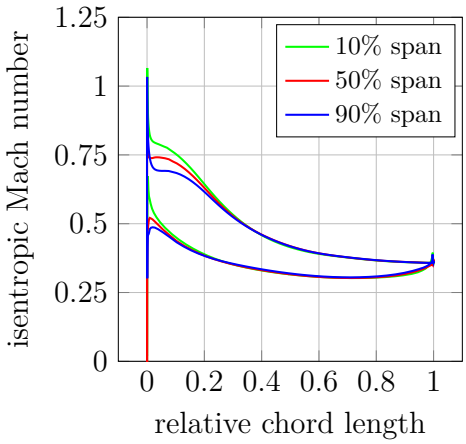

(d) S1 blade plot of stator: MEAN

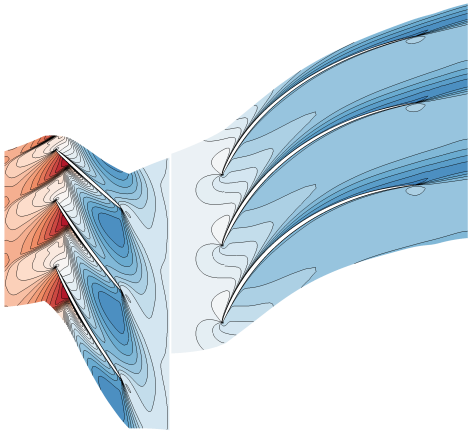

(e) Mach slice of stage: SLOW

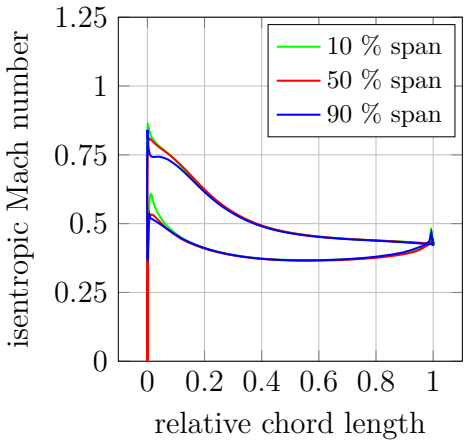

(f) S1 blade plot of stator: SLOW

Figure 6.19: Left: Mach slice in the tip region of the stages; Right: S1 blade plots of the isentropic Mach number of the stators.

hub and shroud without a gap. Together with the low aspect ratio (see Tab. 5.7) there is no reason to assume that the aerodynamic loading could exert a critical structural load on the stator blade.

From the Mach number contours of Fig. 6.19 it can be observed that the majority of the flow deceleration and flow turning in the stators occurs in the first third of the chord length of the blades. In the downstream region the flow is turned without significant flow deceleration. Towards the downstream part of the blades, low momentum flow regions develop from the blades surfaces due to the high diffusion and boundary layer effects. Downstream of the area of high deceleration, a contained low momentum region develops on the pressure side (lower side of the blade). More significantly a greater low momentum region originates from the suction surface which extends downstream in the blade passage and seems to limit the flow turning. All in all these are common flow features for highly loaded stators.

The isentropic Mach number distributions on the right side in Fig. 6.19 provide a more detailed overview of the stator blade loading and its spanwise distribution. The plots confirm that the majority of the flow deceleration occurs in the first 40% chord length of the stators. Downstream of this region, the blade pressure increases only marginally and the blade loading decreases significantly. Towards the trailing edge, the isentropic Mach numbers on suction side and pressure side smoothly converge. Due to the low blade loading near the trailing edge, no significant flow deviation occurs. The isentropic Mach number distributions indicate slightly higher blade loading in the hub trailing edge region of the blade, which decreases towards the tip region. The stator blade loading is highest for the FAST stage design and reduces with reducing rotor design speed. The stator flow is subsonic with no compression shocks, despite the isentropic Mach number peak at the leading edge.

The high blade loading in the front part of the blades results in a notable reduction of wall shear stress (see Figs. A.50 to A.51) in this area, indicating a boundary layer close to separation. Despite the high loading of the stator and the significant low momentum flow regions, there are no major flow separations of the stator flow visible in the wall shear stress contours in Figs. A.48 to A.51. The least stable region of the stator blades is the trailing edge/hub region due to the thick boundary layer developing along the blade and hub wall. Here, confined negative wall shear stress areas develop which indicate a flow separation which reattaches upstream of the trailing edge.

To give an impression of the meridional flow field, Fig. 6.20 shows the circumferentially averaged absolute flow swirl of the compressor stages. These figures illustrate the energy input by the rotor by accelerating the flow in circumferential direction and the static pressure increase in the stator through flow turning by swirl deceleration. In agreement with the analysis above, it can be seen that the flow turning in the stator is largest in the front part of the blade indicating high load and thus high pressure rise. Although the previous analysis shows that there is only minor flow deceleration in the rear part of the blade, Fig. 6.20 shows that the long stator blades still achieve further flow turning in this region. This affirms the underlying design principle of these low aspect ratio stators found in the design process: The stator blades are strongly front-loaded to achieve high pressure rise while the less loaded rear part provides steady, low-loss flow turning to

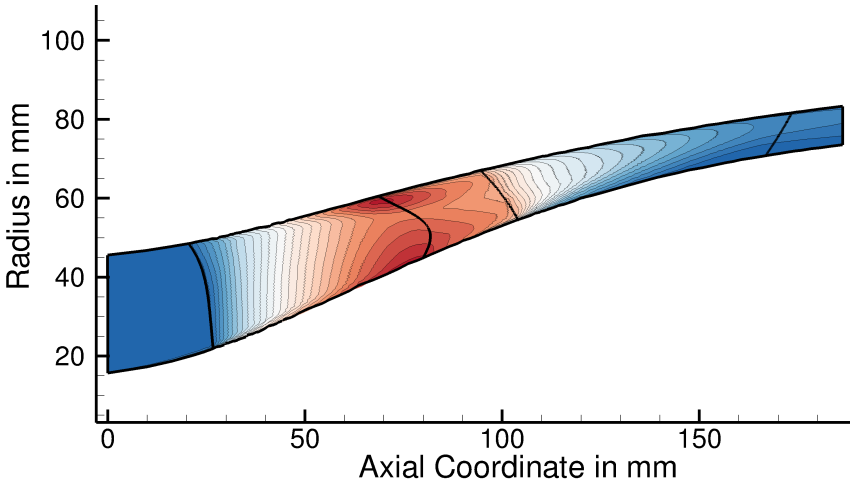

(a) FAST

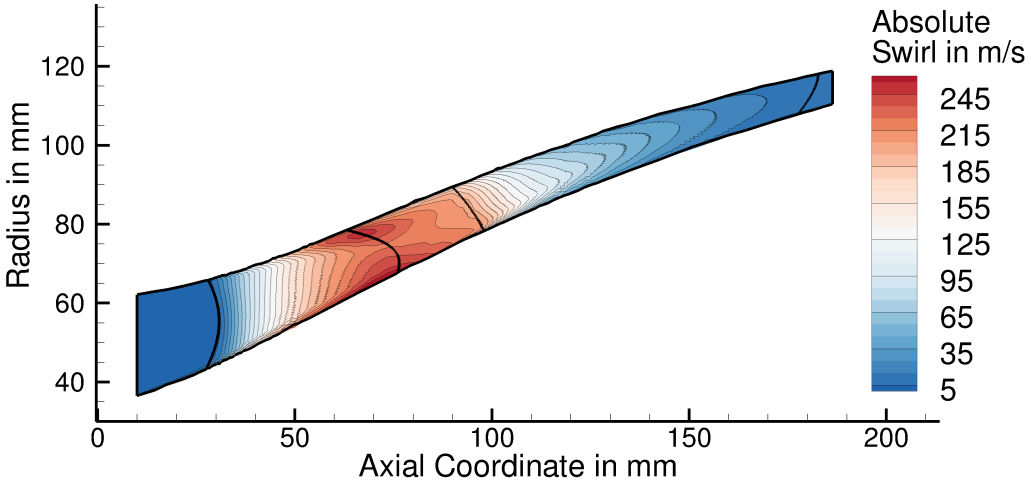

(b) MEAN

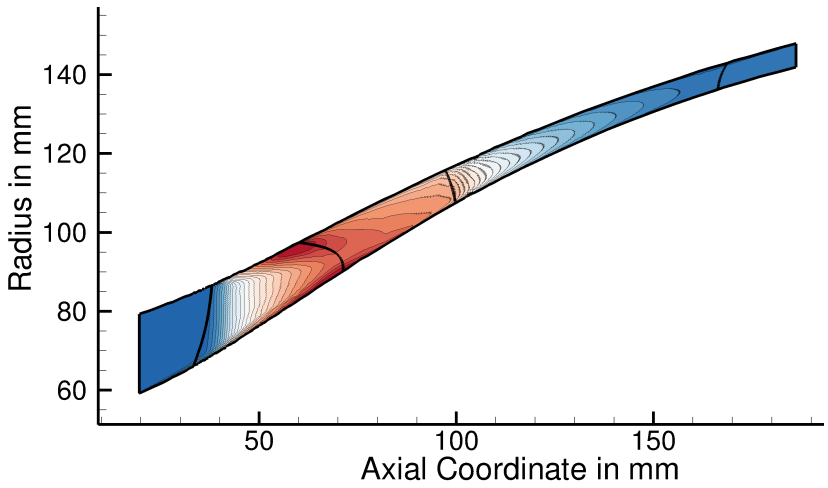

(c) SLOW

Figure 6.20: S2 circumferentially averaged absolute swirl contours of the stages.

achieve low exit swirl. This is supported by the good flow guidance due to the long, low aspect ratio blades as well as by the diffusion and the hub acceleration due the radius increase of the stator passage.

7 Conclusions

In the presented work, an efficient, automated design process for single-stage, transonic compressors is developed. This process is used to design compressors for an electrically powered, active high-lift system for future civil aircraft. The resulting compressor designs satisfy the challenging requirements, namely compact size and high total pressure ratios of up to 2.3 at a corrected mass flow of 1.1 kg/s at high efficiency in the range of 85 to 90%. The design method is based on an axial flow compressor setup, with a rotor stator configuration. The designs resulting from the optimization algorithm controlled process, however most resemble mixed-flow compressors with a significant radial flow component and significant centrifugal compressor work. All relevant designs are characterized by endwall ramp angles between 10° to 25°, mean radius ratios between outlet and inlet in the range of 1.2 to 1.35, hub-to-tip ratios between 0.8 to 0.95, blade aspect ratios between 0.1 to 0.3, and solidities in the range of 2.5 to 3. The compressor map characteristic of the designs matches the duty line of the active high-lift system well, covering all required operating points with sufficient margin to the compressor stability limits.

The optimization algorithm assisted design process allows to cover a wide design space. The results show that for a specific compressor type the conventional design space and the conventional performance levels can be extended by using advanced design methods. In this case the design space of mixed-flow compressors was significantly extended by shifting the established lower bound of specific speeds ω_s for this machine type from 1 to 0.65. It was also shown that these machines can achieve significantly higher specific work at high efficiency than conventionally expected. With the presented design process the maximum isentropic enthalpy rise coefficient $\psi_{g,isen}$ at a global flow coefficient ϕ_g of 0.1 was increased from about 0.55 to 0.7 while still obtaining polytropic total-total rotor efficiencies above 90%. A correlation is provided which represents the obtained design space extension. This correlation may be used as a guide line for future design processes of similar compressors.

The described compressor designs neither resemble typical mixed flow compressors nor with typical axial compressors. Mixed-flow compressors generally resemble centrifugal compressors more closely, using the same design processes often incorporating splitter blades, a more radial directed outlet section and no stator. Typical axial compressors, in contrast, have significantly lower radial flow components and greater aspect ratios. The compressor type presented in this work is thus regarded as a subgroup of mixed-flow compressors with predominantly axial flow compressor characteristics. Depending on the design either centrifugal compression work or blade diffusion is the dominant mode of compression at the design point of the compressor stage.

In exceeding the conventional compressor design limits and covering a wide design space with the developed design method, it was found that there is a significant degree of freedom available to the compressor design for this application. Specifically, it was shown that the required operating range and performance can be obtained over a wide range of compressor rotational speeds and sizes. This was illustrated exemplarily for three stages which achieve the same operating range at total efficiencies between 85% to 90% with significantly different rotational speeds and compressor sizes. At the design point, the rotational speeds of the three stages differ up to 40% relative to the design with highest rotational speed. Having approximately the same tip circumferential speed, compressor designs with high rotational speed have low diameter and vice versa. The maximum diameter of the slowest design is about 75% greater than the diameter of the fastest design. In comparison, designs with greater diameter and lower speed tend to have lower efficiency.

This degree of freedom allows the consideration of external system requirements in the selection of the compressor design. For the EPHLS this includes the interactions of the compressor design with the design of the electrical machine and power electronics as well as the interactions with the aircraft design. The decisive compressor parameters for these interactions are efficiency, speed and size which determine the mass of the EPHLS, the electromagnetic and mechanical design strategy of the EPHLS system and, through its integration, ultimately influence the overall aircraft design.

Concerning the aerodynamic characteristics of the compressor designs a new flow feature was described for mixed-flow compressors with swirl free inlet flow and significant shroud slope. This flow feature can be visualized as a flat, oval, bubble-shaped region of low flow momentum in the tip-trailing edge region of the rotor. In a numerical case study it was shown that the origin of this flow feature are the interaction of high flow deviation and high rotor trailing edge tip loading. These are caused by the high rotor loading and the significant radial component of the compressor which introduces Coriolis acceleration and flow diffusion at the shroud. While the origin of this flow effect is therefore solely inviscid, viscous effects and interaction with the tip clearance flow cause its final, characteristic "bubble" shape. Although this region is associated with the most significant losses in the rotor, the overall efficiency penalty is small and does not deteriorate the compressor performance.

To utilize the significant rotor exit swirl in the stator and achieve almost axial stage exit flow, a low aspect ratio, high solidity stator design proved to be the most efficient design features. These long stator blades allow the required flow turning without excessive total pressure loss. The stator blades are characterized by high front loading, achieving the majority of the static pressure rise in the first 40% of the chord length. Downstream, the flow is turned without significant deceleration, avoiding excessive flow separation. The "bubble" flow effect is a consequence of the design task and of the selected parameterization. For this subgroup of mixed-flow compressors, to achieve the required total pressure ratios requires very high loading. This can only be achieved by a significant radial component and the associated shroud slope. These design features

lead to the significant flow deviation and blade tip loading which are parental to the "bubble" flow effect. The effect cannot be avoided with this design strategy while still achieving the required total pressure ratio. The optimized design process resulted in designs in which this effect does not cause significant loss or prohibitively decreases the compressor operating range.

8 Outlook

The most important step following up on the presented work is the experimental validation of the design process. This concerns the validation of the aerodynamic model as well as the validation of the parametrization.

Generally any CFD-simulation should be validated on the basis of physical measurements to assure correct modeling of the flow field. These models have been developed for the use in conventional applications and are reliable within this range of validity. Available data from comparable machines can be used to select the appropriate models and to evaluate the expected influence of the inherent simplifications. The resulting designs in the present work, however, exceed the established compressor design space. Established models can therefore not be applied with the same confidence in their validity as for conventional machines. The applicability of the boundary layer models used and the turbulence models used for these comparably small, transonic compressors is not proven. Other simplifications such as the consideration of only one blade passage and steady flow have a significant influence on the prediction of the stability limit of compressors. Whether these simplifications allow a reliable prediction of the compressor operating range in this application needs to be confirmed. The aerodynamic validation therefore has two important aspects. The first is to validate the operating range and performance of the compressor. This allows evaluating the suitability of the selected CFD-model for performance prediction. The second aspect is the validation of the prediction of the flow field and governing flow effects, in particular of the "bubble", described in this work using detailed flow measurement techniques.

The validation of the parameterization in turn aims at evaluating whether the current design decisions are appropriate. The design of a prototype for experimental validation requires a highly detailed design process considering all significant mechanical constraints of the compressor system such as mechanical stresses, deformation, vibration and the detailed integration with the electrical components. The consideration of these disciplines in a comparable degree of detail was not achievable in the presented automated design process. These insights from the detailed prototype design process allow an adjustment of the parameterization to better match the requirements of these disciplines.

This knowledge will also allow a closer integration of the design processes considering additional parameters. Requirements of the electrical components and of the mechanical design could be included in the compressor design process to guide the process more towards relevant designs for the EPHLS application. Improved simplified compressor models on the basis of the present work would allow a faster, complete EPHLS design process. This would allow to consider EPHLS and the aircraft design parameters leading to a global optimum considering all significant design requirements. These aspects for future work are addressed in a follow-up project which is also funded by the SFB 880.

Bibliography

Anderson, J. D. (2003): Modern compressible flow: with historical perspective. McGraw-Hill series in aeronautical and aerospace engineering. McGraw-Hill, Boston, third edition. ISBN 978-0-07-242443-0.

ASME (2009): Standard for verification and validation in computational fluid dynamics and heat transfer. American Society of Mechanical Engineers, New York, NY. ISBN 978-0-7918-3209-7. OCLC: 586079545.

Aungier, R. H. (2003): Axial-flow compressors: a strategy for aerodynamic design and analysis. ASME Press, New York. ISBN 978-0-7918-0192-5.

Becker, K.; Heitkamp, K. and Kügeler, E. (2010): Recent progress in a hybrid-grid CFD solver for turbomachinery flows. In: Proceedings fifth European conference on computational fluid dynamics ECCOMAS CFD. volume 2010.

Biollo, R. and Benini, E. (2012): Recent advances in transonic axial compressor aerodynamics. In: Progress in Aerospace Sciences. ISSN 03760421. doi: 10.1016/j.paerosci.2012.05.002. URL http://linkinghub.elsevier.com/retrieve/pii/S0376042112000528.

Bölcs, A. and Suter, P. (1986): Transsonische Turbomaschinen: mit 34 Übungsaufgaben und 4 gasdynamischen Tabellen mit Diagrammen. Wissenschaft und Technik Taschenausgaben. Braun, Karlsruhe. ISBN 978-3-7650-2036-0.

Burnazzi, M. and Radespiel, R. (2013): Synergies of Suction and Blowing for Active High-Lift Flaps. Stuttgart.

Burnazzi, M. and Radespiel, R. (2014): Assessment of leading-edge devices for stall delay on an airfoil with active circulation control. In: CEAS Aeronautical Journal, volume 5(4):p. 359–385. ISSN 1869-5582, 1869-5590. doi:10.1007/s13272-014-0112-5. URL http://link.springer.com/10.1007/s13272-014-0112-5.

Calvert, W. J. and Ginder, R. B. (1999): Transonic fan and compressor design. In: Proceedings of the Institution of Mechanical Engineers, Part C: Journal of Mechanical Engineering Science, volume 213(5):p. 419–436. ISSN 0954-4062, 2041-2983. doi: 10.1243/0954406991522671. URL http://pic.sagepub.com/lookup/doi/10.1243/0954406991522671.

Casey, M. (2008): Lecture notes: Turbokompressoren und Ventilatoren (TVK). Institut für Thermische Strömungsmaschinen und Maschinenlaboratorium (ITSM) - Universität Stuttgart.

Casey, M.; Zwyssig, C. and Robinson, C. (2010): The Cordier Line for Mixed Flow Compressors. In: , p. 1859–1869. doi:10.1115/GT2010-22549. URL http://dx.doi.org/10.1115/GT2010-22549.

Cavazzuti, M. (2013): Optimization Methods. Springer Berlin Heidelberg, Berlin, Heidelberg. ISBN 978-3-642-31186-4 978-3-642-31187-1. URL http://link.springer.com/10.1007/978-3-642-31187-1.

Cebeci, T. (Ed.) (2005): Computational fluid dynamics for engineers: from panel to Navier-Stokes methods with computer programs. Horizons Pub. Inc., ; Springer, Long Beach, Calif. : Berlin. ISBN 978-0-9766545-0-6 978-3-540-24451-6. OCLC: ocm60802091.

Chahine, C.; Seume, J. R. and Verstraete, T. (2012): The Influence of Metamodeling Techniques on the Multidisciplinary Design Optimization of a Radial Compressor Impeller. In: ASME Turbo Expo 2012: Turbine Technical Conference and Exposition. American Society of Mechanical Engineers, p. 1951–1964. URL http://proceedings.asmedigitalcollection.asme.org/proceeding.aspx?articleid=1695019.

Cordier, O. (1953): Ähnlichkeitsbedingungen für Strömungsmaschinen. In: BWK Zeitschrift, volume 5(10):p. 337–340.

Cumpsty, N. A. (2004): Compressor aerodynamics. Krieger Pub, Malabar, Fla. ISBN 978-1-57524-247-7.

Cumpsty, N. A. (2010): Some Lessons Learned. In: Journal of Turbomachinery, volume 132(4):p. 041018. ISSN 0889504X. doi:10.1115/1.4001222. URL http://link.aip.org/link/JOTUEI/v132/i4/p041018/s1&Agg=doi.

de Haller, P. (1953): Das Verhalten von Tragflügelgittern in Axialverdichtern und im Windkanal. In: BWK Zeitschrift, volume 5(10):p. 333–37.

Dhondt, G. D. C. (2004): The finite element method for three-dimensional thermomechanical applications. Wiley, Hoboken, NJ. ISBN 0-470-85752-8.

Dickens, T. and Day, I. (2011): The Design of Highly Loaded Axial Compressors. In: Journal of Turbomachinery, volume 133(3):p. 031007. ISSN 0889504X. doi:10.1115/1.4001226. URL http://Turbomachinery.asmedigitalcollection.asme.org/article.aspx?articleid=1468477.

DIN EN 586-2 : 1994-11, Aluminium and aluminium alloys - Forgings - Part 2: Mechanical properties and additional property requirements"; German Version.

Dixon, S. L. and Hall, C. A. (2010): Fluid mechanics and thermodynamics of turbomachinery. Butterworth-Heinemann/Elsevier, Burlington, MA. ISBN 978-1-85617-793-1. URL http://app.knovel.com/hotlink/toc/id:kpFMTTE022/fluid-mechanics-thermodynamics/fluid-mechanics-thermodynamics.

Ellbrant, L.; Eriksson, L.-E. and Mårtensson, H. (2014): Predictive Capability of CFD Models for Transonic Compressor Design. In: ASME Turbo Expo 2014: Turbine Technical Conference and Exposition. American Society of Mechanical Engineers, p. V02BT39A041–V02BT39A041. URL http://proceedings.asmedigitalcollection.asme.org/data/Conferences/ASMEP/80896/V02BT39A041-GT2014-27019.pdf.

Epple, P.; Durst, F. and Delgado, A. (2010): A theoretical derivation of the Cordier diagram for turbomachines. In: Proceedings of the Institution of Mechanical Engineers, Part C: Journal of Mechanical Engineering Science, volume 1(-1):p. 1–15. ISSN 0954-4062, 2041-2983. doi:10.1243/09544062JMES2285. URL http://pic.sagepub.com/lookup/doi/10.1243/09544062JMES2285.

European Commission (2011): Flightpath 2050: Europe's vision for aviation; maintaining global leadership and serving society's needs; report of the High-Level Group on Aviation Research. Policy / European Commission. Publ. Off. of the Europ. Union. ISBN 978-92-79-19724-6.

Ferziger, J. H. and Perić, M. (2008): Numerische Strömungsmechanik. Springer, Berlin. ISBN 978-3-540-68228-8 978-3-540-67586-0. OCLC: 244010653.

Fischer, A.; Riess, W. and Seume, J. R. (2003): Performance of strongly bowed stators in a 4-stage high speed compressor. In: ASME Turbo Expo 2003, collocated with the 2003 International Joint Power Generation Conference. American Society of Mechanical Engineers, p. 429–435. URL http://proceedings.asmedigitalcollection.asme.org/data/Conferences/GT2003/71965/429_1.pdf.

Fischer-Engineering (2014): Motorenbereiche_Fischer_Precise_Katalog.pdf. URL http://www.fischerspindle.ch/anwendungsgebiete/schnelle,-praezise,-leistungsstarke-rotation/.

Garrett (2016): Turbocharger GT6041 - Garrett by Honeywell. Accessed: 2016-07-21, URL http://www.turbobygarrett.com/turbobygarrett/turbocharger#GT6041.

Gauger, N. R. (2008): Efficient Deterministic Approaches for Aerodynamic Shape Optimization. In: Thévenin, D. and Janiga, G. (Ed.) Optimization and computational fluid dynamics, Springer Verlag, Berlin. ISBN 978-3-540-72152-9.

Gerada, D.; Mebarki, A.; Brown, N. L.; Gerada, C.; Cavagnino, A. and Boglietti, A. (2014): High-Speed Electrical Machines: Technologies, Trends, and Developments. In: IEEE Transactions on Industrial Electronics, volume 61(6):p. 2946–2959. ISSN 0278-0046, 1557-9948. doi:10.1109/TIE.2013.2286777. URL http://ieeexplore.ieee.org/lpdocs/epic03/wrapper.htm?arnumber=6644302.

Giannakoglou, K.; Papadimitriou, D. and Zymaris (2010): The continuous adjoint method for first- and second-order sensitivities in aerodynamic shape optimization.

In: Periaux, J. and Verstraete, T. (Ed.) Introduction to optimization and multidisciplinary design in aeronautics and turbomachinery: May 31-June 4, 2010, Von Karman Institute for Fluid Dynamics, Rhode Saint Genèse, Belgium. ISBN 978-2-87516-009-6.

Govardhan, M.; Krishna Kumar, O. and Sitraram, N. (2007): Computational study of the effect of sweep on the performance and flow field in an axial flow compressor rotor. In: Proceedings of the Institution of Mechanica Engineers.

Grote, K.-H.; Feldhusen, J. and Dubbel, H. (Ed.) (2014): Taschenbuch für den Maschinenbau. Springer Vieweg, Berlin, 24. edition. ISBN 978-3-642-38890-3 978-3-642-38891-0.

Hazby, H.; Casey, M.; Numakura, R. and Tamaki, H. (2014): Design and testing of a high flow coefficient mixed flow impeller. London, IMechE C. ISBN 978-0-08-100034-2.

Hazby, H.; Casey, M.; Numakura, R. and Tamaki, H. (2015): A transonic mixed flow compressor for an extreme duty. In: Journal of Turbomachinery, volume 137(5):p. 051010. URL http://electrochemical.asmedigitalcollection.asme.org/article.aspx?articleid=1915029.

Herrmann, S. (2013): Auslegung und Simulation eines Ansaugkanals zur Grenzschichtabsaugung am Tragflügel. Bachelorarbeit, Institut für Turbomaschinen und Fluid Dynamik, Universität Hannover, Germany.

Jin, R.; Chen, W. and Simpson, T. W. (2001): Comparative studies of metamodelling techniques under multiple modelling criteria. In: Structural and Multidisciplinary Optimization, volume 23(1):p. 1–13. URL http://link.springer.com/article/10.1007/s00158-001-0160-4.

Joly, M. M.; Verstraete, T. and Paniagua, G. (2014): Integrated multifidelity, multidisciplinary evolutionary design optimization of counterrotating compressors. In: Integrated Computer-Aided Engineering, volume 21(3):p. 249–261. URL http://content.iospress.com/articles/integrated-computer-aided-engineering/ica00463.

Kerrebrock, J. L. (1981): Flow in Transonic Compressors. In: AIAA Journal, volume 19(1):p. 4–19. ISSN 0001-1452, 1533-385X. doi:10.2514/3.50919. URL http://arc.aiaa.org/doi/abs/10.2514/3.50919.

Koch, C. C. and Smith, L. H. (1976): Loss sources and magnitudes in axial-flow compressors. In: Journal of Engineering for Power, volume 98(3):p. 411–424. URL http://gasturbinespower.asmedigitalcollection.asme.org/article.aspx?articleid=1419169.

Lieblein, S. (1960): Incidence and Deviation-Angle Correlations for Compressor Cascades. In: Journal of Basic Engineering, volume 82(3):p. 575. ISSN 00219223. doi:10.1115/1.3662666. URL http://FluidsEngineering.asmedigitalcollection.asme.org/article.aspx?articleid=1430601.

Lieblein, S. and Johnsen, I. A. (1961): Résumé of Transonic-Compressor Research at NACA Lewis Laboratory. In: Journal of Engineering for Power, volume 83(3):p. 219. ISSN 00220825. doi:10.1115/1.3673177. URL http://GasTurbinesPower.asmedigitalcollection.asme.org/article.aspx?articleid=1416064.

Lieblein, S.; Schwenk, F. C. and Broderick, R. L. (1953): Diffusion factor for estimating losses and limiting blade loadings in axial-flow-compressor blade elements. technical report, DTIC Document. URL http://oai.dtic.mil/oai/oai?verb=getRecord&metadataPrefix=html&identifier=AD0011178.

Menter, F. R.; Langtry, R. B.; Likki, S. R.; Suzen, Y. B.; Huang, P. G. and Völker, S. (2006): A Correlation-Based Transition Model Using Local Variables—Part I: Model Formulation. In: Journal of Turbomachinery, volume 128(3):p. 413. ISSN 0889504X. doi:10.1115/1.2184352. URL http://Turbomachinery.asmedigitalcollection.asme.org/article.aspx?articleid=1467239.

Müller, G.; Vogt, K.; Ponick, B. and Müller, G. (2011): Berechnung elektrischer Maschinen. Number 2 in Elektrische Maschinen. Wiley-VCH, Weinheim, 6. edition. ISBN 978-3-527-40525-1.

Montgomery, D. C. (2013): Design and analysis of experiments. Wiley, Singapore, 8. edition. ISBN 978-1-118-09793-9.

Mårtensson, H.; Burman, J. and Johansson, U. (2007): Design of the High Pressure Ratio Transonic 1-1/2 Stage Fan Demonstrator Hulda. In: ASME Turbo Expo 2007: Power for Land, Sea, and Air. American Society of Mechanical Engineers, p. 331–340. URL http://proceedings.asmedigitalcollection.asme.org/proceeding.aspx?articleid=1602762.

Mårtensson, H.; Edin, N. and Johansson, T. (2013): Performance Test and Analysis of the Highly Loaded 1 1/2 Stage Transonic Test Compressor HULDA. In: Air Breathing Engines. IInternational Symposium. (ISABE-2013-1127).

NUMECA-International (2016): AutoGrid v10.2. Chaussée de la Hulpe, 189, Terhulpsesteenweg (B-1170 Brussels, BELGIUM).

Osborne, C.; Runstadler Jr, P. W. and Stacy, W. D. (1974): Aerodynamic and mechanical design of an 8:1 pressure ratio centrifugal compressor. In: . URL http://ntrs.nasa.gov/search.jsp?R=19750017116.

Radespiel, R. (2015): SFB 880 - Fundamentals of high-lift for future commercial aircraft: biennial report. Number 2015,04 in Forschungsbericht / Technische Universität Braunschweig, Campus Forschungsflughafen. Techn. Univ, Braunschweig. ISBN 978-3-928628-67-9. URL https://sfb880.tu-braunschweig.de/classtree/filebrowser_sfb880/filebrowserpanel.php?action=download-file&path=%2FServer%2FSFB880%2FZweijahresbericht%2FBiennial_Report_2015.pdf.

Radespiel, R. and Heinze, W. (2014): SFB 880: fundamentals of high lift for future commercial aircraft. In: CEAS Aeronautical Journal, volume 5(3):p. 239–251. ISSN 1869-5582, 1869-5590. doi:10.1007/s13272-014-0103-6. URL http://link.springer.com/10.1007/s13272-014-0103-6.

Rechenberg, I. (1973): Evolutionsstrategie; Optimierung technischer Systeme nach Prinzipien der biologischen Evolution. Problemata, 15. Frommann-Holzboog, Stuttgart-Bad Cannstatt. ISBN 978-3-7728-0373-4.

Reid, L. and Moore, R. D. (1978): Design and overall performance of four highly loaded, high speed inlet stages for an advanced high-pressure-ratio core compressor. Technical Report NASA-TP-1337, NASA Lewis Research Center; Cleveland, OH, United States. URL http://ntrs.nasa.gov/search.jsp?R=19780025165.

Schlichting, H. and Gersten, K. (2006): Grenzschicht-theorie. Springer, Berlin, Heidelberg. New York, 10. edition. ISBN 978-3-540-23004-5.

Smith, L. H. (1958): Recovery Ratio - A Measure of the Loss Recovery Potential of Compressor Stages. In: ASME Transactions, (80):p. 517–524.

Storn, R. and Price, K. (1997): Differential evolution–a simple and efficient heuristic for global optimization over continuous spaces. In: Journal of global optimization, volume 11(4):p. 341–359. URL http://link.springer.com/article/10.1023/A:1008202821328.

Teichel, S.; Verstraete, T. and Seume, J. (2013): Optimized preliminary design of compact axial compressors: A comparison of two design tools. American Institute of Aeronautics and Astronautics. doi:10.2514/6.2013-2651. URL http://arc.aiaa.org/doi/abs/10.2514/6.2013-2651.

Teichel, S. H.; Dörbaum, M.; Misir, O.; Merkert, A.; Mertens, A.; Seume, J. R. and Ponick, B. (2015a): Design considerations for the components of electrically powered active high-lift systems in civil aircraft. In: CEAS Aeronautical Journal, volume 6(1):p. 49–67. ISSN 1869-5582, 1869-5590. doi:10.1007/s13272-014-0124-1. URL http://link.springer.com/10.1007/s13272-014-0124-1.

Teichel, S. H.; Verstraete, T. and Seume, J. (2015b): Optimized Multidisciplinary Design of a Small Transonic Compressor for Active High-Lift Systems. In: Proceedings of International Gas Turbine Congress 2015 Tokyo. Tokyo. ISBN 978-4-89111-008-6.

Traupel, W. (2001): Thermische Turbomaschinen - Band 1, volume 1. Springer Berlin Heidelberg, Berlin, Heidelberg. ISBN 978-3-642-62102-4 978-3-642-17469-8. URL http://link.springer.com/10.1007/978-3-642-17469-8.

van Millingen, R. D. and van Millingen, J. D. (1991): Phase shift torquemeters for gas turbine development and monitoring. In: ASME 1991 International

Gas Turbine and Aeroengine Congress and Exposition. American Society of Mechanical Engineers, p. V005T15A003–V005T15A003. URL http://proceedings.asmedigitalcollection.asme.org/proceeding.aspx?articleid=2197162.

Veres, J. P. (2009): Axial and Centrifugal Compressor Mean Line Flow Analysis Method. technical report. URL https://ntrs.nasa.gov/search.jsp?R=20090042768.

Verstraete, T. (2010a): CADO: a Computer Aided Design and Optimization Tool for Turbomachinery Applications. Lisbon, Portugal.

Verstraete, T. (2010b): Introduction to Optimization and Multidisciplinary Design. In: Periaux, J. and Verstraete, T. (Ed.) Introduction to optimization and multidisciplinary design in aeronautics and turbomachinery: May 31-June 4, 2010, Von Karman Institute for Fluid Dynamics, Rhode Saint Genèse, Belgium. ISBN 978-2-87516-009-6.

Verstraete, T. (2010c): Multidisciplinary Optimization of Turbomachinery Components using Differential Evolution. In: Periaux, J. and Verstraete, T. (Ed.) Introduction to optimization and multidisciplinary design in aeronautics and turbomachinery: May 31-June 4, 2010, Von Karman Institute for Fluid Dynamics, Rhode Saint Genèse, Belgium. ISBN 978-2-87516-009-6.

Wadia, A. R.; Szucs, P. N. and Crall, D. W. (1998): Inner Workings of Aerodynamic Sweep. In: Journal of Turbomachinery, volume 120(4):p. 671. ISSN 0889504X. doi:10.1115/1.2841776. URL http://Turbomachinery.asmedigitalcollection.asme.org/article.aspx?articleid=1465464.

Weiss, T. and Heinze, W. (2015): Overall Design Assessment of CESTOL Aircraft. In: Forschungsbericht / Technische Universität Braunschweig, Campus Forschungsflughafen, p. 193–204. URL https://sfb880.tu-braunschweig.de/classtree/filebrowser_sfb880/filebrowserpanel.php?action=download-file&path=%2FServer%2FSFB880%2FZweijahresbericht%2FBiennial_Report_2015.pdf.

Wennerstrom, A. J. (2000): Design of highly loaded axial-flow fans and compressors. Concepts ETI, White River Junction, Vt. ISBN 978-0-933283-11-4.

Wilcox, D. C. (1988): Reassessment of the scale-determining equation for advanced turbulence models. In: AIAA Journal, volume 26(11):p. 1299–1310. ISSN 0001-1452, 1533-385X. doi:10.2514/3.10041. URL http://arc.aiaa.org/doi/10.2514/3.10041.

Wolpert, D. H. and Macready, W. G. (1997): No free lunch theorems for optimization. In: Evolutionary Computation, IEEE Transactions on, volume 1(1):p. 67–82. URL http://ieeexplore.ieee.org/xpls/abs_all.jsp?arnumber=585893.

Zitzler, E.; Deb, K. and Thiele, L. (2000): Comparison of Multiobjective Evolutionary Algorithms: Empirical Results. In: Evolutionary Computation, volume 8(2):p. 173–195. ISSN 1063-6560, 1530-9304. doi:10.1162/106365600568202. URL http://www.mitpressjournals.org/doi/abs/10.1162/106365600568202.

A Appendix

A.1 Dimensions of the Wingbox of the Compressor Systems

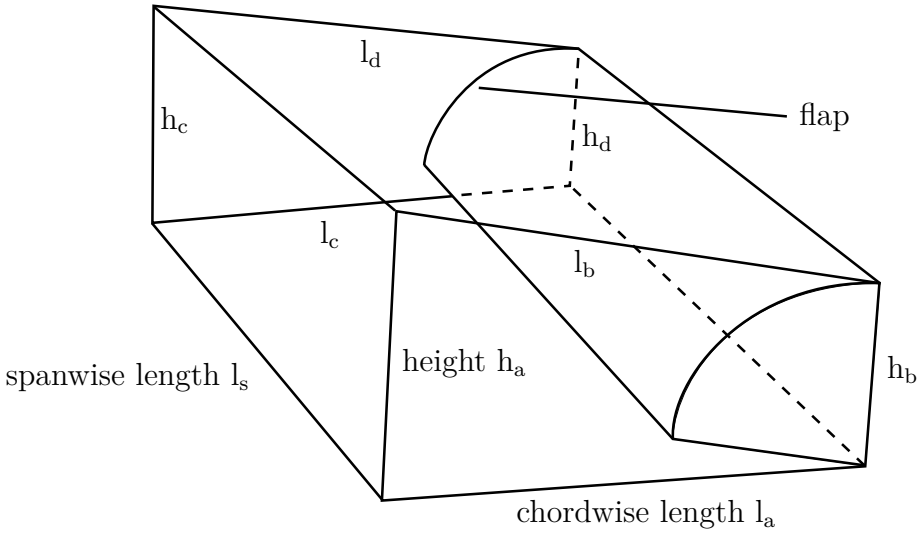

Figure A.1: Wingbox dimensions.

The c-d plane of each wingbox in Fig. A.1 is located on the outer side of the wing, closer to the aileron while the plane a-b is located on the inner side of the wing towards the fuselage

Table A.1: Wing box dimensions in mm.

comp	l_s	h_a	h_b	h_c	h_d	l_a	l_b	l_c	l_d
1	2067	500	335	470	300	620	630	570	570
2	2067	470	300	400	255	570	570	525	525
3	2067	400	255	335	215	525	525	465	475
4	2067	335	215	280	180	465	475	420	430
5	2067	280	180	220	140	420	430	360	370
6	2067	220	140	165	100	360	370	315	320

A.2 Required Compressor Operating Points

Tables A.2 through A.8 summarize the required operating points of the different compressor systems of the AHLS. The notation of the compressors is referenced in Fig. 2.1 where compressor 1 is located in the flap closest to the fuselage and compressor 6 is located closest to the aileron. The operating points of each compressor are each summarized in one separate table except for compressor 6. This compressor does not only need to provide suction and jet momentum for lift generation (Tab. A.7) but also needs to be able to provide additional airflow and momentum to support aircraft maneuver (Tab. A.8). The given compressor inlet conditions consider the heat input of the power electronics and the electric motor upstream of the compressor, assuming 85% polytropic compressor efficiency, 90% motor efficiency and 95% efficiency of the power electronics. These requirements are used in design process presented in this work. The corresponding operating points of the compressors concerning mass flow rate and total pressure ratio are illustrated in Figs. A.2 through A.5. The actual duty lines of each compressor are shown in Fig. 2.7 using total pressure ratio and corrected mass flow rate.

Table A.2: Required operating points of compressor 1

operating point of the AHLS			compressor parameters			
flight attitude	altitude in m a.s.l.	ambient temp. in K	total inlet temp. in K	total inlet pressure in Pa	total pressure ratio	mass flow rate in kg/s
take-off	0	233.15	242	88100	1.65	1.54
		288.15	299	88100	1.65	1.38
		323.15	335	88100	1.65	1.31
	1500	233.15	233	70700	1.76	1.39
		288.15	290	73800	1.73	1.28
		323.15	326	75200	1.72	1.22
approach	0	233.15	242	88100	1.65	1.53
		288.15	299	88100	1.65	1.38
		323.15	335	88100	1.65	1.30
	1500	233.15	233	70700	1.75	1.39
		288.15	290	73800	1.73	1.27
		323.15	326	75200	1.72	1.21
landing	0	233.15	242	87800	1.73	1.64
		288.15	299	87800	1.73	1.47
		323.15	336	87800	1.73	1.39
	1500	233.15	234	70300	1.86	1.48
		288.15	291	73400	1.83	1.36
		323.15	327	74900	1.82	1.29

Table A.3: Required operating points of compressor 2

operating point of the AHLS			compressor parameters			
flight attitude	altitude in m a.s.l.	ambient temp. in K	total inlet temp. in K	total inlet pressure in Pa	total pressure ratio	mass flow rate in kg/s
take-off	0	233.15	242	88100	1.65	1.37
		288.15	299	88100	1.65	1.24
		323.15	242	88100	1.65	1.17
	1500	233.15	233	70700	1.76	1.24
		288.15	290	73800	1.73	1.14
		323.15	326	75200	1.72	1.09
approach	0	233.15	242	88100	1.65	1.37
		288.15	299	88100	1.65	1.23
		323.15	335	88100	1.65	1.16
	1500	233.15	233	70700	1.75	1.24
		288.15	290	73800	1.73	1.14
		323.15	326	75200	1.72	1.08
landing	0	233.15	242	87800	1.73	1.47
		288.15	299	87800	1.73	1.32
		323.15	336	87800	1.73	1.25
	1500	233.15	234	70300	1.86	1.32
		288.15	291	73400	1.83	1.22
		323.15	327	74900	1.82	1.16

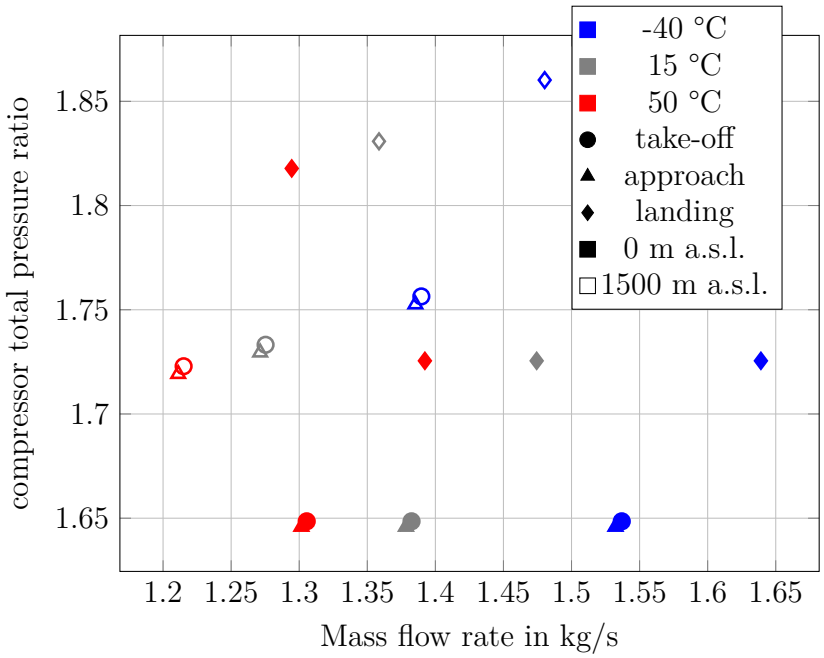

(a) Required operating points of compressor 1.

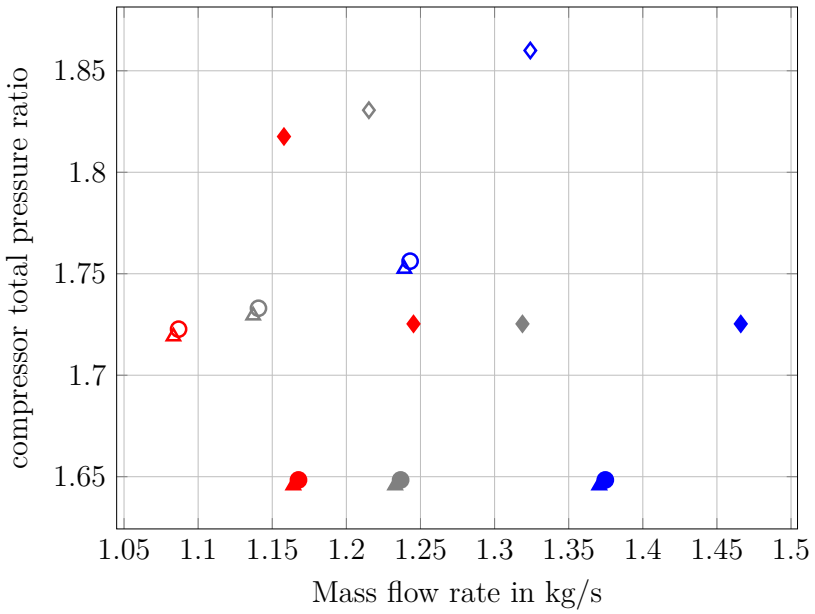

(b) Required operating points of compressor 2.

Figure A.2: Required operating points of compressor 1 and 2..

Table A.4: Required operating points of compressor 3

operating point of the AHLS			compressor parameters			
flight attitude	altitude in m a.s.l.	ambient temp. in K	total inlet temp. in K	total inlet pressure in Pa	total pressure ratio	mass flow rate in kg/s
take-off	0	233.15	242	88100	1.65	1.21
		288.15	299	88100	1.65	1.09
		323.15	335	88100	1.65	1.03
	1500	233.15	233	70700	1.76	1.10
		288.15	290	73800	1.73	1.01
		323.15	326	75200	1.72	0.96
approach	0	233.15	242	88100	1.65	1.21
		288.15	299	88100	1.65	1.09
		323.15	335	88100	1.65	1.03
	1500	233.15	233	70700	1.75	1.09
		288.15	290	73800	1.73	1.00
		323.15	326	75200	1.72	0.96
landing	0	233.15	242	87800	1.73	1.29
		288.15	299	87800	1.73	1.16
		323.15	336	87800	1.73	1.10
	1500	233.15	234	70300	1.86	1.17
		288.15	291	73400	1.83	1.07
		323.15	327	74900	1.82	1.02

Table A.5: Required operating points of compressor 4

operating point of the AHLS			compressor parameters			
flight attitude	altitude in m a.s.l.	ambient temp. in K	total inlet temp. in K	total inlet pressure in Pa	total pressure ratio	mass flow rate in kg/s
take-off	0	233.15	242	88100	1.65	1.05
		288.15	299	88100	1.65	0.94
		323.15	335	88100	1.65	0.89
	1500	233.15	233	70700	1.76	0.95
		288.15	290	73800	1.73	0.87
		323.15	326	75200	1.72	0.83
approach	0	233.15	290	73800	1.73	0.87
		288.15	299	88100	1.65	0.94
		323.15	242	88100	1.65	1.05
	1500	233.15	233	70700	1.75	0.95
		288.15	290	73800	1.73	0.87
		323.15	326	75200	1.72	0.83
landing	0	233.15	242	87800	1.72	1.12
		288.15	299	87800	1.72	1.01
		323.15	336	87800	1.72	0.95
	1500	233.15	234	70300	1.86	1.01
		288.15	291	73400	1.83	0.93
		323.15	327	74900	1.82	0.88

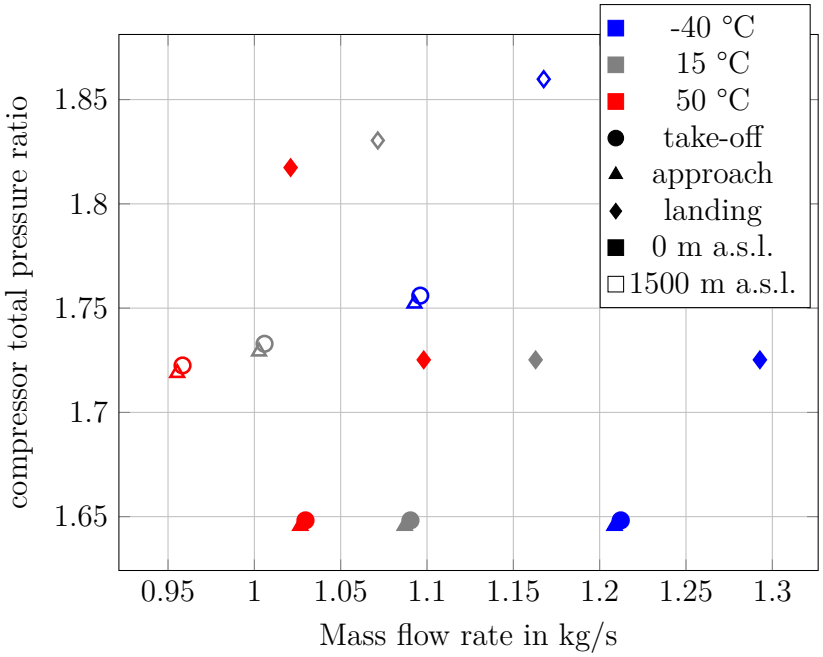

(a) Required operating points of compressor 3.

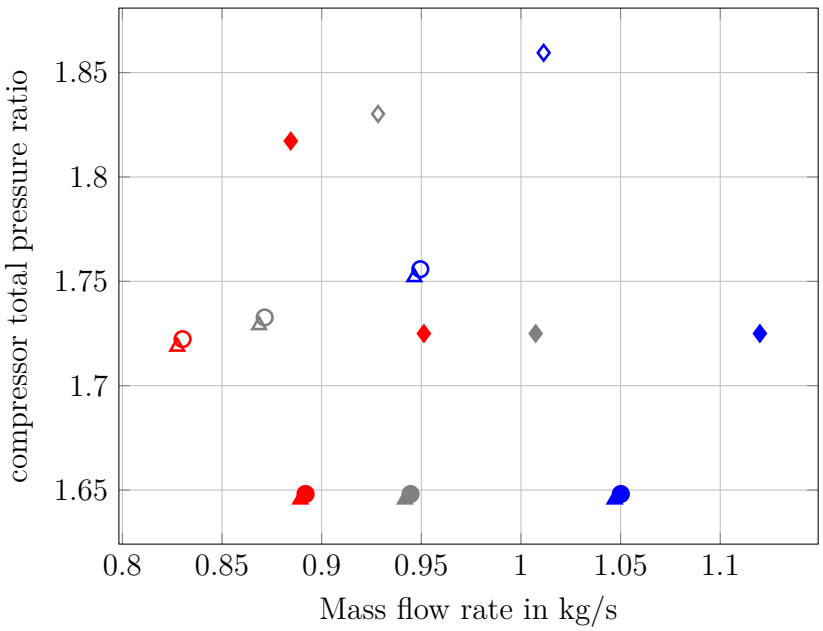

(b) Required operating points of compressor 4.

Figure A.3: Required operating points of compressor 3 and 4..

Table A.6: Required operating points of compressor 5

operating point of the AHLS			compressor parameters			
flight attitude	altitude in m a.s.l.	ambient temp. in K	total inlet temp. in K	total inlet pressure in Pa	total pressure ratio	mass flow rate in kg/s
take-off	0	233.15	242	88100	1.65	0.89
		288.15	299	88100	1.65	0.80
		323.15	335	88100	1.65	0.75
	1500	233.15	233	70700	1.76	0.80
		288.15	290	73800	1.73	0.74
		323.15	326	75200	1.72	0.70
approach	0	233.15	242	88100	1.65	0.89
		288.15	299	88100	1.65	0.80
		323.15	335	88100	1.65	0.75
	1500	233.15	233	70700	1.75	0.80
		288.15	290	73800	1.73	0.73
		323.15	326	75200	1.72	0.70
landing	0	233.15	242	87800	1.72	0.95
		288.15	299	87800	1.72	0.85
		323.15	336	87800	1.72	0.80
	1500	233.15	234	70300	1.86	0.86
		288.15	291	73400	1.83	0.79
		323.15	327	74900	1.82	0.75

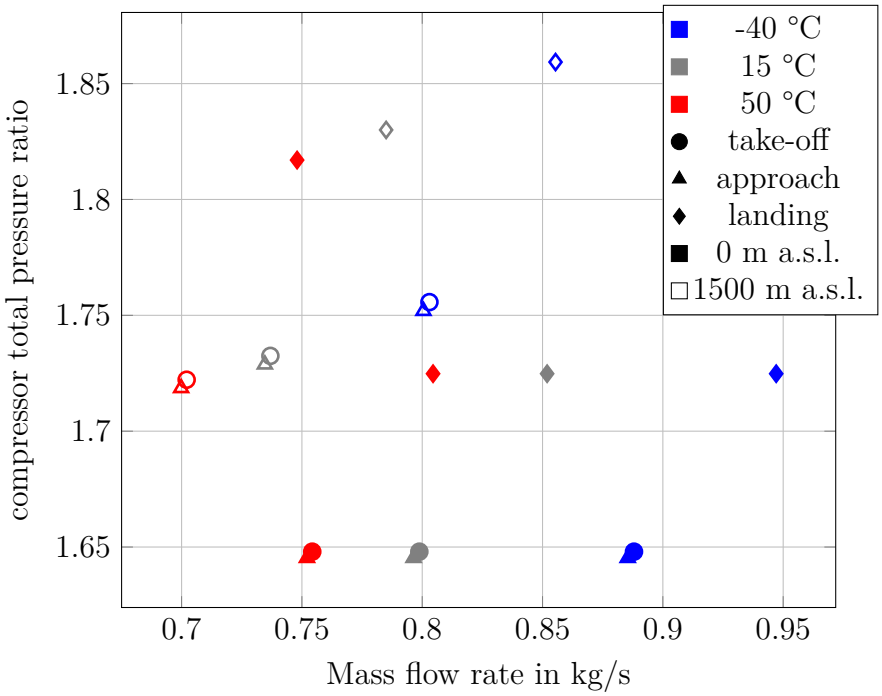

Figure A.4: Required operating points of compressor 5.

Table A.7: Required operating points of compressor 6 - lift generation

operating point of the AHLS			compressor parameters			
flight attitude	altitude in m a.s.l.	ambient temp. in K	total inlet temp. in K	total inlet pressure in Pa	total pressure ratio	mass flow rate in kg/s
take-off	0	233.15	242	88100	1.65	0.73
		288.15	299	88100	1.65	0.65
		323.15	335	88100	1.65	0.62
	1500	233.15	233	70700	1.76	0.66
		288.15	290	73800	1.73	0.60
		323.15	326	75200	1.72	0.57
approach	0	233.15	242	88100	1.65	0.72
		288.15	299	88100	1.65	0.65
		323.15	335	88100	1.65	0.61
	1500	233.15	233	70700	1.75	0.65
		288.15	290	73800	1.73	0.60
		323.15	326	75200	1.72	0.57
landing	0	233.15	241	87800	1.56	0.64
		288.15	297	87800	1.56	0.58
		323.15	333	87800	1.56	0.55
	1500	233.15	231	70300	1.63	0.58
		288.15	288	73400	1.62	0.53
		323.15	324	74900	1.61	0.51

Table A.8: Required operating points of compressor 6 - maneuver support

operating point of the AHLS			compressor parameters			
flight attitude	altitude in m a.s.l.	ambient temp. in K	total inlet temp. in K	total inlet pressure in Pa	total pressure ratio	mass flow rate in kg/s
take-off	0	233.15	246	88100	2.07	0.95
		288.15	304	88100	2.07	0.86
		323.15	341	88100	2.07	0.81
	1500	233.15	238	70700	2.34	0.85
		288.15	296	73800	2.28	0.79
		323.15	333	75200	2.25	0.75
approach	0	233.15	246	88100	2.06	0.95
		288.15	304	88100	2.06	0.85
		323.15	341	88100	2.06	0.81
	1500	233.15	238	70700	2.33	0.85
		288.15	296	73800	2.27	0.78
		323.15	333	75200	2.24	0.75
landing	0	233.15	244	87800	1.86	0.85
		288.15	301	87800	1.86	0.76
		323.15	338	87800	1.86	0.72
	1500	233.15	235	70300	2.04	0.77
		288.15	293	73400	2.00	0.70
		323.15	329	74900	1.98	0.67

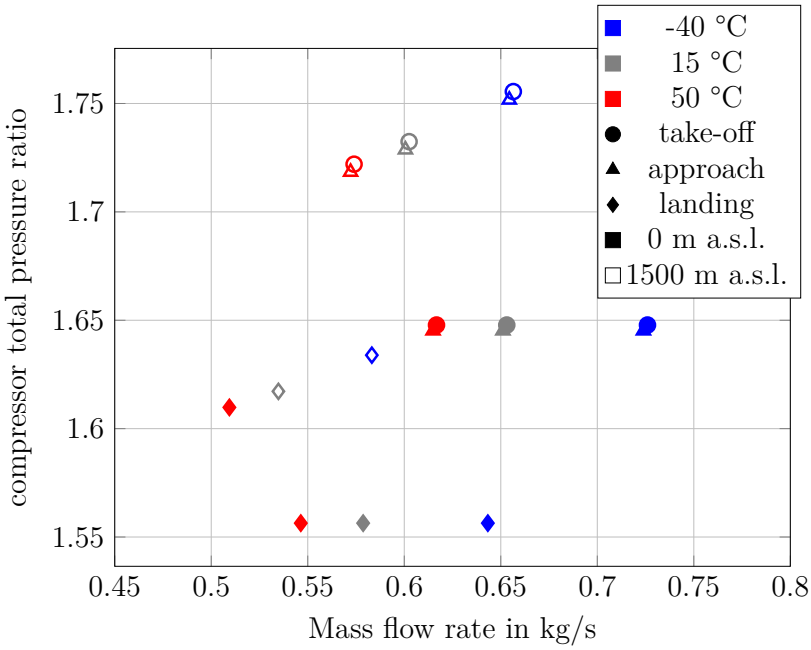

(a) Required operating points of compressor 6 during lift generation.

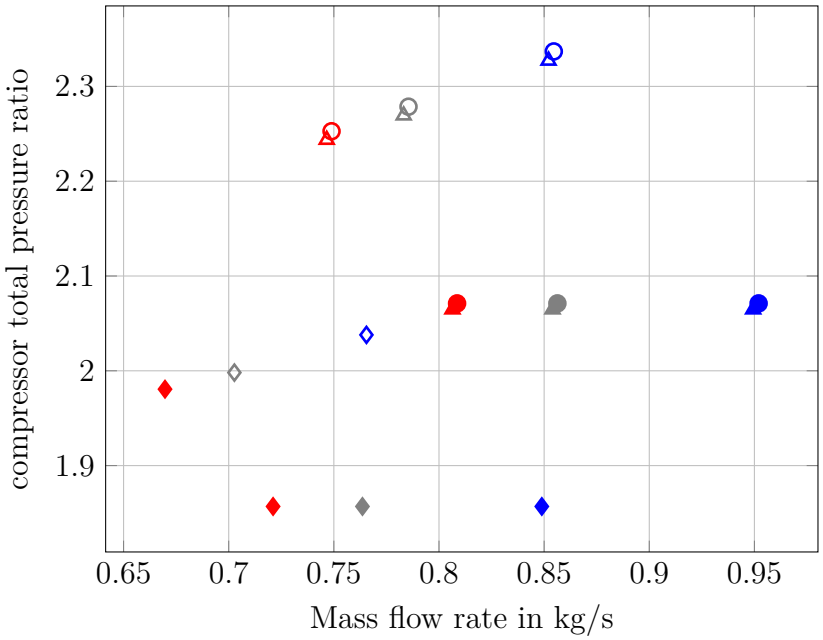

(b) Required operating points of compressor 6 during maneuver support

Figure A.5: Required operating points of compressor 6 during lift generation and maneuver support.

A.3 Grid Convergence Study

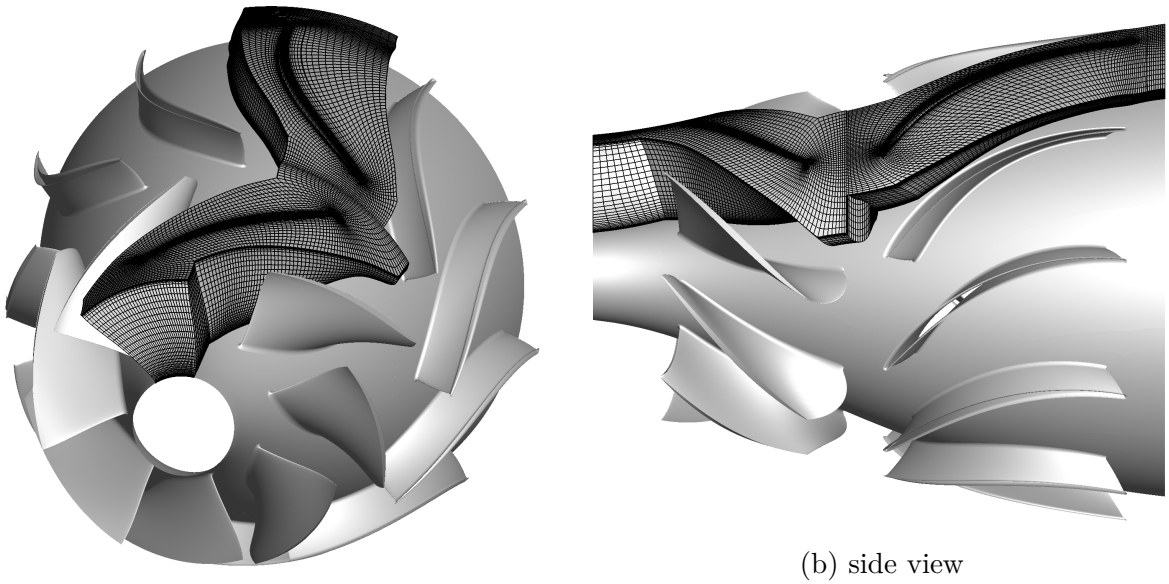

(a) front view

(b) side view

Figure A.6: Exemplary illustration of grid used for the simulation of the FAST compressor.

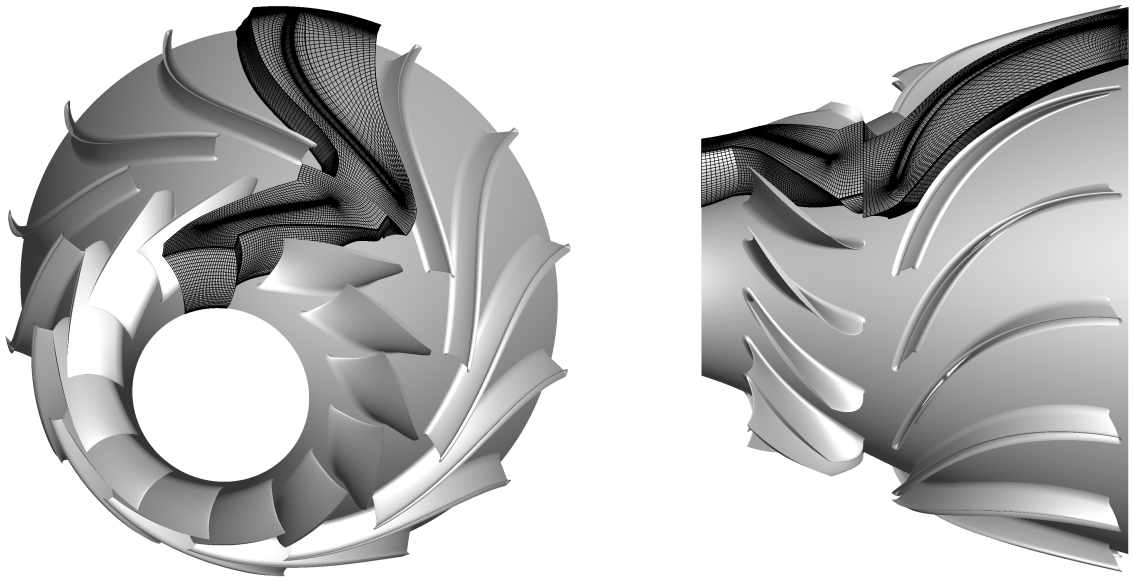

(a) front view

(b) side view

Figure A.7: Exemplary illustration of grid used for the simulation of the MEAN compressor.

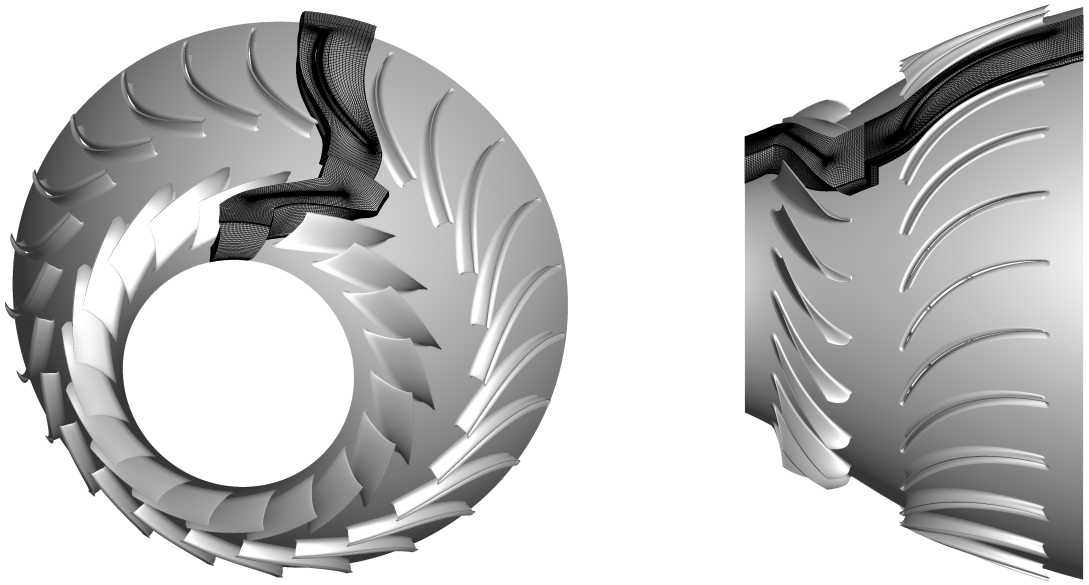

(a) front view (b) side view

Figure A.8: Exemplary illustration of grid used for the simulation of the SLOW compressor.

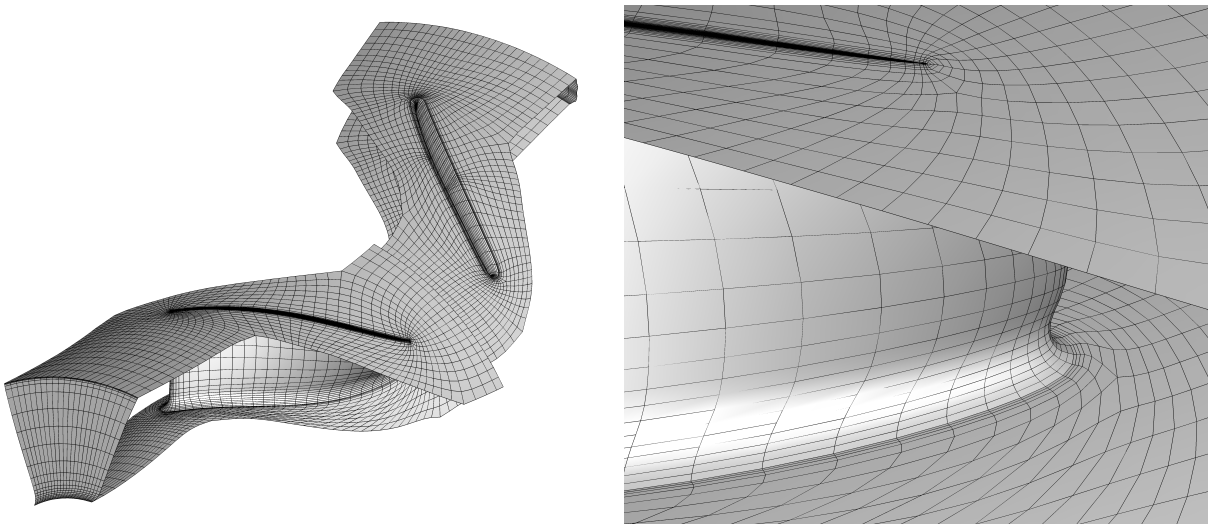

(a) passage grid (b) trailing edge region

Figure A.9: Coarse GCI wall functions grid: 80,936 elements; $y^+_{\text{mean}} = 34.5$; $y^+_{\text{max}} = 94.0$

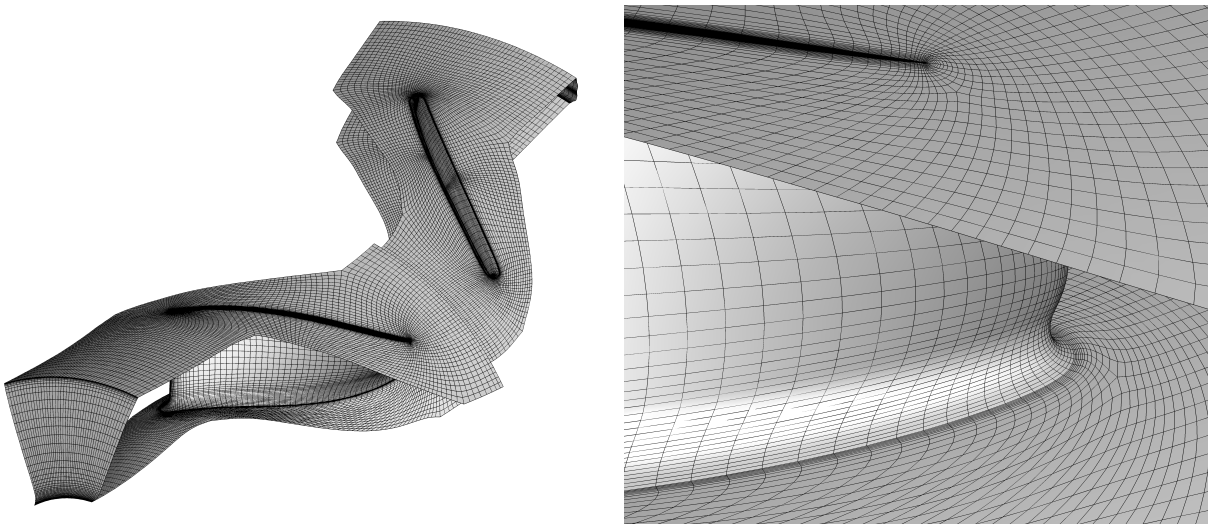

(a) passage grid (b) trailing edge region

Figure A.10: Medium GCI wall functions grid: 647,488 elements; $y^+_{\text{mean}} = 18.8$; $y^+_{\text{max}} = 48.8$

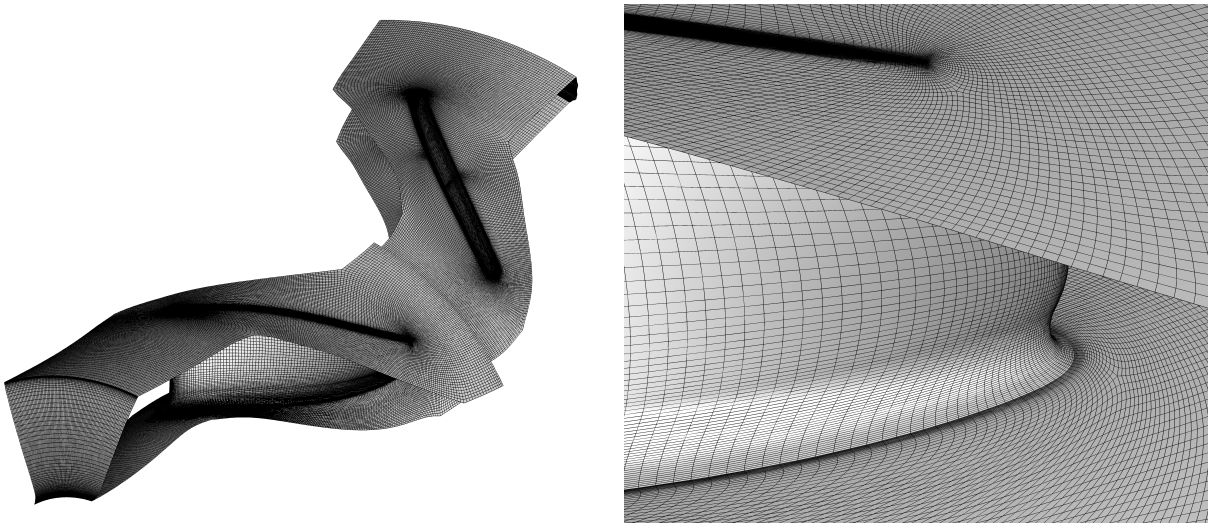

(a) passage grid (b) trailing edge region

Figure A.11: Fine GCI wall functions grid: 5,179,904 elements; $y^+_{\text{mean}} = 10.7$; $y^+_{\text{max}} = 27.8$

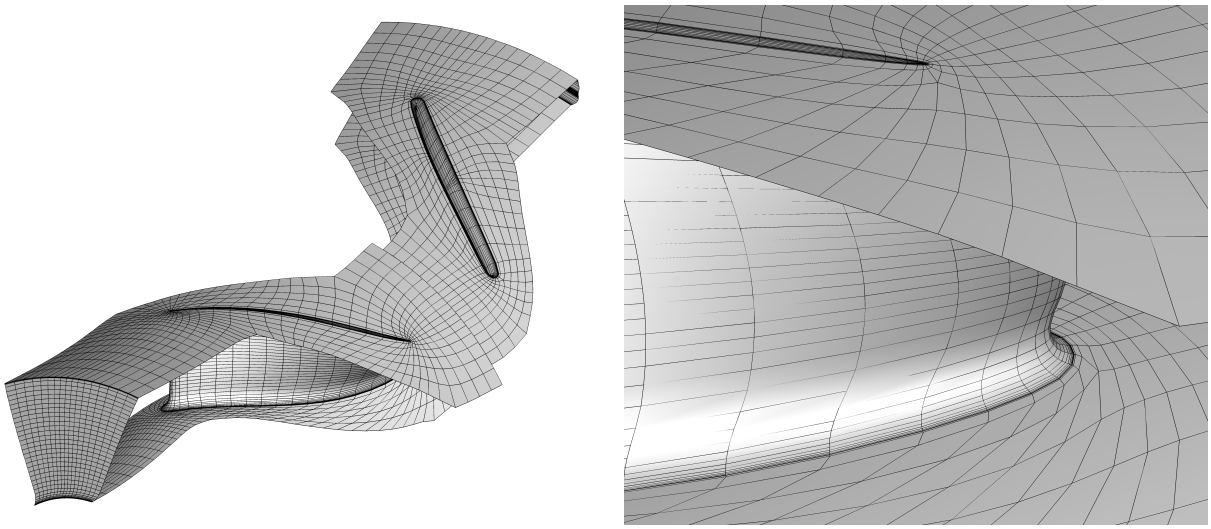

(a) passage grid (b) trailing edge region

Figure A.12: Coarse GCI low Reynolds grid: 74,448 elements; $y^+_{\text{mean}} = 3.9$; $y^+_{\text{max}} = 11.9$

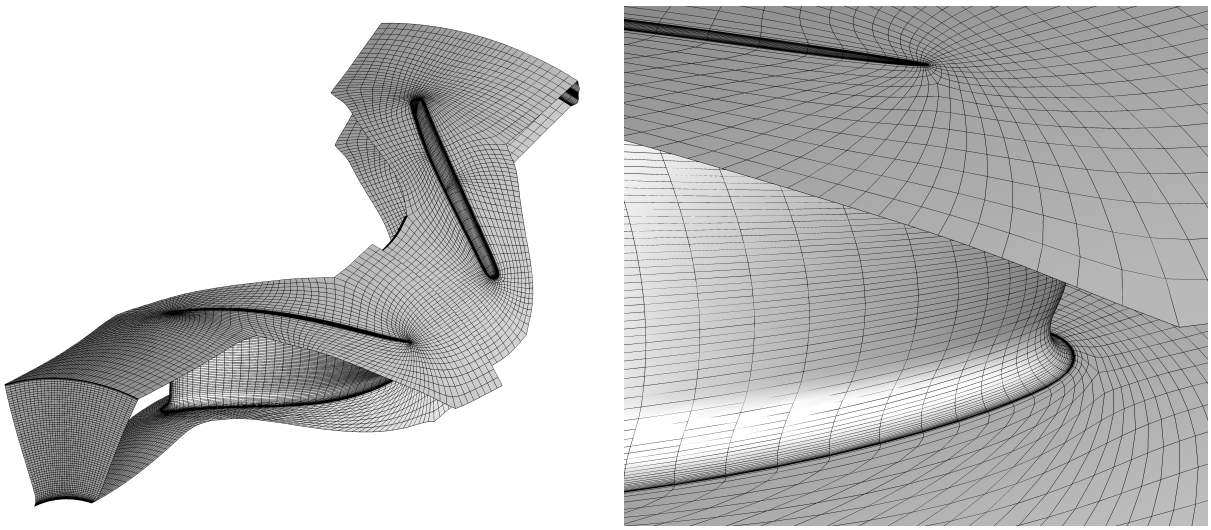

(a) passage grid (b) trailing edge region

Figure A.13: Medium GCI low Reynolds grid: 595,584 elements; $y^+_{\text{mean}} = 1.5$; $y^+_{\text{max}} = 6.4$

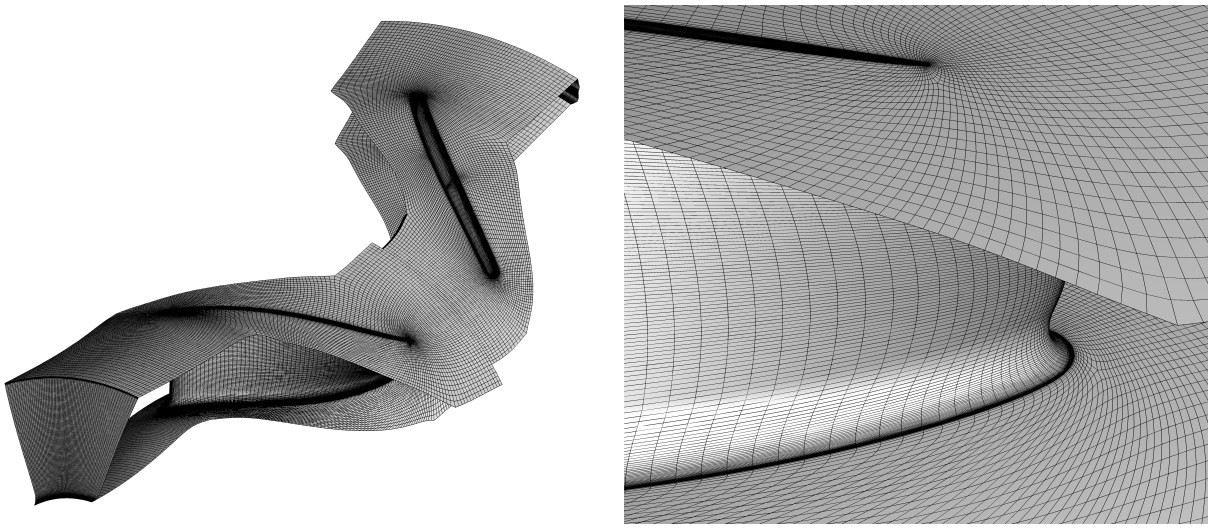

(a) passage grid (b) trailing edge region

Figure A.14: Fine GCI low Reynolds grid: 4,764,672 elements; $y^+_{\text{mean}} = 0.7$; $y^+_{\text{max}} = 4.0$

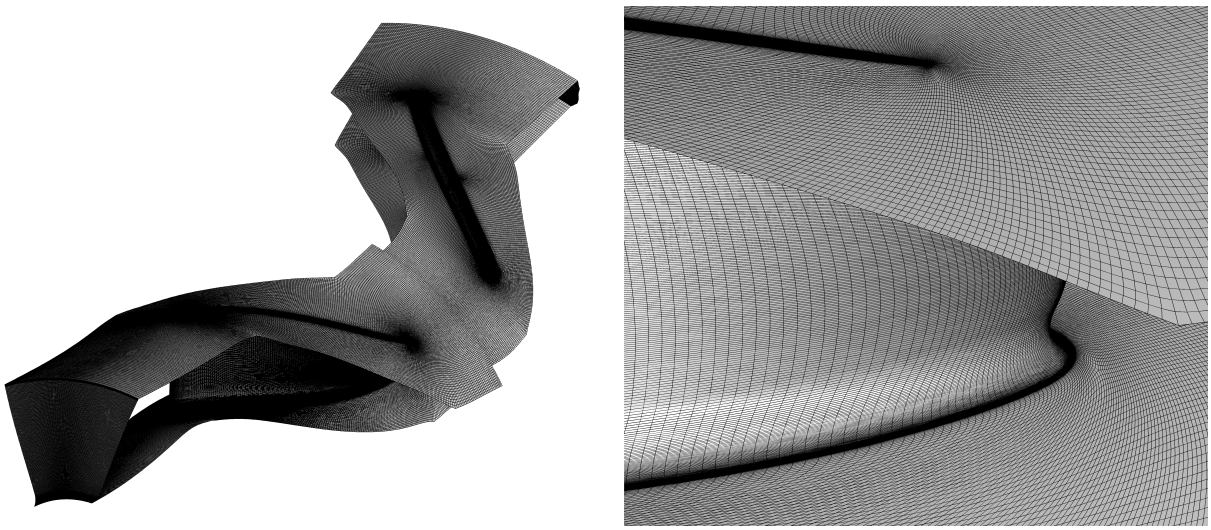

(a) passage grid (b) trailing edge region

Figure A.15: Very fine GCI low Reynolds grid: 38,117,376 elements; $y^+_{\text{mean}} = 0.35$; $y^+_{\text{max}} = 2.7$

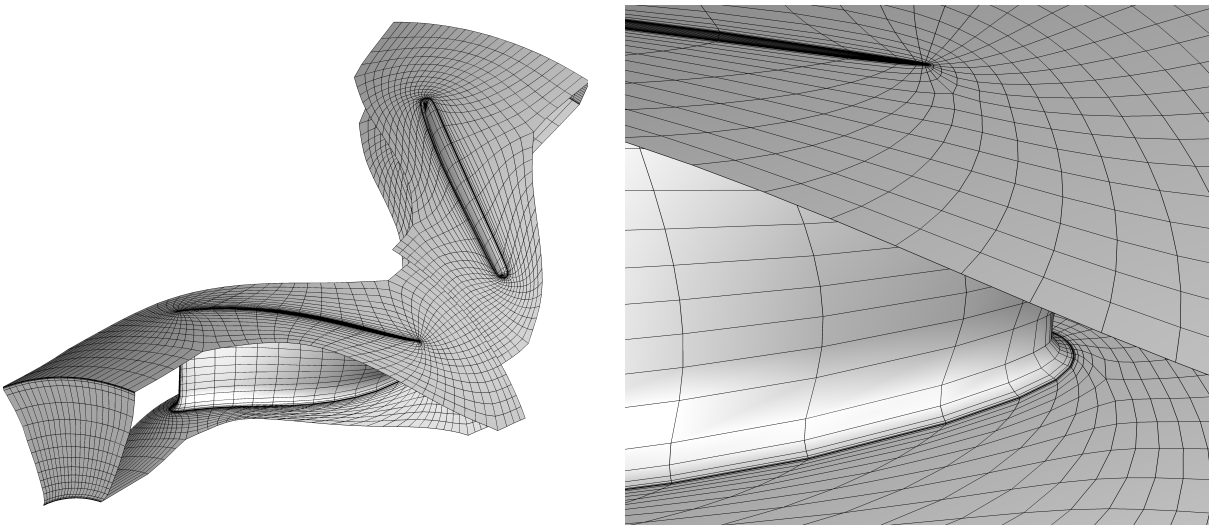

(a) passage grid (b) trailing edge region

Figure A.16: Coarse low Reynolds grid: 76,032 elements; $y^+_{\text{mean}} = 0.66$; $y^+_{\text{max}} = 3.69$

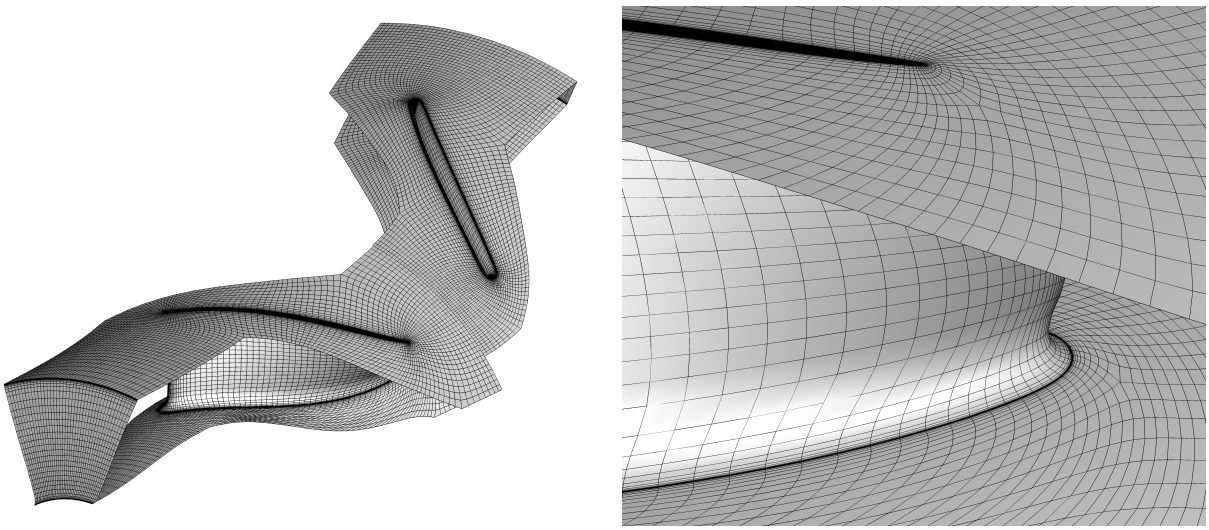

(a) passage grid (b) trailing edge region

Figure A.17: Medium low Reynolds grid: 573,440 elements; $y^+_{\text{mean}} = 0.67$; $y^+_{\text{max}} = 3.74$

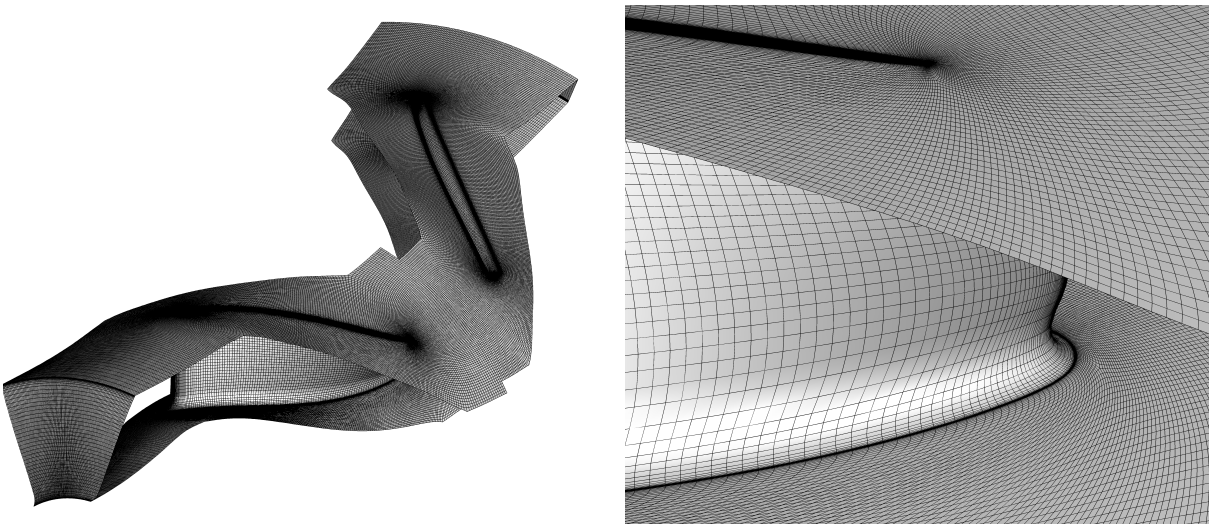

(a) passage grid (b) trailing edge region

Figure A.18: Fine low Reynolds grid: 5,035,712 elements; $y^+_{\text{mean}} = 0.68$; $y^+_{\text{max}} = 3.96$

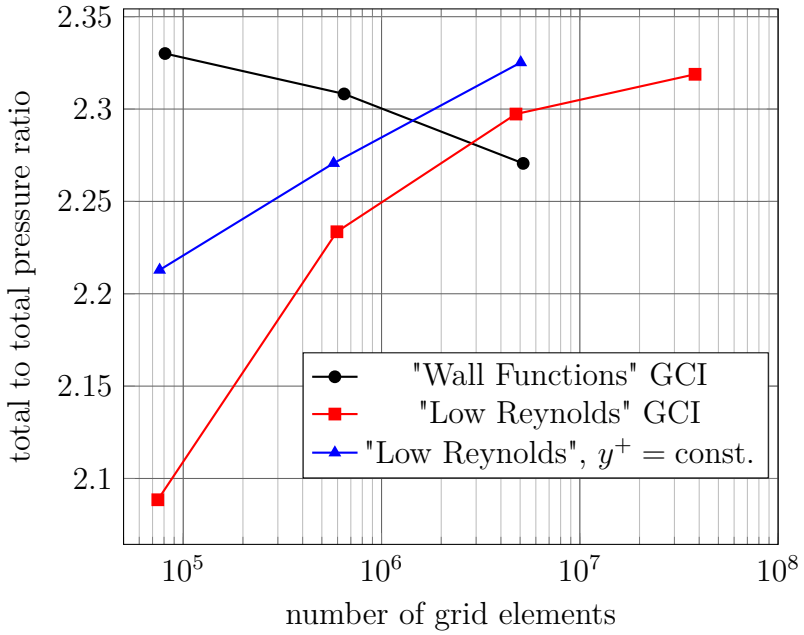

Figure A.19: Grid sensitivity of reference compressor from Teichel et al. (2015b).

Table A.9: Results of the GCI study

	wall functions		low reynolds	
variable	values for $\eta_{poly,tt}$	values for Π_{tt}	values for $\eta_{poly,tt}$	values for Π_{tt}
N_4	-		74448	
N_3	80.936		595,584	
N_2	647,488		4,764,672	
N_1	5,179,904		38,117,376	
r_{43}	-		2	
r_{32}	2		2	
r_{21}	2		2	
$f_{c,1}$	87.3637	2.2706	88.4408	2.3188
$f_{c,2}$	88.5892	2.3082	87.5461	2.2973
$f_{c,3}$	88.8444	2.3301	85.1709	2.336
$f_{c,4}$	-		79.7755	2.0885
p	-1.5092	-0.5213	1.4086	1.5666
f_e	88.9115	2.3605	88.9814	2.3298
F_S	1.25		1.25	
GCI_1	-0.0221	-0.0495	0.0076	0.0059
GCI_2	-0.0045	-0.0283	0.0205	0.0177
GCI_3	-0.001e-04	-0.0165	0.0544	0.0524
GCI_4	-		0.1444	0.1551
$GCI_2/GCI_{1r_{2r}p}$	0.9862	0.9837	1.0102	1.0094
$EREE_1$	0.0174	0.0381	0.0061	0.0047
$EREE_2$	0.0036	0.0221	0.0161	0.0139
$EREE_3$	0.0008	0.0129	0.0428	0.0413
$EREE_4$	-		0.1035	0.1036
$f_{e,p=1}$	86.6935	2.2500	89.3354	2.3403
$GCI_{1,p=1}$	0.0096	0.0113	0.0126	0.0116
$GCI_{2,p=1}$	0.0020	0.0065	0.0339	0.0347
$GCI_{3,p=1}$	0.0056	0.0183	0.0678	0.0694
$GCI_{4,p=1}$	-		0.1357	0.1387
$EREE_{1,p=1}$	0.0077	0.0091	0.01	0.0092
$EREE_{2,p=1}$	0.0219	0.0259	0.02	0.0184
$EREE_{3,p=1}$	0.0248	0.0356	0.0466	0.0456
$EREE_{4,p=1}$	-		0.1070	0.1076

A.4 Optimization Results Rotor

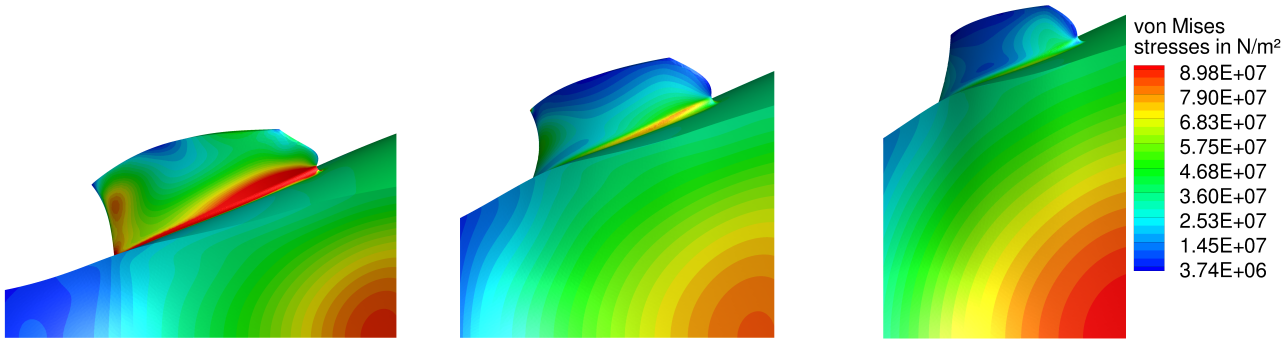

(a) FAST (b) MEAN (c) SLOW

Figure A.20: suction side view of von Mises stress of the rotor designs.

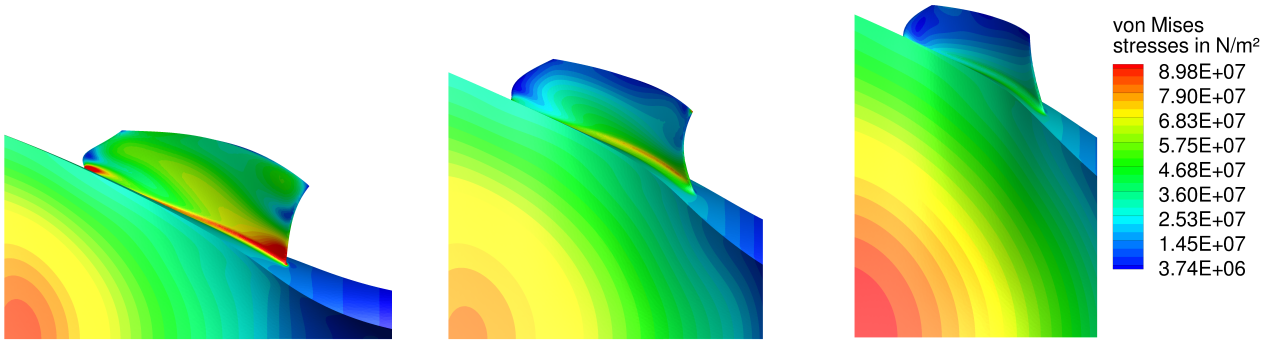

(a) FAST (b) MEAN (c) SLOW

Figure A.21: pressure side view of von Mises stress of the rotor designs.

A.5 Optimization Results Stage

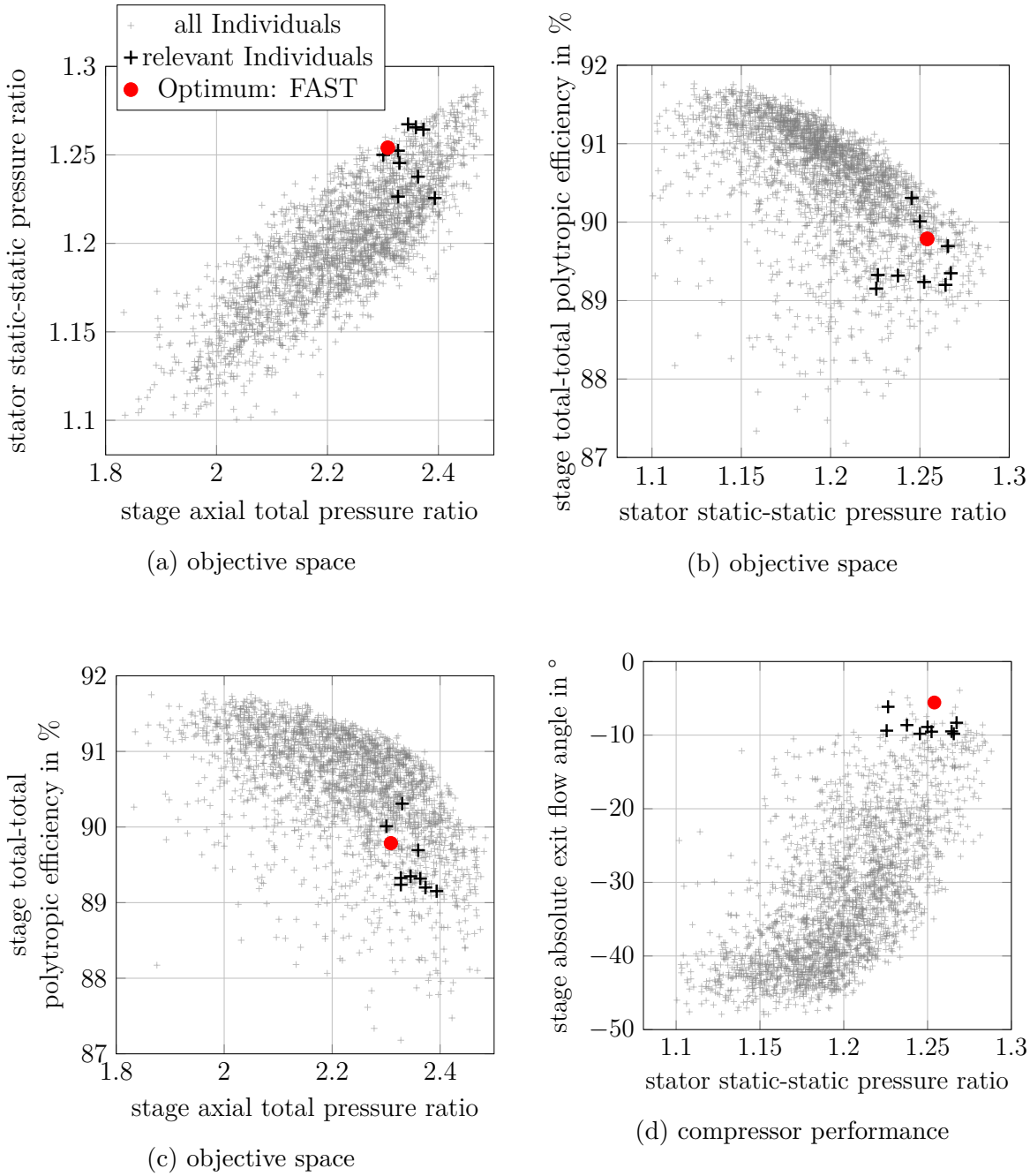

(a) objective space

(b) objective space

(c) objective space

(d) compressor performance

Figure A.22: Results of the stage optimization with FAST rotor: Objective space and compressor performance of all relevant individuals.

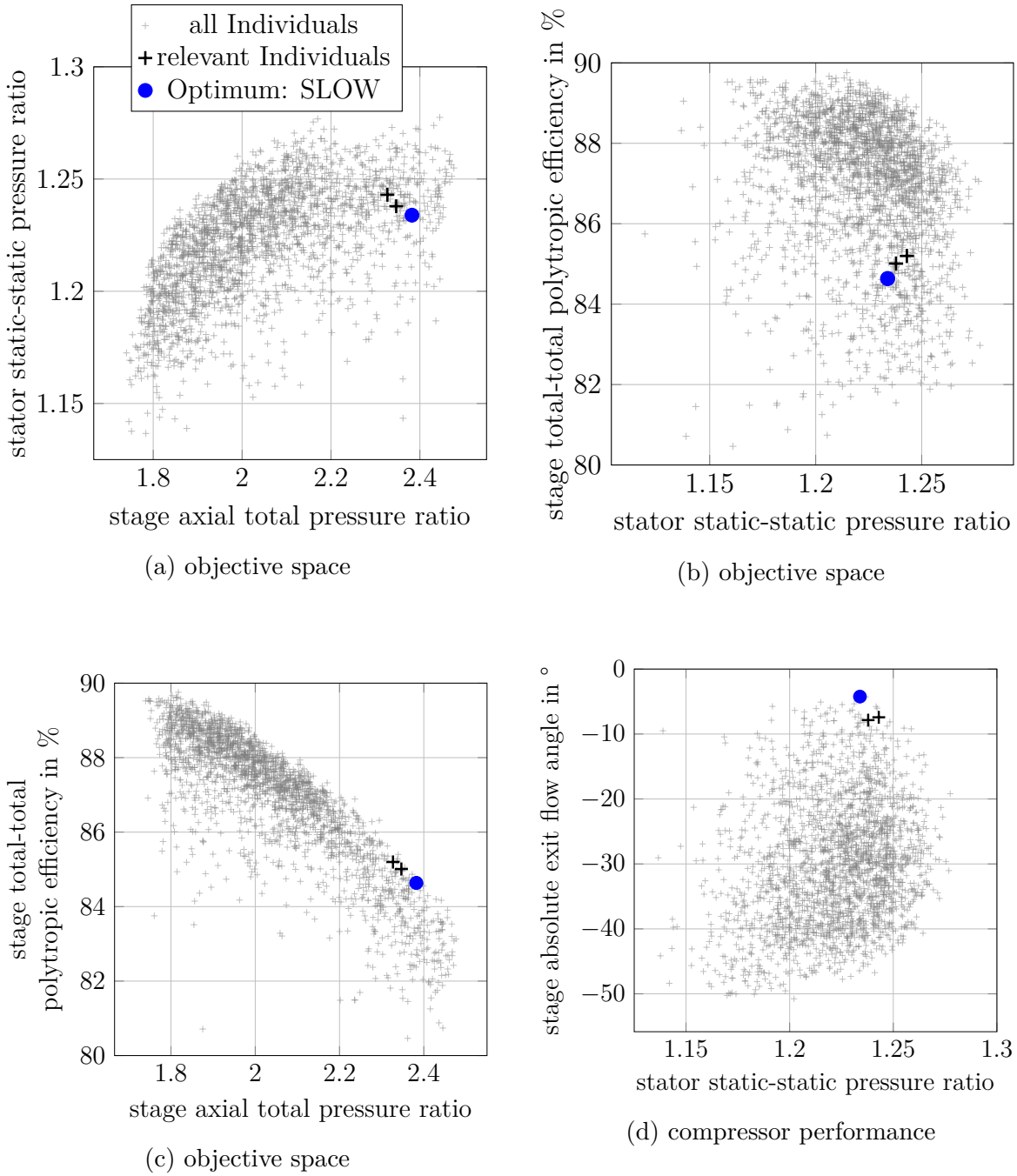

(a) objective space

(b) objective space

(c) objective space

(d) compressor performance

Figure A.23: Results of the stage optimization with SLOW rotor: Objective space and compressor performance of all relevant individuals.

A.6 Compressor Maps

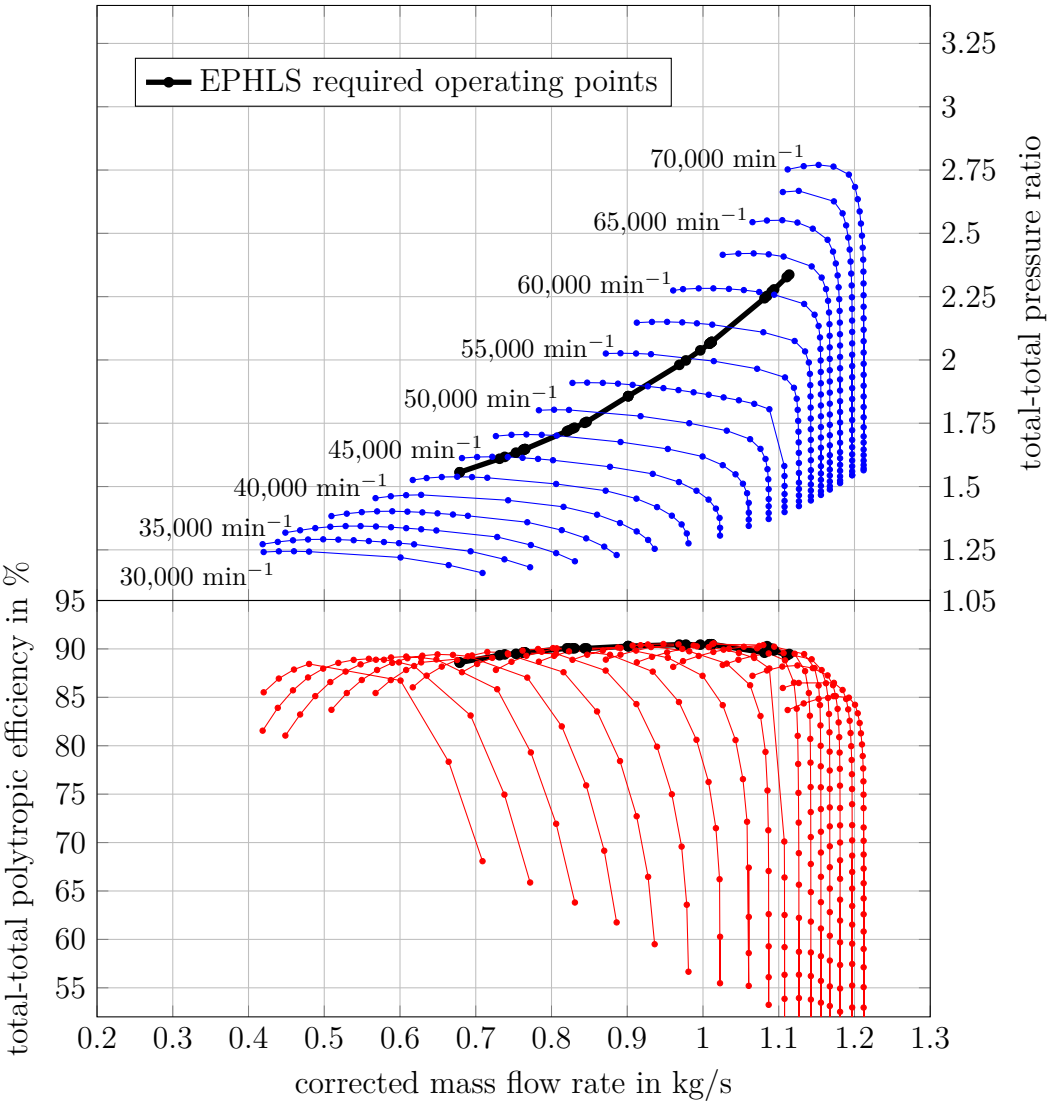

Figure A.24: Compressor map of scaled FAST compressor.

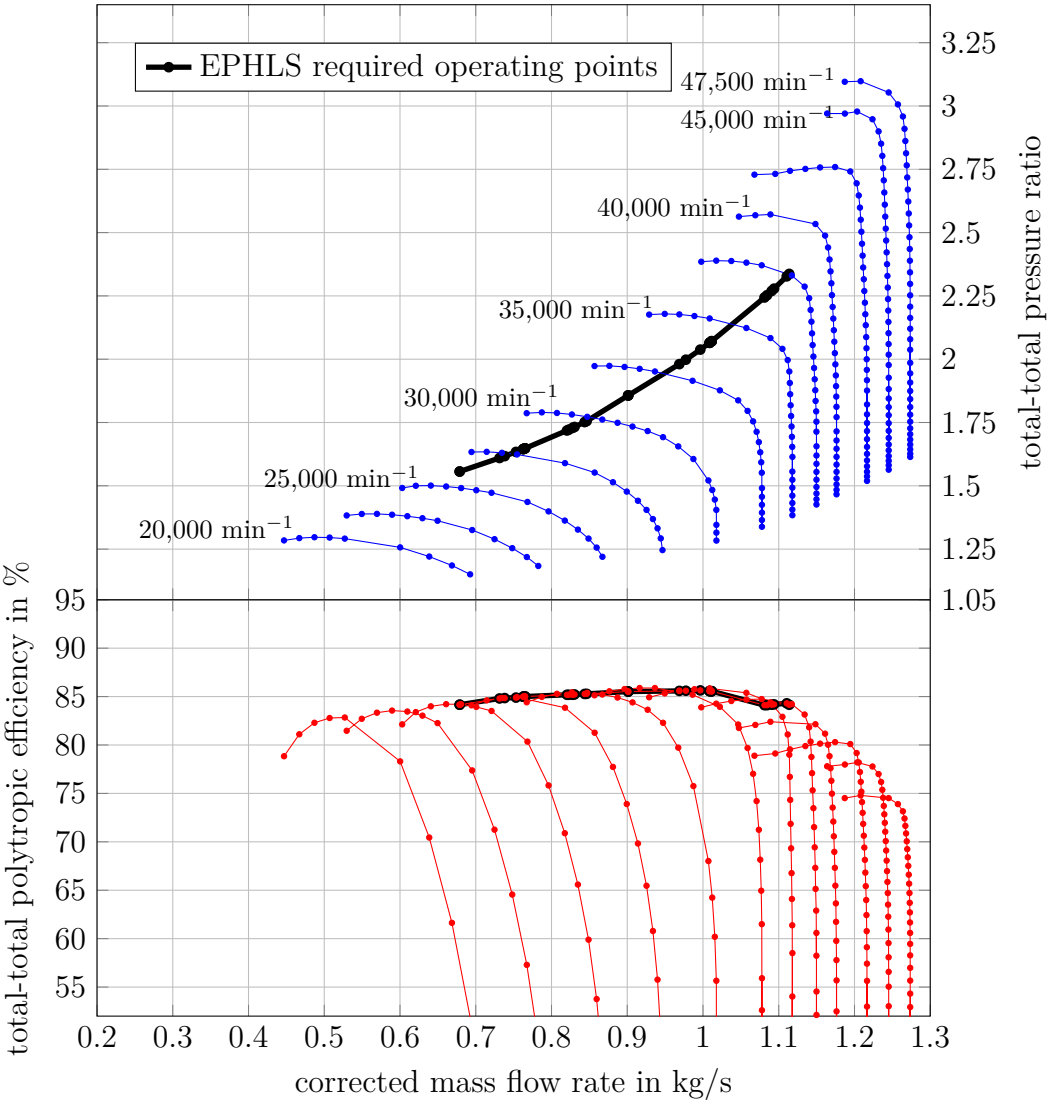

Figure A.25: Compressor map of scaled SLOW compressor.

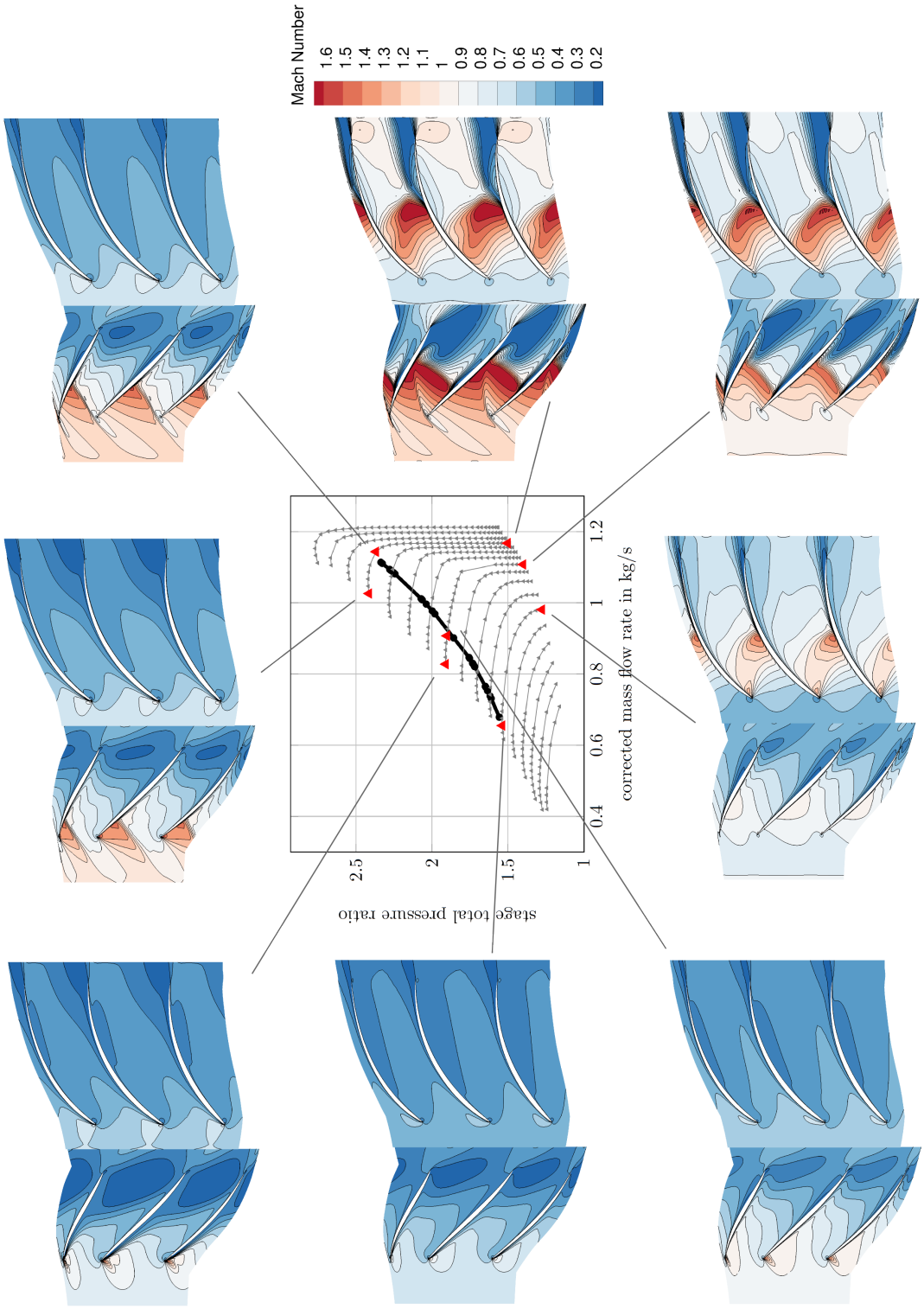

Figure A.26: Mach contours at different operating conditions of the FAST stage.

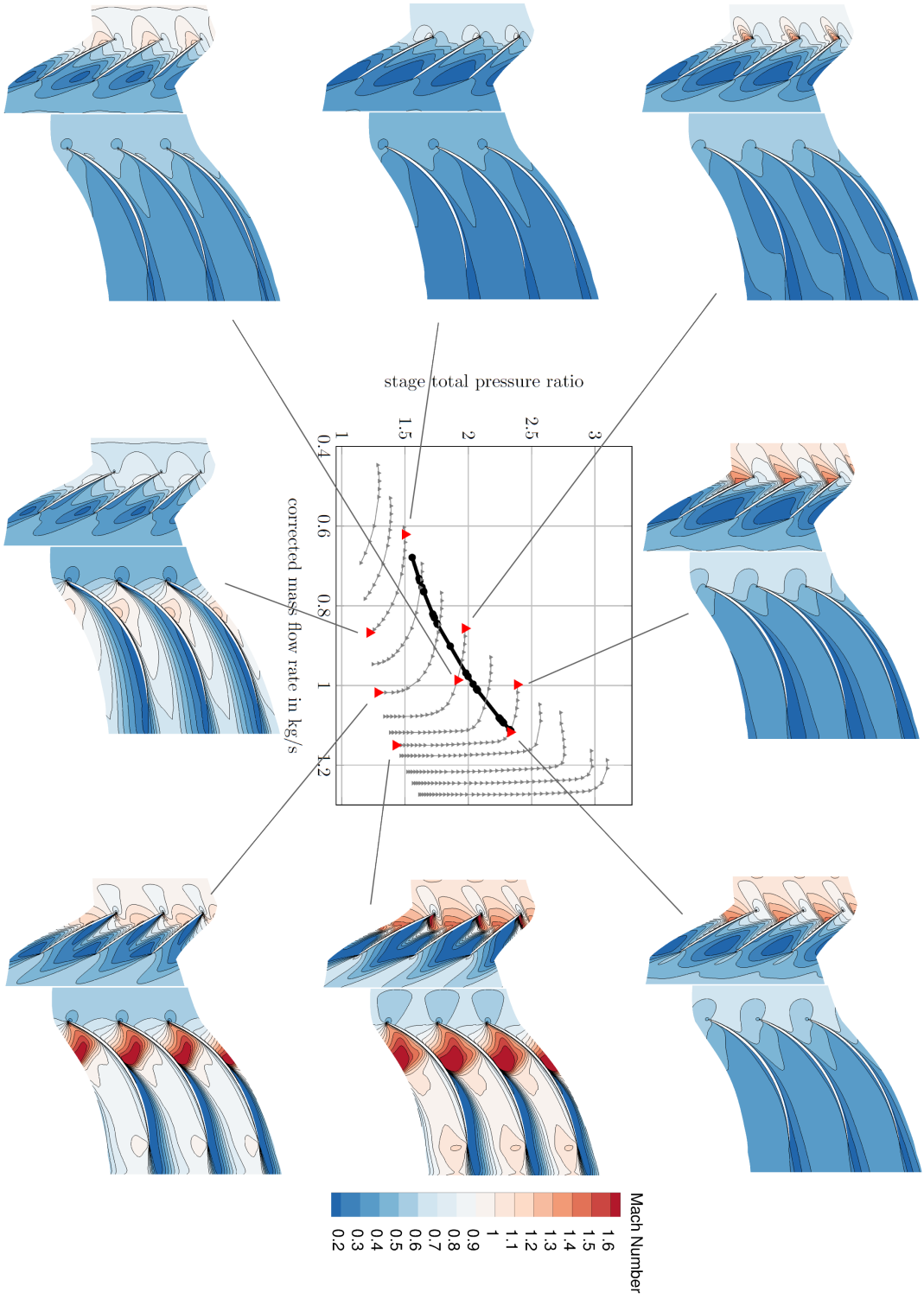

Figure A.27: Mach contours at different operating conditions of the SLOW stage.

A.7 Rotor: Aerodynamic Effects

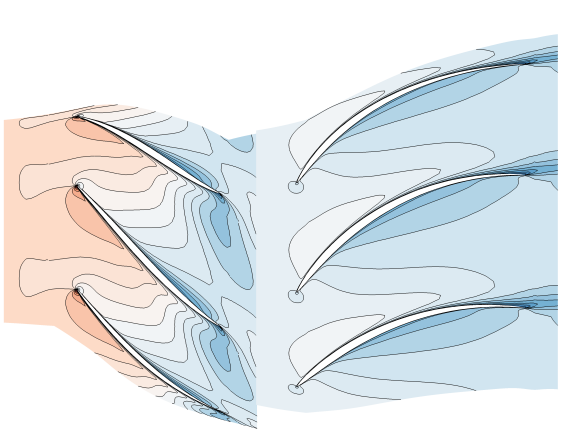

(a) Mach slice of scaled stage: FAST

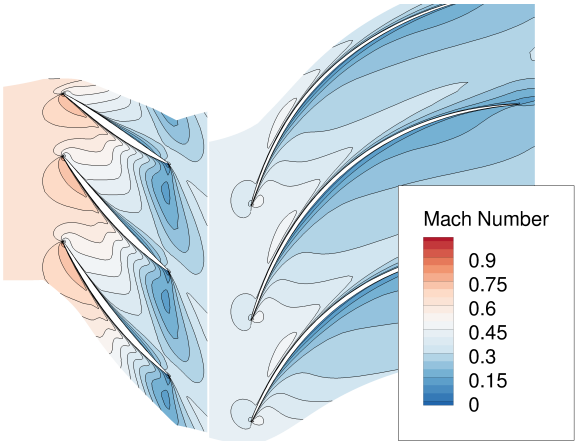

(b) Mach slice of scaled stage: MEAN

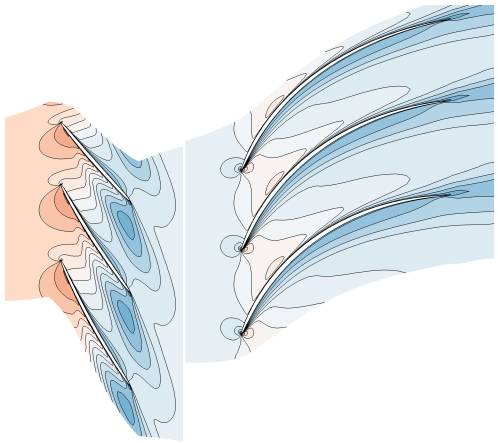

(c) Mach slice of scaled stage: SLOW

Figure A.28: Mach slice in the tip region of the scaled stages at part load ($\dot{m}_{\text{corr}} \approx 0.75$ kg/s and $\Pi_{\text{tt}} \approx 1.45$).

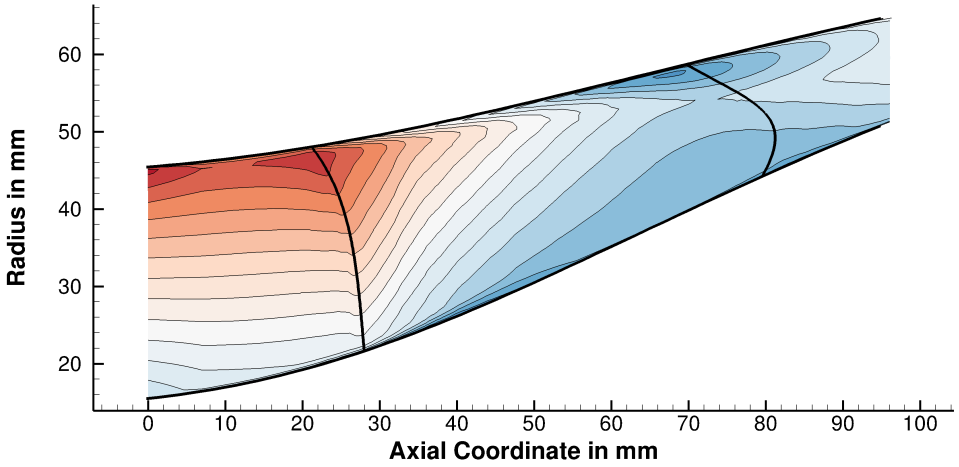

(a) S2 Mach contour of rotor: FAST

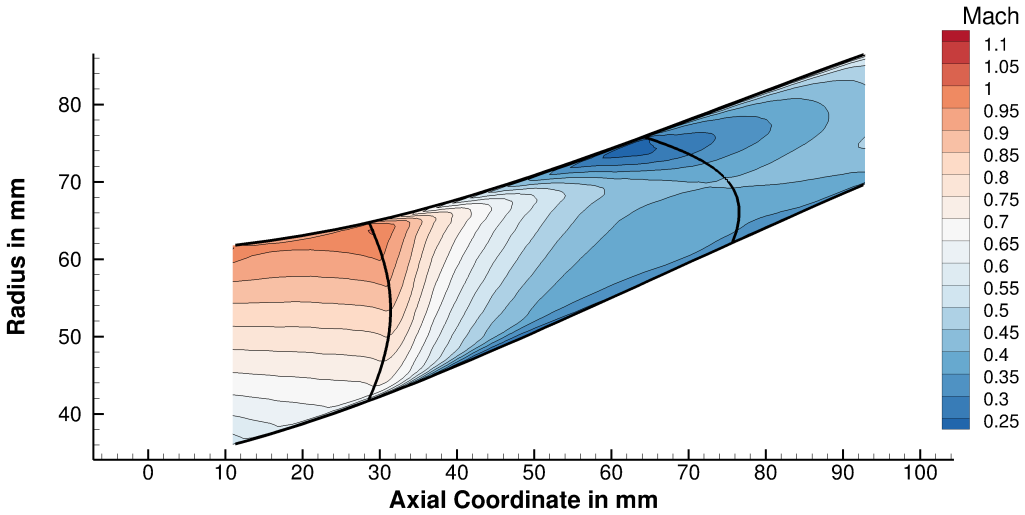

(b) S2 Mach contour of rotor: MEAN

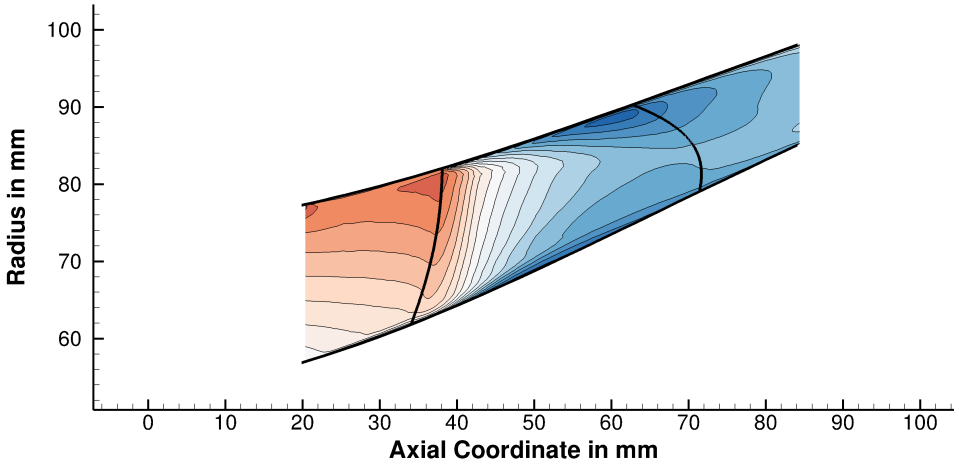

(c) S2 Mach contour of rotor: SLOW

Figure A.29: S2 circumferentially averaged Mach contour of the rotors.

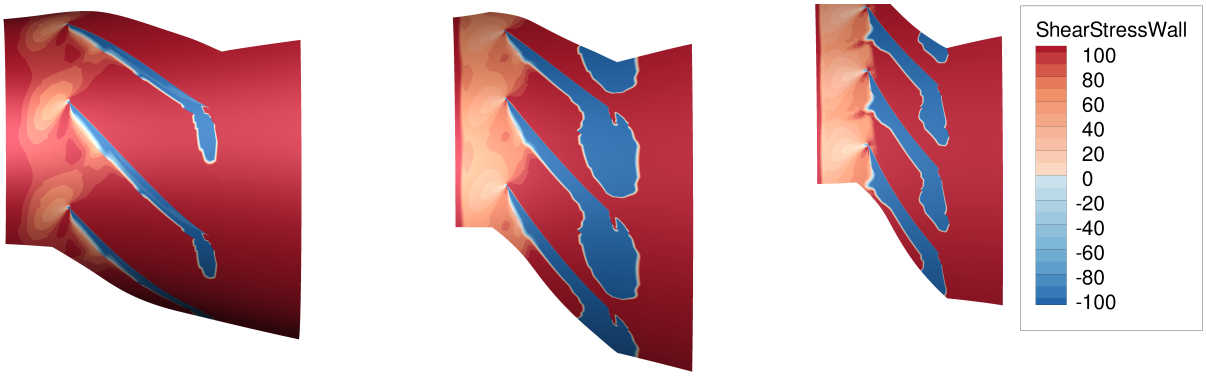

(a) FAST (b) MEAN (c) SLOW

Figure A.30: Wall shear stress contour at casing of reference rotor designs.

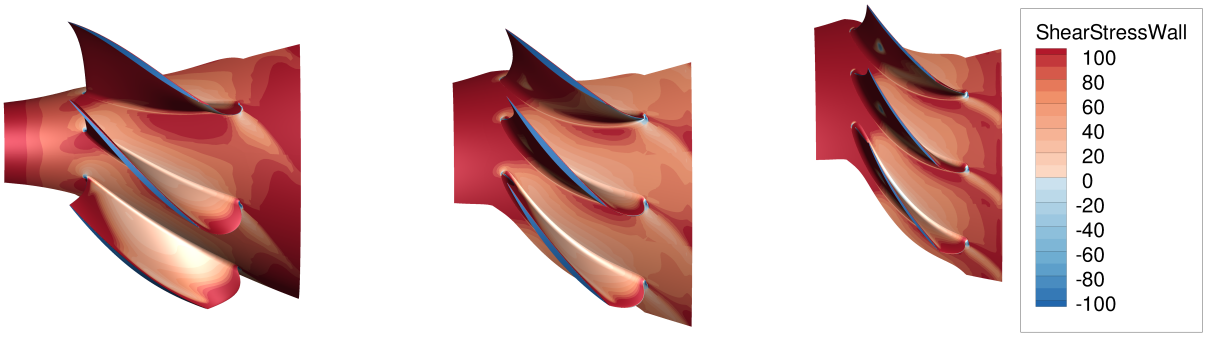

(a) FAST (b) MEAN (c) SLOW

Figure A.31: Wall shear stress contour at hub of reference rotor designs.

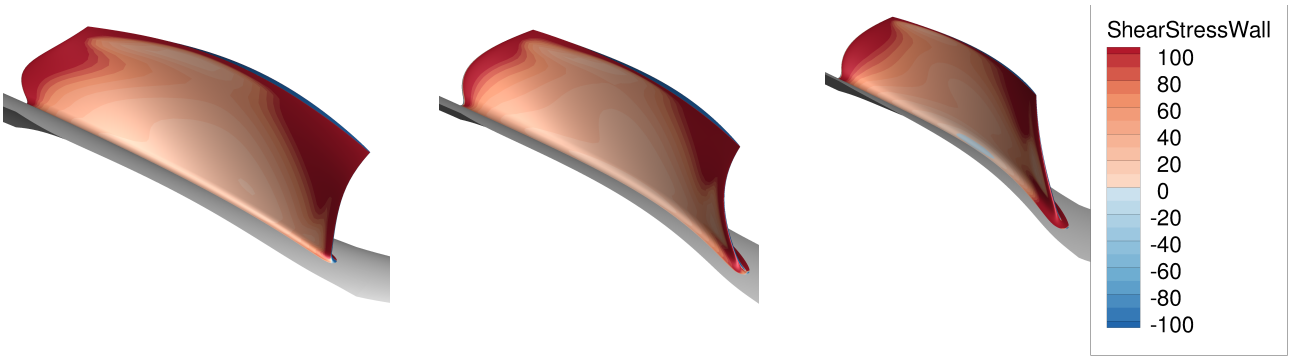

(a) FAST (b) MEAN (c) SLOW

Figure A.32: Wall shear stress contour at pressure side of reference rotor designs.

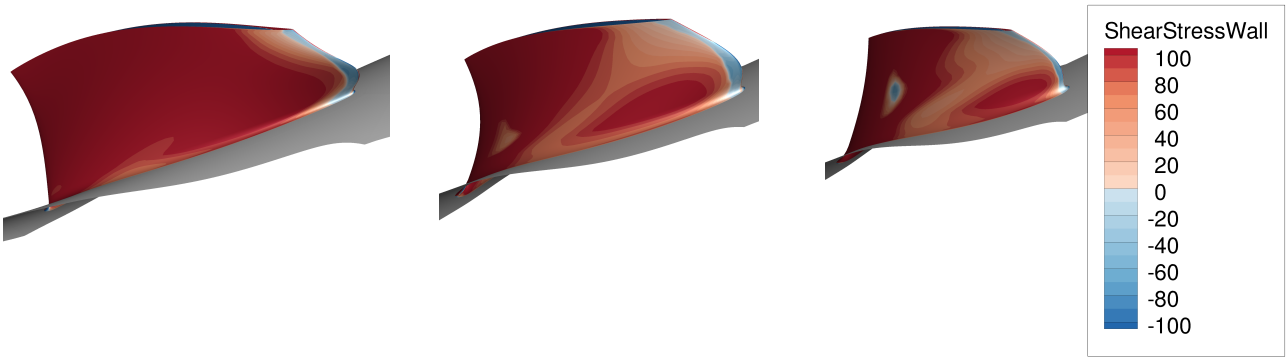

(a) FAST (b) MEAN (c) SLOW

Figure A.33: Wall shear stress contour at suction side of reference rotor designs.

Table A.10: Performance data of the MEAN rotor CFD model studies at a corrected mass flow rate of 1.107 kg/s and a corrected rotational speed of 43750 min^{-1}.

CFD study	total total polytropic efficiency		total total pressure ratio	
	value	rel. deviation	value	rel. deviation
reference	0.93	0 %	2.27	0 %
"no gap"	0.94	1 %	2.3	1.2 %
"Euler"	0.995	6.4 %	2.4	4.7 %
"straight"	0.969	3.6 %	1.58	-30.5 %

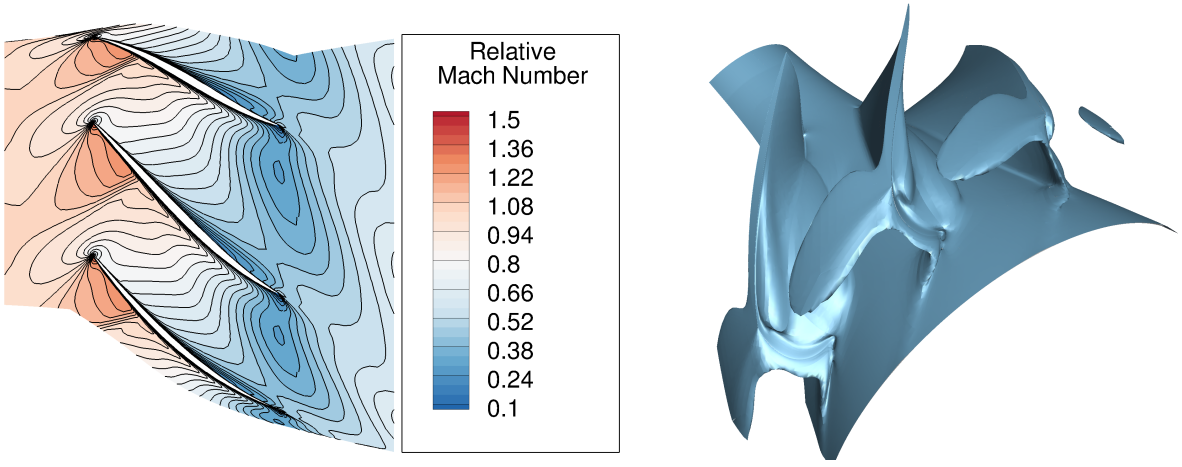

Figure A.34: FAST rotor: Overview of low momentum region of the comprehensive reference CFD model.

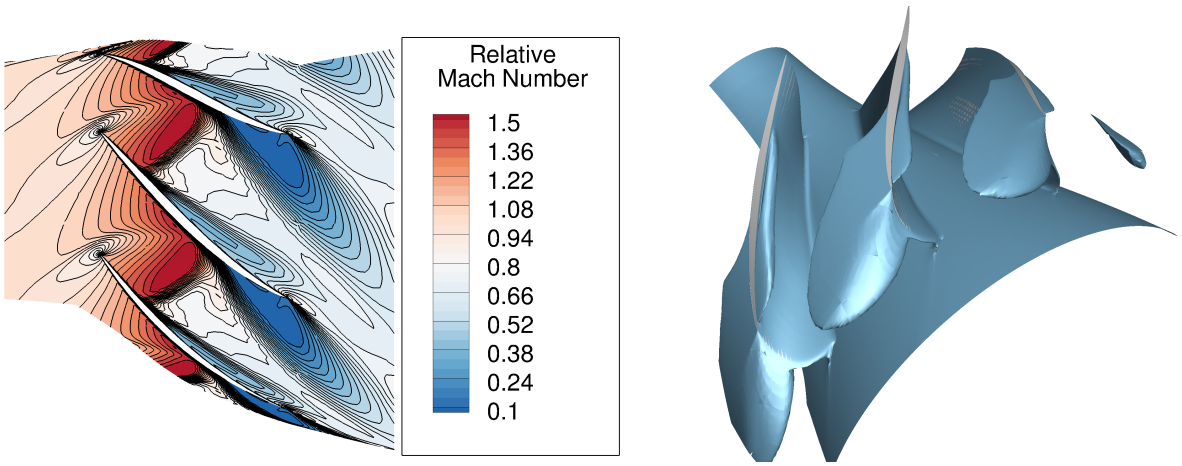

Figure A.35: FAST rotor: Overview of low momentum region of the CFD "no gap" model without tip clearance.

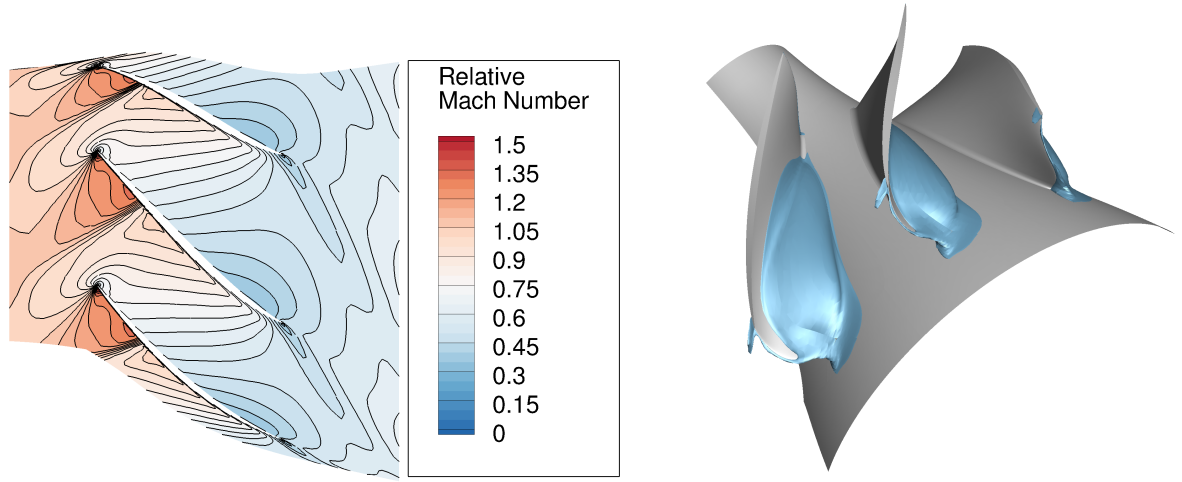

Figure A.36: FAST rotor: Overview of low momentum region of the CFD "Euler" model without tip clearance, wall friction, and viscous flow effects.

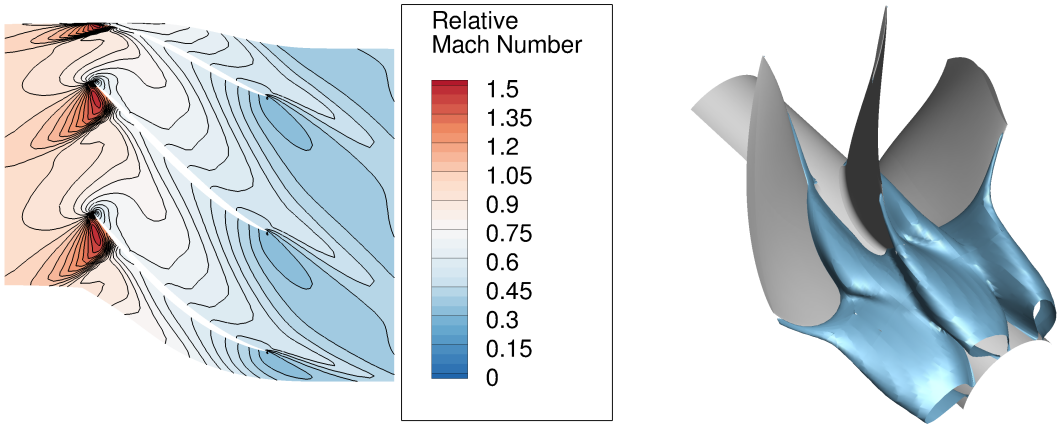

Figure A.37: FAST rotor: Overview of low momentum region of the CFD "straight" model without tip clearance and wall friction, and with a straight meridional channel.

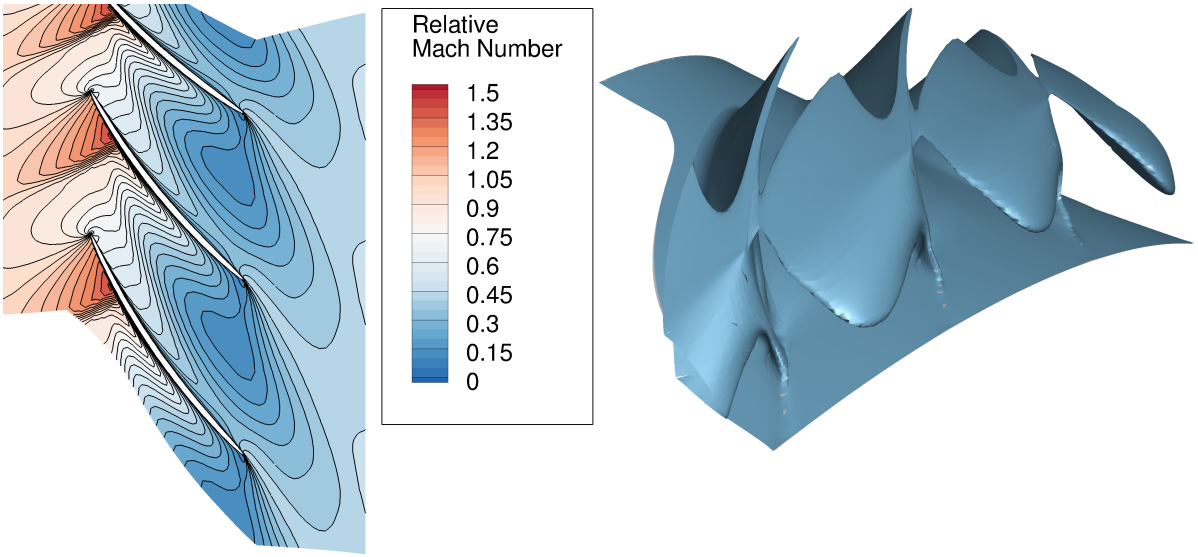

Figure A.38: SLOW rotor: Overview of low momentum region of the comprehensive reference CFD model.

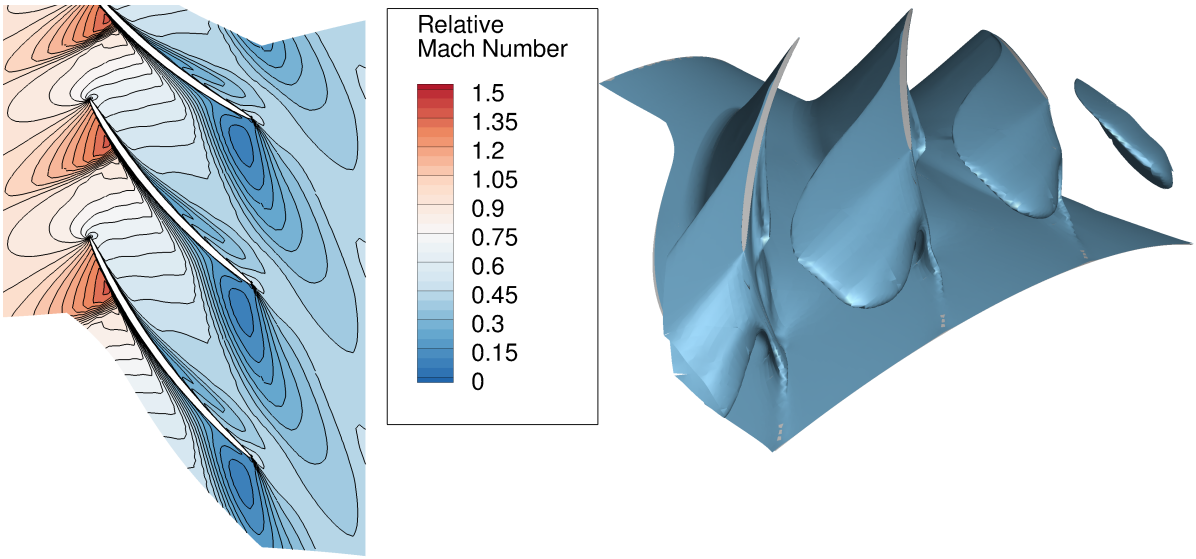

Figure A.39: SLOW rotor: Overview of low momentum region of the CFD "no gap" model without tip clearance.

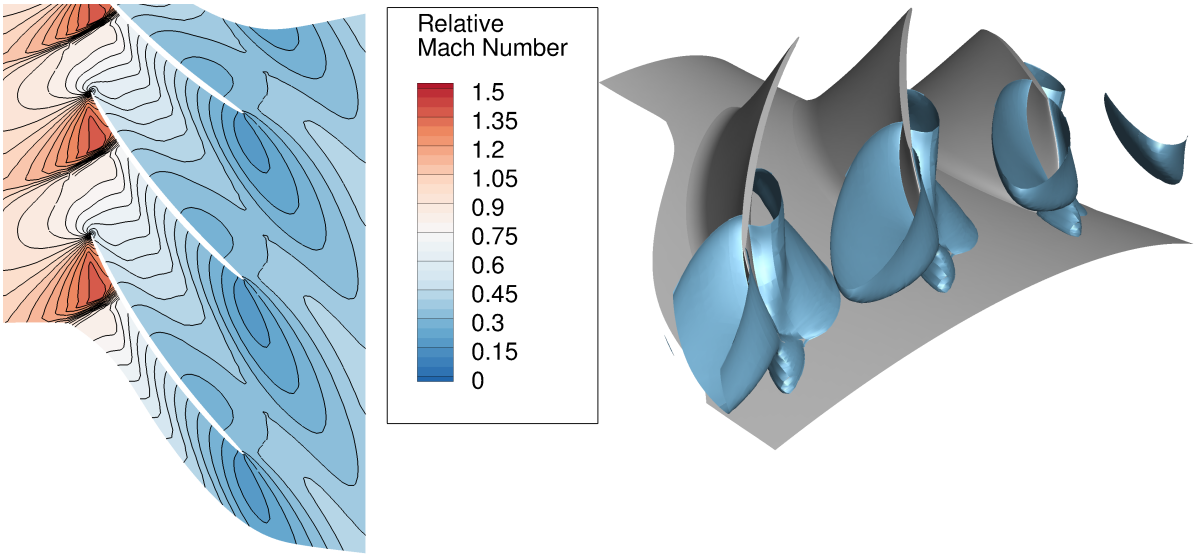

Figure A.40: SLOW rotor: Overview of low momentum region of the CFD model without tip clearance, wall friction but k-ω-turbulence model.

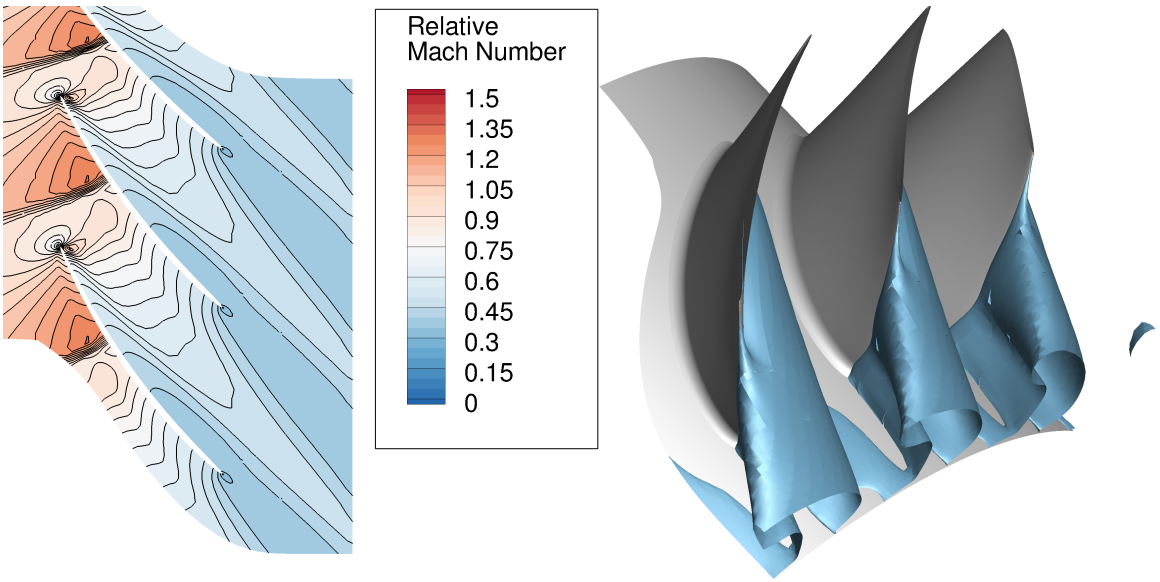

Figure A.41: SLOW rotor: Overview of low momentum region of the CFD "straight" model without tip clearance and wall friction, and with a straight meridional channel.

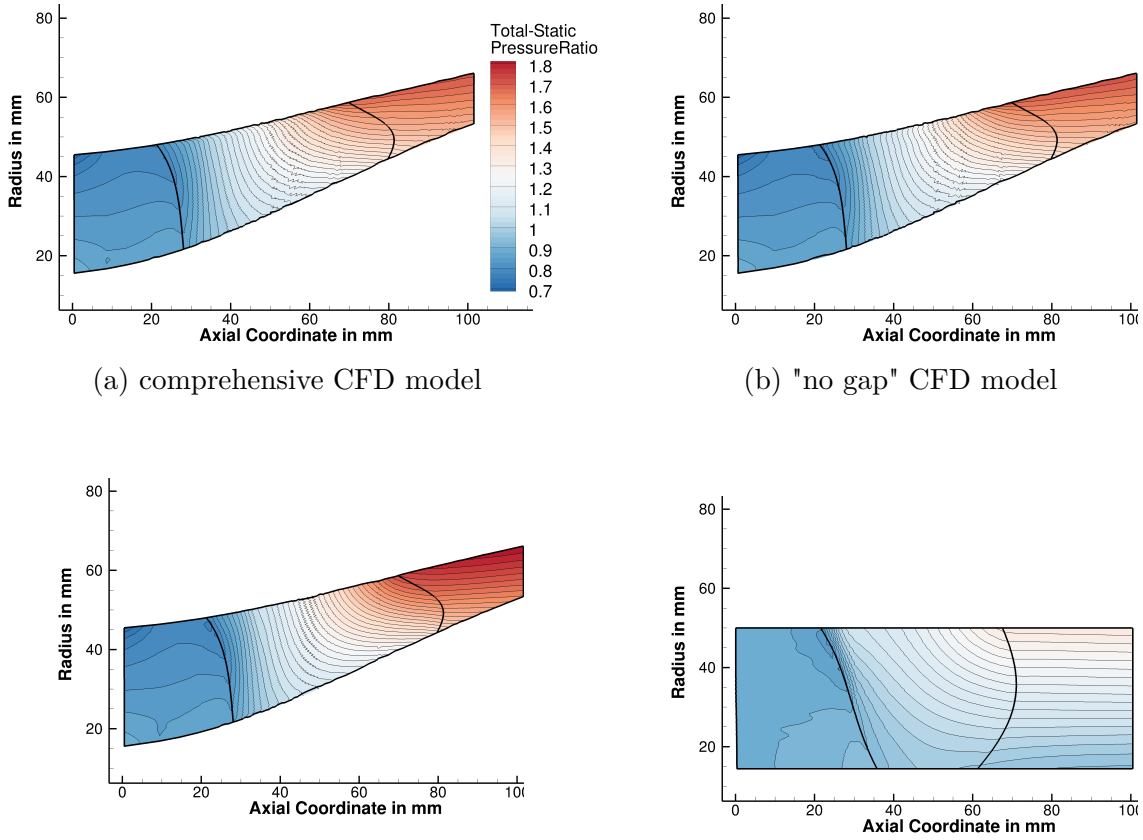

(a) comprehensive CFD model

(b) "no gap" CFD model

(c) "no gap" without wall friction model CFD model

(d) "straight" CFD model

Figure A.42: S2 static pressure contours of FAST rotor normalized by the absolute total inlet pressure.

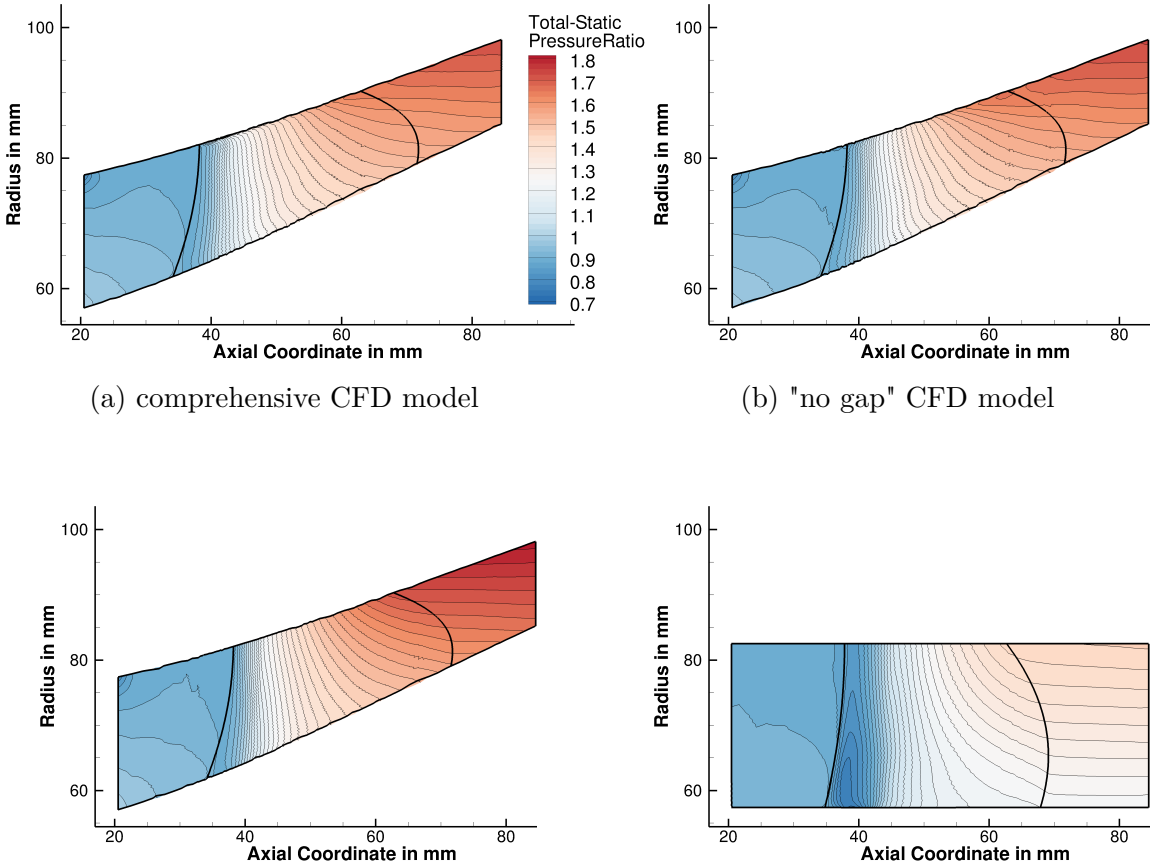

(a) comprehensive CFD model

(b) "no gap" CFD model

(c) "Euler" CFD model

(d) "straight" CFD model

Figure A.43: S2 static pressure contours of SLOW rotor normalized by the absolute total inlet pressure.

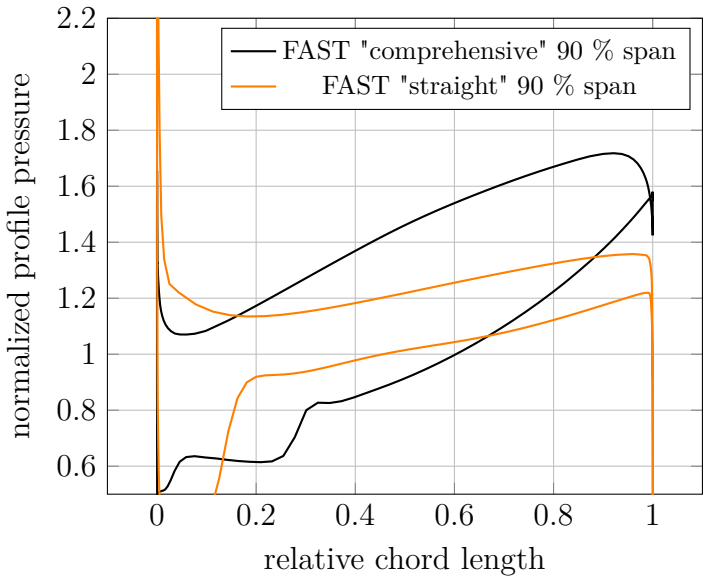

Figure A.44: Comparison of the profile pressure distribution, normalized by the absolute total inlet pressure, for the "comprehensive" and "straight" CFD model of the MEAN rotor.

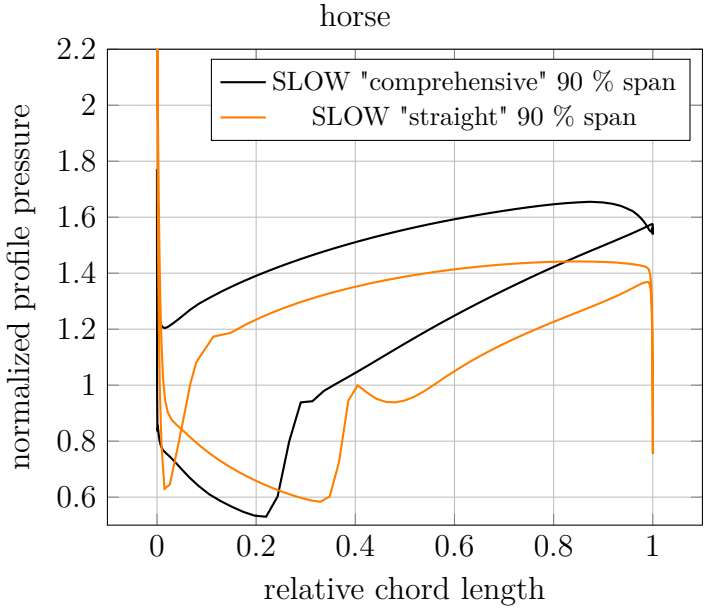

Figure A.45: Comparison of the profile pressure distribution, normalized by the absolute total inlet pressure, for the "comprehensive" and "straight" CFD model of the MEAN rotor.

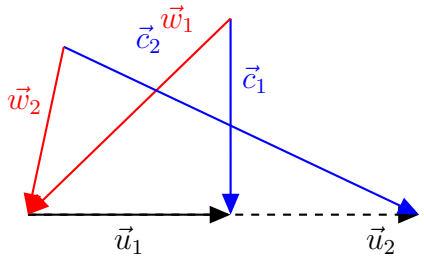

(a) 10% span

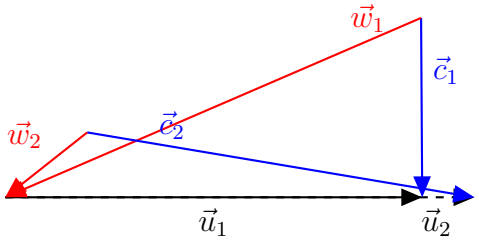

(b) 50% span

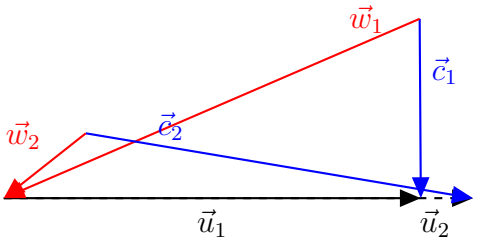

(c) 90% span

Figure A.46: Comparison of the velocity triangles of the FAST rotor, "comprehensive" CFD model at different spanwise positions.

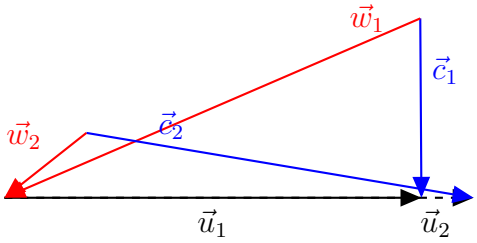

(a) 10% span

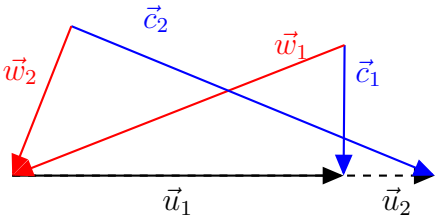

(b) 50% span

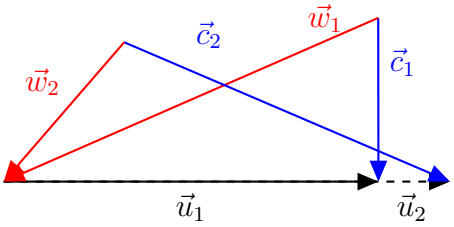

(c) 90% span

Figure A.47: Comparison of the velocity triangles of the SLOW rotor, "comprehensive" CFD model at different spanwise positions.

A.8 Stage: Aerodynamic Effects

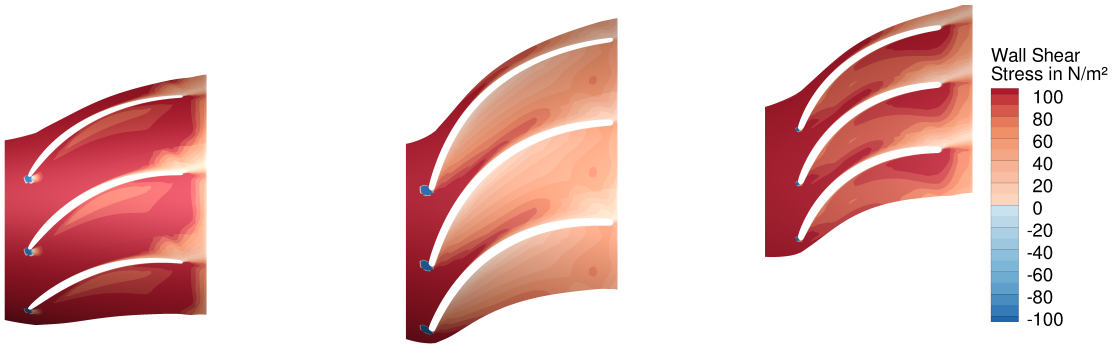

(a) FAST (b) MEAN (c) SLOW

Figure A.48: Wall shear stress contour at casing of reference stator designs.

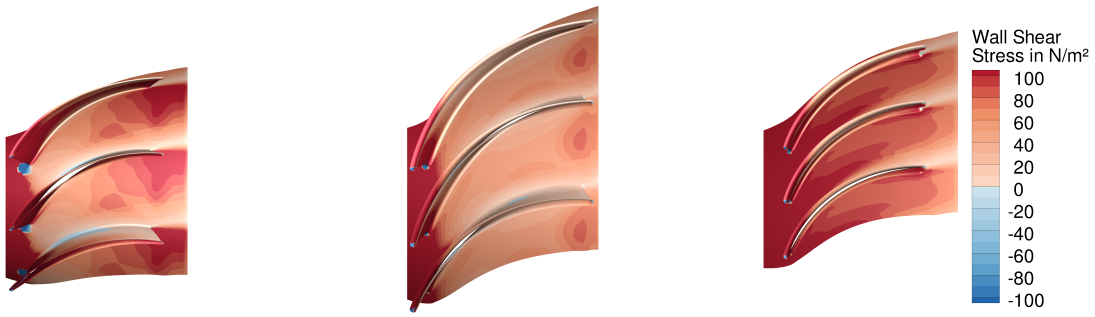

(a) FAST (b) MEAN (c) SLOW

Figure A.49: Wall shear stress contour at hub of reference stator designs.

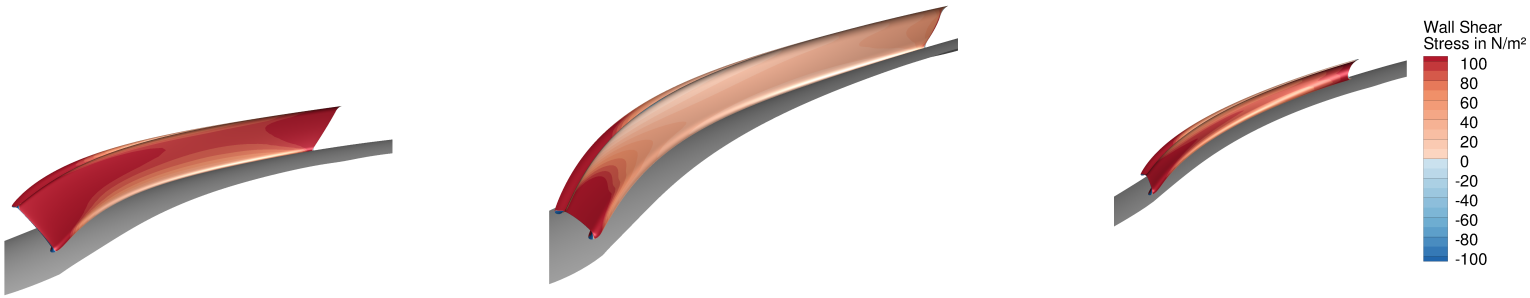

(a) FAST (b) MEAN (c) SLOW

Figure A.50: Wall shear stress contour at pressure side of reference stator designs.

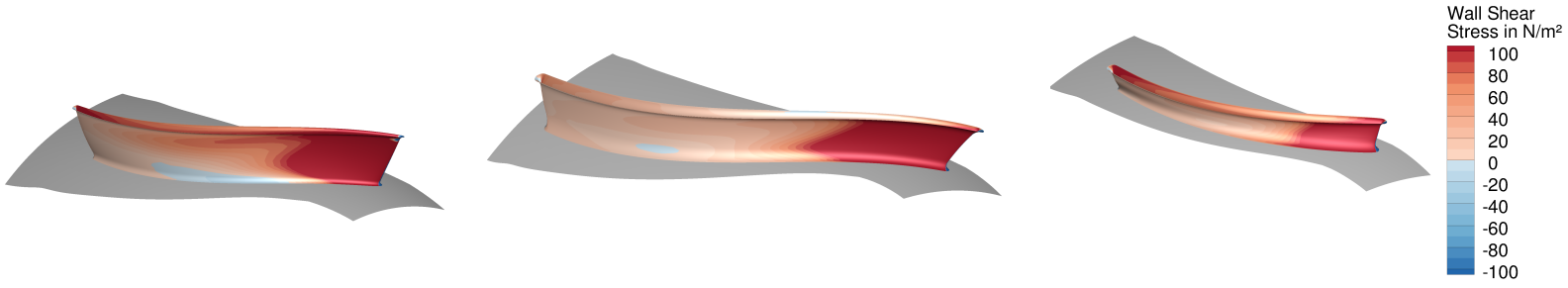

(a) FAST (b) MEAN (c) SLOW

Figure A.51: Wall shear stress contour at suction side of reference stator designs.

Educational Background

Personal Information

name	Sönke Holger Teichel
date of brith	May 14th 1986
place of birth	Hamburg, Germany
martial status	married

School Education

1998 - 2005	Humboldtschule Hannover Gymnasium

Military Service

2005 - 2006	Medical Service, Nienburg an der Weser

Academic Studies

2006 - 2010	Leibniz Universität Hannover Study: Mechanical Engineering
2010 - 2012	University of Wisconsin Madison, USA Degree: Master of Science in Mechanical Engineering
2012 - 2017	Leibniz Universität Hannover PhD study Mechanical Engineering

Occupation

since 2017	Development Engineer at IHI Charging Systems International GmbH, Heidelberg
2012 - 2016	Research Assistant at the Institute of Turbomachinery and Fluid Dynamics of the Leibniz Universität Hannover

Hannover, July, 2018